

**PALACKÝ UNIVERSITY
OLOMOUC
FACULTY OF SCIENCE**

DOCTORAL DISSERTATION

Ladislav Stanke

2016

**PALACKÝ UNIVERSITY
OLOMOUC
FACULTY OF SCIENCE**

DEPARTMENT OF EXPERIMENTAL PHYSICS



DOCTORAL DISSERTATION

**Design and Analysis of Optical Elements and Devices for
PW Laser Systems**

Author:	RNDr. Mgr. Ladislav Stanke
Study Programme:	Physics
Field of Study:	Applied Physics
Form of study:	Full-time
Supervisor:	Ing. Jaromír Křepelka, CSc.
Submission date:	

*On a certain day when the Blessed One dwelt at
Jetavana, the garden of Anathapindika,
a celestial deva came to him in the shape of
a Brahman enlightened and wearing clothing as
white as snow.*

The deva said,

*What is the greatest gain? What is the greatest
loss? Which armour is invulnerable? What is
the best weapon?*

The Blessed One replied,

*The greatest gain is to give to others; the
greatest loss is to greedily receive without
gratitude; an invulnerable armor is **patience**;
the best weapon is **wisdom**.*

*I would like to dedicate this dissertation
to my dear parents and my beloved
girlfriend Lucie*

Statement:

The undersigned author confirms that the doctoral thesis presented here has been developed independently under the supervision of Ing. Jaromír Křepelka, CSc. and all sources are cited.

September 8, 2016, in Olomouc

.....

Acknowledgement:

The author acknowledges the kind help and support of the following people, institutions and funding bodies.

First of all, he would like to thank his supervisor, Ing. Jaromír Křepelka, CSc., for wise and kind leadership during the preparation process of the proposed dissertation. Another important person that needs to be mentioned is RNDr. Miroslav Palatka, who has been an outstanding consultant in the area of optical system design. And thanks to Dr. Anita Thakur for her long-term cooperation on beamline simulations. The author is also grateful to the Institute of Physics of the Academy of Sciences of the Czech Republic, most of all he appreciates the support of ELI-Beamlines, and technical director Prof. Bruno Le Garrec for granting the author's internship in the group of Applied Computational Optics at the Institute of Applied Physics of the Friedrich-Schiller-Universität Jena, Germany. He is also very thankful to group leader Prof. Dr. Frank Wyrowski, who invited him for a research internship to Jena and supported his work on the doctoral dissertation presented here. The author would also like to thank Mick Thompson, who did the proofreading of this dissertation.

Dissertation research has been supported by Internal Grant of Palacky University (IGA_PrF_2015_004).



Bibliografická identifikace:

Jméno a příjmení autora:	RNDr. Mgr. Ladislav Stanke
Název práce:	Návrh a analýza optických prvků a zařízení pro PW laserové systémy
Typ práce:	Doktorská
Pracoviště:	Společná laboratoř optiky Univerzity Palackého a Fyzikálního ústavu Akade- mie věd České republiky
Vedoucí práce:	Ing. Jaromír Křepelka, CSc.
Rok obhajoby práce:	2016

Abstrakt: Hlavním cílem předložené disertační práce je vylepšení procesu optického návrhu řešením Maxwellových rovnic za pomoci v současnosti jednoho z nejpokročilejších optických simulačních programů – Wyrowski VirtualLab Fusion, který je rovněž testován před integrací do struktury VBL (Virtual Beamline). Proces přednávrhu optických soustav je proveden pomocí programu Zemax|OpticStudio 15 za použití běžného trasování paprsků, zatímco jejich ověření a optimalizace z hlediska fyzikální optiky je provedena metodou Unified Field Tracing v programu VirtualLab Fusion. Práce je zaměřena zejména na analýzu přenosových soustav pro vysokovýkonové lasery vycházejících z jejich návrhu. Nově představený postup si klade za cíl ukázat další možnosti vývoje optických prvků s využitím metod vlnové optiky v pracovním procesu optického designéra.

Klíčová slova:	difraktivní/geometrické/unifikované trasování polí, optické modelování a simulace, přenos svazků, transportní optika, ultrakrátké pulzy, Wyrowski VirtualLab Fusion, Zemax OpticStudio;
Počet stran:	168
Počet příloh:	2
Jazyk:	anglický

Bibliographical identification:

Author's first name and surname: RNDr. Mgr. Ladislav Stanke
Title: Design and Analysis of Optical Elements
and Devices for PW Laser Systems
Type of thesis: Doctoral
Department: Joint Laboratory of Optics of Palacky
University and Institute of Physics
of the Czech Academy of Sciences
Supervisor: Ing. Jaromír Křepelka, CSc.
Year of presentation: 2016

Abstract: The goal of this thesis is to show a method for enhancing the lens designing process by solving Maxwell's equations, with the help of advanced optical simulation software – Wyrowski VirtualLab Fusion. The predesigning process (ray-tracing) is conducted by Zemax|OpticStudio 15, whereas the physical optics analysis and optimization is accomplished by Unified Field Tracing within VirtualLab Fusion. This software has also been tested before its implementation to VBL (Virtual Beam-line) framework, however this thesis is focused on the design of relay systems for high power lasers. The suggested approach for this novel lens designing process reveals new possibilities for optical engineering workflow.

Keywords: Beam transport, Diffractive/Geometric/Unified field tracing, optical modelling and simulation, relay optics ultrashort pulses, Wyrowski VirtualLab Fusion Zemax OpticStudio;

Number of pages: 168
Number of appendices: 2
Language: English

Contents

1	Introduction	11
2	Structure of the Dissertation	14
3	State of the Art	16
3.1	Optical Systems in High Power Laser Facilities	18
3.2	Relay Trains and Afocal Systems	30
3.3	Simulation Software in High Power Laser Facilities	34
4	Hypothesis	44
4.1	Aims and Objectives	44
5	Contribution to Knowledge	47
6	Optical Simulation Software	48
6.1	Zemax OpticStudio	48
6.1.1	Physical Optics Propagation	50
6.2	Wyrowski VirtualLab Fusion	61
6.2.1	Free Space Operators	63
6.2.2	Geometric Field Tracing Plus (Beta)	67
7	Suggested Workflow	69
8	Optical Modeling and Design	72
8.1	Free Space Propagation	72
8.1.1	Continuous Wave Propagation	74
8.1.2	Ultra-short Pulse Propagation	83
8.2	Beam Clipping	85
8.3	Focusing by an Ideal Lens	86
8.3.1	Fits of logarithmed values of $ E_x $	89
8.3.2	Strehl Ratio	93
8.3.3	Encircled Energy	94
8.4	Transmissive Optics	99
8.4.1	4- f Relay Systems	99
8.4.2	Beam Expanders/Reducers	102
8.5	Reflective Optics	114
8.5.1	Beam Relaying	114
8.5.2	Catoptric Reducers	124
8.5.3	Telescopes for Beam Diagnostics	136

8.6	Beamlines	145
8.6.1	L1-E1	147
8.6.2	L3-E3	150
9	Overall Discussion and Assessment	162
10	Conclusions and Future Work	167
	Photo Attachment	169
	References	175
	List of Author's Publications	181
	Index	186
	Appendix	187
	Summary of Ongoing Optical Simulations	187
	L3 - E3: Holey Mirror simulations	213

1 Introduction

Extreme Light Infrastructure (ELI) Beamlines [1] is a highly challenging project in terms of both scientific and engineering aspects. These two specific aspects are also characteristic for the two distinct phases of the project. While the preparatory stage should be handled by means of various engineering approaches, the latter, operational phase, will mostly be the domain for the application of miscellaneous experimental scientific methods.

In the first stage, optical engineering plays one of the vital roles in the ELI-Beamlines project. The two main tasks to be solved in this dissertation are the two main tasks of optical designers and engineers, beam transport and beam focustion. Both of these tasks have also been somewhat solved by ELI predecessors, but ELI represents a whole new level of laser intensities and ultra short pulse durations, which can be accessed by this new facility. According to the ELI Whitebook [2], ELI will be the first infrastructure to achieve intensities $I > 10^{24} \text{ W} \cdot \text{cm}^{-2}$. Huge surface power will be obtained by producing kJ of energy over 10 fs and focusing of such energy over a micrometer size spot will lead to the achievement of highest intensity, including extraordinary beam sizes. The L4¹ top-hat beam is inside a $400 \times 400 \text{ mm}^2$ aperture, and if the misalignments are considered, the simulation area for such a beam should be at least $600 \times 600 \text{ mm}^2$ [3]. It is obvious that not only the fabrication of optical elements for such a laser facility will be challenging, but also simulation of the optical systems themselves. Due to the high peak power, diffraction effects and extreme short pulse duration, these simulations are not typically solved by common optical designer's software, like Zemax. According to the author's master thesis [4] LightTrans VirtualLab seems like a good tool for simulations of optical systems – mainly relaying and focusing optics for large aperture pulsed beams of top-hat intensity profile.

On September 8 and 9 of 2014 a *Beam propagation method workshop* took place in the ELI office building in Harfa, Prague. It was agreed that VirtualLab represents one of the most sophisticated tools for solving this significant task that was commercially available at that time, which also meets the requirements of ELI facility.

The author was given a unique opportunity to stay for an internship (April – July 2015) in the Applied Computational Optics group [5], lead by professor Frank Wyrowski, at the Institute of Applied Physics of the Friedrich-Schiller-Universität, Jena. Moreover, the author was directly connected with all of the creators of VirtualLab in Jena, Germany, where LighTrans International UG (haftungsbeschränkt) [6], and Wyrowski Photonics UG (haftungsbeschränkt) [7] are also located. These companies were founded personally by the professor Frank Wyrowski. His PhD students

¹One of the beams. Beams are designated L1, L2, L3 and L4.

in the Applied Computational Optics group not only use VirtualLab for innovative simulations, but also maintains a close relationship with the developers and steadily improve the software.

Before this research internship could happen numerous minor, but also important, problems were addressed and solved via electronic communication during earlier years of study. This tight relationship and collaboration of the dissertation author with the creators of VirtualLab enabled the software creators to tune this software exactly to meet the highly specific expectations of ELI Beamlines. Besides all of this, the author was invited to become an alpha tester working on the early version of the brand new Wyrowski VirtualLab Fusion.

Wyrowski VirtualLab Fusion is a powerful optical simulation software bundle of the new generation that is not based on ray-tracing methods. The concept of so-called *Field tracing*, first introduced in LightTrans VirtualLab, evolved into two specific approaches for solving Maxwell's equations. One of these approaches is called *Geometric field tracing* [8], which can be summarized as "smart" ray tracing and it is useful in all wavefront dominated simulation scenarios. The latter one, called *Diffraction field tracing*, is especially advantageous in all situations where focusing of the field occurs. In these cases, the transverse dimensions of the electromagnetic field are too small to be wavefront dominated, and the fusion of these two methods create so called *Unified field tracing*.

Unfortunately, on November 13, 2015 the tendering process for the public contract "Performance Software: Beam Propagation Method (BPM)" was officially cancelled by the director of the Institute of Physics. Resultingly, this thesis cannot show the designs of all optical systems and their simulations within the BPM software. Rather, it demonstrates all possible scenarios and workflows within the ELI-Beamlines facility that can be solved by VirtualLab Fusion. With the persistent technical support from Wyrowski Photonics, the author continues to conduct the majority of tasks originally assigned to the whole BPM group, which was also dismantled during February of 2016.

This thesis will show how this software can solve typical ELI Beamlines' simulation scenarios and how this software can entirely change the optical designer's thinking.

The main method used throughout this thesis is to apply a brand new and more advanced approach to optical systems' analysis and their design, employing a more sophisticated and physically precise technique than just ray-tracing. The original goal of analyzing optical systems was based on the solution of two specific tasks. Firstly, assessment and assistance with improving VirtualLab Fusion before its implementation to the BPM (*Beam Propagation Method*) within the frame of the VBL (*Virtual Beamline*). Secondly, designing optical systems specifically created for ELI-Beamlines specifications and their modelling and simulation in VirtualLab Fusion.

The main point of this thesis focused on the temporal effects of optical systems and their thin film optical structures applied to ultra-short pulses, and diffraction effects caused either by finite dimensions of optical systems, or by beam propagation itself. These aspects are typically not the center of interest for most designers developing visual systems for non-coherent light conditions.

As of 2016, the author also aids other subgroups with optical simulations needed to solve their own specific tasks - for example, calculation of focal spots for betatron simulations (in collaboration with Dr. Anita Thakur, Dr. Kateřina Falk and Dr. Michal Šmíd), which are included instead of some previously planned simulations.

2 Structure of the Dissertation

The principal parts of this doctoral dissertation consist of a description of the state-of-the-art (Chapter 3), specification of chosen methods (Chapter 6) and the author's results with his contribution to knowledge (Chapter 8).

The complete structure of this doctoral dissertation is presented as follows:

Chapter 1 introduces the reader to the topic being solved within this dissertation. A brief characterization of the ELI-Beamlines facility is included as well. The thesis' aims and goals are presented concisely.

Chapter 2 describes the structure of this dissertation.

Chapter 3 provides an insight into the state-of-the-art of the issues being solved in this dissertation thesis. This includes designs of relay optical systems that are typically used, especially reflecting afocal systems, optical systems in high power laser facilities with the emphasize on those used by the LLNL (Lawrence Livermore National Laboratory, USA) and finally optical simulation software being used to solve tasks within these facilities.

Chapter 4 formulates the hypothesis and describes the main tasks and objectives to be solved within the framework of this doctoral dissertation.

Chapter 5 summarizes the author's contribution to knowledge.

Chapter 6 describes the two main software bundles that aid the author's endeavor to fulfill the aims and goals presented in the previous chapters. These are specifically Zemax OpticStudio and Wyrowski VirtualLab Fusion. This chapter mainly serves to introduce the methods represented by these softwares to the readers that are using other optical design and simulation software bundles (for example OSLO, GLAD etc.) and are possibly not familiar with those used in this dissertation. Content of this chapter is created predominantly by user manuals and papers written by the software creators and their collaborators.

Chapter 7 suggests a workflow to be used within the framework of this doctoral dissertation. This chapter demonstrates how the chosen methods, the two software bundles described in the previous chapter – Zemax OpticStudio and Wyrowski VirtualLab Fusion – should be used and how they fit together within the suggested workflow.

Chapter 8 is called “Optical modeling and design”, which represents the core of this doctoral dissertation. Chapter 8 recaps several task scenarios conducted within the ELI-Beamlines facility, especially within the framework of the BPM team. In particular it presents author’s results for the free space propagation simulation, focusing by ideal lenses, use of transmissive and reflective optics, simulation of several beamlines, with the inclusion of diffraction, surface irregularities and tolerancing.

Chapter 9 contains a discussion and assessment of the results achieved within the framework of this doctoral dissertation.

Chapter 10 is a conclusion outlining the achievements presented throughout this doctoral dissertation, and proposals for possible future research.

3 State of the Art

According to the ELI Whitebook [2], today's top specifications of high power laser systems are characterized by a peak power between one and two petawatts at very low (sub Hz) repetition rates, this being unchanged for over a decade now. The majority of high power systems, however, still rest at the 100 TW level. ELI and its national predecessor projects, like ILE and Vulcan 10 PW, will boost the peak power of single lasers (modules) into the 10 PW or multi-10 PW regime at much higher repetition rates, constituting an evolution of more than one order of magnitude in both of these parameters. ELI will be the first laser research infrastructure, which is the result of a co-ordinated effort of the multi-national scientific laser community. Other communities (high energy physics, synchrotrons, astronomy etc.) have long standing traditions in the operation of international user facilities. Lasers, having evolved 50 years ago from small table-top devices, are only now at the edge of such a mode of operation, and ELI is the first world-wide installation to take that step.

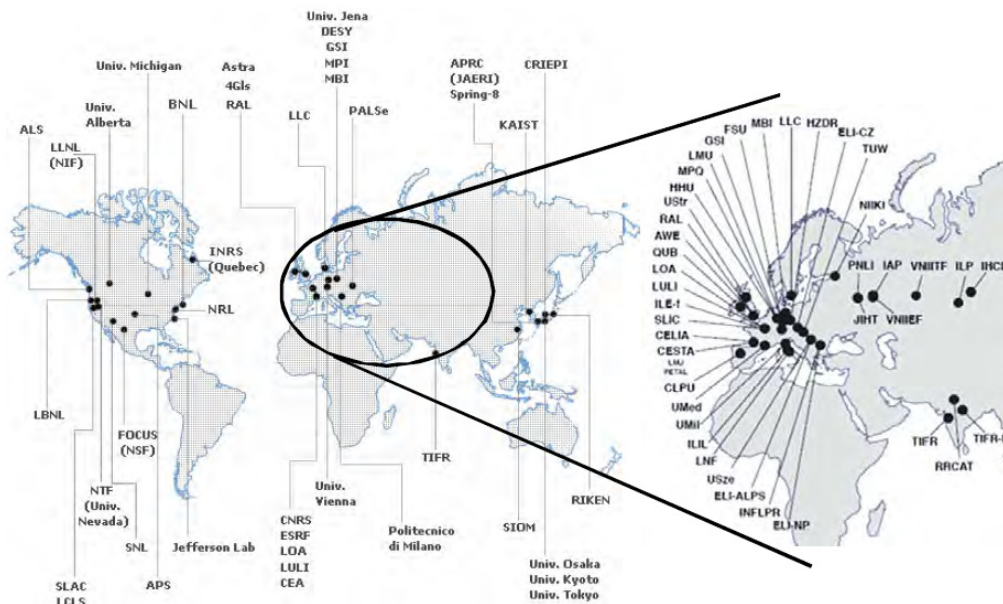


Figure 1: World map of high intensity systems in 2006 (left) and the current situation in Europe, Russia and India by the end of 2010 (right), taken from [9].

Fig. 1 shows the world map of high intensity systems in 2006 and the current situation in Europe, Russia and India by the end of 2010. The left part of the figure shows that high power lasers are pre-dominantly located in three global regions at moderate northern latitudes: North America (USA and Canada), Europe (including Russia), and the Asian-Pacific region (including India). This general feature has not changed since 2006 except that now (in 2010) the overall number of such systems has

considerably increased. The increase, however, was most dramatic in Europe (right part of Fig. 1). The European Commission has recently counted optics and photonics as one of the 5 key enabling technologies to tackle the Grand Societal Challenges of the 21st century. Hence, Europe appears as a particularly fertile ground for laser technologies, laser development and laser applications at the national level. ELI, however, goes beyond the national capabilities of most countries. That was a brief description of the state of the art from the facility point of view as it was written in the ELI Whitebook.

Three subchapters follow: the first one summarizes the history of high peak power laser facilities' development, predominantly the lasers within the LLNL are briefly described. In the next subchapter the short theory of afocal systems is given. In the last subchapter there is an overview of the software bundles used in high peak power facilities. These software bundles are namely: Malaprop, ARTEMIS and *Miró*.

3.1 Optical Systems in High Power Laser Facilities

To review optical systems of already existing high power facilities it is very useful to study not only research papers, but especially annual reports [10, 11, 12] and user guides [13, 14, 15] containing valuable technical information from laser facilities around the world. The prospective user guides usually contain some helpful information regarding beam transport.

The Lawrence Livermore National Laboratory in the United States has very long history of high power laser facility development. Some of the lasers built at LLNL are described in the following text – Janus, Cyclops, Argus, Shiva, Nova and most recently NIF. Of course, LLNL is not the only American laboratory involved in high power laser facility development. One of the many examples is the LLE’s (Laboratory for Laser Energetics) National Laser User’s Facility. The European continent also recently started to play an important role in high power laser facility science. The most famous project is French Laser Mégajoule. The Czech Republic also has its own laser facility, but it is much smaller in size and power in comparison with the previously mentioned large facilities. This facility – PALS (Prague Asterix Laser System) [16] is based on the Asterix IV [17] iodine laser system, originally designed and built in Germany by the Max-Planck-Institut für Quantenoptik in Garching.

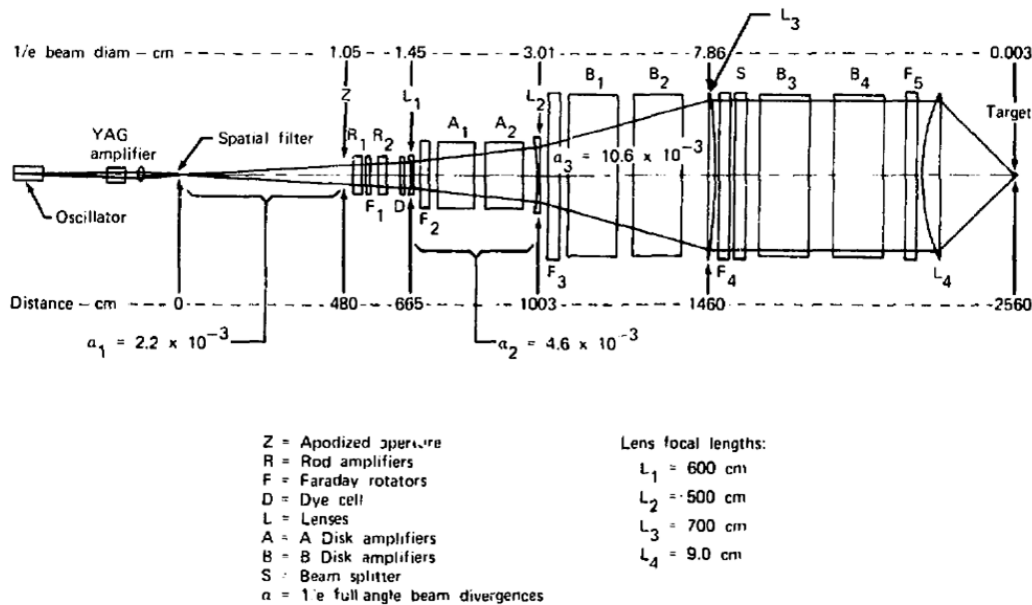


Figure 2: Janus laser system beam size and location of principal components, adopted from [10].

Janus

The beginning of laser experiments at LLNL is connected with the Janus system, which dates back to 1973.

The Janus [10] laser is a neodymium laser system that is designed for one- and two-beam irradiation of laser-fusion targets with 100 ps pulses. The system is made of components with the B-size (10 cm aperture) disk amplifiers. Fig. 2 is a schematic drawing of the Janus optical system; it shows the beam size and the location of the major components.

Cyclops

The Cyclops [10] laser facility is a prototype laser chain that has been used for on-line laser component evaluation and propagation experiments. The system has been operated through the C-size disk amplifiers (20 cm aperture). In this configuration, the laser has achieved an output energy of 270 J in less than 200 ps.

The Cyclops system represented a major program commitment to laser technology development and served as an experimental test bed for the evaluation of hardware and techniques. Specifically, all key components through D-size (30 cm aperture) disk amplifiers have been tested on Cyclops.

The spatial filter [10] has been relocated in the amplifier chain so that no optical elements appear between the spatial filter pinhole and the apodized aperture. It was earlier found that beam-turning mirrors exhibit an irreversible long-term degradation, thus producing small-scale artifacts on the beam. In combination with the turning mirror pair the spatial filter serves to “point” the beam as well to as to filter it; thus, when the system is aligned, the beam appears to originate from a point source at the pinhole center. Furthermore, the beam is centered on the apodized aperture by means of two orthogonal translation stages supporting the turning mirror. With this arrangement, alignment procedures requiring “walking” of gimballed mirror pairs are unnecessary, and the turning mirrors themselves are rigidly supported (thus eliminating long-term drifting of gimbal and/or torsional support elements).

Two additional mirrors are used to (1) extend the beam path between the oscillator and the spatial filter, and (2) provide convenient beam pickoff points for the streak-camera diagnostic. These mirrors are mounted in conventional kinematic mounts; beam-pointing stability (up to the spatial filter pinhole) could be improved by their elimination, if space were available.

The apodized aperture function is to superimpose a prescribed intensity profile on the propagating beam. The profile chosen has been a working compromise between diffraction ripple build-up and the amplifier filing factor, and has been characterized as a 5 TW super-Gaussian. However, there are arguments, based on beam aberrations, for an entirely different functional form of the profile (quadratic with a smooth rolloff). Computer simulation studies of the propagation and focusing obtained with this profile have been encouraging.

The position of the apodized aperture defines the beam-pointing direction and full-

angle divergence ϑ with respect to all components later in the train; hence mounting must be very stable.

The Cyclops system through the four C modules (20 cm clear aperture) has been successfully operated at full blank input energy (1.6 MJ). The optical configuration employed is shown schematically in Fig. 3.

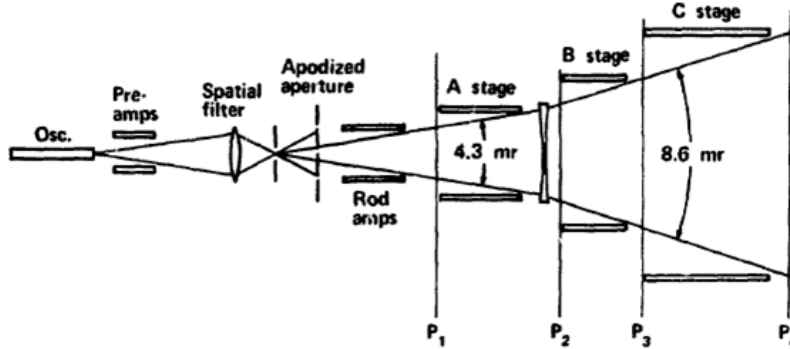


Figure 3: Cyclops system C-module configuration, adopted from [10].

Polaroid photographs showing the beam profile at various amplifier stage outputs is presented in Fig. 4.

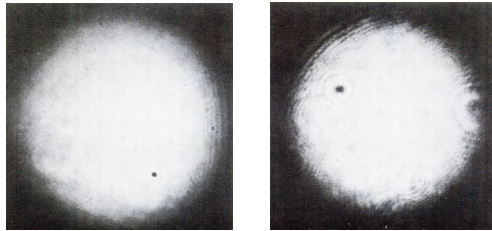


Figure 4: Cyclops beams at various amplifier stages, adopted from [10].

Left – rod amplifier output; beam diameter ~ 2.5 cm, beam energy ~ 1.0 J. The fringes on the right hand side arise from an off-line diagnostic aperture. The small bright diffraction rings arise from dirt on the camera filter. The larger faint rings arise from surface dirt early in the amplifier chain.

Right – beam profile at A amplifier output; beam diameter ~ 4 cm, beam energy ~ 5.8 J. The fringes appearing at the upper left arise from an off-line diagnostic aperture. The opaque spots at 3 and 10 o'clock are believed to arise from “burning surface dirt”. Photographs taken with a fast-framing camera suggest that the opaque spots arise from particulate matter that is caused to burn by the absorption of flashlamp radiation.

Argus

Argus, dated back to the 1976 (see the schematic in Fig. 5), is a two-beam target

irradiation facility that is, at the time of writing the annual report [10], under construction. The system consists of two parallel laser chains, each similar to the Cyclops system in size and performance.

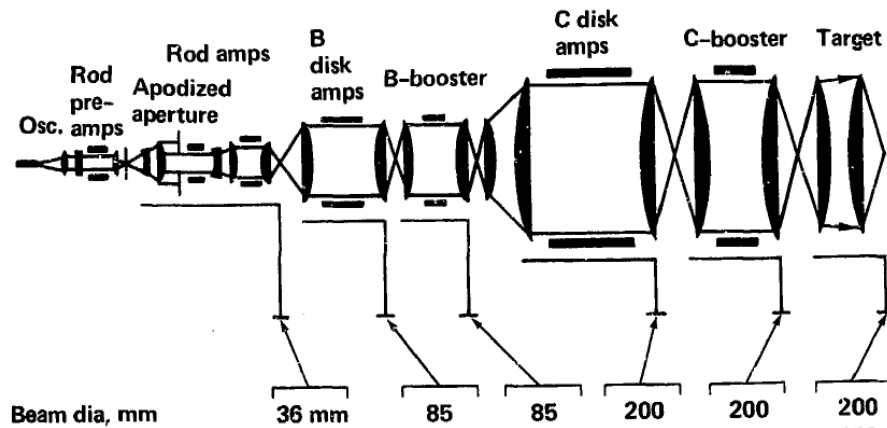


Figure 5: Argus laser system layout showing relay telescopes, adopted from [18].

As a two-beam system, with each aperture being 20 cm in diameter, Argus should deliver more than 3 TW of focusable power in a pulse of 100 ps FWHM. The beam breakup as a dominating influence on chain design for a high-power laser operation had led to adopting a staging philosophy directed primarily toward minimizing these effects. Argus was to be constructed using components that had been thoroughly tested on Cyclops. The criterion for optimal design was maximum focusable power on small targets; the strategy for achieving this involved deploying spatial filters at locations in the amplifier chain that minimized the small-scale beam breakup.

An important change from the previous design can also be seen in Fig. 5 – relay telescopes. Due to the higher energies employed, a larger beam is used. Previously, the Cyclops system used units of centimeters, while the Argus system has a beam size of tens of centimeters.

Shiva

Shiva, built in 1973 (see the schematic in Fig. 6) is the 10 kJ laser portion of the High Energy Laser Facility (HELFF). This system represents an increase with respect to Argus of approximately one order of magnitude in target irradiation energy and number of beams on the target.

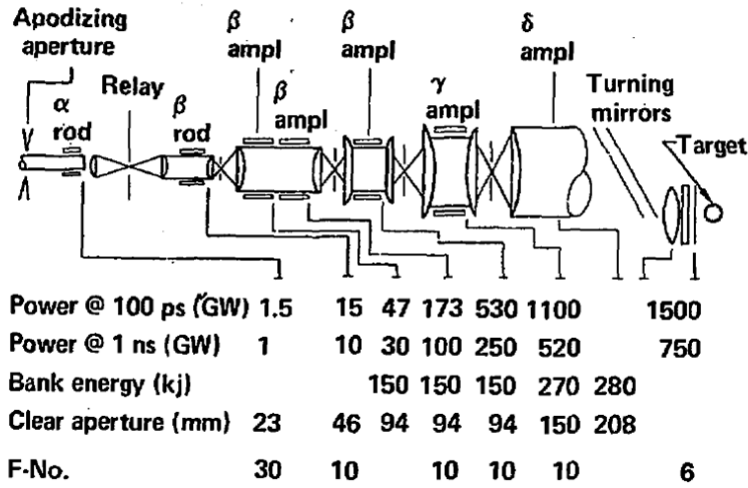


Figure 6: Shiva laser system layout, adopted from [19].

The optical relay telescope that is used between the preamplifier table and the arms of Shiva is depicted schematically in Fig. 7.

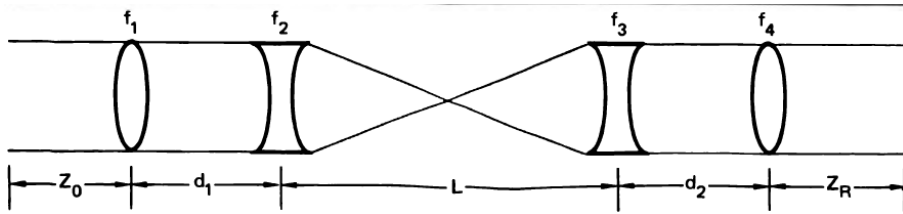


Figure 7: Schematic of the Shiva penthouse optical relay, adopted from [12].

It uses four lenses mounted on an evacuated tube [12]; the lens pairs form two telephoto lenses with effective focal lengths of f_1 and f_0 . The relay distance of this combination is given by

$$Z_R = M \left(f_1 + f_0 - \frac{f_1 d_2}{f_3} - \frac{f_0 d_1}{f_2} \right) - M^2 Z_0, \quad (1)$$

where Z_0 is the object distance and M is the optical system magnification. This relay provides a much longer relay distance than what is possible with a comparably sized two-lens relay. In addition, it can be used over a wide range of magnifications by merely adjusting d_1 , d_2 , and L .

Nova

The 1984 Nova chains will be spatially filtered and fully relayed (see the schematic in Fig. 8). The object plane of the relay will be a “hard” aperture (i.e., an aperture without graded edges) placed at the entrance to each chain, with successive image

planes occurring at the input lens of each spatial-filter/relay element, and at the final-focusing lens.

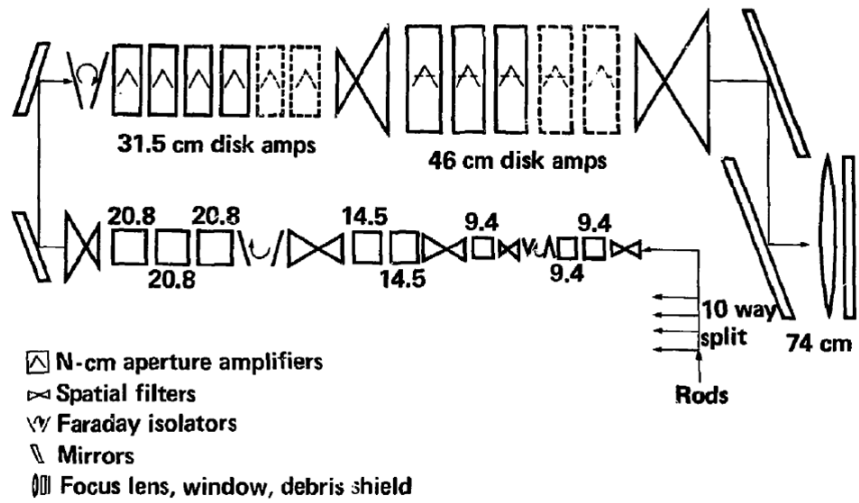


Figure 8: Nova laser system layout, adopted from [20].

Fig. 9 compares the sizes and spacings of the Nova spatial-filter/relay elements with those of Argus and Shiva.

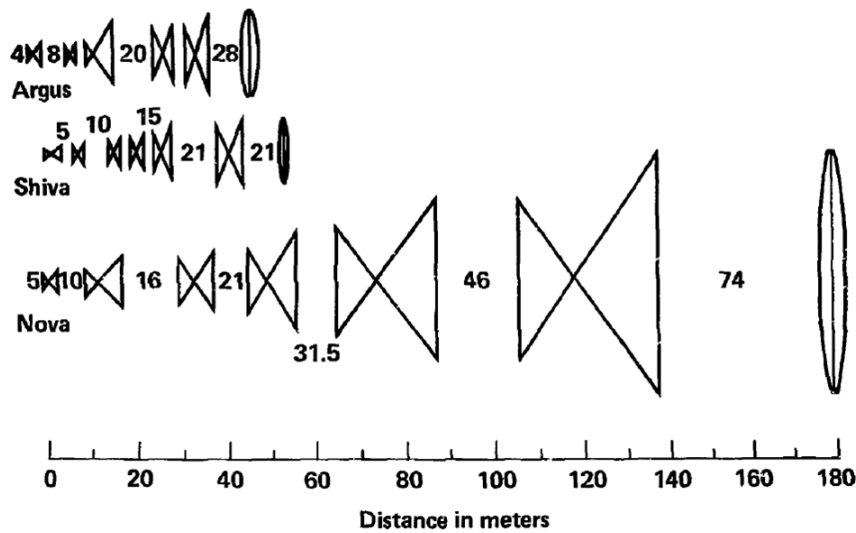


Figure 9: Nova laser chain comparison, adopted from [18].

The lenses used in Nova are spatial-filter lenses and focusing lenses, which are located in the laser beam, and various diagnostic lenses, which are not located in the beam. Because of the particularly high fluence level on the input spatial-filter lenses, the baseline design calls for these lenses to be uncoated.

The largest lenses in the system are those used in the 740 mm output beam; these large lenses include, for each beam, the output spatial-filter lens, the focusing lens, and

the beam-diagnostics objective lens. The overall diameter of these lenses is actually 800 mm, which allows 30 mm of additional clear aperture for alignment and 30 mm for mounting,

The spatial-filter lenses are $f/20$, so that the 740 mm output lenses, which are bent for minimum coma, require about $1\ \mu\text{m}$ of asphericity for the correction of spherical aberration. The 460 mm spatial-filter input lenses, which are meniscus-shaped, require about $3\ \mu\text{m}$ of asphericity.

The focusing lenses and the diagnostic lenses are significantly more aspherical than the spatial-filter lenses. For the focusing lenses, the aspheric deviation from the best-fit sphere is 0.31 mm at the edge of the clear aperture (770 mm) for a focal ratio of $f/2.88$; for the diagnostic lenses, the aspheric deviation is 1.10 mm for a focal ratio of $f/1.92$.

Spatial filters, which control beam propagation, are vacuum tubes that are sealed at both ends with lenses, and that contain an aperture located around the beam waist at the focal points of the lenses. These devices smooth the beam, magnify it between amplifier sections, and relay the image of an input aperture through the amplifier stages to the target chamber.

NIF

The National Ignition Facility [21] is a target irradiation facility for research in Inertial Confinement Fusion. This new (2009) system includes 192 beamlines. For each beamline, the major optical subsystems are: the main laser, the transport mirrors, and the final optics (see the schematics in Fig. 10).

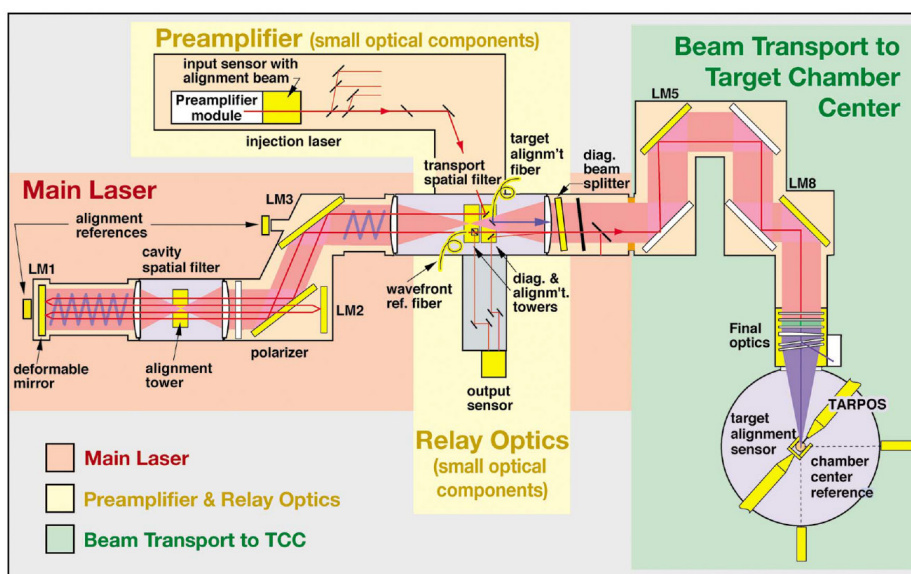


Figure 10: NIF Beam scheme, adopted from [22].

The main laser system is a four pass regenerative amplifier operating at 1053 nm that includes Nd:glass Brewster's angle amplifier slabs. The maximum output energy is approximately 20 kJ, in an effective pulse length of 3 ns. The transport mirror system brings the beams from the output of the main laser to the target chamber. The final optics assembly includes frequency conversion crystals and the target focus lens, the light incident on target is at the third harmonic of the laser wavelength, 353 nm. The incident energy on target for each beam is approximately 12 kJ.

The main laser system for each beam comprises up to thirty large aperture optical elements. The optical components are shown schematically in Fig. 11.

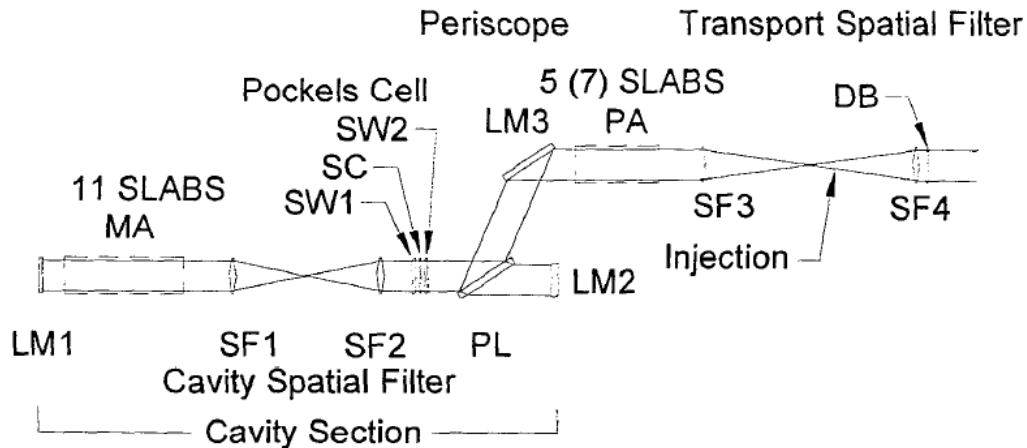


Figure 11: NIF Optical layout, adopted from [21].

The system is organized into cavity, transport and periscope sections. The cavity section includes: two end mirrors (LM1 is the deformable mirror used for wavefront control), 11 Brewster's angle Nd:glass amplifier slabs, the cavity spatial filter (CSF), and the Pockels cell (PC, with two windows and a switch crystal). The transport section includes: either 5 or 7 amplifier slabs, the transport spatial filter (TSF), and a diagnostic beam sampling optic designated as the diagnostic beamsplitter. These sections are connected by the periscope, which is made up of the polarizer and the elbow mirror.

The optical layout (see Fig. 11) [21] is determined by several factors. The first is relay imaging: LM2 is conjugate to LM1 via the cavity spatial filter. This imaging is complicated by pupil astigmatism due to the tipped plates. However LM 1 is exactly conjugate to itself for the multipass beam center rays. An image of the last (toward +z) slab of the power amplifier is relayed approximately 50 m from the transport spatial filter lens SF4 (this is from 12 m to 24 m from final optics assemblies at the target chamber.) The second factor is ghost stay-out zones: this sets the clearance of the MA from SF1 and the clearance between SF2 and the PC. SF3 is tilted by 2.8° in order to reduce the clearance between the PA and SF3 (SF4 is also tilted).

The packaging constraints are also important: All large optics are mounted in line replaceable units (LRUs) and clearance between subassemblies is needed for transport and handling access. This is illustrated in the figure, which shows a detail of the periscope region. Packaging constraints set the clearance between the PCs and the lowest polarizer, and the clearance between the top elbow mirror and the cavity end mirrors (LM2s). The beam spacings are set by the amplifier geometry. Beam walk in the amplifier slabs and polarizer also affect the layout.

The main laser configuration and lens design is maintained and optimized using ray trace models.

The optic sizes were established using a clear aperture budget. This budget has allocations for: the maximum beam size of 372 mm^2 (at the 10^{-4} relative irradiance contour of the apodizer); beam walk due to the pinhole separation; diffraction (an image of the beam apodizer is put at LM 1, diffraction is modeled as ray slopes in nominally collimated space that would clear the maximum size pinholes); component and alignment reference location errors of 1 mm to 3 mm; alignment system control errors of 2 mm centering and 5 mrad beam rotation; lens wedges of 20 arc sec maximum; and second order effects caused by component placement errors. The resulting specified dimensions for each optic are: the optical clear aperture (OCA), which includes all allocations except diffraction and is the optic test aperture; the mechanical hard aperture (MHA), which is the OCA plus the diffraction allocation and is the keep-out zone for all mechanical structure; and the optic size, which is the MHA plus mounting and fabrication “freeboard”. The OCAs and optic sizes are given in table 1. The dimensions shown are in millimeters; the amplifier slab size shown includes the edge cladding. The design limiting aperture for the main laser system is the 400 mm square aperture of the amplifier slabs.

Table 1: Component sizes, adopted from [21].

Component	OCA [mm]	Size [mm]
LM1	392×392	450×434×15
LM2	392×392	412×312×80
LM3	396×392	740×417×80
PL	396×396	740×417×90
MA, PA	400×400	805.5×458×41
SC	397×397	410×410×10
SW	397×397	430×430×35
SF1-4	410×406	438×434×46
DB	410×406	438×434×10

The material used for all of the spatial filter lenses is synthetic fused silica. The center thickness is 46 mm. The lenses are vacuum barriers. The lens shape is no-

minally symmetric bi-convex. This was chosen to minimize stress birefringence. The inside (vacuum-facing) surface of each lens is spherical; the outside surface is aspherical. Each lens is corrected for spherical aberrations individually. The back focal distance for the cavity spatial filter lenses is 11751.5 mm ($\sim f/21$ referred to the aperture diagonal). The aspheric surfaces of these lenses are conics; the maximum aspheric departure is 1.4 μm . The back focal distance of each transport spatial filter lens is 30 m ($\sim f/55$ referred to the aperture diagonal). These lenses are more complicated because of the 2.8° tilt. The aspheric surface is bilaterally symmetric, containing surface terms in x^2 , y^2 , $x(x^2 + y^2)$ and $(x^2 + y^2)^2$. The maximum aspheric departure is 7.8 μm .

Because of the multipass configuration, the lenses (except SF4) are used off axis. This contributes a small amount of internal wavefront error. In the cavity spatial filter the wavefront error due to a single lens is -0.06 waves peak-to valley (P-V, at 1053 nm), mainly coma. The coma is corrected each pass. The astigmatism is exactly corrected by the 4 pass symmetric use. The 4 pass field curvature is < 0.02 waves. The wavefront error at pinhole 4 is 0.11λ P-V (0.017λ RMS). In the transport spatial filter the wavefront error due to 1 pass through SF3 is -0.05λ P-V, mainly astigmatism. The wavefront error at pinhole 4 is 0.015λ P-V (0.004λ RMS). The full system design wavefront error is 0.006λ P-V (0.001λ RMS) 4 pass, not including the effect of tolerances or fabrication errors. The specified maximum tilt error for the lenses is 0.1° . The multipass wavefront errors due to lens tilts are: for SF1 and SF2, 0.38λ P-V (0.05λ RMS); for SF3, 0.32λ P-V (0.08λ RMS); for SF4, 0.16λ P-V (0.04λ RMS). The many Brewster's angle amplifier slabs (and polarizer) cause significant pupil astigmatism in the main laser. For a pupil located in the injection system, the longitudinal pupil astigmatism for the multipass is: 328 mm at LMI for pass 1; 488 mm at LM2 for pass 2; 650 mm at LM1 for pass 3; and 980 mm at the output, at the LMI conjugate that is approximately 43 m (toward +z) from SF4. However, this is much less than the diffraction limited depth of focus for beam (pupil) imaging. The 90% contrast diffraction depth of focus at $\pm 150 \mu\text{rad}$ is 16.6 m.

The switchyard and target area beam transport system is made up of 832 mirrors. This system maps the rectangular arrangement at the laser output to a spherical-geometry configuration at the target chamber. The path length from the transport spatial filter output lens (SF4) to the focus lens varies from 62 m to 74 m. Each path has either 4 or 5 mirrors. All reflections at the mirrors are in-plane (either S or P). The beam path through the transport system is constrained at both ends. The alignment references at the main laser output are pointing with respect to the center of the pass 4 TSF pinhole and beam centering at the crossover. The alignment references at the target chamber are centering at the focus lens and beam pointing with respect to target chamber center. On-line system alignment is achieved by tilting the second

and last transport mirrors (LM5 and LM8).

To study the control of beam rotation and the setting of mirror apertures, ray trace models have been set up for all 192 beams.

Two large confocal spatial filters (nominally 25 m and 60 m in length) use pinholes as low-pass filters to remove high spatial frequency noise and image relay the propagating beams to the target chamber. The equi-convex lenses used at both ends of the spatial filters have a slight aspheric correction applied to one side. The lenses are fabricated from fused silica and have back-focal lengths of 11.6 and 29.7 m, respectively, measured to an accuracy of about one part in 10,000.

Asterix IV (PALS)

The Prague Asterix Laser System, formerly known as Asterix IV [17] (see the schematic in Fig. 12), represents the latest experience with high power laser facilities in the Czech Republic so far.

In contrast with previously shown systems PALS is an iodine laser. This laser type is capable of delivering multi-kilojoule pulses with durations around 1 ns at a nearly diffraction-limited beam quality. Laser action occurs at a wavelength of $\lambda = 1315$ nm. The iodine laser is less subject to problems of optical damage by self-focusing effects than solid-state highpower lasers and provides a greater flexibility in choosing the most suitable operating conditions. This is due to the fact that the stimulated emission cross section of the laser transition can easily be adjusted to its optimal value by pressure broadening through a buffer gas. In addition, the value of the saturation energy density of about 1 J/cm^2 is very favorable for efficient single-pass energy extraction out of an amplifier.

At first the 300 J/1 TW Asterix III laser was built and applied for laser plasma experiments until 1985. Since 1989 these investigations and additional X-ray laser experiments have been carried out with Asterix IV. This laser is a completely new design, based on the know-how gained with Asterix III and on the support of a well-proven 1-D pulse propagation code developed at MPQ. It was used to optimize the amplifier chain concerning extraction efficiency and to follow the pulse shortening caused by saturation in amplifier and absorbers. This latter information is helpful in two respects. Firstly, it eases the identification of possible damage sites in the chain due to too high a beam loading resulting from pulse compression. Secondly, it reveals how sensitively the output pulse duration is correlated to the input pulse duration under various operating conditions. This knowledge is important for laser plasma experiments where the pulse duration is a critical issue. The main goals in constructing Asterix IV was to get more energy than Asterix III at a better overall efficiency and a beam profile being as close as possible to a top hat.

Therefore, a new amplifier layout and a beam guiding system comprising image

relaying combined with spatial filtering was introduced.

To maintain an optimal filling factor for the pulse at high loading a rectangular and smooth intensity profile has to be generated. Since an initially smooth intensity profile will be distorted by diffraction effects, image relaying has to be applied. For this purpose the image of a homogeneously illuminated aperture with a clear diameter of 8 mm positioned at the entrance of the first telescope is successively imaged through the amplifier chain from one amplifier exit to the next. The telescopes of this system also serve for beam expansion and spatial filtering. This filtering performed by apertures with 10 times diffraction-limited diameters is required to remove the high spatial frequency components from the angular beam spectrum which may arise from medium inhomogeneities, diffraction, and self-focusing effects.

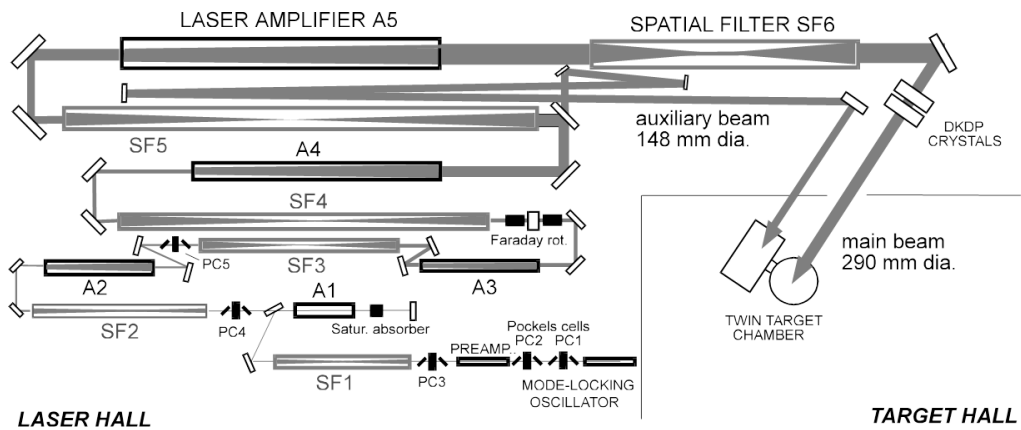


Figure 12: PALS scheme, adopted from [19].

Summary of the high power laser systems – historical overview

The main objective of this historical overview of high peak power laser facilities was to illustrate the increase in power over the years, which is mainly connected with the increase of beam and optical component size. Another parameter which is steadily changing is pulse duration. Pulse duration is decreasing over the years. While using transmissive optics is possible for some ns level pulses, with the introduction of fs pulses reflective optics is necessary to avoid high levels of GVD. The requirement for low wavefront errors can be satisfied only by relay telescopes with a very long total length, as the f -number is the major contributor to optical quality.

3.2 Relay Trains and Afocal Systems

A critical part of ELI-Beamlines are optical relay systems [23–26], which will need to be used in a similar manner as used in the previously mentioned historical overview. Top-hat beams, unlike Gaussian, change their profiles while propagating. Therefore it has to be relay imaged [27] to successive optical elements of the laser system to avoid hot spots and laser damage [28]. In high-power laser systems relay imaging is often combined with other optical systems, such as beam expanders and spatial filters [29]. The most common relays are 4f systems.

In the last decade, there has been a significant increase of interest in laser relay systems of all kinds. Relay optics serve not only as a beam transport in high power laser facilities, but more commonly for near-earth laser communications [30–32] or defense purposes [33]. There are several reasons why the use of relay optics can be advantageous. The most prominent one is that it enables light to avoid obscurations in the beam path. In optical communication, the propagation distance can also be significantly enhanced by the introducing the relay optics system. To illustrate how relay optics is important in defense research and development, there is a quote from the Defense Science Board Task Force on Directed Energy Weapons dated December 2007 [34]: “The most significant activity in advanced beam control was in the relay mirror area. In 2006 the contractor and the Air Force Research Laboratory (AFRL) used a subscale relay mirror system in a significant ground-based demonstration. The relay mirror was hung on a crane, and a low-power laser was relayed from a ground station two miles away and onto a target. The ABL beam-control system is currently being flight tested. Completion of these tests will be a major milestone for the ABL (Airborne Laser), but in terms of advanced technology, this system was largely designed over a decade ago.” In the same report the need for proper modeling and simulation capabilities are stressed, these needs are also highly emphasized in the case of ELI -Beamlines, which is presented in this dissertation.

Many applications require remote viewing because the object to be viewed is in an environment hostile to the viewer, or because the object is inaccessible to the viewer without undesirable damage to its environment [35]. Military applications are in the first category, and medical applications fall into the second one. For these applications, instrumentation is needed to gather light from the object, transport the light to a location more advantageous for viewing, and dispense the light to the viewing instruments. Collecting and dispensing optical images is mostly done by focusing lenses. Relay trains, however, are commonly made up of a set of unit power afocal lenses, and are one of the most essential applications of finite conjugate afocal lenses [35].

Several factors are important in designing relay trains [35]. First, it is preferable to minimize the number of relay stages in the relay train, both to maximize transmittance and to minimize the field curvature induced by the large number of positive lenses. Second, the outside diameter of the relay train is typically restricted, so the choice of image and pupil diameter inside the relay is critical. Third, economic considerations make it desirable to use as many common elements as possible, while minimizing the total number of elements. Fourth, it is preferable to keep internal images well clear of optical surfaces where dust and scratches can obscure portions of the image. Fifth, the number of relay stages must be either odd or even to provide the demanded output image orientation.

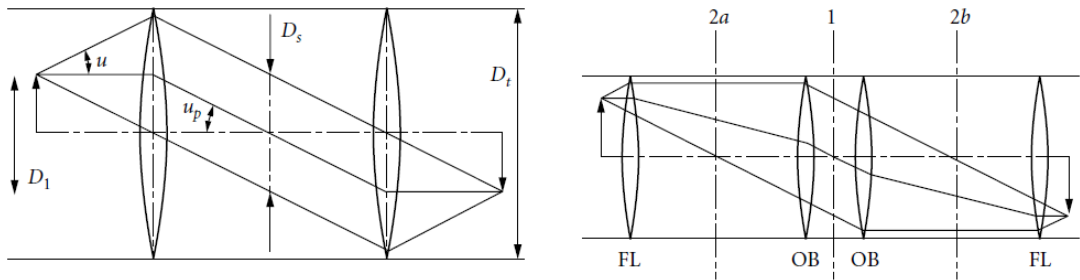


Figure 13: Basic unit power transmissive afocal lens designs. Left: Minimum number of lenses. Right: Minimum tube diameter, adopted from [35].

Fig. 13 shows thin-lens models of the two basic afocal lens designs which can be applied to relay train designs. Central to both designs is the use of symmetry fore and aft of the central stop to control coma, distortion, and lateral color, and matching the image diameter D_i and stop diameter D_s to maximize the stage length to diameter ratio. In paraxial terms, if $D_i = D_s$, then the marginal ray angle u matches the principal ray angle u_p , in accordance with the optical invariant. If the relay lens is both aplanatic and distortion free, a better model of the optical invariant is [35]

$$D_i \sin u = D_s \tan u_p \quad (2)$$

and either the field of view $2u_p$ or the numerical aperture $NA = n \sin u$ must be adjusted to match pupil and image diameters. For some applications, maximizing the optical invariant which can pass through a given tube diameter D_t in a minimum number of stages is also critical. If maximizing the ratio $D_i \sin u / D_t$ is not critical, Fig. 13 (left) shows how the number of elements can be minimized by using a Keplerian afocal lens with the stop at the common focus, eliminating the need for field lenses between stages. The required tube diameter in this example is at least twice the image diameter. If maximizing $D_i \sin u / D_t$ is critical, field lenses FL must be added to the

objectives OB as shown in Fig. 13 (right), and the field lenses should be located as close to the image as possible within limits set by obstructions due to dirt and scratches on the field lens surfaces. Symmetry fore and aft of the central stop at 1 is still necessary for aberration balancing. If possible within performance constraints, symmetry of OB and FL with respect to the planes 2a and 2b is economically desirable, making OB and FL identical. The rod lens design developed by H. H. Hopkins can be considered an extreme example of either approach, making a single lens so thick that it combines the functions of OB and FL. Examples utilizing rod lens design can be found in H. H. Hopkins' patents [36, 37] and some of his papers [38].

Afocal lenses can be designed with powered mirrors or combinations of mirrors and refractors. Several such designs have been developed in recent years for use mainly in the photolithography of microcircuits. All-reflecting afocal lenses are classified in the following text accordingly to the number of powered mirrors they contain, in the order of increasing complexity.

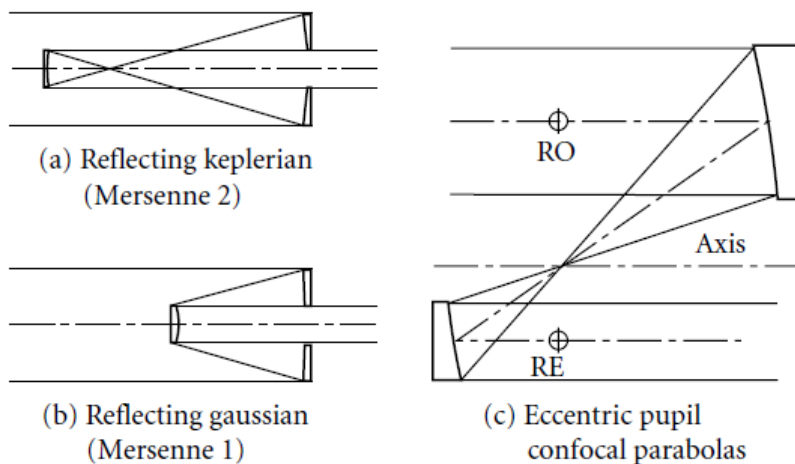


Figure 14: Reflecting Afocal Systems, adopted from [35].

The simplest reflecting afocal lenses are the variants of the Galilean and Keplerian telescopes [35] shown in Figs. 14a and 14b. They may also be thought of as afocal Cassegrainian and Gregorian telescopes. The Galilean/Cassegrainian version is often called a Mersenne telescope. In fact, both Galilean and Keplerian versions were proposed by Mersenne in 1636, so his name should not be associated solely with the Galilean variant. More information about the Mersenne telescope design can be found in the literature [39, 40, 41]. Making both mirrors parabolic corrects all third-order aberrations except field curvature. This property of confocal parabolas has led to their periodic rediscovery and to subsequent discussions of their merits and shortcomings. The problem with both designs, in the forms shown in Figs. 14a and 14b, is that their eyepieces are buried so deeply inside the design that their usable field of

view is negligible. The Galilean form is used as a laser beam expander where field of view and pupil location is not a factor, and where elimination of internal foci may be vital. Eccentric pupil versions of the Keplerian form of confocal parabolas, as shown in Fig. 14c, have proven useful as lens attachments. RO, RE, and the internal image are all accessible when RO is set one focal length ahead of the primary, as shown. It is then possible to place a field stop at the image and pupil stops at RO and RE, which very effectively blocks stray light from entering the following optics. Being all-reflecting, confocal parabolas can be used at any wavelength, and such attachments have seen use in infrared designs. Especially when dealing with ultra-intense ultra-short optical pulses these designs are superior. Also for the purposes of transport telescopes within the ELI-Beamlines systems like Mersenne or Cassegrain are considered for implementation.

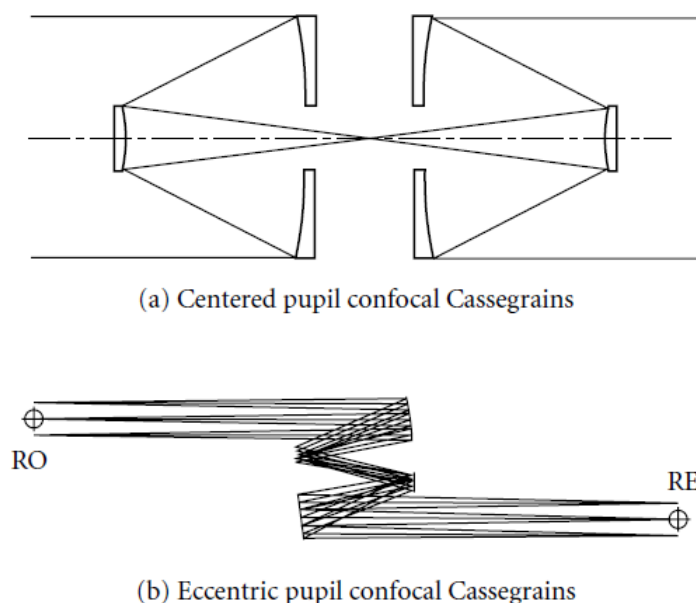


Figure 15: Four-powered-mirror afocal lenses, adopted from [35].

The confocal parabola principle can be extrapolated [35] one step further by replacing both parabolas with classical Cassegrainian telescopes, as shown in Fig. 15a. Each Cassegrainian is corrected for field curvature independently, and the image quality of such confocal Cassegrainians can be quite good. The most useful versions are eccentric pupil. Fig. 15b shows an example from Wetherell. Since both objective and eyepiece are telephoto designs, the separation between entrance pupil RO and exit pupil RE can be quite large. An afocal relay train made up of eccentric pupil confocal Cassegrainians will have very long collimated paths. If the vertex curvatures of the primary and secondary mirrors within each cassegrainian are matched, the relay will have zero field curvature as well. In general, such designs work best at or near unit magnification.

3.3 Simulation Software in High Power Laser Facilities

For the successful operation of ELI-Beamlines optical engineers, physicists, researchers and engineers alike require several software tools to aid in the design, simulation, optimization and running of various laser systems as well as to predict system performance and tolerances. Advanced numerical simulations will play a crucial role in the efficient design and optimization of the many laser systems and beamlines necessary for the success of ELI-Beamlines. Development of a fully functional computational software package, namely a Beam Propagation Method (BPM) software, to simulate all the optical aspects of laser beamlines is therefore demanded [42]. Due to the long time and difficulty required to develop such software internally, ELI-Beamlines will take advantage of already existing software bundles and collaborate in the development of these bundles in order to fulfil all the simulation requirements of ELI-Beamlines.

The BPM is a mathematical simulations program, which will determine spatio-temporal parameters of ultra-short pulses as they propagate from the laser systems through optical setups and come to a focus at the target while taking into account the effect imposed by various components (mirrors, beam-splitter, coatings and gratings), and required optical parameters (spatial, temporal, spectral and energetics). This will enable the user's experimental requirements to be critically assessed ahead of time, and will ultimately be used to design, optimize as well as to determine and predict system performance and tolerances. Due to the complexity of the optical setups that will be implemented in ELI-Beamlines, the software package will involve simulations of the optical systems in both paraxial and non-paraxial regimes, ultra-short pulses with large bandwidths, tightly focused system with low f -number ($f < 1$), and non-linear effects such as small scale focusing. In order to have a full description of the optical process, the BPM software must also take into account environmental conditions such as thermal management, and the resultant stress and strain imposed on the optical components and mounts.

The information about the current state of the art of optical simulations and modeling in high power laser facilities is also based on the latest knowledge shared by the experts of these facilities during the BPM (Beam Propagation Method) workshop in Prague. This workshop was arranged by Dr. Michael Morrissey on behalf of Prof. Bruno Le Garrec. Dr. Michael Morrissey also gave a presentation with detailed requirements that ELI have for the anticipated simulation environment.

According to Dr. Morrissey's talk [3], ELI-Beamlines requires the development of a Virtual Beamline (VBL, flowchart shown in Fig. 16) for various reasons, in particular:

- VBL: for ELI staff
 1. Laser system visualisation.
 2. Simulation of the laser transport.
 3. Integration with LPOM (laser performance operations model) and monitoring.

- VBL: for ELI users
 1. Experimental hall visualisation.
 2. Beam characteristics & performance database.
 3. Experiment simulations.
 4. Online monitoring & remote control
 5. E-learning and training

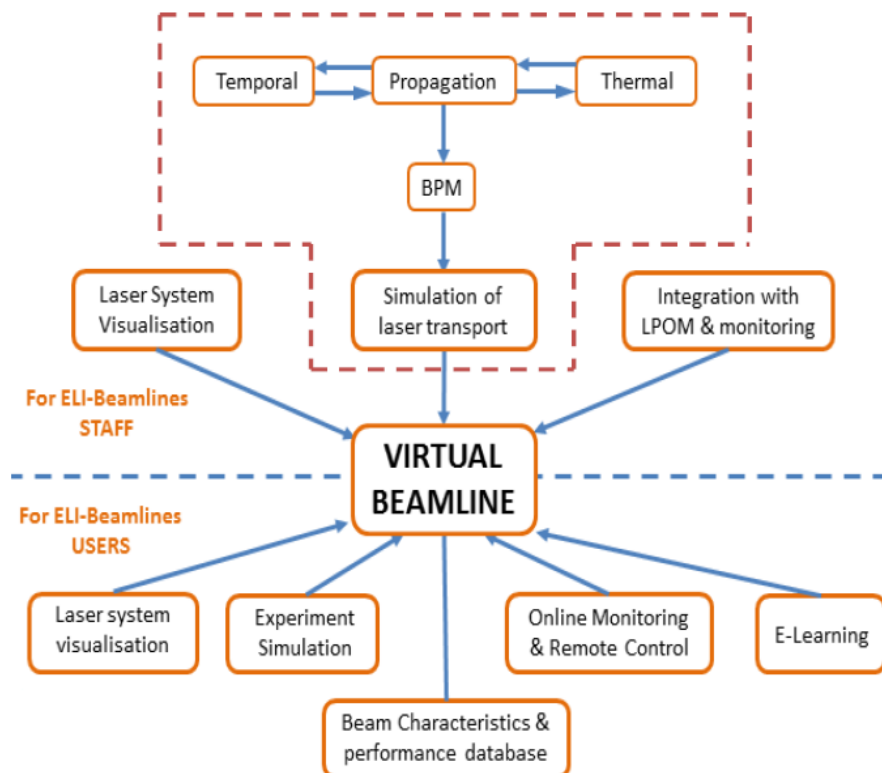


Figure 16: The VBL schematic diagram, adopted from [3].

In the context of this thesis the most relevant item is the development of the so-called Beam Propagation Method (BPM) itself (see the flowchart in Fig. 17). It is important to be able to determine all the parameters of the beam at various points of alignment, transport, diagnostics and target systems. Comparing the results of the

simulations with experimental data will allow understanding of the behaviour of the systems which can be optimized. Several BPM software bundles already exist:

- Malaprop and Prop92 LLNL, USA,
- Fresnel at the GPI, Moscow, Russia,
- *Miró* at CEA, Bordeaux, France.

Similar software to run the ELI facility is required.

The intensity at the focal spot is the main deliverable. ELI staff must be able to tell the user the laser energy, pulse duration, power, size, beam quality and pulse duration. The BPM method will start with this information:

- 2-D spatial intensity profile $I(x, y)$
- 2-D wavefront profile $\vartheta(x, y)$

Additional dimensions providing

- Spectral (λ) parameters
- Temporal (t) parameters.

A pseudo dimension is added through the propagation of the beam along its axis (z). Thus the required VBL software system will be a 7-D solution.

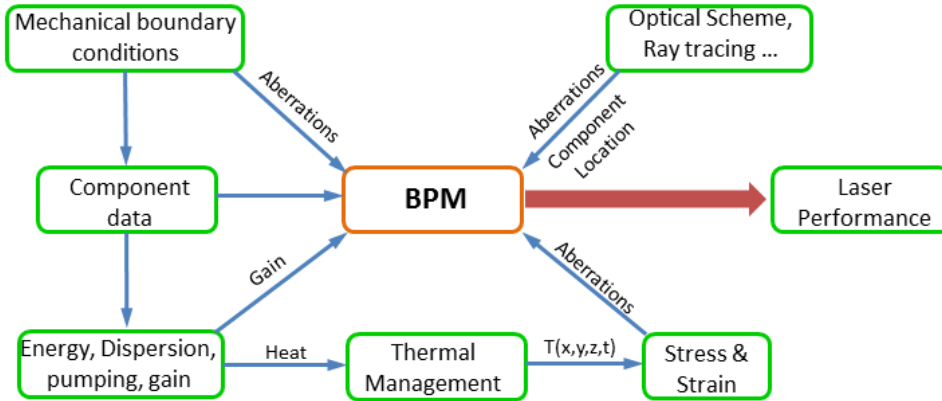


Figure 17: The BPM schematic diagram (Adopted from [3]).

In the following text there is a brief overview and description of simulation software used across the high power laser facilities around the world in past few decades.

Malaprop

Malaprop is a CDC 7600 computer Light Propagation Code [43] able to simulate laser light propagation through a variety of regions. The primary program task is the integration of the partial differential equation

$$2in_0k_0 \left[\frac{\partial}{\partial z} - g(z) \right] \psi + \nabla^2 \psi + 2n_0^2 k_0^2 \left(\frac{n_2}{n_0} \right) |\psi|^2 \psi = 0 \quad (3)$$

for propagation of a light beam represented by the complex array ψ . The above equation is computationally integrated for regions with or without gain ($g(z)$) and for any indices of refraction (n_0, n_2). In addition, the beam may be spatially filtered or relayed (using FFT methods), expanded or split or passed through an aperture (followed by a no-gain propagation region with a non-linear index of refraction = 0.) Relative amplitude or phase noise may be added to the beam at selected surfaces.

Two versions exist allowing for one or two beam dimensions:

1. One space dimension (x ; propagation in z) (with saturation).
2. Two space dimensions (x, y ; propagation in z) (without saturation).

Optional output includes intensity/phase information (plots and printout) power spectral density information, computed B integral and saturation information.

Initial beam configuration is essentially limited only by array sizes. Each beam dimension is limited to 128 mesh points or 128×128 points all together.

ARTEMIS

ARTEMIS is another code made by Lawrence Livermore Laboratory and used as a diffraction model for laser light propagation. The program is described in [44] as follows.

Diffraction theory provides a convenient method for studying both the propagation and focusing properties of intense laser light passing through a chain of optical elements. Large scale phenomena such as gain amplification and whole beam aberration are often addressed by conventional geometric ray tracing methods. When optical path lengths become large and/or intensity profiles display severe gradients however, the geometric approach quickly breaks down. This is especially true within the focal region of a lens where it is desirable to understand detailed aspects of the light intensity profile.

The development, optimization and understanding of large laser systems such as those constructed and utilized by the Laser Program at Lawrence Livermore Laboratory are dependent on a diffraction analysis of light propagation. Because of the high power yields associated with the laser systems at LLL, the analysis of such systems is dominated by the nonlinear effects upon the light – the result of passing intense fields through largely glass optical elements. Efforts to understand and combat these effects has resulted in the development of a computer-based simulation, employing diffraction theory, to model current and proposed glass laser systems.

The computer program, ARTEMIS, developed for the LLL-CDC 7600 computers, simulates the nonlinear propagation and focusing of laser light through a simplified chain of optical elements. Its specific capabilities include: diffraction, spatial filter

transmission, non-uniform gain, gain saturation, whole beam self-focusing, nonlinear propagation in both rod and disk-type amplifiers, focusing, thin lens combinations, nonlinear ripple growth, “soft” apertures and Seidel aberrations.

Only radially symmetric beams are allowed², thus limiting the types of distortions; and of the basic Seidel aberrations, only spherical aberration is considered. The effects of astigmatism and coma have previously been studied, and are assumed correctable for the purposes of ARTEMIS’ simulation. In addition to the radial (spatial) profile of the laser pulse, it is possible to model the temporal dependence – the basis for encountering gain saturation.

The wave function for the initial beam injected into a laser system of optical components may be approximated by a generalized Fourier decomposition. In which the basis functions are the familiar Laguerre-Gauss mode functions. The propagation of the beam in terms of its (Fourier) decomposition coefficients and modal phase is well understood, and is defined in terms of a single complex propagation parameter, q , and an element transformation matrix, \mathbf{T} . The temporal dependence of the wave function is accomplished by considering the (radial) wave function at a number of discrete planes of fixed value t in a time frame moving along with the wave form. For short pulses, typically only the zero position of the time envelope is modeled. For long pulses, the effect of gain saturation may be important and a time history is required. A set of decomposition coefficients is obtained for each time slice and propagation for each is effected.

The amplitude envelope of the initial wave function is typically Gaussian temporally and super-Gaussian (top-hat) spatially. Phase distortions may be present initially as a uniform intensity ripple. Once the initial profile is characterized by a set of decomposition coefficients, free space (vacuum passage) propagation is effected by a simple (diffraction) phase accumulation that is only dependent on propagation distance. The wave function may be reconstructed in any downstream position from its original coefficients and distance-dependent phase.

Optical elements placed in the path of the propagating beam are characterized by a transformation matrix. Passive elements are those which serve only to alter the phase of the associated wave function, or specifically, the modal phases of each Laguerre-Gauss basis function used in decomposition. Typical passive elements are (thin) lens and free space propagation (treated as an “optical element”). Active elements combine a phase change with an amplitude change and, to account for non-uniform spatial amplification and the subsequent remixing of the Laguerre-Gauss modal functions, the decomposition coefficients are actually altered. Both passive and active elements may have associated with them an incremental static distortion

²This would be a serious restriction for the purposes of the ELI-Beamlines. The VirtualLab Fusion, that is primarily used in this dissertation, does not have such a limitation.

(Seidel aberration) or intensity dependent nonlinear distortion. The wave function is then reconstructed from its current decomposition, the additional distortions folded in, and a new set of modal coefficients obtained. In terms of program logic, beam propagation starts afresh at each decomposition, and only the relative diffraction-propagated phase between such decompositions is necessary to reconstruct the wave function at intermediary planes. The most significant program output is a series of plots showing beam intensity profiles at various selected points in the laser chain of optical elements. Certain tabulated information is also provided.

The most crucial aspect to a successful propagation simulation is ARTEMIS' ability to suitably decompose a given wave function into a finite number of modal functions. Given a wave function, $\psi(r, z, t)$, it is necessary to form the approximation

$$\bar{\psi}_i(r, z) \cong \psi(r, z, t_i). \quad (4)$$

It is assumed that the time variable, t , may be fixed at suitably placed coordinate positions and a vector of approximation is formed. For purposes of discussion, only one component of this vector will be expanded. The form chosen for $\bar{\psi}$ is:

$$\bar{\psi}(r, z) = \sum_{m=i}^N \gamma_m \Lambda_m e^{-i\phi_m} \quad (5)$$

where the basis functions are

$$\Lambda_m = \frac{\sqrt{2}}{w(z)} L_m \left[\left(\frac{r}{w(z)} \right)^2 \right] e^{-\frac{1}{2} \left(\frac{r}{w(z)} \right)^2}, \quad (6)$$

and the modal phase is separated as:

$$\phi_m = (2m + 1) \phi, \quad (7)$$

$$\phi = \tan^{-1} \left(\frac{-R(z)}{kw^2(z)} \right). \quad (8)$$

L_m is the m^{th} order Laguerre polynomial, k is the wave number, and $R(z)$ curvature radius and $w(z)$ Gaussian waist parameter are obtained from the complex propagation parameter q :

$$\frac{1}{q} = \frac{1}{R(z)} - \frac{i}{kw^2(z)}. \quad (9)$$

Elementary analysis provides the decomposition coefficients as

$$\gamma_m = e^{i\phi_m} \int_0^a \psi(r, z) \Lambda_m r dr \quad (10)$$

where a defines the aperture radius in a given decomposition plane. Initially, $\psi(r, z)$ arises from an analytic expression of the general form:

$$\psi(r, z) = A(r) e^{-i\phi_0} \quad (11)$$

where $A(r)$ is some radial amplitude profile such as Gaussian, quadratic, super-Gaussian etc; and ϕ_0 is an initial phase to be specified. At other decomposition planes, $\psi(r, z)$ itself arises from an expression like Eq. 5.

In order to accommodate gain amplification, incremental nonlinear distortion and incremental static (Seidel) aberrations, it is convenient to treat ϕ_m above as only providing the appropriate free-space phase change in the wave function as propagation proceeds; all other properties are absorbed by the coefficients γ_m . It should be noted that each γ_m is really a function of the parameter $w(z)$. In the initial fitting procedure, $w(z)$ is chosen to minimize the power residual. In all other decompositions $w(z)$ is obtained from the complex propagation parameter q .

The following discussion provides details of the methods ARTEMIS employs to alter the wave function as it propagates through a chain of optical elements. At a fixed (r, z) position, let ψ be the wave function evaluated either analytically or from a prior decomposition. Let $\hat{\psi}$ be the wave function as it is modified to account for any amplitude or phase changes.

An attribute of laser amplifiers is that the gain they provide is typically non-uniform across the spatial dimensions of the amplifier. ARTEMIS will allow a radially varying gain profile of the form:

$$G(r) = e^{(g_0+g(r))l} \quad (12)$$

where l is the effective length of the gain medium, g_0 is the small signal gain coefficient, and $g(r)$ describes the radial non-uniformity. Thus, the first modification to the wave function to allow for gain amplification is simply:

$$\hat{\psi}(r, z) \sim \psi(r, z) G^{\frac{1}{2}}(r) \simeq \psi(r, z) e^{\frac{1}{2}(g_0+g(r))l}. \quad (13)$$

Desiring to place any amount of static (Seidel) distortion on the beam requires a further change, in the form of a phase alteration. ARTEMIS will allow lumped phase alterations of the form

$$\phi_s = f_1(r) + f_2(r) f \dots, \quad (14)$$

where e.g.:

$$f_1(r) = \alpha \left(\frac{r}{a}\right)^2 \left(1 - \left(\frac{r}{a}\right)^2\right) \quad (15)$$

is a typical form for spherical aberration. This second modification results in:

$$\hat{\psi}(r, z) \sim \psi(r, z) e^{\frac{1}{2}(g_0+g(r))l} e^{i\phi_s}. \quad (16)$$

Nonlinear phase distortion is similar to the static aberration, but is intensity (and therefore gain) dependent. It is characteristic of a glass medium and the phase alteration may be written as:

$$\phi_B = \frac{\nu |\chi(r, z)| (e^{(g_0+g(r))l} - 1)}{g_0 + g(r)} \quad (17)$$

where ν is the nonlinear refractive index for the medium. Thus the final expression for $\hat{\psi}$ becomes:

$$\hat{\psi}(r, z) \sim \psi(r, z) e^{\frac{1}{2}(g_0+g(r))l} e^{i\phi_s} e^{i\phi_B}. \quad (18)$$

The phase alterations are all incremental distortions accumulated since the previous decomposition. ψ , itself, contains a history of all preceding phase and amplitude modifications. New coefficients, $\hat{\gamma}_m$, can be calculated from an expression like Eq. 10. Propagation in the region prior to the next decomposition plane is accomplished by keeping the $\hat{\gamma}_m$ fixed, evaluating new phase terms, ϕ_m , and calculating the new wave function as:

$$\psi(r, z) = \sum_1^N \hat{\gamma}_m \Lambda_m e^{-i\phi_m}. \quad (19)$$

It is worthwhile to remark that the expression for gain (Eq. 12) and nonlinear distortion (Eq. 17) are valid only for unsaturated media. Suitable expressions are utilized for expressing the phenomenon of gain saturation.

The propagation through space and/or certain passive elements can in general be described by a ray-transformation matrix, \mathbf{T} :

$$\mathbf{T} = \begin{pmatrix} A & B \\ C & D \end{pmatrix}. \quad (20)$$

If q , is the initial complex parameter, then after propagation

$$q_2 = \frac{Aq_1 + B}{Cq_1 + D}. \quad (21)$$

From q_2 the quantities $R(z)$, $w(z)$, and ϕ_m can be appropriately calculated (Eq. 7, 8 and 9). ARTEMIS is originally intended for transformation of the more specific kind:

$$\mathbf{T} = \begin{pmatrix} 1 & B \\ C & 1 \end{pmatrix} \quad (22)$$

where one of B or C is zero. $B \neq 0$ provides an incremental free space propagation distance. $C \neq 0$ provides a focal length for the appropriate (thin) lens transformation. For passive elements the only change effected to the wave function decomposition is a change in the modal phases, ϕ_m . If incremental distortions are also specified for the element, a redecomposition also takes place. It has been unnecessary to associate distortions with every passive element traversed to successfully model existing systems at LLL. It is only necessary to lump distortions in strategic points along the optical chain.

In a crued sense, the code handles “nearly perfect” laser system conditions and easily provides criteria for relative merit of alternatives to or variations of a given system. It is less useful in providing criteria for a “bad” system.

Miró

*Miró*³ [45, 46, 47] is a general code that simulates the creation and propagation of coherent beams. *Miró* also simulates linear and nonlinear interaction processes.

Miró is constructed around calculation modes and generic components. The calculation of propagation is based on the paraxial (or high frequency) approximation. The high frequency approximation of the linear phase fields gives two types of propagation according to the beam’s scales: the optical geometric propagation of parallel beam or the Fresnel’s propagation including diffraction effects. In both cases the description of the beam is limited to a finite number N of envelopes $\mathbf{E}_l(x, y, z, t)$ ⁴. In the geometric optic approximation, the envelopes $\mathbf{E}_l(x, y, z, t)$ are solutions of transport equations coupled with source terms:

$$\frac{\partial \mathbf{E}_l}{\partial t} + v_g^l \cdot \nabla \mathbf{E}_l + h(x, y, z, t, \mathbf{E}_1, \dots, \mathbf{E}_N) = 0, \quad (23)$$

where v_g^l is the group velocity of the envelope l , and $h(x, y, z, t, \mathbf{E}_1, \dots, \mathbf{E}_N)$ is an operator dependent on the type of interaction in the medium where the light wave propagates. In the case of the Fresnel diffraction model with a broad spectrum, the fields $\mathbf{E}_l(x, y, z, t)$ are solutions of non-elliptic Schrödinger equations coupled with

³The choice of this name comes from the custom in the old *Département de mathématiques appliquées* in Limeil to choose painter names for the codes of electromagnetism. It is also possible to create a French acronym from this name: Mathématiques et Informatique pour la Résolution des problèmes d’Optique (Mathematics and computer science to solve optical problems).

⁴The vector $\mathbf{E}_l(x, y, z, t)$ is complex and perpendicular to the direction of propagation. The real field is determined by:

$$\epsilon(x, y, z, t) = \sum_{l=1}^N \sqrt{\frac{1}{2n(\omega_l) c \epsilon_0}} \mathbf{E}_l e^{i(\omega_l t - k_l z)} + \text{c.c.}$$

where ω_l and k_l are the frequencies and numbers of the laser wave in the medium respectively, in accordance with the Siegman’s convention.

the source terms:

$$-2ik_l \left(\frac{\partial \mathbf{E}_l}{\partial t} + v_g^l \cdot \nabla \mathbf{E}_l \right) + \xi_l \Delta_{\perp} \mathbf{E}_l + G_l \frac{\partial^2 \mathbf{E}_l}{\partial t^2} - 2ik_l h_l(x, y, z, t, \mathbf{E}_1, \dots, \mathbf{E}_N) = 0, \quad (24)$$

where G_l characterizes group velocity dispersion in the medium. Having a basic scheme adapted to one or other of these models, it then has to be applied for the various interactions present in the media. The laser/solid interactions taken into account are mainly: amplification, absorption, Kerr effect, birefringence and frequency conversion. Each optical component is the seat of one or more of these effects.

The optical system is constructed on the worksheet by “dragging & dropping” of the component icon that is required to be incorporated in the system. A symbolic representation of the optical system is thus obtained⁵.

⁵This is somehow similar to the symbolic representation presented in the VirtualLab Fusion.

4 Hypothesis

Most of the high power laser facilities rely on the combination of standard ray-tracing software and some kind of beam propagation method or specialized software, typically designed in-house specifically for the purposes of these facilities. Examples of such software bundles include Malaprop, ARTEMIS and *Miró*, which have already been presented.

In the author's previously written master thesis [4] it was described how advantageous it can be to exploit more advanced methods and software packages for free-space propagation simulations and designing optical systems for the ELI-Beamlines facility. The strong potential of Field tracing [48], first introduced by LightTrans VirtualLab, can be exploited to solve the task of the BPM.

The aims and objectives of this thesis are to define the potential capability of VirtualLab's Field tracing to improve the way optical designers think and to put more stress on the physical propagation methods that make tracing through the optical systems "smarter". Ray-tracing offers very limited field information to be useful for the extreme conditions of ELI-Beamlines. Conversely, Field tracing offers the fully vectorial description of electromagnetic fields.

The overall goal of this thesis is to demonstrate that VirtualLab Fusion can offer more detailed information about the propagated fields and improve the optical designer's workflow, while showing these capabilities on ELI-Beamlines' test case scenarios.

The ability to propagate such extreme fields through the beamlines highlights the capability of VirtualLab Fusion. This ability is exploited for tasks that are normally solved by simple ray-tracing methods. Also a new possibility of simulating high numerical aperture systems arises with the introduction of Field tracing.

4.1 Aims and Objectives

The author collaborated with the systems engineering team lead by professor Bruno Le Garrec. The systems engineering team's (see the flowchart in Fig. 18) goal at the facility level is to develop the technology to either describe or construct the laser's path from its source to the target area (focal point). This technology is namely comprised of:

- Alignment (lasers to experiments)
- Diagnostics

- Beam Transport (central wavelengths 800 nm and 1060 nm)
 - L1: Gaussian shape included inside a 75 mm diameter aperture (20 fs pulse)
 - L2, L3, L4_{sa}: “top-hat” included inside $200 \times 200 \text{ mm}^2$ square aperture (L2, L3: 20 - 30 fs pulse)
 - L4_{fa}: “top-hat” included inside $400 \times 400 \text{ mm}^2$ square aperture (150 fs pulse)
 - telescoped for image-relay planes in the beam transport sections
 - deformable mirrors and off-axis parabolas for focusing on target(s)
- Control system
- Hardware – software
- Performance – Virtual Beamline Model

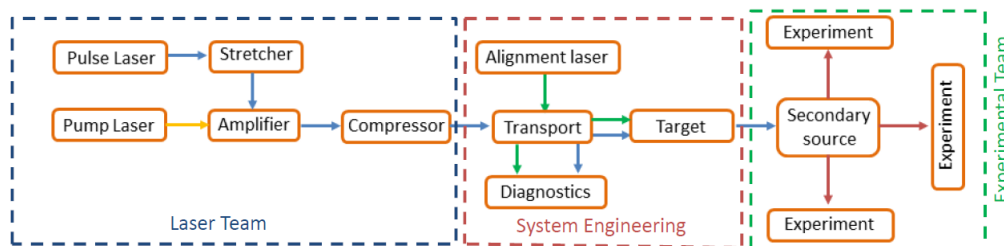


Figure 18: Three ELI-Beamlines teams: Laser Team, System Engineering and Experimental Team, and their specific tasks and responsibilities, adopted from [3].

The aim of this PhD study is to use the means of optical simulations and modeling to design and assess performance of relay telescopes and other optical systems necessary to transport, magnify and demagnify, or focus large aperture top-hat, super-Gaussian or Gaussian beams of femtosecond duration. A part of this aim is to collaborate with LightTrans International UG (haftungsbeschränkt), Wyrowski Photonics UG (haftungsbeschränkt) and the Applied Computational Optics group at the Institute of Applied Physics of the Friedrich-Schiller-Universität Jena. The collaboration with professor Wyrowski’s teams should ensure fast and effective development of VirtualLab Fusion in accordance with ELI-Beamlines’ required specifications. VirtualLab Fusion could play the following role in the Virtual Beamline Model – beam propagation simulation and time domain analysis.

The specific aims and objectives are given below:

Aims

- Find strengths and weaknesses of Wyrowski VirtualLab Fusion in comparison with Zemax OpticStudio.
- Help with creating the missing user scenarios and to identify typical ELI-Beamlines simulation tasks and assign proper simulation methods.
- Discuss possible improvements of VirtualLab Fusion with professor Wyrowski and his co-workers.
- Assist with testing of the new VirtualLab Fusion improvements to check if they match the ELI-Beamlines criteria.
- Design the author's own optical systems and assess existing systems by means of optical simulation in VirtualLab Fusion and/or Zemax OpticStudio.

Objectives

- Simulate a free space propagation of Gaussian, super-Gaussian and/or top-hat beams.
- Explore the possibility to scale commercially available doublets and assess the performance of scaled optical systems.
- Analyse the proper aperture size of the mirrors for beam transportation systems.
- Design and assess performance of the relay telescopes and/or reducers/expanders.
- Test the optical systems' resistance to mirror tilts and decentrations by means of tolerancing.
- Test the influence of form deviations to beam properties using the optical systems described in this thesis.
- Simulate the beamlines of the ELI-Beamlines facility by means of Field tracing.

5 Contribution to Knowledge

The contributions to knowledge produced by this PhD thesis are as follows:

- Use of VirtualLab Fusion for the purposes of the high power laser facility ELI-Beamlines and determination of the software's efficiency to fulfill the BPM requirements.
- Assessment and reporting of relay telescopes, beam reducers, expanders and other optical systems' feasibility and performance.
- Analyses and optimisation of the optical systems for the needs of ELI-Beamlines.
- Beamlines simulations and their performance analyses.
- Recommendations based on the information gathered by the aforementioned analyses and optimisations.

6 Optical Simulation Software

There are two specific optical simulation software bundles used to aid in fulfilling the aims of this thesis. Namely Zemax|OpticStudio 15 [49] and Wyrowski VirtualLab Fusion [6, 7]. These two software bundles are described with the help of the manuals provided, or other publications when possible. Readers experienced in using the aforementioned software bundles may skip this chapter, which is mainly provided for other optical design software users' convenience.

6.1 Zemax|OpticStudio

OpticStudio [49] is the industry standard for optical system design software, combining sequential lens design, analysis, optimization, tolerancing, physical optics, non-sequential optical system design, polarization, thin-film modeling and mechanical CAD Import/Export in a single, easy-to-use package.

This software is typically used by the optical designers for ray-tracing simulations. However Professional and Premium editions of this software also contain the means of physical optics propagation.

An excerpt from the OpticStudio 15 manual follows [50].

Geometrical optics is the modeling of optical systems by tracing rays. Rays are imaginary lines which represent normals to the surfaces of constant phase, called the wavefront. Either rays or wavefronts can be used to represent a beam. However, rays and wavefronts are propagated differently. Rays propagate along straight lines without interfering with one another, wavefronts propagate while coherently interfering with themselves. For this reason, the ray model and the wavefront model yield different representations of the beam as it propagates through free space or through optical components. The ray method is fast, flexible and extremely useful for modeling almost any optical system. However, rays are not well suited to modeling certain important effects, primarily diffraction. Zemax does have some ray based diffraction computations, such as the diffraction MTF or PSF. These diffraction computations make a simplifying approximation: that all the important diffraction effects occur going from the exit pupil to the image. This is sometimes called the "single step" approximation. Rays are used to propagate the beam from the object, through all the optics and intervening spaces, all the way to the exit pupil in image space. The ray distribution in the exit pupil, with transmitted amplitude and accumulated OPD used to compute the phase, is used to form a complex amplitude wavefront. Then, in a single step, a diffraction computation is used to propagate this complex amplitude wavefront to the region near focus. Geometrical optics and the single step approxi-

mation work quite well for the majority of traditional optical designs, where the beam is not near focus anywhere except the final image. However, the model breaks down for several important cases:

- When the beam comes to an intermediate focus, especially near optics that truncate the beam (rays by themselves do not predict the correct distribution near focus).
- When the diffraction effects far from focus are of interest (rays remain uniform in amplitude and phase, wavefronts develop amplitude and phase structure).
- When the propagation length is long and the beam is nearly collimated (collimated rays will remain collimated over any distance, real beams diffract and spread).

Physical optics is the modeling of optical systems by propagating wavefronts. The beam is represented by an array of discretely sampled points, analogous to the discrete sampling using rays for a geometric optics analysis. The entire array is then propagated through the free space between optical surfaces. At each optical surface, a transfer function is computed which transfers the beam from one side of the optical surface to the other. The physical optics model allows very detailed study of arbitrary coherent optical beams, including:

- Gaussian or higher order multi-mode laser beams of any form (beams are user definable).
- Beams may be propagated along any arbitrary field position (skew beams).
- Amplitude, phase and intensity may be computed at any surface in the optical system.
- Effects of finite lens apertures, including spatial filtering, may be modeled. Accurate computation of propagation through any optical component Zemax can model via ray tracing.

The physical optics model is generally more accurate at predicting the detailed amplitude and phase structure of the beam away from focus than conventional ray tracing. However there are some disadvantages to the physical optics propagation analysis:

- Physical optics computational method is generally slower than geometrical optics. Because the entire beam array must be stored in computer memory at once, the required RAM may be quite large for large sampling arrays.
- The sampling limits the amount of aberration in the beam that can be accurately modeled. For highly aberrated systems, geometrical optics should be used.

The following text will summarize the physical optics propagation algorithms [50].

6.1.1 Physical Optics Propagation

The methods used in Zemax are based upon references [51, 52]. Only the material relevant to using the physical optics propagation feature in the Zemax will be summarized here.

Representation of the Electric Field

The electric field may be represented in three dimensions as [50]

$$\vec{E}(x, y, z) = E_x \hat{x} + E_y \hat{y} + E_z \hat{z} \quad (25)$$

where the E values are all complex and \hat{x} , \hat{y} , and \hat{z} are the Cartesian unit vectors. The coordinate system used by Zemax is that the beam propagates primarily down a local z axis. The z axis used to represent the beam is aligned with a reference chief ray in each optical space, and therefore this z axis is not generally the same as the z axis defined by the Lens Data Editor which is used to position optics. Because the beam is propagating along the local z direction, the first approximation made is to neglect the E_z component. Since the electric field must always be normal to the ray propagation direction, E_z can be reconstructed from other data when required, as will be described later. By keeping track of the electric field components along both the x and y axes, effects due to polarization may be studied, such as transmission and reflection losses, polarization aberrations, and of course the polarization state of the beam. If polarization effects are not required, the y component of the field may be ignored, speeding the computations.

Statements presented above are very important when later comparing the OpticStudio to the VirtualLab Fusion.

The Fresnel Number

A very useful concept in physical optics modeling is the Fresnel number [50]. Strictly speaking, the definition of the Fresnel number only applies to unaberrated rotationally symmetric beams with a finite extent. However, the concept is still useful in cases that do not meet these criteria. The Fresnel number depends upon the diameter of the beam, the radius of curvature of the wavefront phase, and the distance to an observation point where the complex amplitude of the field is desired. Conceptually the Fresnel number is the number of annular “Fresnel zones” from the center of the beam to the edge. Fresnel zones are the radial zones where the phase as seen from the observation point changes by π . A perfectly collimated beam will have a Fresnel number given by

$$F_n = \frac{2}{\lambda} \left[\sqrt{Z^2 + A^2} - Z \right] \quad (26)$$

which for Z greater than A reduces to approximately

$$F_n = \frac{A^2}{\lambda Z} \quad (27)$$

where A is the radial size of the beam and Z is the distance from the beam to the observation point. The Fresnel number becomes small as Z grows large. For beams that are not collimated, the concept is the same. A converging beam will have a very small Fresnel number if the observation point is near focus. A perfectly spherical beam converging to focus will have a Fresnel number of zero, since there are no zones where the observed phase reaches π . As the observation point moves from the focal region, the Fresnel number increases.

Near and Far Field

If the Fresnel number is small, less than roughly 1, then the beam at the observation point is said to be in the “far field” relative to the current beam [50]. For Fresnel numbers larger than 1, the beam at the observation point is said to be in the “near field” relative to the current beam. It is important to consider the terms near and far as being relative to the propagation from the present location of the beam to the observation point at which the Fresnel number is computed, rather than having any rigid relationship to the beam position alone. For example, a beam in the exit pupil of an optical system is typically called the near field because the far field is at focus. However, a short propagation from focus to a slightly out of focus observation point is likely a near field propagation if the defocus is small. The decision as to whether propagation is in the near or far field will determine the choice of diffraction propagation methods [50].

Angular Spectrum Propagation

A plane wave is represented by [50]

$$e^{i\mathbf{k}\cdot\mathbf{z}} \quad (28)$$

where \mathbf{k} is the wave vector, with magnitude $\frac{2\pi}{\lambda}$, and \mathbf{z} is the local z direction. The vector \mathbf{k} points along the normal to the wavefront in the direction of propagation. This normal vector has direction components α , β , and γ , where

$$\alpha^2 + \beta^2 + \gamma^2 = 1. \quad (29)$$

The plane wave can then be written as

$$e^{\frac{i2\pi}{\lambda}(\alpha x + \beta y + \gamma z)}. \quad (30)$$

Now recall the definition of the Fourier transform and the inverse Fourier transform:

$$\mathcal{F}[A(\xi, \eta)] \equiv \int_{-\infty}^{\infty} \int_{-\infty}^{\infty} [A(x, y)] e^{-i2\pi(x\xi + y\eta)} dx dy, \quad (31)$$

$$\mathcal{F}^{-1}[B(x, y)] \equiv \int_{-\infty}^{\infty} \int_{-\infty}^{\infty} [B(\xi, \eta)] e^{i2\pi(x\xi + y\eta)} d\xi d\eta. \quad (32)$$

Let $G = \mathcal{F}[E]$, that is, G is the Fourier spectrum representation of the electric field E . By definition then

$$E(x, y) = \int_{-\infty}^{\infty} \int_{-\infty}^{\infty} G(\xi, \eta) e^{i2\pi(x\xi + y\eta)} d\xi d\eta. \quad (33)$$

The electric field can therefore be interpreted as being the integral of a collection of plane waves propagating with direction cosines

$$\alpha = \lambda\xi, \quad \beta = \lambda\eta, \quad \text{and } \gamma = \sqrt{1 - (\lambda\xi)^2 - (\lambda\eta)^2}. \quad (34)$$

Eliminating γ and making the approximation that the plane wave propagates at a small angle with respect to the z axis, the plane wave equation can be rewritten

$$e^{\frac{i2\pi z}{\lambda} \sqrt{1 - \alpha^2 - \beta^2}} \approx e^{\frac{i2\pi z}{\lambda}} e^{\frac{-i\pi z(\alpha^2 + \beta^2)}{\lambda}}. \quad (35)$$

The term $e^{\frac{i2\pi z}{\lambda}}$ is just a phase propagation term that is normally neglected. The term which depends upon α and β is the transfer function for a plane wave in free space. Defining $\rho^2 = \xi^2 + \eta^2$ the plane wave transfer function can then be rewritten as

$$G(\xi, \eta, z) = G(\xi, \eta, 0) e^{-i\pi\lambda z \rho^2}. \quad (36)$$

To propagate an electric field from one plane to another, the field needs to be Fourier transformed, the plane wave propagator applied, and then the resulting distribution inverse Fourier transformed. These operations may be summarized by defining the plane to plane (PTP) operator:

$$E(x, y, z_2) = PTP[E(x, y, z_1), (z_2 - z_1)], \quad (37)$$

where

$$PTP(E, \Delta z) \equiv \mathcal{F}^{-1}[T(\Delta z) FF[E]], \quad (38)$$

and

$$T(\Delta z) = e^{-i\pi\lambda\Delta z\rho^2}. \quad (39)$$

Note that the transfer function $T(\Delta z)$ has unity amplitude but a complex phase. This phase varies slowly from point to point in the frequency domain representation G if $\lambda\Delta z\rho^2$ is small. But if $\lambda\Delta z\rho^2$ grows large, the phase variations become increasingly rapid. If the phase changes by more than about 2 between adjacent points in the finite array, the phase becomes ambiguous, and a phenomenon known as aliasing occurs. For this reason, the angular spectrum method works very well if the propagation distances are fairly short or if the beam is nearly collimated. Although the diffraction theory is accurate for any propagation distance, when the beam is represented by a finite sized array of discrete points, the phase of the beam cannot be accurately represented if the phase of the angular spectrum propagator changes too rapidly between points. When using the angular spectrum propagator, the phase of the electric field is measured relative to a plane. Positive phase indicates the wavefront is advanced along the local $+z$ axis relative to the plane, regardless of the direction of propagation. The angular spectrum propagator is useful when the Fresnel number is large. This includes the important case of propagating a beam a short distance. However, the angular spectrum propagator also works well for propagating a large distance when the divergence of the beam (and thus ρ) is small. A good rule of thumb to use is that if the beam does not change size significantly, the angular spectrum propagator may be used. To propagate beams with small Fresnel numbers, where the beam will change size significantly, requires a separate theoretical and numerical method.

Fresnel Diffraction

For small Fresnel numbers the appropriate theory is Fresnel diffraction [51]. The key assumptions in Fresnel theory require that the field being computed is not too close to the initial field, namely, if $z_2 - z_1 = \Delta z$, then Δz is large compared to the region over which the field at z_2 is to be determined. That means the beam cannot diverge too quickly; very fast $f/\#$ beams cannot be accurately modeled with Fresnel diffraction theory. In the Fresnel region the electric field distribution is given by

$$E(x_2, y_2, z_2) = \left[\frac{e^{ikz}}{i\lambda\Delta z} \right] q(r_2, \Delta z) \int_{-\infty}^{\infty} \int_{-\infty}^{\infty} E(x_1, y_1, z_1) q(r_1, \Delta z) e^{-\frac{i2\pi}{\lambda\Delta z}(x_1x_2+y_1y_2)} dx_1 dy_1, \quad (40)$$

where

$$q(r, \Delta z) = e^{\frac{i\pi r^2}{\lambda\Delta z}}. \quad (41)$$

Each of the terms in the above expression has a clear physical interpretation. The leading term indicates that as the beam propagates, the phase changes along the

z axis, just like the plane wave described earlier. The amplitude also decreases linearly with distance, or the intensity ($E \times E$) falls quadratically. The expression for $q(r, \Delta z)$, called the quadratic phase factor, indicates that the phase is referenced to a sphere of radius Δz (strictly speaking it is a parabola, but we have already assumed in the Fresnel development that $r_2 \ll \Delta z$). This is a very useful property; all that is required in the representation of the electric field is the phase difference relative to the reference sphere. This significantly reduces the number of sample points needed to accurately define the phase of the beam. When using the Fresnel propagator, the phase of the electric field is measured relative to a reference sphere with a radius equal to that of the distance from the beam waist. This is not the same radius as the phase radius of curvature of the Gaussian beam. Positive phase indicates the wavefront is advanced along the local $+z$ axis relative to the reference sphere, regardless of the direction of propagation. Another important property of $q(r, \Delta z)$ is that as Δz gets larger, $q(r, \Delta z)$, varies more slowly in phase. This is the opposite of the $T(\Delta z)$ operator, which varies rapidly in phase as Δz gets larger. Accordingly, Fresnel diffraction is useful when the Fresnel number is small.

Selecting the Correct Propagator

Zemax automatically chooses the angular spectrum propagator when the Fresnel number is large, and the Fresnel propagator when the Fresnel number is small [50]. However, there are times when the angular spectrum propagator is a better choice than the Fresnel, and Zemax supports a surface specific option to choose the angular spectrum propagator rather than the default choice.

Fraunhofer Diffraction

Consider the Fresnel diffraction expression. If Δz is very large, then $q(r, \Delta z)$ may be neglected [50]. This yields the Fraunhofer diffraction expression, which is

$$E(x_2, y_2, z_2) = \left[\frac{e^{ikz}}{i\lambda\Delta z} \right] \int_{-\infty}^{\infty} \int_{-\infty}^{\infty} E(x_1, y_1, z_1) e^{\frac{i2\pi}{\lambda\Delta z}(x_1x_2+y_1y_2)} dx_1 dy_1, \quad (42)$$

or

$$E(x_2, y_2, z_2) = FF(E(x_1, y_1, z_1)), \quad (43)$$

where phase and amplitude factors are omitted. The far field distribution is just a scaled version of the Fourier transform of the near field distribution. Fraunhofer diffraction is only valid if the Fresnel number is nearly zero. The ray based diffraction features in Zemax, such as the diffraction MTF and PSF assume Fraunhofer diffraction. This is why Zemax cannot compute the ray based diffraction MTF or PSF if the beam is too much out of focus. The Fraunhofer assumption is never used by the physical optics propagation algorithm in Zemax, it is presented here for completeness.

The Pilot Beam

Consider a Gaussian beam with waist w_0 . The Rayleigh range is given by [50]

$$z_R = \frac{\pi w_0^2}{\lambda}. \quad (44)$$

The phase radius if curvature of the beam is a function of the distance from the beam waist, z :

$$R(z) = z + \frac{z_R^2}{z}. \quad (45)$$

Note that the radius is infinite at $z = 0$, reaches a minimum of $2z_R$ at $z = z_R$, and asymptotically approaches infinity as z approaches infinity. The phase of the Gaussian beam along the axis is defined by the Gouy shift, given by

$$\varphi(z) = \tan^{-1} \left(\frac{z}{z_R} \right). \quad (46)$$

For example, the axial phase is $\pi/4$ at a distance of plus one Rayleigh range. The beam size is also a function of the distance from the waist:

$$w(z) = w_0 \left[1 + \left(\frac{z}{z_R} \right)^2 \right]^{1/2}. \quad (47)$$

Note, for large distances the beam size expands linearly. The divergence angle of the beam is given by

$$\theta = \tan^{-1} \frac{w_0}{z_R}. \quad (48)$$

Now consider the problem of numerically representing this beam by a discrete sampling of points. If a constant spacing between points is used, the beam will expand beyond the edges of the array if the propagation proceeds too far from the waist. Therefore, far from the waist, a linearly expanding coordinate system where the point spacing is proportional to z is best. However, near the waist, the beam size does not decrease to zero, but remains reasonably constant. In this domain, a constant sampling is most convenient. The compromise sampling system is to use a constant spacing near the waist, and a linearly scaled spacing far from the waist. The diffraction theory developed earlier did not assume any particular shape or form to the electric field being propagated. The algorithms are for the most part independent of the field distribution. However, the problem of sampling remains. It is also impractical to compute (or even define) Fresnel numbers for arbitrary, aberrated beams with irregular or non-existent apertures. For this reason, a pilot beam is used to assist the physical optics propagation algorithm in determining which propagation algorithm to select. The pilot beam is an ideal Gaussian beam, with a waist, beam size, phase radius, and relative z position. The initial parameters may be generated by fitting

the Gaussian beam equations to the initial distribution. The pilot beam is then propagated from surface to surface. At each surface, new beam parameters, such as the new waist, phase radius, or position are computed. The properties of the pilot beam are then used to determine if the actual distribution is inside or outside the Rayleigh range, and what propagation algorithms are appropriate. After passing through an aperture that significantly truncates the beam, such as a pinhole aperture, it may be required to recompute the pilot beam parameters, as described later.

Sign Conventions for Phase Data

As shown in the previous sections, the angular spectrum propagator works best when the beam is nearly collimated, while the Fresnel theory works best when the beam is diverging [50]. When using the angular spectrum propagator, the phase of the electric field is referenced to a plane. Once the beam propagates past the Rayleigh range, the Fresnel propagator is used, and the phase of the electric field is referenced to a sphere whose radius is the distance from the beam waist to the current position of the pilot beam. The sign of the phase is positive if the wavefront is to the “right” of the reference surface, with “right” being towards the positive local z axis direction. For a beam propagated to the $+z$ side just inside the Rayleigh range, the phase slope is negative because the wavefront is left of the reference plane. Just outside of the Rayleigh range, the phase slope is positive because the wavefront is now to the right of the reference sphere. Therefore, the slope of the phase of the electric field will “flip” from negative to positive when crossing from inside to outside the Rayleigh range on the $+z$ side.

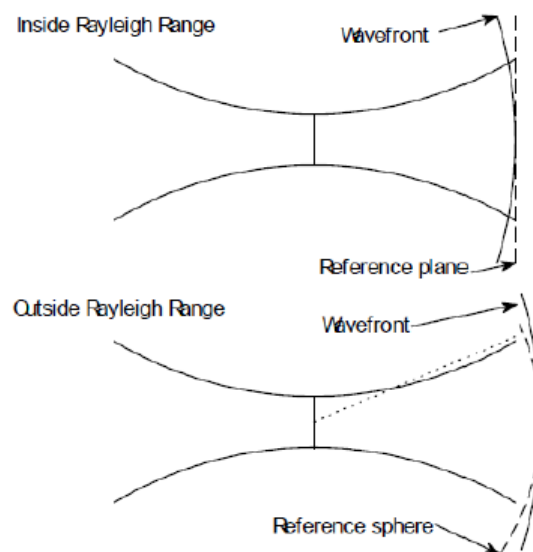


Figure 19: Gaussian beam propagation inside and outside the Rayleigh range, adopted from [47].

For example, consider a Gaussian beam. At the waist, the phase is zero everywhere on the reference plane. If the beam is propagated (see Fig. 19) to just inside the Rayleigh range on the positive side of the waist, the phase at the center of the beam will change to $\pi/4$ radians, this is the Gouy shift given by $\varphi = \tan^{-1}\left(\frac{z}{z_R}\right)$. The phase radius of the curvature of the beam will become twice the Rayleigh range distance. The wavefront phase will be increasingly negative relative to the center of the wavefront as the radial aperture is increased, because the curved wavefront phase is measured relative to a plane. If the beam now propagates a small distance so the pilot beam is now just on the far side of the Rayleigh range, the phase will remain $\pi/4$ radians at the center but will now be referenced to a sphere whose radius is the distance to the waist, which is the Rayleigh range for this case. Because the radius of the reference sphere is smaller than the curvature of the wavefront, the slope of the phase of the beam will now “flip” to be increasingly positive with radial aperture. Finally, as the beam propagates further past the Rayleigh range, the phase relative to the reference sphere will tend toward a constant value of $\pi/2$ radians (the limiting value of the Gouy shift). The two representations of the beam are equivalent, however care must be taken for the proper phase reference surface when constructing or comparing different beams.

Propagating in and out of the Rayleigh Range

The naming conventions used in this section are from the Lawrence reference cited earlier in this help file. It has already been shown that short propagations are well modeled using the *PTP* operator [50]. This operator has the property that the sample spacing remains constant. It is most convenient to use the Fresnel propagator when the beam is already at the waist of the pilot beam, and the field is desired far from the waist relative to a reference sphere. For this reason, the Fresnel propagator is redefined as the waist to sphere (*WTS*) operator:

$$E(x_2, y_2, z_2) = WTS[E(x_1, y_1, 0), z_2], \quad (49)$$

where

$$WTS(E, \Delta z) \equiv \left[\frac{1}{i\lambda z_2} \right] \mathcal{F}^s [q(r_1, z_2) E], \quad s = \frac{z_2}{|z_2|}, \quad (50)$$

$$\Delta x_2 = \frac{\lambda |z_2|}{n_x \Delta x_1}, \quad \text{and} \quad \Delta y_2 = \frac{\lambda |z_2|}{n_y \Delta y_1}, \quad (51)$$

where n_x and n_y are the number of points in the x and y directions of the array. The last two expressions yield the new linearly scaled sample spacings after application of the operator. Reversing the order of operations results in the sphere to waist (*STW*) operator:

$$STW(E, \Delta z) \equiv q(r_1, z_2) \mathcal{F}^s [i\lambda z_2 E], \quad (52)$$

with a similar change in the sample spacing. There are four possible general propagation cases to consider:

- II: propagation from inside to inside the Rayleigh range.
- IO: propagation from inside to outside the Rayleigh range.
- OI: propagation from outside to inside the Rayleigh range.
- OO: propagation from outside to outside the Rayleigh range.

All these cases can be handled with the appropriate combination of the *PTP*, *WTS*, and *STW* operators:

- $II(z_1, z_2) = PTP(z_2 - z_1)$
- $IO(z_1, z_2) = WTS(z_2 - z_0)PTP(z_0 - z_1)$
- $OI(z_1, z_2) = PTP(z_2 - z_0)STW(z_0 - z_1)$
- $OO(z_1, z_2) = WTS(z_2 - z_0)STW(z_0 - z_1)$ where z_0 is the pilot beam waist position, z_1 is the starting beam position and z_2 is the end beam position.

Point Spacing and Sampling

Although the total number of array points n_x and n_y , remain constant, the array size and point spacings Δx and Δy will change as the beam propagates. If the array width is very large at the beam waist relative to the waist size, then there are relatively few points across the beam waist. This will result in a smaller array size far from the waist, with a relatively large number of points across the beam size. Conversely, if the array size is small at the waist, the array size will grow large compared to the beam far from the waist, leaving few sample points to represent the beam. This inverse relationship is a necessary but frequently inconvenient product of the Fourier transform theory used to model the diffraction. The exact equations describing the change in point spacing are given in the previous section. There is clearly a tradeoff between good sampling of the beam near the waist and good sampling far from the waist. It can be shown that to achieve approximately uniform sampling relative to the beam size at both the waist and far from the beam waist the array size at the beam waist in the X and Y directions should be

$$X = \omega_{0x} \sqrt{\pi n_x}, Y = \omega_{0y} \sqrt{\pi n_y}. \quad (53)$$

The physical optics analysis feature settings include an “Auto” button which will use this formula to set a suggested initial array width.

Propagation Through Arbitrary Optical Surfaces

The methods described thus far are good for propagating through homogeneous space [50]. However, the prime interest is in propagating the beam through optical components such as lenses and apertures. It is not practical to directly perform a diffraction propagation through an arbitrary surface shape. The difficulty lies in the representation of the complex amplitude at discrete points in a plane or spherical phase referenced array. When the beam is incident on a curved surface, different parts of the beam intercept the surface at different points along the local z axis. To avoid this problem, the properties of the pilot beam are used to generate a set of rays that represent the wavefront incident upon the surface. This set of rays, called probing rays, is then traced through the optical surface using conventional geometric optics. The path length of each ray, and the positional and angular aberrations generated are then used to reconstruct the pilot beam and complex amplitude after (behind) the surface. The probing ray set is used to generate the transfer through the surface. The probing ray set can be used to determine the effective power of the surface with respect to the pilot beam, the direction of the beam after leaving the surface, the polarization phase and amplitude transmission of a surface, and the vignetting of the surface with any supported surface apertures (or ray errors). Note that surfaces without defined hard apertures will pass the entire beam without vignetting, independent of how the system aperture is set. The probing ray method can be applied to propagation through a single surface, or multiple surfaces at once. This is a very desirable property, because geometrical optics may be used to propagate through whole optical components that would be difficult to model with physical optics propagation. These include highly tilted surfaces and gradient index lenses, to name a few. Propagating through multiple surfaces at once using rays also speeds up the analysis. Some special surfaces, such as the ABCD matrix surface, and some types of Fresnel surfaces, do not allow POP analysis at all because there is no way to compute the effective phase of these surface types. A warning has been issued by Zemax if the POP analysis cannot proceed due to the presence of these special surface types.

Accounting for Polarization

If polarization is used, Zemax will use polarization ray tracing [50] to determine the properties of the probing ray set and corresponding transfer function. Polarization ray tracing permits the modeling of the effects of optical coatings on the phase and amplitude of the transmitted or reflected beam. Zemax assumes the E_x and E_y portions of the field account for all the energy in the beam at any given array point. However, the E_z component is required for polarization ray tracing. Zemax recreates the E_z as needed by applying the condition that E must be perpendicular to the propagation vector \mathbf{k} . The vector \mathbf{k} is computed from the pilot beam properties

and the phase errors present on the beam. The E_x and E_y fields are renormalized to account for the correct beam intensity. After polarization propagation, the E_x and E_y components are renormalized to again hold the energy present in the E_z component, which is then discarded.

6.2 Wyrowski VirtualLab Fusion

VirtualLab Fusion [6, 7] is the latest step in the development of the first available commercial field tracing [48] software bundle. LightTrans VirtualLab [53], which brought the concept of Field tracing to the optical community, has changed its name to VirtualLab Fusion [54] and delivered yet another unique concept for optical simulations. This new concept is called Geometric Field Tracing [8]. By the unification of these two specific concepts, Unified Field Tracing has been created.

Table 2: Unified Field Tracing structure.

Unified Field Tracing		
Geometric Field Tracing	Diffractive Field Tracing	
-	Rigorous	Approximative

As per the creator's paper [48]: Field tracing is the generalization of ray tracing and enables electromagnetic system modeling. Harmonic fields are traced through the optical system instead of ray bundles. This allows the smooth combination of different modeling techniques in different subdomains of the system, e.g. to use the rigorous spectrum-of-plane-wave operator for homogeneous media, geometrical optics to trace through a lens and finite element methods to include the effect of scatterers. All modeling techniques are formulated for vectorial harmonic fields.

Table 3: Example of available Field Tracing Techniques.

Field Tracing Techniques	
Free-space propagation:	Spectrum of plane wave integral (SPW)
	Fresnel integral
	Far field integral
	Geometric field tracing
	Automatic selection operator
Tilt operator	(electromagnetic fields on arbitrary planes)
Rigorous modeling	(for plane interfaces, prisms, cubes etc.)
Geometric field tracing	
Thin element approximation	(TEA)
Beam propagation method	(Split-step)
Fourier modal method	(FMM)
Integral method	(WIAS)
Finite element method	(FEM)

Field tracing considers [55] a decomposition of an optical system into subdomains. Contrary to ray tracing, electromagnetic harmonic fields are traced through the system. This approach provides three fundamental advantages: (1) Field tracing enables unified optical modeling. Its concept allows the utilization of any modeling technique that is formulated for vectorial harmonic fields in different subdomains of the system. (2) The use of vectorial harmonic fields as a basis of field tracing permits a great flexibility in light-source modeling. By propagating sets of harmonic field modes through the system, light that is partially both temporally and spatially coherent, as well as ultrashort pulses can be investigated. (3) In system modeling and design, the evaluation of any type of detector function is essential. The use of vectorially formulated harmonic fields enables unrestricted access to all field parameters, and therefore it allows the introduction and evaluation of any type of detector. In field tracing, local Maxwell problems for subdomains are solved. These local problems often have properties that give rise to solutions in certain subspaces of all admissible functions. Then, approximate Maxwell solvers are accurate enough and are typically much cheaper than rigorous Maxwell solvers. The goal of field tracing is to construct a problem dependent solver, which is as fast as possible and as accurate as needed by combining different subdomain solvers [55]. Maxwell solvers for free space are summarized in 6.2.1.

In 2014, Wyrowski Photonics [56] took over the development of the next generation of VirtualLab in order to provide the simulation technologies required for the challenges of modern optics. VirtualLab Fusion introduces the new geometric field tracing engine using smart rays which carry complete light field information. The user of VirtualLab Fusion builds up the optical system once, and has three optical modeling engines available.

- Ray Tracing: this engine provides a fast analysis of the performance of optical system based on conventional ray tracing technology. It delivers 2D ray information including position, direction, optical path length and absorption.

- Geometric Field Tracing Plus: this engine delivers complete electric and magnetic field information. It solves Maxwell's equations in its geometric approximation. It is as fast as ray tracing but includes amplitude, phase, polarization, spatial and temporal coherence, interference, and speckles. It delivers 2D ray information on the detector surface including all ray tracing quantities, the electric field (E_x , E_y , E_z) and the magnetic field (H_x , H_y , H_z).

- Classic Field Tracing: this engines combines geometric modeling techniques with numerous diffractive modeling techniques. More wave-optical effects, in particular diffraction, are included in the simulation.

6.2.1 Free Space Operators

Spectrum of Plane Waves - Rigorous Free Space Operator

The spectrum of the plane waves [54] propagation operator $\mathcal{P}_{\Delta z}^{SPW}$ is used for simulating the propagation of a field $U(x, y)$ with a wavelength λ by a distance Δz through an infinite homogeneous medium with a given refractive index n

$$\mathcal{P}_{\Delta z}^{SPW}U = \mathcal{F}^{-1} \left(\exp \left[i2\pi \sqrt{\frac{n^2}{\lambda^2} - \hat{x}^2 - \hat{y}^2} \Delta z \right] \mathcal{F}U(x, y) \right), \quad (54)$$

where \hat{x} and \hat{y} are spatial frequencies, i.e. pixel coordinates of the Fourier transformed field. The spectrum of the plane waves propagation operator $\mathcal{P}_{\Delta z}^{SPW}$ as given in the previous equation can be derived without using any physical approximations. That is, its accuracy is limited only by numerical errors.

The main reason for these numerical errors is the sampling of the phase term in Eq. 54 by a finite sampling distance δx , which can cause sampling problems during the numerical evaluation of this equation. These issues vanish if the propagation distance Δz is sufficiently small. The following formula gives an approximate maximum value Δz_{\max} for propagation distance, such as in the case of $\Delta z < \Delta z_{\max}$, where the numerical error in the application of $\mathcal{P}_{\Delta z}^{SPW}$ is often negligible,

$$\Delta z_{\max} = \frac{1}{2} \left[\sqrt{\left(\frac{n}{\lambda}\right)^2 - (U_0 - \delta U)^2} - \sqrt{\left(\frac{n}{\lambda}\right)^2 - U_0^2} \right]^{-1}, \quad (55)$$

where $U_0 = 1/(2\delta x)$ and $\delta U = 1/(n_x \delta x)$. It should be mentioned that in general the numerical error for all propagation distances $\Delta z > 0$ is never zero but just decreases with decreasing propagation distance. The numerical error can be decreased for a given propagation distance Δz by appending sampling points (with a value of zero) at the borders of the field. The number of sampling points is increased from n_x to $n_{x,\min}$ by doing so. The recommended value for $n_{x,\min}$ can be calculated approximately by

$$n_{x,\min} = \frac{2}{1 - 2\delta x \sqrt{\left(\frac{n}{\lambda}\right)^2 - a^2}} \quad (56)$$

where

$$a = \frac{1}{2\Delta z} + \sqrt{\left(\frac{n}{\lambda}\right)^2 - \left(\frac{1}{2\delta x}\right)^2}. \quad (57)$$

Rayleigh Sommerfeld Operator - Rigorous Free Space Operator

The propagation integral used in Rayleigh Sommerfeld propagation [54] simulates the propagation of a field $U(x, y)$ with a wavelength λ by a distance Δz through an

infinite homogeneous medium with a given refractive index n . It is defined as:

$$\left[\mathcal{P}_{\Delta z}^{RS}U(x, y)\right](x', y') = \frac{1}{2\pi} \int_{-\infty}^{\infty} dx dy U(x, y) \frac{\partial \exp(ikR)/R}{\partial z}, \quad (58)$$

where

$$\frac{1}{2\pi} \frac{\partial \exp(ikR)/R}{\partial z} = \frac{z \exp(ikR)(1 - ikR)}{2\pi R^3} \quad (59)$$

and

$$R = \sqrt{(x - x')^2 + (y - y')^2 + \Delta z^2}. \quad (60)$$

The Rayleigh Sommerfeld propagation integral can be derived without any physical approximation. Actually the propagation integral is a convolution of a harmonic field and a spherical phase function. It is possible to solve this convolution by using fast Fourier transforms. In this case the propagation integral has a form

$$\left[\mathcal{P}_{\Delta z}^{RS}U(x)\right](x') = \mathcal{F} \left[\mathcal{F}^{-1} \left(\frac{z \exp(ikR)(1 - ikR)}{2\pi R^3} \right) \mathcal{F}^{-1}U(x) \right]. \quad (61)$$

If the convolution is evaluated by fast Fourier transforms it is also called Rayleigh Sommerfeld Convolution. In contrast the integral can also be numerically evaluated by simple summation. In comparison with the calculation of the convolution by fast Fourier transforms, the pure summation is much more time-consuming, but has the advantage of free choice of the number of sampling points and sampling distance of the propagated field. This propagation method is accurate for large propagation distances. For smaller distances numerical errors will occur because of an undersampling of the spherical phase function. The critical distance Δz_{\min} can be estimated by

$$\Delta z_{\min} = \frac{n}{\lambda} \sqrt{\left[\left(\frac{\lambda}{2n} \right)^2 - x_0^2 - (x_0 - \delta x)^2 \right]^2 - 4x_0^2(x_0 - \delta x)^2}. \quad (62)$$

x_0 is the radius of the field and is defined as $x_0 = \frac{n_x}{2} \Delta x$. It should be mentioned that for all propagation distances $\Delta z \neq 0$ the numerical errors never vanish but just decrease more and more with increasing distance. For propagation distances $\Delta z < \Delta z_{\min}$, numerical errors can be reduced by interpolating the harmonic field before propagation. The necessary sampling distance $\delta_{x, \min}$ can be estimated by

$$\delta_{x, \min} = \frac{\pi}{kx_0} \sqrt{x_0^2 + (\Delta z)^2}, \quad (63)$$

where

$$k = \frac{2\pi n}{\lambda}. \quad (64)$$

Fresnel Propagation Operator - Paraxial Free Space Operator

The Fresnel propagation operator $\mathcal{P}_{\Delta z}^{\text{Fresnel}}$ [54] for simulating the propagation of a field $U(x, y)$ with a wavelength λ by a distance Δz through an infinite homogeneous medium with a given refractive index n can be derived using the paraxial Fresnel approximation:

$$\left[\mathcal{P}_{\Delta z}^{\text{Fresnel}} U(x, y) \right] (x', y') = \frac{A}{i} \exp(ik\Delta z) \exp\left(\frac{ik}{2\Delta z}(x'^2 + y'^2)\right) \cdot \left[\mathcal{F}\left(U(x, y) \exp\left[\frac{ik}{2\Delta z}(x^2 + y^2)\right]\right) \right] \left(\frac{k}{2\pi\Delta z}x', \frac{k}{2\pi\Delta z}y'\right), \quad (65)$$

where A denotes a real-valued factor.

In contrast to the spectrum of the plane waves operator for the application of the Fresnel propagation operator, the numerical errors become larger for shorter propagation distances Δz because of the quadratic phase term in the previous equation. The critical minimum distance Δz_{\min} can be estimated by

$$\Delta z_{\min} = \frac{\delta x^2 n n_x}{\lambda}. \quad (66)$$

It should be mentioned that for all propagation distances $\Delta z \neq 0$ the numerical errors never vanish but just decrease more and more with increasing distance. For propagation distances $\Delta z < \Delta z_{\min}$ numerical errors can be reduced by interpolating the field before the propagation to a smaller sampling distance $\delta_{x,\min}$, which can be calculated approximately by

$$\delta_{x,\min} = \frac{n_x \delta x}{2} - \sqrt{\left(\frac{n_x \delta x}{2}\right)^2 - \frac{\Delta z \lambda}{n}}. \quad (67)$$

In contrast to most of the other homogeneous medium propagation algorithms, the sampling distance of the field is scaled during the Fresnel propagation. The sampling distance of the propagated field follows from

$$\Delta x' = \frac{\lambda \Delta z}{n n_x \Delta x}. \quad (68)$$

Combined SPW/Fresnel Operator

This propagation automatically combines the spectrum of plane waves propagation and Fresnel propagation to achieve an efficient propagation of paraxial waves free of numerical errors [54]. For propagation of harmonic fields close to the waist of a wave, the spectrum of plane waves is used. For larger distances Fresnel propagation is used. Since Fresnel propagation is more efficient the automatic paraxial propagation always tries to use Fresnel propagation if the distance from the waist is larger than the minimum distance Δz_{\min} . If the spectrum of plane wave propagation is used, the harmonic field will be automatically embedded in order to reduce numerical errors.

In general, a combination of both propagation methods is necessary depending on the distances from the waist of the wave $\Delta z_{w,\text{start}}$ of the harmonic field before propagation and $\Delta z_{w,\text{end}}$ of the harmonic field after propagation. The following table shows which combinations of propagation operators may occur.

Table 4: Use of appropriate propagation operators for different propagation distances.

DISTANCE $ \Delta Z_{W,\text{START}} $	DISTANCE $ \Delta Z_{W,\text{END}} $	USED PROP. ALGORITHMS
$= 0$	$< \Delta z_{\text{min}}$	<i>SPW</i>
$= 0$	$\geq \Delta z_{\text{min}}$	<i>FRT</i>
$< \Delta z_{\text{min}}$	$< \Delta z_{\text{min}}$	<i>SPW</i>
$< \Delta z_{\text{min}}$	$\geq \Delta z_{\text{min}}$	<i>SPW</i> to waist and <i>FRT</i>
$\geq \Delta z_{\text{min}}$	$\geq \Delta z_{\text{min}}$	<i>FRT</i> to waist and <i>FRT</i>
$\geq \Delta z_{\text{min}}$	$< \Delta z_{\text{min}}$	<i>FRT</i> to waist and <i>SPW</i>

Far Field Operator

Far field propagation [54] simulates the propagation of a field $U(x, y)$ with a wavelength λ by a distance Δz through an infinite homogeneous medium with a given refractive index n . Propagation can be simulated from the waist to the far field, from the far field to the waist, and from one far field distance to another. Far field propagation is the far field approximation of the Rayleigh Sommerfeld propagation integral, thus it contains no paraxial approximation. Propagation is defined as:

$$\left[\mathcal{P}_{\Delta z}^{\text{FarField}} U(x, y) \right] (x', y') \sim -\frac{ikz}{2\pi r} \frac{e^{ikr}}{r} \int_{-\infty}^{\infty} \int_{-\infty}^{\infty} dx dy U(x, y) e^{-\frac{ik}{r}(xx' + yy')} \quad (69)$$

with

$$r = \sqrt{x^2 + y^2 + z^2} \quad (70)$$

and

$$k = \frac{2\pi n}{\lambda}. \quad (71)$$

Propagation Operators for Real Components

In this thesis an OIS (Optical Interface Sequence) component [54] will mainly be used. Inside this component two possible propagation methods can be chosen: Collins integral by ABCD matrix or geometrical optics operator.

The Geometrical Optics Propagation Operator is based on the principles of geometrical optics. The propagation is performed along rays. In this case, the direction

of rays is defined by so called Channels. Rays within one channel have different positions, but the same direction. The operator first builds up the channels. In the second step, rays are propagated. In the first step, the directions of the channels have to be computed in the initial plane from the field data. In particular, the phase of the field is used. The actual phase of the field is replaced by a fitted phase using different levels of approximation: constant phase, linear phase, linear and spherical phase, as well as linear, spherical and cylindrical phase. From this phase approximation, the directions of the channels are computed. Alternatively, the local gradient of the phase can be used to define the channel directions. Furthermore, the channels are defined throughout the system by stepping from interface to interface. Depending on the settings of the operator, this procedure may take refraction into account or not. Once the channels are defined, the rays carrying the field information are propagated through the system. The paths of the rays are defined by the channels. Depending on the settings of the operator, Fresnel Effects and Cross Talk may be taken into account or not.

If the optical interfaces of a component, or rather their optical effects, can be described by the ABCD matrix formalism, one can decide to use the propagation algorithm given by Collins.

6.2.2 Geometric Field Tracing Plus (Beta)

Geometric field tracing presents the newest technique introduced within the Wyrowski VirtualLab Fusion. The principles of this latest improvement to VirtualLab were also presented during the DGaO conference in Brno, 2015 [8].

Until now, geometric and wave optics were commonly understood as two opposite branches. Often, scientists and engineers expect that phenomena like diffraction, interference, coherence and polarization cannot be included in geometrical optics. However, Prof. Wyrowski and his team propose another view on geometrical optics. They applied geometrical-optics based arguments for the development of a fast Maxwell equation solver in its geometric field approximation.

In order to overcome limitations of geometrical optics/ray-tracing, optical modeling and design must be based on physical optics. Therefore Maxwell's equations need to be solved. However, typical Maxwell solvers like FEM or FDTD cannot be used in most optical system due to their extraordinarily high numerical effort. Of course these solvers are important for simulations that consider very small features, but they are not practical for common lens systems. Consequently, there are two contradictory demands - the need to solve the Maxwell's equations and a reasonable numerical effort. The result is that specialized and/or approximated approaches need to be applied to solve Maxwell's equations. There are already several of these methods like Rayleigh

integral for homogeneous media, or Fresnel integral for paraxial light. These methods are being combined within the physical optics modeling concept referred to as Field tracing [48].

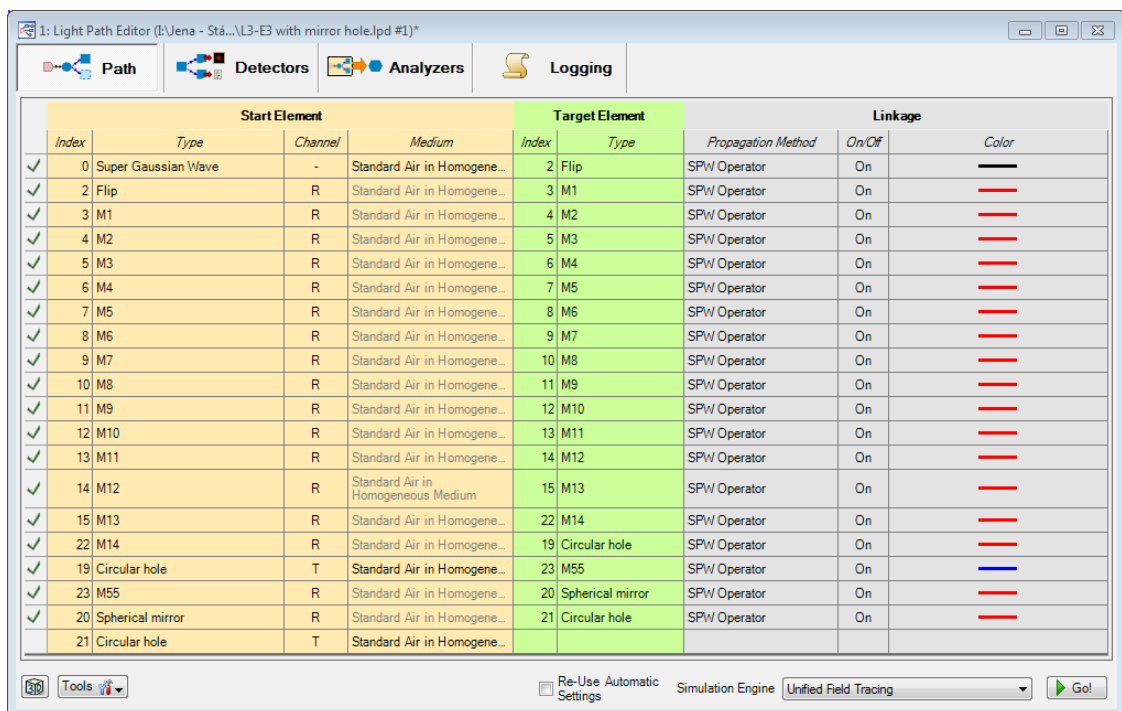
An interesting point to make is how geometrical optics can be used to achieve similar results. Huygens already used the ray concept in the context of wavefronts. Prof. Wyrowski in his paper refers to Born and Wolf's Principles of Optics, where the geometrical approximation to solve the Maxwell's equations is already suggested. Wyrowski Photonics further developed and implemented this concept to obtain a geometric field tracing technique, which solves Maxwell's equations in its geometric approximation [8]. The geometric approximation leads to Maxwell's equations for local plane waves, which deliver accurate solutions in regions in which the spatial evolution of a field is dominated by its wavefront. In practice, the solution to Maxwell's equations in geometric approximation is obtained by a ray tracing algorithm with smart rays [8]. Smart rays have the following properties:

- Smart rays know the full electromagnetic field information at their position. That includes amplitudes and phases of the electric and magnetic field components, and because of that, also polarization.
- Smart rays know and remember their neighbors on the wavefront in the source plane. This is done by an appropriate ray index concept (wavefront indices). This method is combined with different lateral interpolation techniques for all field quantities which are allocated to a ray. Interpolation techniques include spline interpolation and mesh-based interpolation with barycentric coordinates.
- Smart rays come with another index concept (spatial coherence indices), which enables their association to mutually coherent and incoherent modes, and their combination. That allows the modeling of partially spatially coherent light, including the special cases of fully coherent and incoherent light.
- In order to include color, temporal coherence, and ultrashort pulses, the frequencies which are allocated to a ray also come with an index to distinguish frequency contributions to stationary and pulsed light (frequency indices).

By tracing smart rays they obtained a solver for Maxwell's equations, which overcomes most of the limitations of conventional ray tracing, but delivers the results just as fast as ray tracing.

7 Suggested Workflow

Currently⁶, VirtualLab Fusion does not contain a lens designing toolbox or environment similar to Zemax OpticStudio. In practice, that means the classical (pre)design process needs to be conducted by ray tracing in Zemax OpticStudio. This is caused by the lack of specific plot generators (e.g. ray fans, field curvatures, chromatic aberrations etc.) and other evaluating tools that are needed for a classical lens design task. For example, in the case of reducers, the system will be prepared in Zemax OpticStudio, where it can be optimized with the use of a common merit function and then evaluated using conventional aberration theory. After this step, the system can be transferred into VirtualLab Fusion for further simulations with the use of the physical optics approach. Transferring the system to VirtualLab Fusion does not necessarily mean the automated importing of Zemax files supported by VirtualLab Fusion. This is due to the fact, that by importing the Zemax file to VirtualLab, only a single OIS (Optical Interface Sequence) subdomain is created. Quite often it is better to prepare the whole system manually, while maintaining only a single lens per OIS subdomain. The main advantage of this procedure is that physical optics propagation between the components is accessible. In that case, an aperture can be added to provide spatial filtering as well.



The screenshot shows the 'Light Path Editor' window with a table of optical elements. The table is organized into columns for 'Start Element', 'Target Element', and 'Linkage'. The 'Start Element' column includes 'Index', 'Type', 'Channel', and 'Medium'. The 'Target Element' column includes 'Index' and 'Type'. The 'Linkage' column includes 'Propagation Method', 'On/Off', and 'Color'. The table lists 21 elements, starting with a Super Gaussian Wave and ending with a Circular hole. The propagation method for all elements is 'SPW Operator', and they are all 'On'. The color of the linkage varies, with most being red and one being blue.

Start Element				Target Element		Linkage		
Index	Type	Channel	Medium	Index	Type	Propagation Method	On/Off	Color
✓ 0	Super Gaussian Wave	-	Standard Air in Homogene...	2	Flip	SPW Operator	On	—
✓ 2	Flip	R	Standard Air in Homogene...	3	M1	SPW Operator	On	—
✓ 3	M1	R	Standard Air in Homogene...	4	M2	SPW Operator	On	—
✓ 4	M2	R	Standard Air in Homogene...	5	M3	SPW Operator	On	—
✓ 5	M3	R	Standard Air in Homogene...	6	M4	SPW Operator	On	—
✓ 6	M4	R	Standard Air in Homogene...	7	M5	SPW Operator	On	—
✓ 7	M5	R	Standard Air in Homogene...	8	M6	SPW Operator	On	—
✓ 8	M6	R	Standard Air in Homogene...	9	M7	SPW Operator	On	—
✓ 9	M7	R	Standard Air in Homogene...	10	M8	SPW Operator	On	—
✓ 10	M8	R	Standard Air in Homogene...	11	M9	SPW Operator	On	—
✓ 11	M9	R	Standard Air in Homogene...	12	M10	SPW Operator	On	—
✓ 12	M10	R	Standard Air in Homogene...	13	M11	SPW Operator	On	—
✓ 13	M11	R	Standard Air in Homogene...	14	M12	SPW Operator	On	—
✓ 14	M12	R	Standard Air in Homogeneous Medium	15	M13	SPW Operator	On	—
✓ 15	M13	R	Standard Air in Homogene...	22	M14	SPW Operator	On	—
✓ 22	M14	R	Standard Air in Homogene...	19	Circular hole	SPW Operator	On	—
✓ 19	Circular hole	T	Standard Air in Homogene...	23	M55	SPW Operator	On	—
✓ 23	M55	R	Standard Air in Homogene...	20	Spherical mirror	SPW Operator	On	—
✓ 20	Spherical mirror	R	Standard Air in Homogene...	21	Circular hole	SPW Operator	On	—
✓ 21	Circular hole	T	Standard Air in Homogene...					

Figure 20: VirtualLab Fusion: LightPath Editor containing data of L3-E3 system.

⁶As of fall 2015

Conversely, systems containing only folding mirrors⁷ can be easily implemented directly into VirtualLab Fusion due to more flexible manipulation of axes (see the LightPath Editor in the Fig. 20), that do not require the use of coordinate breaks. The frequent presence of coordinate breaks is often unavoidable in Zemax OpticStudio. This causes the beamlines' lens data sheet to be exceedingly long (see the Lens Data in the Fig. 21). Coordinate breaks actually form a bigger part of the lens data sheet than the optical elements themselves.

In the case of each beamline (for example L3-E3⁸, as seen on Zemax ray-tracing in Fig. 22), mechanical design requirements and constraints are typically available. Such input data is provided by mechanical engineers. Based on this data a proper light path can modeled.

Surf.Type	Comment	Radius	Thickness	Material	Coating	Semi-Diameter	Conic	TCE x 1E-6	Par 1(unused)	Par 2(unused)	Par 3(unused)	Par 4(unused)	Par 5(unused)	Par 6(unused)
0 OBJECT	Standard	Infinity	Infinity			0,000	0,000	0,000						
1 STOP	Standard	Infinity	0,000			0,000 U	0,000	0,000						
2	Standard	Infinity	-1500,000			0,000 U	0,000	0,000						
3	Coordinate Break	M1 rotate	0,000			0,000			0,000	0,000	-45,000	0,000	0,000	0
4 (aper)	Standard	Laser Room	0,000	MIRROR		250,000 U	0,000	0,000						
5	Coordinate Break	M1-M2	3100,000			0,000			0,000	0,000	-45,000 P	0,000	0,000	0
6	Coordinate Break	M2 Rotate	0,000			0,000			0,000	0,000	0,000	-45,000	0,000	0
7 (aper)	Standard	Flip mirror	0,000	MIRROR		250,000 P	0,000	0,000						
8	Coordinate Break		-1,495E+004			0,000			0,000	0,000	0,000	-45,000 P	0,000	0
9	Coordinate Break		0,000			0,000			0,000	0,000	45,000	0,000	0,000	0
10 (aper)	Standard	E3 Mirror	0,000	MIRROR		250,000 P	0,000	0,000						
11	Coordinate Break		1300,000			0,000			0,000	0,000	45,000 P	0,000 P	0,000 P	0
12	Coordinate Break		0,000			0,000			0,000	0,000	0,000	0,000	0,000	0
13 (aper)	Standard		0,000	MIRROR		250,000 P	0,000	0,000						
14	Coordinate Break		-4250,000			0,000			0,000	0,000	0,000 P	-45,000 P	0,000	0
15	Coordinate Break		0,000			0,000			0,000	0,000	0,000	45,000	0,000	0
16 (aper)	Standard		0,000	MIRROR		250,000 P	0,000	0,000						
17	Coordinate Break		2890,000			0,000			0,000	0,000	0,000	45,000 P	0,000	0
18	Coordinate Break		0,000			0,000			0,000	0,000	45,000	0,000	0,000	0
19 (aper)	Standard		0,000	MIRROR		250,000 P	0,000	0,000						
20	Coordinate Break		-9395,000			0,000			0,000	0,000	45,000 P	0,000 P	0,000 P	0
21	Coordinate Break		0,000			0,000			0,000	0,000	-45,000	0,000	0,000	0
22 (aper)	Standard	1st MOB mirror	0,000	MIRROR		250,000 P	0,000	0,000						
23	Coordinate Break		1520,000			0,000			0,000	0,000	-45,000 P	0,000 P	0,000 P	0
24	Coordinate Break		0,000			0,000			0,000	0,000	45,000	0,000	0,000	0
25 (aper)	Standard		0,000	MIRROR		250,000 P	0,000	0,000						
26	Coordinate Break		-445,000			0,000			0,000	0,000	45,000 P	0,000	0,000	0
27	Coordinate Break		0,000			0,000			0,000	0,000	45,000	0,000	0,000	0
28 (aper)	Standard		0,000	MIRROR		250,000 P	0,000	0,000						
29	Coordinate Break		2597,000			0,000			0,000	0,000	45,000 P	0,000	0,000	0
30	Coordinate Break		0,000			0,000			0,000	0,000	0,000	45,000	0,000	0
31 (aper)	Standard		0,000	MIRROR		250,000 P	0,000	0,000						
32	Coordinate Break		-750,000			0,000			0,000	0,000	0,000 P	45,000 P	0,000 P	0
33	Coordinate Break		0,000			0,000			0,000	0,000	0,000	45,000	0,000	0
34 (aper)	Standard		0,000	MIRROR		250,000 P	0,000	0,000						
35	Coordinate Break		1747,000			0,000			0,000	0,000	0,000	45,000 P	0,000	0
36	Coordinate Break		0,000			0,000			0,000	0,000	45,000	0,000	0,000	0
37 (aper)	Standard		0,000	MIRROR		250,000 P	0,000	0,000						
38	Coordinate Break		-1221,000			0,000			0,000	0,000	45,000 P	0,000 P	0,000	0
39	Coordinate Break		0,000			0,000			0,000	0,000	-45,000	0,000	0,000	0
40 (aper)	Standard		0,000	MIRROR		250,000 P	0,000	0,000						
41	Coordinate Break		1130,000			0,000			0,000	0,000	-45,000 P	0,000	0,000	0
42	Coordinate Break		0,000			0,000			0,000	0,000	15,000	0,000	0,000	0
43 (aper)	Standard	Deformable mirror	0,000	MIRROR		250,000 P	0,000	0,000						
44	Coordinate Break		-970,200			0,000			0,000	0,000	15,000 P	0,000	0,000	0
45	Coordinate Break		0,000			0,000			0,000	0,000	-15,000	0,000	0,000	0
46 (aper)	Standard	leaky mirror	0,000	MIRROR		250,000 P	0,000	0,000						
47	Coordinate Break		1,240E+004			0,000			0,000	0,000	-15,000 P	0,000	0,000	0
48	Coordinate Break		0,000			0,000			0,000	0,000	0,000	45,000	0,000	0
49 (aper)	Standard		0,000	MIRROR		250,000 P	0,000	0,000						
50	Coordinate Break		-750,000			0,000			0,000	0,000	0,000	45,000 P	0,000	0
51	Coordinate Break		0,000			0,000			0,000	0,000	0,000	-45,000	0,000	0
52 (aper)	Standard		0,000	MIRROR		250,000 P	0,000	0,000						
53	Coordinate Break		2488,000			0,000			0,000	0,000	0,000	-45,000 P	0,000	0
54	Coordinate Break		0,000			0,000			0,000	0,000	0,000	0,000	0,000	0
55 (aper)	Standard	Off-Axis Parabola	-6000,0...	0,000	MIRROR	250,000 U	0,000	0,000						
56	Standard		-3000,000			0,000 U	0,000	0,000						
57 IMAGE	Standard		Infinity			0,000 U	0,000	0,000						

Figure 21: Zemax OpticStudio: Lens Data containing prescription of L3-E3 system including all coordinate breaks to describe folding mirrors.

⁷A large portion of the beamline is typically comprised of folding mirrors (approximately 15–20 mirrors), beamsplitters and some focusing element (typically an off-axis parabola) in the end.

⁸which means laser 3 to experimental hall 3.

The aim of this workflow is to show the advantage of stepping up from common ray tracing to physical optics represented by so-called Field tracing [48]. Physical optics is required to simulate the effects of diffractive beam propagation, aperture or stop diffraction. To some extent physical optics is also presented in the Zemax OpticStudio. Its restrictions are described in the software's manual, the contents of which are also presented in subchapter 6.1. The Field tracing approach is also advantageous when temporal effects have to be shown. This will also be exploited to assess the effects of group velocity dispersion of reducers and expanders, since the temporal broadening caused by these systems can be directly investigated within VirtualLab Fusion.

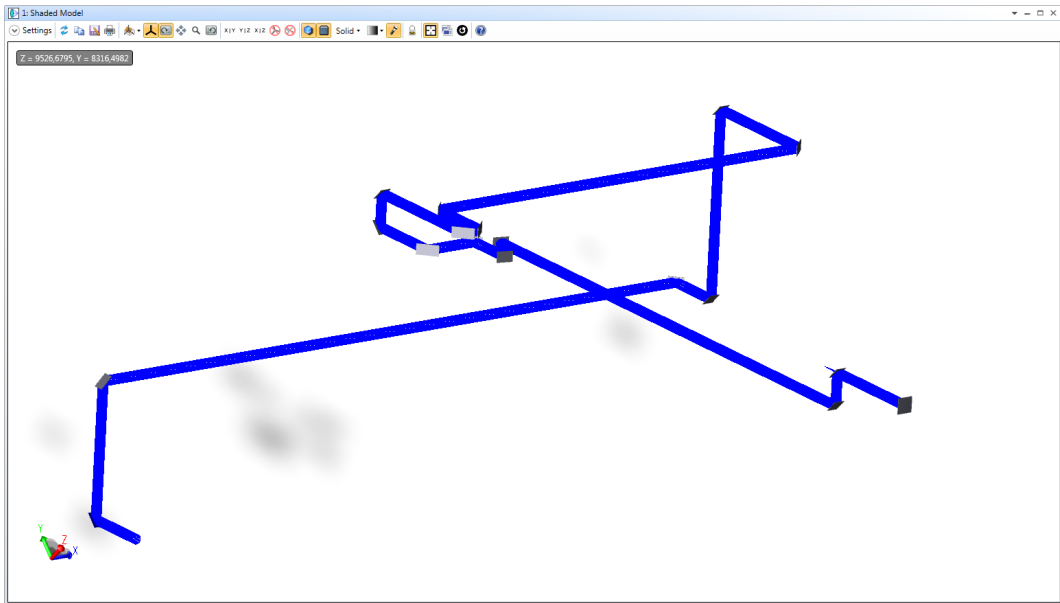


Figure 22: Zemax OpticStudio: Ray-tracing of the L3-E3 beamline from the data shown in the Fig. 21.

In situations where the numerical effort to use Classic Field tracing will be too high, the latest Geometric Field Tracing Plus (Beta) will be employed to solve the demanded task.

8 Optical Modeling and Design

Optical modeling and design represents a core chapter of this doctoral dissertation showing the author's results, either conducted independently or in collaboration with colleagues from the Joint Laboratory of Optics of Palacky University and the Institute of Physics of the Academy of Sciences of the Czech Republic and/or ELI-Beamlines facility. It contains the case scenarios being solved within the ELI-Beamlines facility.

The chapter is divided into several subchapters containing various simulation and modeling scenarios, including:

- Free space propagation – which is a basic element of every consecutive simulation.
- Determination of the physical restrictions of ideal beams – influence of hard apertures and apodizations.
- Focusing by an ideal lens – physical limit of beam focusing.
- Design and simulation of transmissive optics for beam relaying or demagnification.
- Design and simulation of reflective optics for beam relaying or demagnification.
- Beamline simulations and performance analyses.

The beams used throughout the presented dissertation are either circular Gaussians or squared super-Gaussians.

8.1 Free Space Propagation

From the geometrical optics point of view, free space propagation is not very interesting to investigate. Rays pass the homogenous free space without any change at all – rays in homogeneous media are straight [35]. This is typically not a limiting simplification when considering an optical setup for imaging purposes only. For rays originating at a single point, a geometrical wavefront is a surface that is a locus of constant optical path length from the source. If the source point is located at \mathbf{x}_0 and light leaves at a given time t_0 , then the wavefront can be calculated for any time by following formula [35]

$$V(\mathbf{x}_0; \mathbf{x}) = c(t - t_0).$$

The function $V(\mathbf{x}_0; \mathbf{x})$, as a function of \mathbf{x} , satisfies the eikonal equation [35]

$$n(\mathbf{x}_0)^2 = \left(\frac{\partial V}{\partial x}\right)^2 + \left(\frac{\partial V}{\partial y}\right)^2 + \left(\frac{\partial V}{\partial z}\right)^2 = |\Delta V(\mathbf{x}; \mathbf{x}_0)|^2. \quad (72)$$

In isotropic media, the rays and wavefronts are perpendicular to each other everywhere, a condition referred to as orthotomic. According to the Malus-Dupin principle, if a group of rays emanating from a single point is reflected and/or refracted any number of times, the perpendicularity of rays to wavefronts is maintained. The direction of a ray from \mathbf{x}_0 at \mathbf{x} is that of the gradient [35] of $V(\mathbf{x}_0; \mathbf{x})$

$$\mathbf{p} = n\mathbf{r} = \nabla V \quad (73)$$

or

$$n(\alpha, \beta, \gamma) = \left(\frac{\partial V}{\partial x}, \frac{\partial V}{\partial y}, \frac{\partial V}{\partial z} \right) \quad (74)$$

In a homogeneous medium, all wavefronts can be found from any one wavefront by a construction. Wavefront normals, i.e., rays, are projected from the known wavefront, and the loci of points equidistant therefrom are other wavefronts. This describes wavefronts in both directions, that is, both subsequent and previous wavefronts. The construction also gives virtual wavefronts, those which would occur or would have occurred if the medium were to be extended infinitely. This construction is related to that of Huygens' for wave optics. The geometrical wavefront is an approximation of the surface of constant phase in wave optics, and the eikonal equation can be obtained from the wave equation within the limit of the small wavelength in comparison with transverse dimensions of the electromagnetic field. A way in which wave optics differs from ray optics is that the phase fronts can be modified by phase changes that occur on reflection, transmission, or in passing through foci [35]. These are exactly the principles upon which Geometric Field Tracing Plus (Beta) works.

When the designer wants to create an optical system for transmitting or reflecting coherent laser beams, it is also highly desirable to take into account diffraction effects, at least for beams that are diffraction dominated (e.g. near the focus). In reality this means that the optical designer needs to step up from ray-tracing to more precise physical optics methods. In such situations the optical designer normally switches Zemax from ray-tracing to Physical Optics Propagation (POP), which is described in the previous chapter. There are, of course, many other methods than those already contained in the POP. Some of them were described in the author's master thesis [4]. POP cannot be understood as a general nor rigorous method, however, for many cases this method can be used. Usually for the Gaussian laser beams of common dimensions, when there is none or very tiny inclination of the field, this method has sufficient results. The main drawback of POP is, that it completely neglects the longitudinal E_z component of the field. This is not a problem as long as the field propagated through free space is not being transported by high NA off-axis parabolas or being focused by the same type of optical element.

The free space propagation topic can be understood as self-contained, but in this

dissertation it is merely shown as a basic building block for more complex simulations, and also for comparison of the output spatio-temporal shape of the beams propagated with and without use of a relaying optical system.

In the next few subchapters a free space propagation of Gaussian, super-Gaussian and arbitrary beams are simulated. In the end there is also a simulation showing free space propagation of ultra-short pulses. Propagation of ultra-short fs pulses is a key element in the simulation portfolio conducted for the ELI-Bamlines facility. This is also another important reason to step-up to Unified Field Tracing, since the ray-tracing software bundles (like the Zemax OpticStudio, OSLO and others) do not contain any feature to propagate ultra-short pulses.

8.1.1 Continuous Wave Propagation

Before the simulation of ultra-short pulse free space propagation is conducted, a simple comparison between Zemax' POP and Wyrowski VirtualLab Fusion's Unified Field Tracing is performed. For these simulations two principal wavelengths are chosen - 800 nm and 1060 nm. These wavelengths are chosen because high power lasers typically operate in the near infrared region.

Ideal Gaussian Beams

Analogously to the author's master thesis [4], a comparison of free space propagation of an ideal Gaussian beam is performed. To check the accuracy of the results a simple formula is derived

$$z_{2w_0} = \sqrt{3} \frac{w_0^2 \pi}{\lambda}, \quad (75)$$

this formula shows, in what distance z_{2w_0} the Gaussian beam with waist radius w_0 and the wavelength λ will spread to the double the waist radius.

The following tables (Table 5 and 6) show the input radii w_0 , calculated distances z_{2w_0} and the resulting radii acquired by the POP algorithm in Zemax and by Unified Field Tracing in VirtualLab Fusion. The tables also show the operator type selected by VirtualLab Fusion. The first three input radii have been chosen randomly, the last one is the actual size of one of the beams used in ELI.

Table 5: Gaussian beam with various w_0 waist radius free space propagation to the distance of z_{2w_0} ($\lambda = 800$ nm).

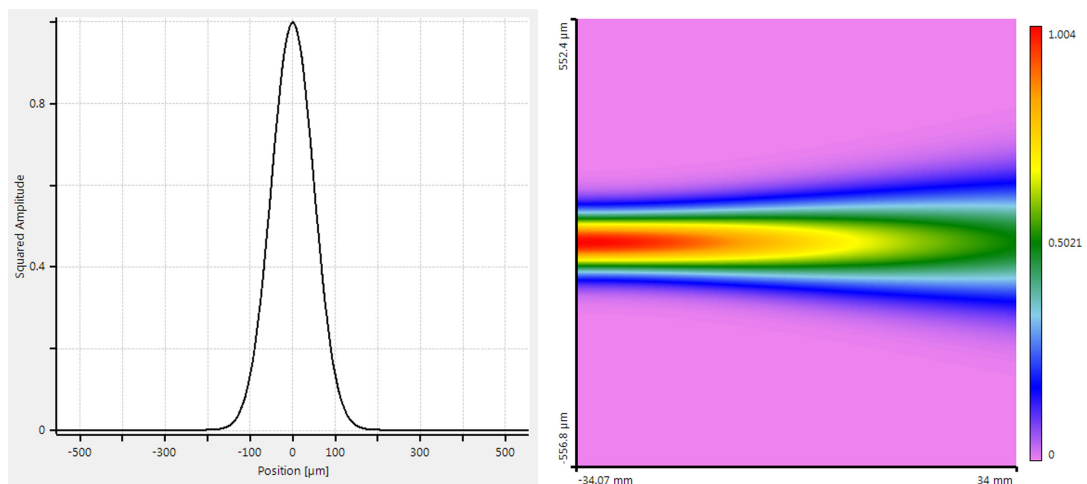
λ [nm]	800 nm			
w_0 [μm]	100	1000	10000	37500
z_{2w_0} [m]	0.068	6.802	680.175	9565
Zemax radius [μm]	199.96	2000	20000	75018
VirtualLab radius [μm]	200	2000	20000	75000
Selected operator	Fresnel	Fresnel	Fresnel	Fresnel

Table 6: Gaussian beam with various w_0 waist radius free space propagation to the distance of z_{2w_0} ($\lambda = 1060$ nm).

λ [nm]	1060 nm			
w_0 [μm]	100	1000	10000	37500
z_{2w_0} [m]	0.051	5.133	513.339	7219
Zemax radius [μm]	199.90	2000	20000	75013
VirtualLab radius [μm]	200	2000	20000	75000
Selected operator	Fresnel	Fresnel	Fresnel	Fresnel

The reader can see from the tables that results acquired by VirtualLab Fusion are flawless in all cases. On the other, hand POP also performs quite well in these situations.

Another possibility for beam propagation visualization in VirtualLab Fusion is so-called Depth Composite Output for one-dimensional fields. The depth composite output is a harmonic field showing the $x - z$ -plane or the $y - z$ -plane, where z is the propagation direction [54]. The following figures (Figs. 23 and 24) show the composite outputs of beam propagations from Table 5.

**Figure 23:** Profile of the Gaussian beam with a 100 μm radius (left) and its depth composite output in $x - z$ plane (right).

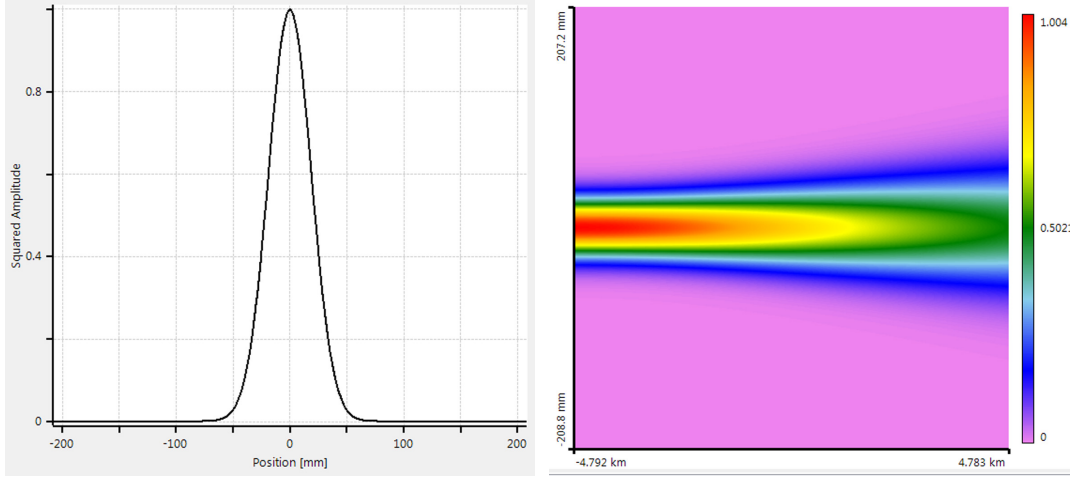


Figure 24: Profile of the Gaussian beam with a $37500 \mu\text{m}$ radius (left) and its depth composite output in $x - z$ plane (right).

Of course, since all beams have regular Gaussian profiles, they look exactly the same. The only difference is in measurements of profile widths and consequently the propagation distances.

Ideal Super-Gaussian and Top-Hat Beams

For the purposes of this dissertation it will be advantageous to simulate a free space propagation for a super-Gaussian beam to a distance of 20 m. This is also a distance to which the considered relay optical systems should transport the input beam. The reader can later compare the free space propagation of these beams and their relaying by optical systems. Propagation of super-Gaussian beams is also much more interesting from the simulation point of view, since the diffraction effects are becoming more pronounced and are also causing other effects than just beam spreading.

The amplitude of the isotropic⁹ super-Gaussian beams used in VirtualLab are defined by the following equation [54]

$$\mathcal{U}(x, y) = \mathcal{U}(0, 0) \exp \left[- \left(\frac{r}{w_0} \right)^m \right], \quad (76)$$

where w_0 denotes the waist radius at the amplitude level of $1/e$, m denotes the order of the super-Gaussian¹⁰ and

$$r = \sqrt{x^2 + y^2}. \quad (77)$$

However, in the case of ELI-Beamlines, separable¹¹ super-Gaussians are of greater

⁹Circular symmetric

¹⁰ $m=2$ corresponds to a regular Gaussian beam

¹¹Square symmetric

importance. These are described by a modified equation [54]

$$\mathcal{U}(x, y) = \mathcal{U}(0, 0) \exp \left(- \left(\frac{x}{w_{0,x}} \right)^{m_x} - \left(\frac{y}{w_{0,y}} \right)^{m_y} \right), \quad (78)$$

where order and waist radius are given for the both x - and y -direction of the field. The user can define the waist radius w at any amplitude or intensity level k above the minimum edge level, i.e. different from w_0 , as defined above. Waist radius w is connected to w_0 by

$$w_0 = \frac{w}{\sqrt[m]{-\ln k}}, \quad (79)$$

with an amplitude level of $0 < k < 1$ that is given as a fraction of the maximum amplitude of the super-Gaussian in its center.

For top-hat like beams, where only the “sharpness” of the edges is known, but not the required order of the super-Gaussian, then it is also possible to enter the width Δr_e of the edge between a lower (minimum) and an upper (maximum) level (y_l and y_u). The relation between edge width (Fig. 25) and order of the super Gaussian is

$$\Delta r_e = w \left(\sqrt[m]{\frac{\ln y_l}{\ln k}} - \sqrt[m]{\frac{\ln y_u}{\ln k}} \right). \quad (80)$$

The purpose of the following beam propagation study is to show the amount edge diffraction effects on the beam, and eventually demonstrate the need for optical relaying systems.

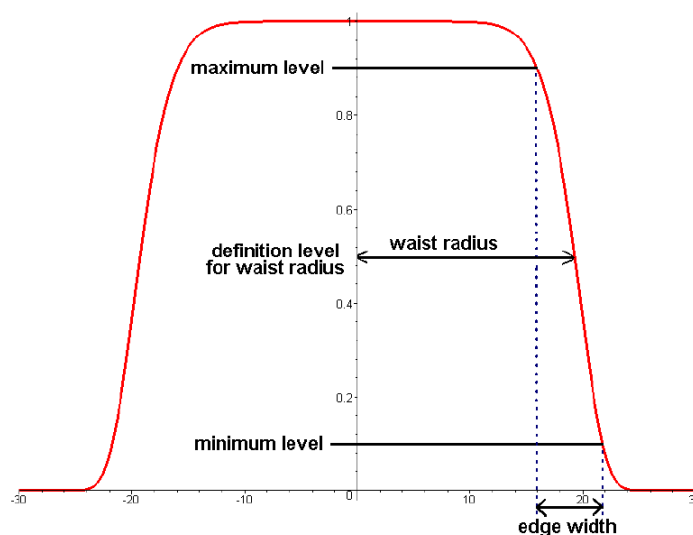


Figure 25: Super-Gaussian beam’s edge width and waist radius, adopted from [51].

A reference distance of 20 m has been chosen to describe the beam’s diffraction effects. This distance is similar to the length of the proposed 4- f systems. It is

anticipated that such simulations should demonstrate whether there is a need to optically relay super-Gaussian beams of specific orders by transport telescopes. To compare the diffraction effects, beams are observed at distances of 5, 10, 15 and 20 meters. The beam orders used are m equals to 20, 100 and 500. The lowest order $m = 20$ is closest to the real situation. The higher orders are chosen to show the effect of diffraction by propagating the beam in the free space over the specified distance. Results are shown in Tables 7, 8 and 9.

Results in Table 7 clearly demonstrate that a beam of order $m = 20$ does not exhibit diffraction effects at any of the shown target planes. However, it needs to be stressed that all beams used in the simulations described in this dissertation are ideal, i.e. without any intensity, phase distortions or modulations.

The beam of order $m = 100$ in Table 8 still does not exhibit strong diffraction effects. Only at the distance of 20 m from the source does the beam finally have some diffraction spikes along the edges.

Conversely, the beam of order $m = 500$ manifests strong diffraction effects at all distances. Nevertheless, one also needs to take into account image aliasing when assessing the diffraction effects. The zoomed part of the beam, where the spike is located, exhibits much more physical behavior than the image of the unzoomed part (see Fig. 26). Such edge spikes can be higher than the LIDT and can consequently cause damage to the optics.

If we only consider diffraction effects, the following conclusion can be made: A beam that has an equal shape at the 20 m distance as an initial beam has less need to be optically relayed than a beam that exhibits pronounced diffraction effects.

Table 7: Propagation of order 20 super-Gaussian beam with 107 mm radius (5 m, 10 m, 15 m and 20 m propagation distance, respectively).

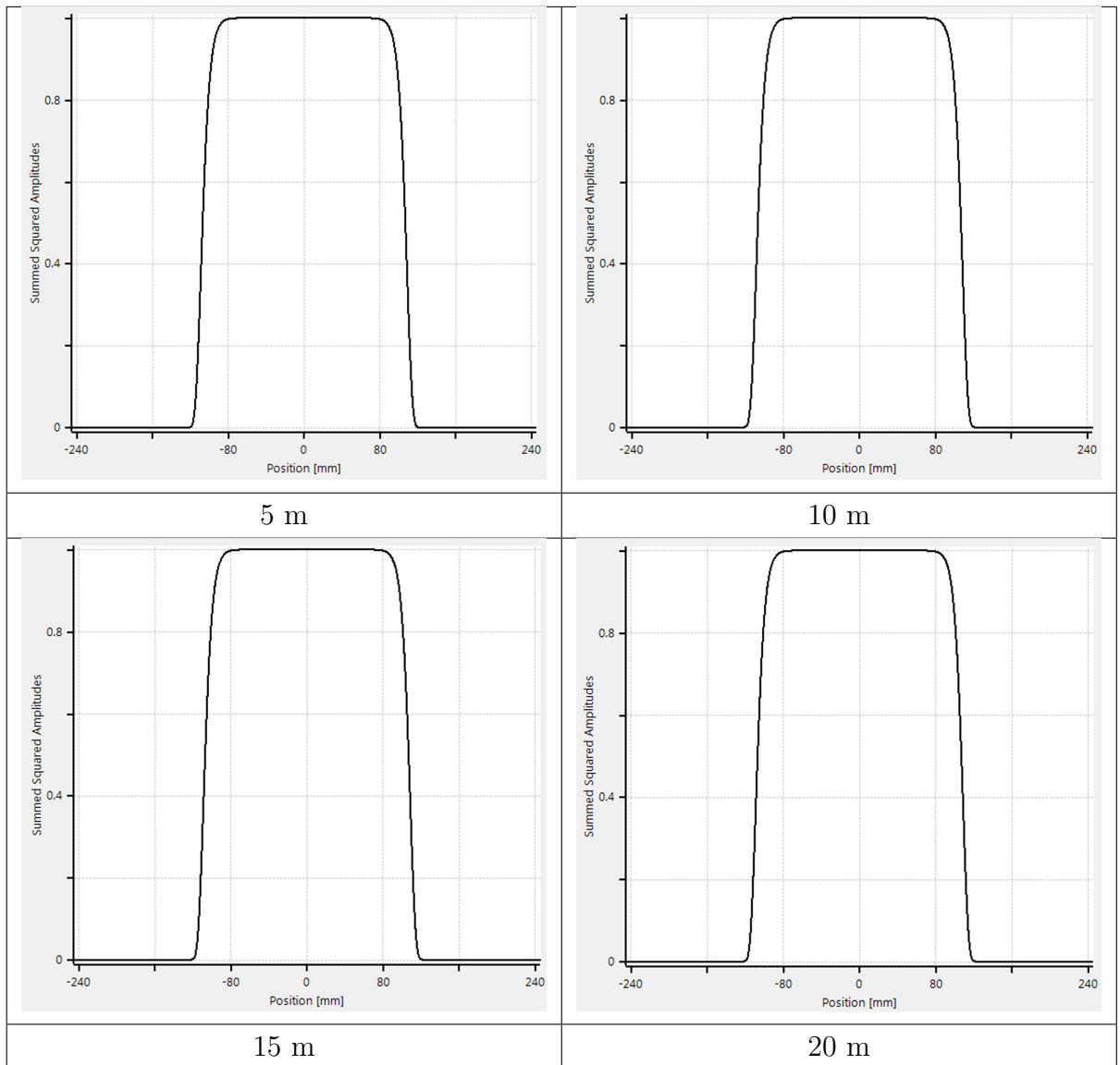


Table 8: Propagation of order 100 super-Gaussian beam with 107 mm radius (5 m, 10 m, 15 m and 20 m propagation distance, respectively).

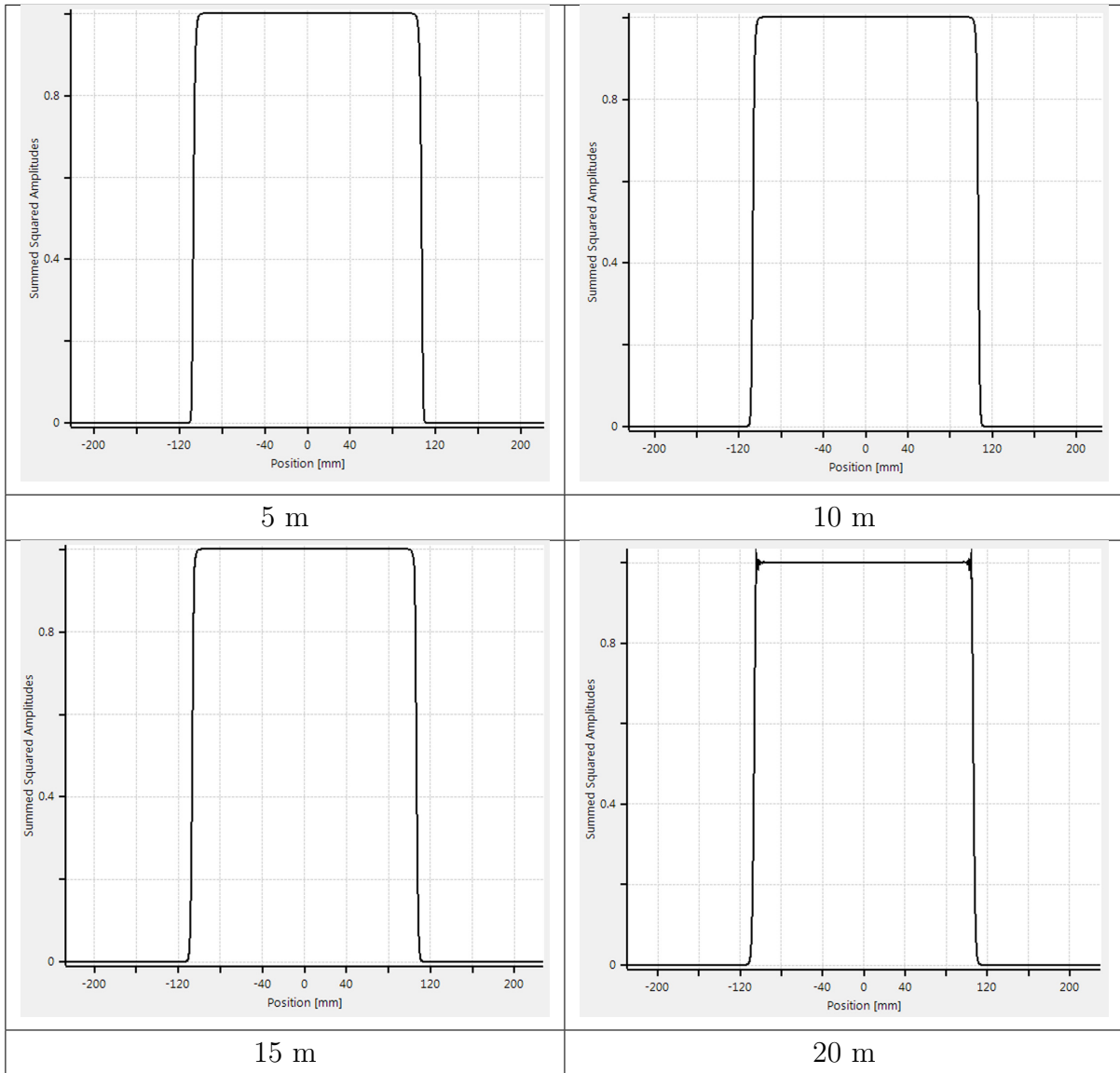


Table 9: Propagation of order 500 super-Gaussian beam with 107 mm radius (5 m, 10 m, 15 m and 20 m propagation distance, respectively).

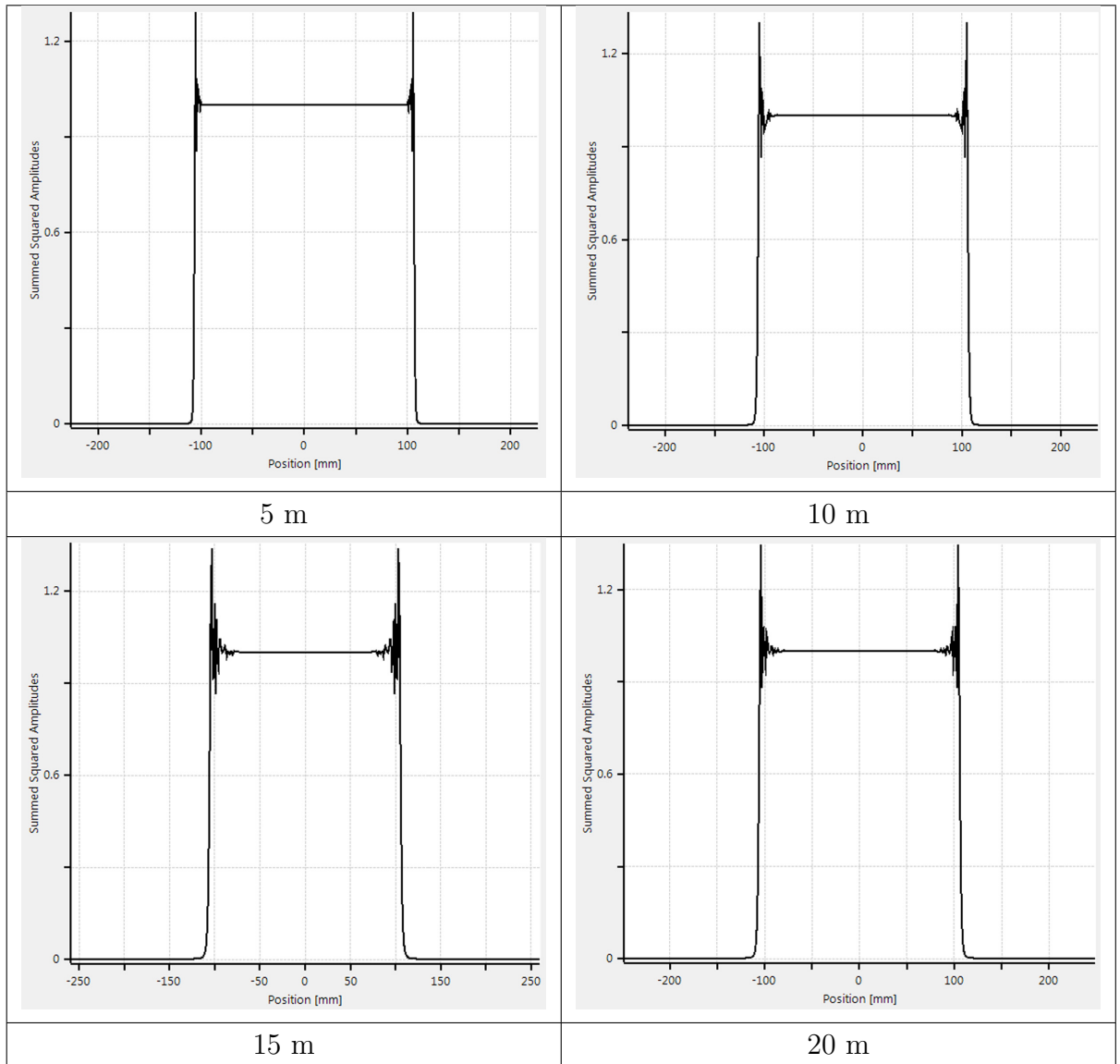


Fig. 26 shows a detail of a beam propagated to a 20 m distance and demonstrates the aliasing of unzoomed pictures.

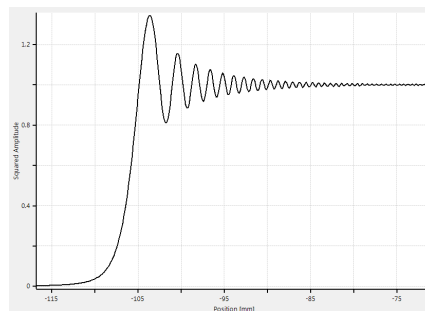


Figure 26: A detail of the diffraction effect of the order 500 super-Gaussian beam propagated to a 20 m distance.

Arbitrary Beams

VirtualLab Fusion has the ability to trace any arbitrary field shape through free space or optical systems. The intensity profile of an arbitrary input beam can be imported simply by loading a picture in some commonly used digital image format (e.g. jpeg, png) containing intensity information.

As an example a fractal shaped harmonic field is used. The fractal shown is the so-called Koch snowflake named after Swedish mathematician Helge von Koch, who introduced this type of fractal in 1904. For its hexadic symmetry the curve is called the snowflake curve. More on this topic can be found in [57].

Recently several publications have been written on both Fresnel [58] and Fraunhofer [59] diffraction on snowflake apertures, thus making them interesting for the following simulations and analyses.

Fig. 27 shows a Koch snowflake used as an input field for a free-space propagation simulation.

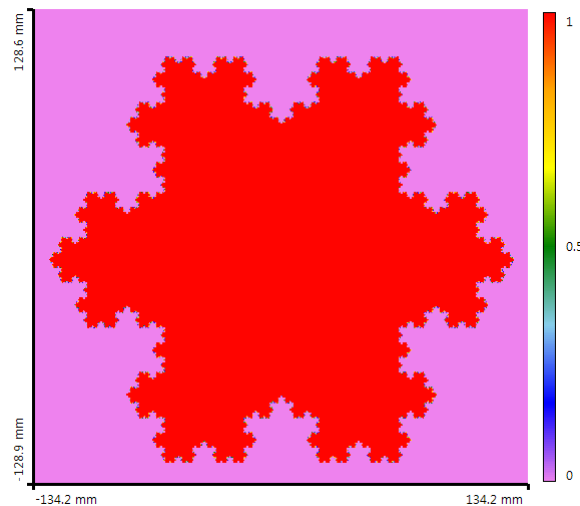
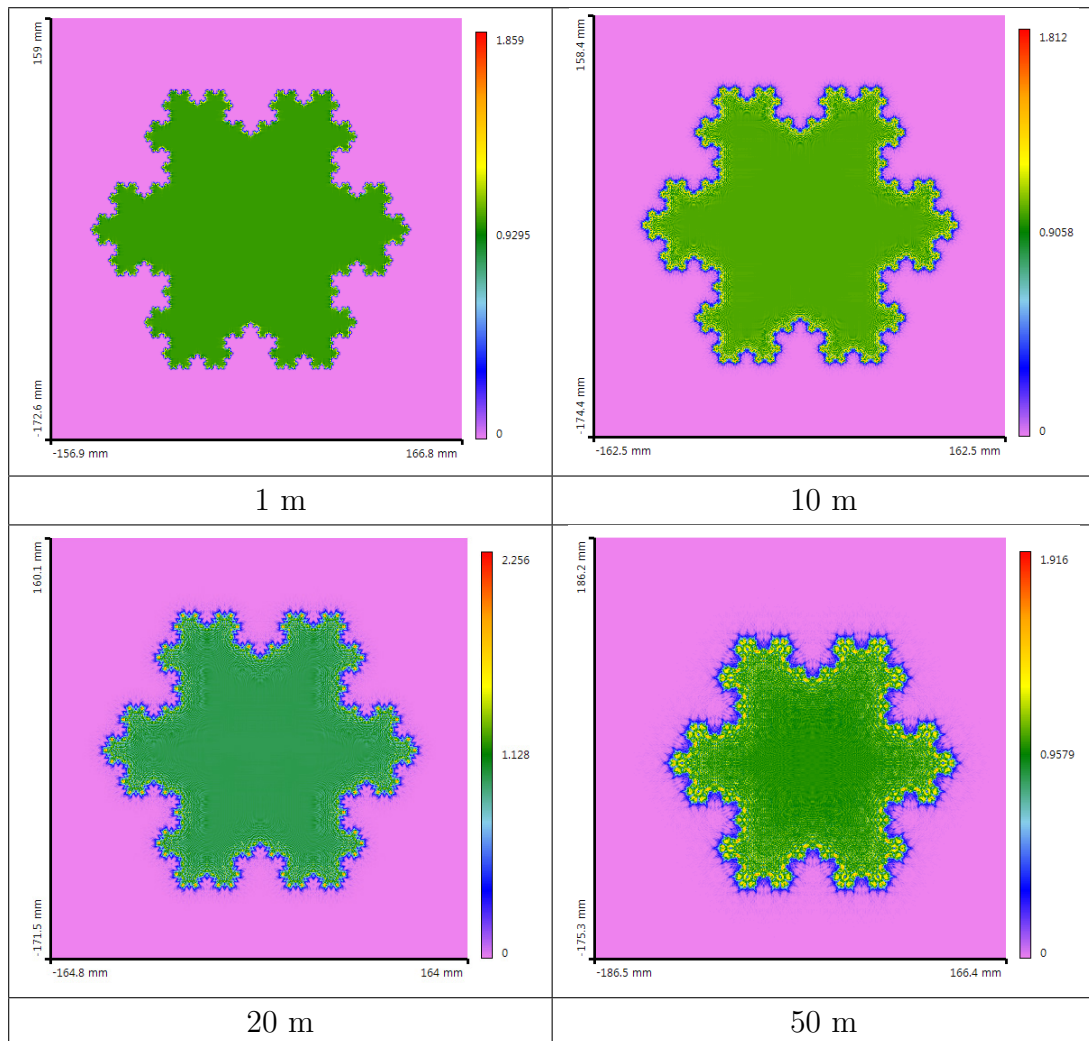


Figure 27: Koch snowflake as an input beam.

Similar to the super-Gaussian beam propagation cases shown previously, the current beam is also shown after propagating to several specific target planes (1, 10, 15 and 20 m, respectively). Reader can compare the results from table 10 with those presented in [58]. Pictures acquired with the aid of VirtualLab Fusion are clearly in coincidence with those presented in the paper [58], also demonstrating VirtualLab's ability to simulate diffraction effects while propagating beams through such complicated apertures.

Table 10: Koch snowflake-like beam diffractive propagation (1 m, 10 m, 15 m and 20 m propagation distance, respectively).



8.1.2 Ultra-short Pulse Propagation

In the case of ultra-short pulse free space propagation, two specific phenomena are observed – spatial diffraction and temporal spreading. These two effects can be studied separately or together. A very handy tool to study temporal effects separately is a software bundle from Laser Quantum called vCHIRP [60]. vCHIRP [61] allows calculation of the dispersion characteristics of a femtosecond laser pulse propagating through various media and elements.

In the ELI-Beamlines facility the beam path lengths will be quite extraordinary. While looking at Table 11, it can be seen that the longest path is almost 81 m. The meaning of the L3–E2, L3–E3, L3–E4 and L3–E5 is as follows – L3 means laser 3, whereas the E2 through E5 stand for experimental halls. Each of the experimental halls has its special purpose:

- E2 – X-ray sources

- E3 – Plasma Physics
- E4 – Proton acceleration
- E5 – Electron acceleration

Even free space propagation can cause drastic stretching of the pulse caused by air dispersion. This can be controlled by air pressure. Fig. 28 shows how the pulse duration is changes with the pressure inside the chamber where the propagation will take place.

Table 11: Beam path lengths inside various beamlines.

Beamline	L3–E2	L3–E3	L3–E4	L3–E5
Beam path length [mm]	62687	65400	80773	69916

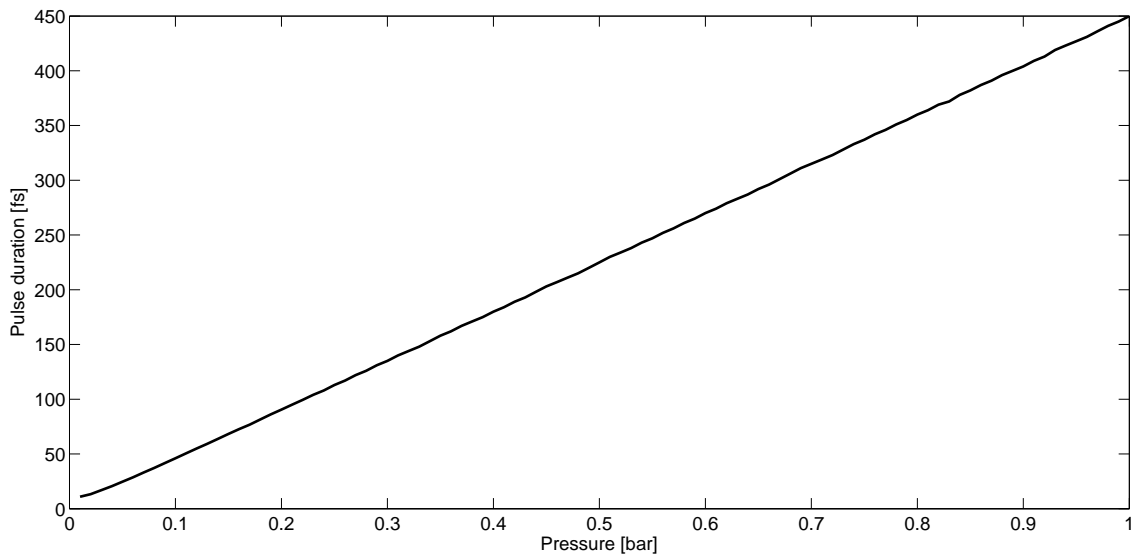


Figure 28: Relation between the pressure inside the chamber and the output beam's pulse duration after the free-space propagation on the length of L3–E4.

From this figure the reader can see that even free space propagation in atmospheric pressure conditions can increase the pulse duration on the order of several magnitudes. Due to this fact, the laser chamber will be enclosed in vacuum. Thus the dispersion caused by free space propagation can be neglected in our simulations described in the following sections of this dissertation.

Summary

Simulations in this subchapter are limited to cases of ideal beams only (i.e. without phase irregularities). These can be extrapolated to include artificial phase irregularities as shown in the Zemax simulations inside the research report contained within the appendix of this thesis. However, the exact data of the input HAPLS (The High-Repetition-Rate Advanced Petawatt Laser System) beam delivered by the LLNL was not available to the author. When the measurement of the HAPLS becomes available, it will be possible to improve the precision of the simulations by importing real world phase irregularities. Also the influence of non-linear effects was not considered, as they are not yet included in the VirtualLab Fusion engine.

8.2 Beam Clipping

Among optical designers it is very well known that the clear optical aperture to transmit Gaussian beams has to be greater than the beam's actual waist radius. This is simply caused by the shape and spread of the Gaussian beam distribution.

Anthony E. Siegman suggests in his famous book [62] a criterion of

$$d = \pi w, \quad (81)$$

where d is a diameter of the aperture and the w is the beam's waist radius, respectively. If this criterion is fulfilled over 99 % of the energy will pass the aperture. If the aperture radius equals the beam radius, approximately 86 % of the energy passes the aperture.

Table 12 is shows the power losses of a Gaussian beam for various apertures.

Table 12: Power loss in percents for various A/D ratios. A - physical circular aperture diameter, D - laser beam diameter in $1/e^2$. This table is valid for ideal TEM₀₀ Gaussian beams.

A/D	0.8	1.0	1.2	1.4	1.6	1.8	2.0
Power loss [%]	27.8	13.5	5.6	1.98	0.6	0.15	0.03

However, the typical beam to be used within ELI-Beamlines is a squared super-Gaussian. Therefore it also makes sense to investigate the scenarios involving this type of beam of various orders. Cases with both square and circular apertures are shown in the plots in Fig. 29. All the results for beam clipping were acquired within VirtualLab Fusion with the use of a so-called "parameter run" and the power detector.

Previous plots represent a mere rule of thumb to set proper mirror sizes for various beam diameters and orders. Of course, the situation is getting far more complicated when edge diffraction effects are taken into account. The following subchapter shows the influence of hard and apodizing apertures on beam focusing properties.

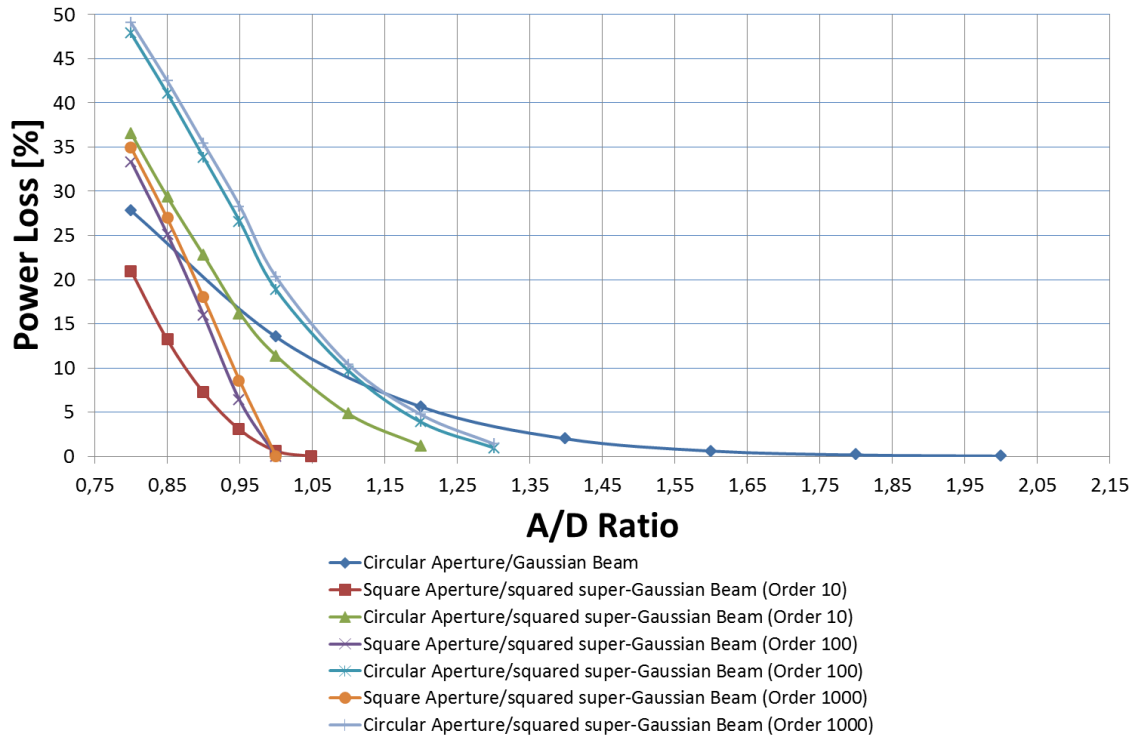


Figure 29: Power losses for various beam types and orders on circular and square apertures.

8.3 Focusing by an Ideal Lens

The following simulations were envisioned by an experimental team preparing the experiments for focusing the beam onto a capillary tube. In these experiments it is advantageous to know what the limitations caused by diffraction are when focusing squared super-Gaussian laser beams of various orders. In this chapter miscellaneous metrics are used to assess the beam quality in the focal region. Knowing the diffraction limit of the focused squared beams will help with several experiments conducted within the ELI-Beamlines facility.

In the practice of optical engineering, there exist numerous metrics for image or beam quality assessment. These metrics can be divided into two basic groups – geometric and diffraction. The most simple one is spot size. However, even determining the spot size can be complicated due to aberrations and/or the eccentricities in the optical system. Another widely used criterion in lens design is wavefront distortion. Generally, if the distortions are smaller than one wave, it is far better to use diffraction metrics. These comprise PSF¹² [63, 64, 65], MTF¹³ [35] or the Strehl ratio [64, 65, 66, 67]. In contrast to the common approach for accessing these metrics, Maxwell’s equations are directly solved in the cases presented in this subchapter.

¹²Point spread function

¹³Modulation transfer function

These can be solved either approximately or in a rigorous way by the application of the spectrum of the plane waves (*SPW*) operator that is used to propagate the field in the vicinity of the focal plane in order to investigate the Strehl ratio evolution of defocused beams. This is conducted in Wyrowski VirtualLab Fusion with the use of the Unified Field Tracing concept. The influence of the squared super-Gaussian beam order and its apodization is also considered. Results of the acquired metrics are plotted.

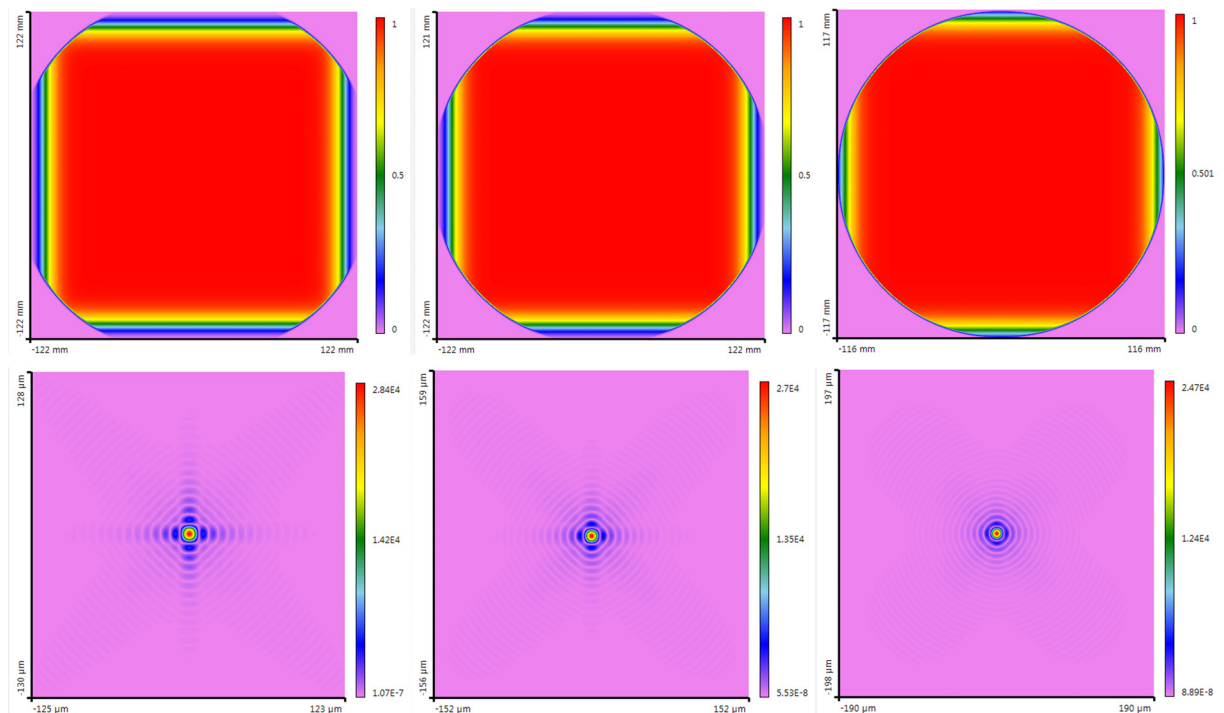


Figure 30: Beams after a hard aperture (upper part of the figure) and diffraction patterns in the focal plane (lower part of the figure). Aperture diameters are from the left 270 mm, 250 mm and 230 mm, respectively.

It is very important to know how the aperture or apodizing mask will change the diffraction pattern in the focal plane. In Fig. 30 there are three previously mentioned cases (270 mm, 250 mm and 230 mm diameter) for a hard aperture (1 % edge width). For each of the input beams, its diffraction pattern is shown in the focal plane. If the hard aperture is used to clip the input square beam, a typical star-like shape appears in the focal plane. This is caused by the polygon-like shape of the input field. If the only homogenous part of the beam is selected, the beam behaves like a top-hat beam, thus the focal spot more resembles the Airy disk.

According to the preliminary information on one of the facility's beamlines (abbreviated L3), the source to be tested has expected properties that are as follows: FWHM size 214 mm, beam order 20, wavelength 820 nm. These parameters are used

for defining the first LPD subdomain – a super-Gaussian wave. Another subdomain is the aperture. With this subdomain, either hard apertures or gradient apodizations can be set based on the aperture width. In this case we are specifically interested in four cases. Without an aperture, and also with 270 mm, 250 mm and 230 mm circular apertures, respectively. These values were proposed by the experimental team. The width of the aperture edge is set to 1 % or 10 % - defined relatively to the smaller of both values of diameter [54]. That means that in the first case scenario the aperture can be considered as a hard aperture, whereas the latter scenario simulates an apodizing mask. The next subdomain in the simulation sequence is a $2f$ -Setup that embodies an ideal lens. In the scenario presented, a 2 m focal length is chosen. For visualization purposes Virtual Screens are added to the light path wherever the field distribution is of interest.

Fig. 31 consists of apodized input beams and corresponding diffraction patterns in the focal planes. If an apodizing mask of the same diameter is applied instead of a hard aperture, the star-like diffraction is suppressed, while achieving higher values of amplitude in the spot's center. The quality of all these diffraction patterns is assessed in the following text by application of various metrics.

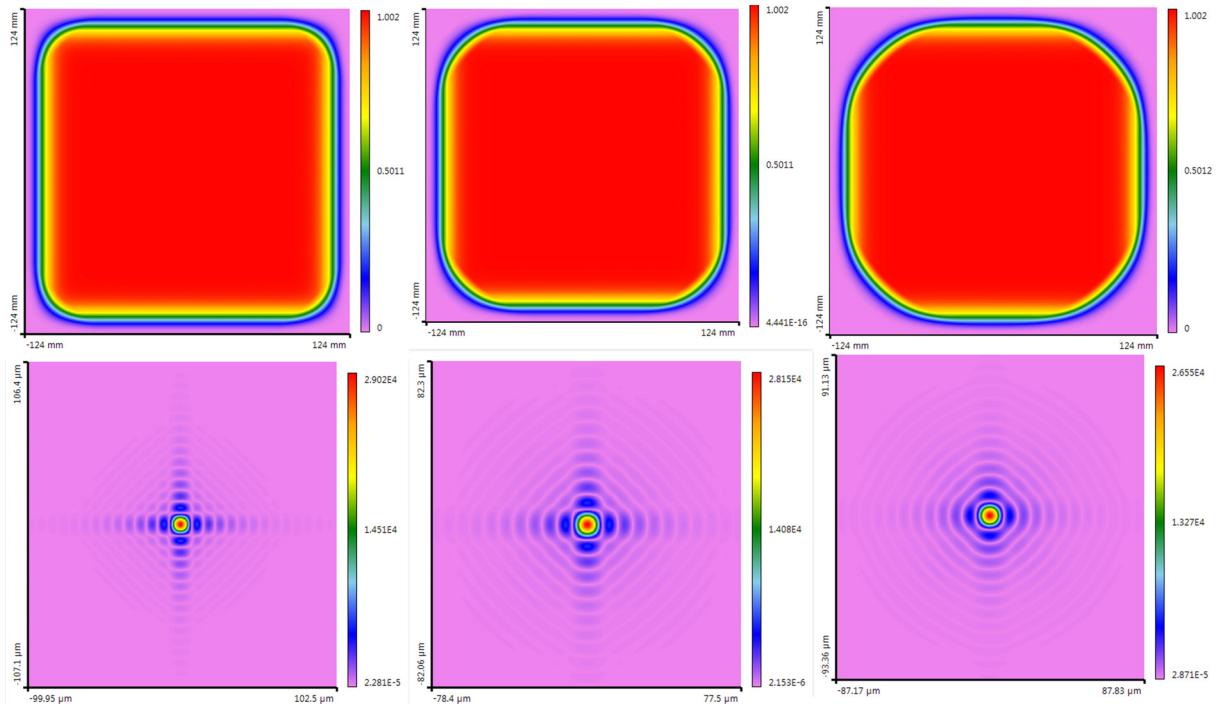


Figure 31: Beams after a 10 % apodization (upper part of the figure) and diffraction patterns in the focal plane (lower part of the figure). Aperture diameters from the left are 270 mm, 250 mm and 230 mm, respectively.

8.3.1 Fits of logarithmed values of $|E_x|$

To investigate and compare diffraction patterns, it is advantageous to observe the fitted values of the $|E_x|$ field component rather than its actual values in order to avoid overlapping of high frequency parts of the plots. Fig. 32 serves as a reference, because there is no aperture nor apodization contained in the LPD used for generation of this set of plots. This figure compares fitted values of the diffraction patterns' $|E_x|$ component of four specific beam orders – 5, 10, 20 and 50.

On the following pages there is an analysis of the hard aperture and apodization mask behavior. The fitted values of $|E_x|$ are compared for the different apertures and apodization mask sizes. Their influence on the aforementioned beam orders (5, 10, 20 and 50) is scrutinized.

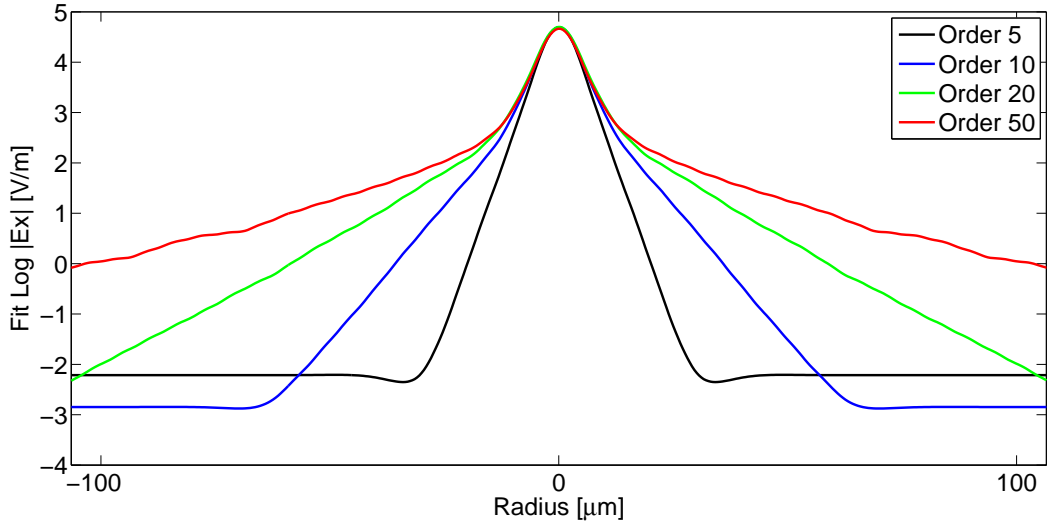


Figure 32: Fitted values of amplitudes of the $|E_x|$ component of the field for various input beam orders (without any aperture or apodization).

Hard Aperture

In this part, the fitted values of $|E_x|$ are shown in the case of a 1 % aperture edge width (corresponding to Fig. 35). Figs. 33, 34 and 35 contain focal spot calculations for aperture diameters of 270 mm, 250 mm and 230 mm, respectively.

Readers can see for themselves that upon decreasing the sizes of the aperture, the decrease of the fitted values of $|E_x|$ are less steep. Also, the smaller the aperture, the more difficult it is to distinguish between beam orders, which is only logical since the circular aperture is only selecting the homogeneous part of the super-Gaussian beam.

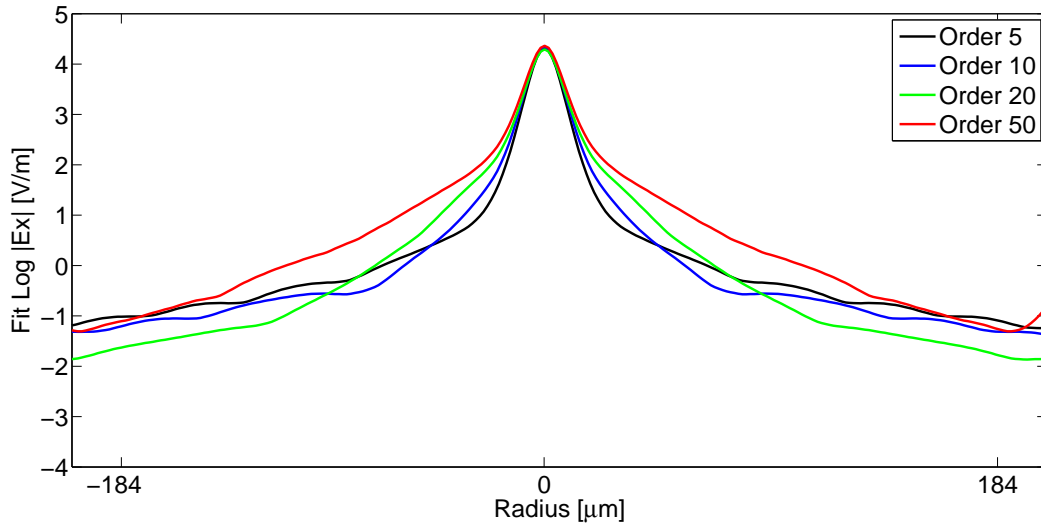


Figure 33: Fitted values of amplitudes of the $|E_x|$ component of the field for various input beam orders (in the presence of a circular aperture with a 270 mm diameter).

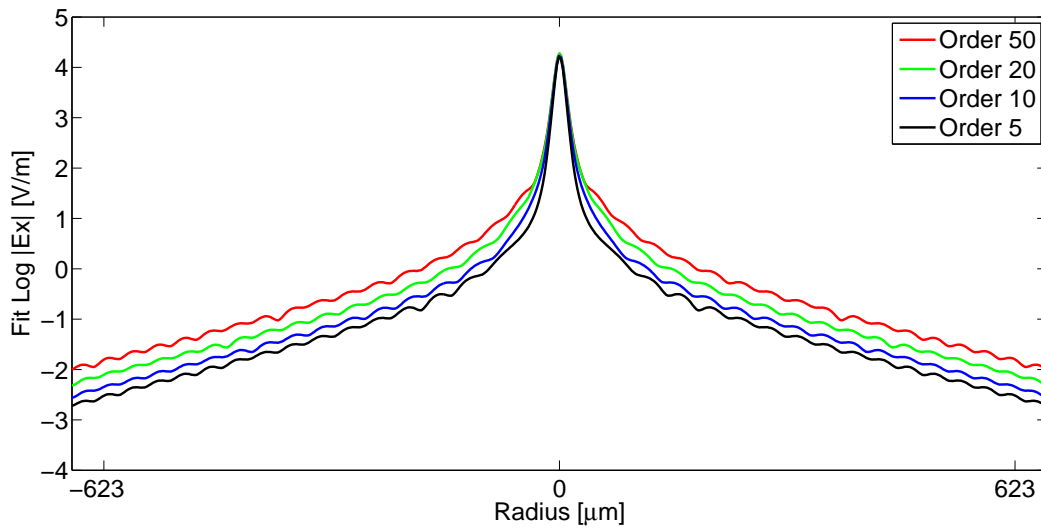


Figure 34: Fitted values of amplitudes of the $|E_x|$ component of the field for various input beam orders (in the presence of a circular aperture with a 250 mm diameter).

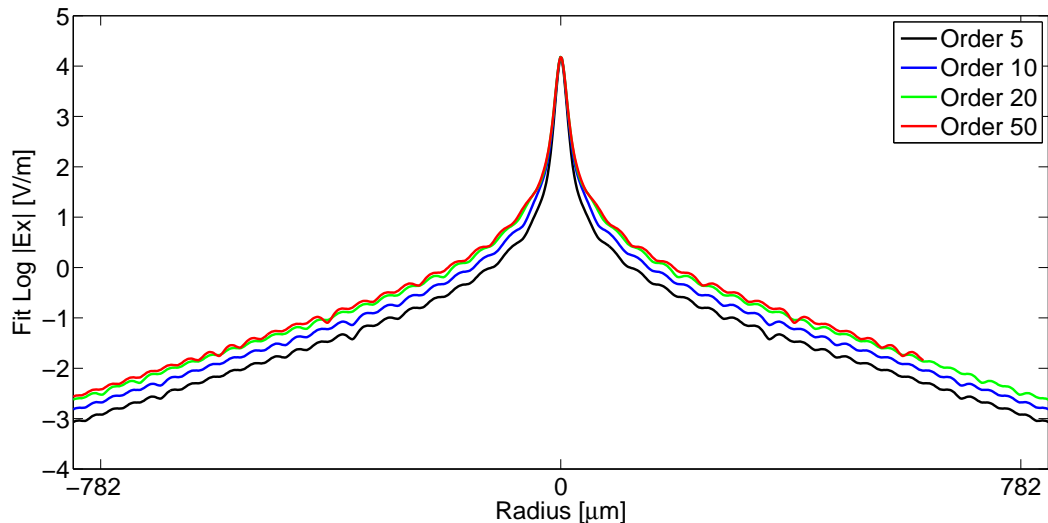


Figure 35: Fitted values of amplitudes of the $|E_x|$ component of the field for various input beam orders (in the presence of a circular aperture with a 230 mm diameter).

Apodization

The following page shows the fitted values of $|E_x|$ in the case of a 10% aperture edge width, which represents an apodization mask. Figs. 36, 37, and 38 contain focal spot calculations for apodization diameters of 270 mm, 250 mm and 230 mm, respectively.

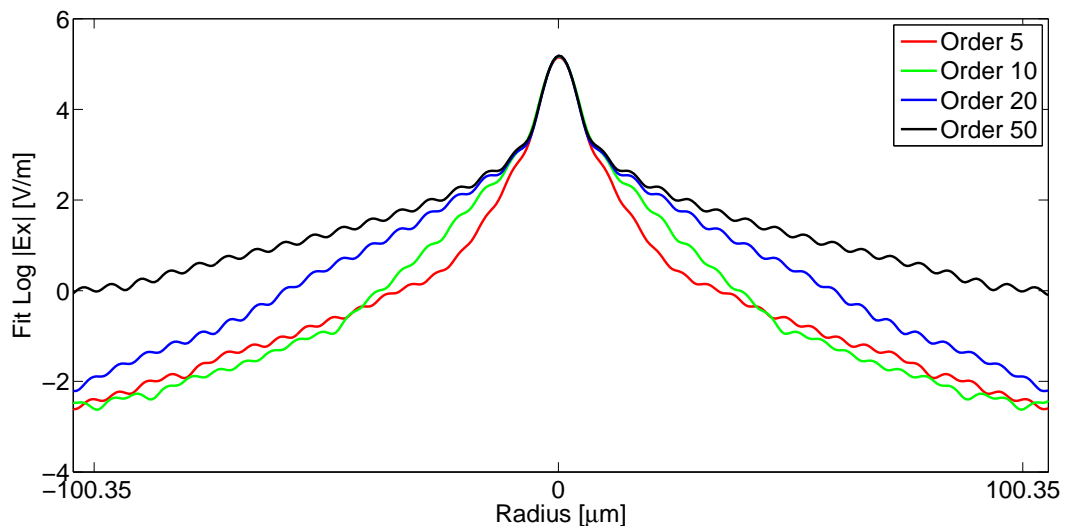


Figure 36: Fitted values of amplitudes of the $|E_x|$ component of the field for various input beam orders (in the presence of a circular apodization with a 270 mm diameter).

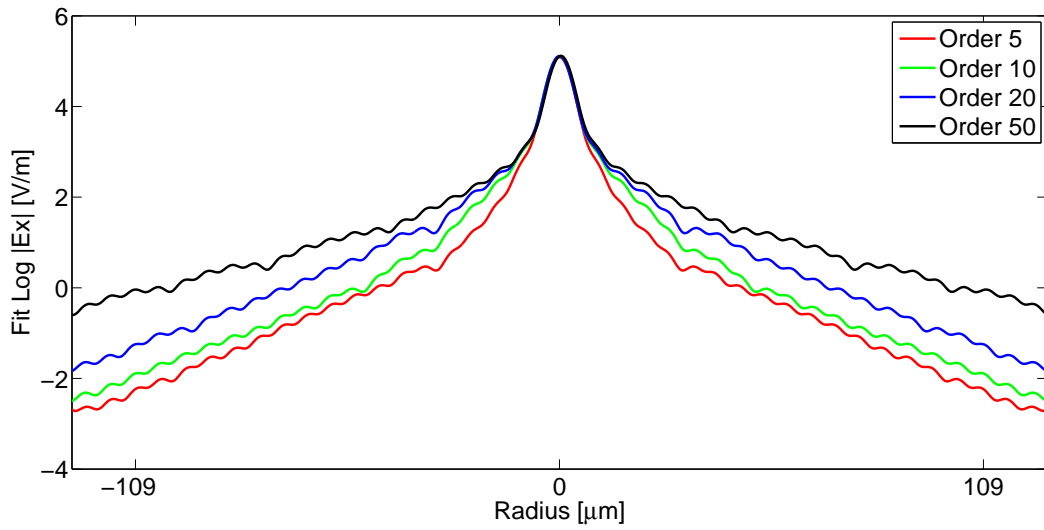


Figure 37: Fitted values of amplitudes of the $|E_x|$ component of the field for various input beam orders (in the presence of a circular apodization with a 250 mm diameter).

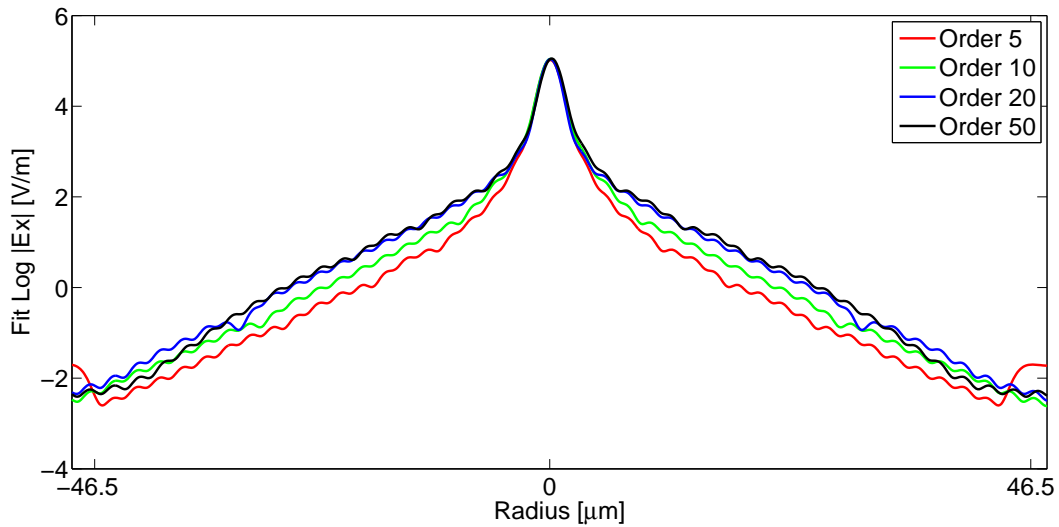


Figure 38: Fitted values of amplitudes of the $|E_x|$ component of the field for various input beam orders (in the presence of a circular apodization with a 230 mm diameter).

The previous pages have shown how the magnitude of the electric field vector can be controlled by apertures or apodizing masks. The plots shown should help the experimenters to choose the proper size of the aperture or apodizing mask to create the field in the focal plane according to their specifications.

8.3.2 Strehl Ratio

The Strehl ratio was introduced by K. Strehl in 1902 [67]. Since then it is often used to describe the behavior of systems [68 – 73]. It defines the ratio between aberrated diffraction pattern peak intensity and non-aberrated diffraction pattern peak intensity. Generally it is related to the image intensity of the point source. For the purposes of the following study a super-Gaussian input field of various orders is used instead of a point source. To bring this field to the focal region a $2f$ setup is employed. This function represents a special kind of Fourier transform done with a focusing lens [54] in VirtualLab Fusion. Far Field propagation of a paraxial field can also be exploited to demonstrate Fourier transform. First the beam is brought to focus by a $2f$ system to acquire a non-aberrated diffraction pattern. Then, with the use of a "parameter run" the vicinity of the focal plane is scanned to acquire aberrated (defocused) spots. The metrics calculation can then be conducted. Propagation of the beam in front of the focal plane and behind the focal plane is conducted with the rigorous *SPW* operator. Notice that no ray tracing approach whatsoever is used.

The resulting evolution of the Strehl ratio around the vicinity of the focal plane of the ideal lens is shown in Fig. 39. As a consequence of ideal lens use the only present aberration is defocus. It is shown that higher order beams are slightly more resistant against defocus, which is proven by the demonstrated values of the Strehl ratio. The typical acceptable value for telescopes is a Strehl ratio equal to 0.82. In that case we can achieve approximately $\pm 200 \mu\text{m}$ defocusing tolerance when an order 50 beam is in use. The lower the order, the lower the defocusing tolerance is as well. With an order 5 beam this tolerance falls to approximately $\pm 120 \mu\text{m}$.

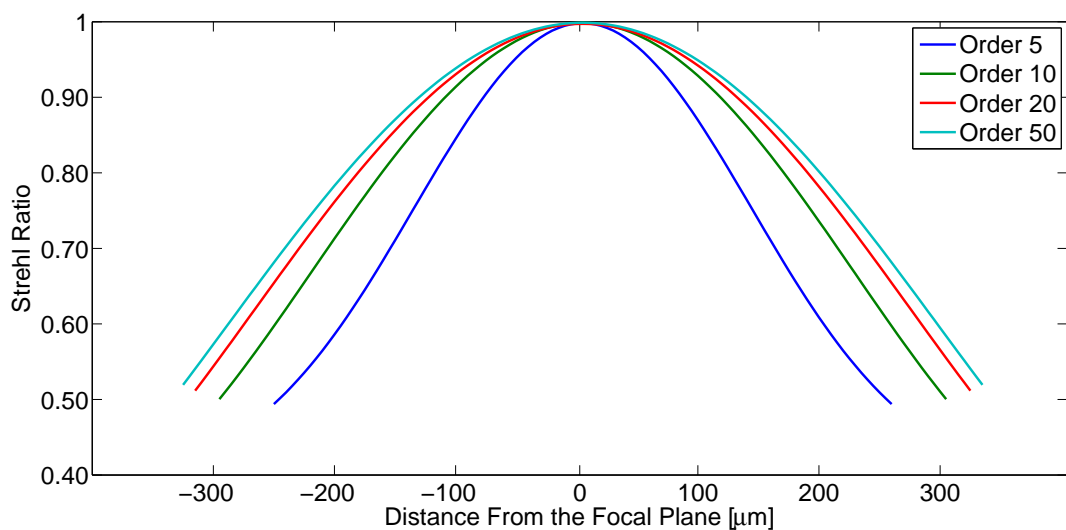


Figure 39: Strehl ratio evolution near the focal plane for different orders of super-Gaussian beams.

8.3.3 Encircled Energy

The last useful metric to demonstrate the focusing properties of a super-Gaussian beam is encircled energy [74]. The encircled energy is the percentage of the total energy enclosed as a function of distance from either the chief ray or the PSF centroid at the image of a point source. It gives the designer an idea of how much light can be collected within the area defined by the radius, and it is a very useful indication of the performance of an optical system. The encircled energy curve can also be compared with that of the diffraction-limited curve so that the designer knows how much light is lost because of optical aberrations. Encircled energy can be calculated from PSF irradiance. For a symmetrical PSF, the encircled energy of a beam with the intensity profile $I(r)$ within an area of radius R can be calculated as [74]:

$$EE = \frac{\int_0^R I(r) 2\pi r dr}{\int_0^\infty I(r) 2\pi r dr}$$

where R is the radius to the PSF centroid or reference point.

Since there is not any precise relation defined between radiometric and field values, it is simply assumed that the intensity I is proportional to the squared value of the electric field component in absolute value, e.g. $|E_x|^2$ or $|E_y|^2$. The encircled energy is then calculated by

$$EE = \frac{\int_0^R |E_x(r)|^2 2\pi r dr}{\int_0^\infty |E_x(r)|^2 2\pi r dr} \quad (82)$$

or

$$EE = \frac{\int_0^R |E_y(r)|^2 2\pi r dr}{\int_0^\infty |E_y(r)|^2 2\pi r dr}. \quad (83)$$

Unlike the most common practice, the results presented here are not calculated by means of ray tracing, but rather with the use of a rigorous Maxwell equation solver. For this purpose the *SPW* operator is employed to calculate the harmonic field in focus. Encircled energy is then calculated by the application of the aforementioned equations directly to the harmonic field.

As a reference, the encircled energy of the beam's diffraction pattern, without any preceding aperture, is plotted in Fig. 40.

Two types of analyses are again conducted similar to 8.3.1 – for hard apertures and for apodization masks.

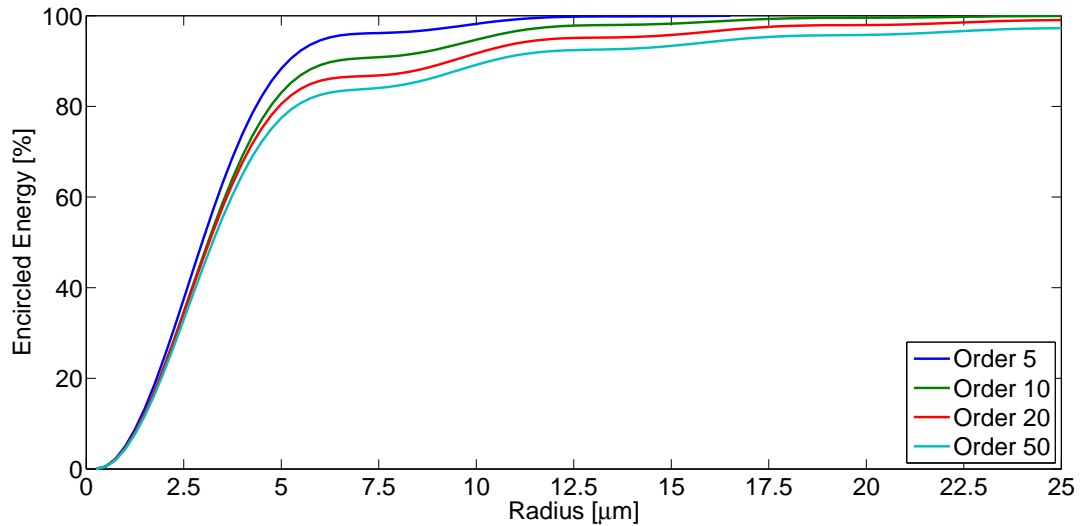


Figure 40: Encircled energy of the focused super-Gaussian beam of different orders without any aperture or apodization.

Hard Aperture

The influence of three aperture sizes on encircled energy is investigated. Sizes are the same as in 8.3.1 – 270, 250 and 230 mm respectively. The resulting encircled energies are shown in the descending order of aperture diameter sizes in Fig. 41 – 43.

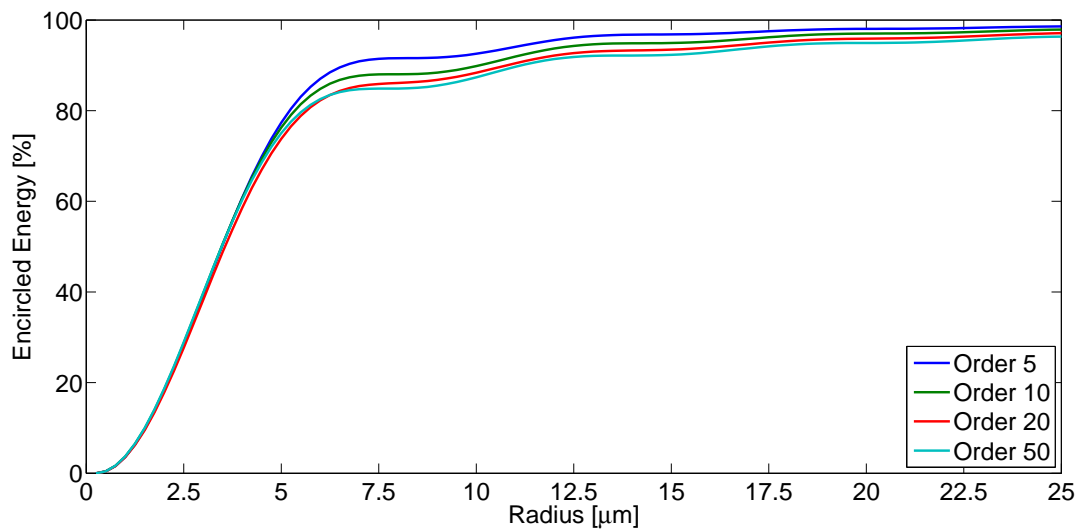


Figure 41: Encircled energy of the focused super-Gaussian beam of different orders with a circular hard aperture introduced (270 mm diameter).

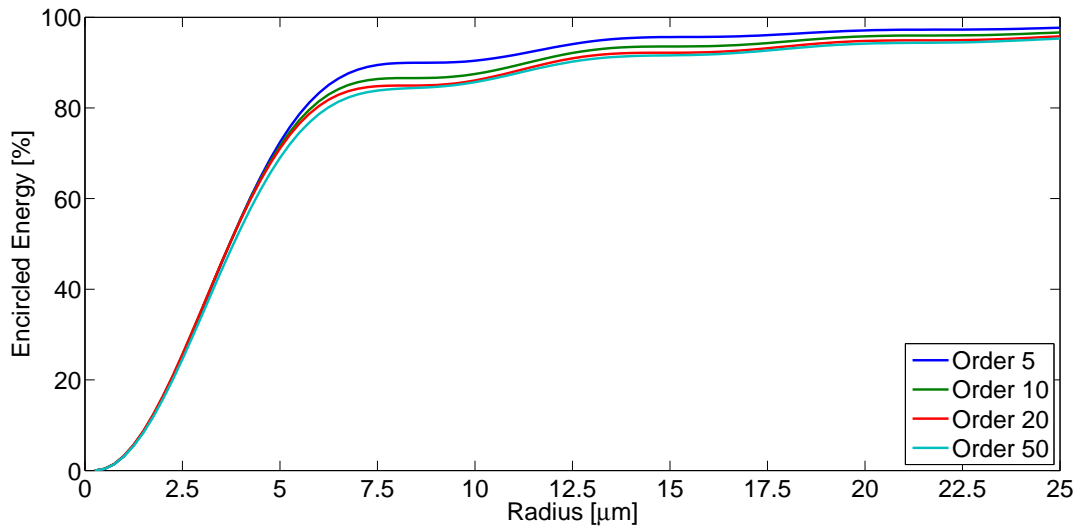


Figure 42: Encircled energy of the focused super-Gaussian beam of different orders with a circular hard aperture introduced (250 mm diameter).

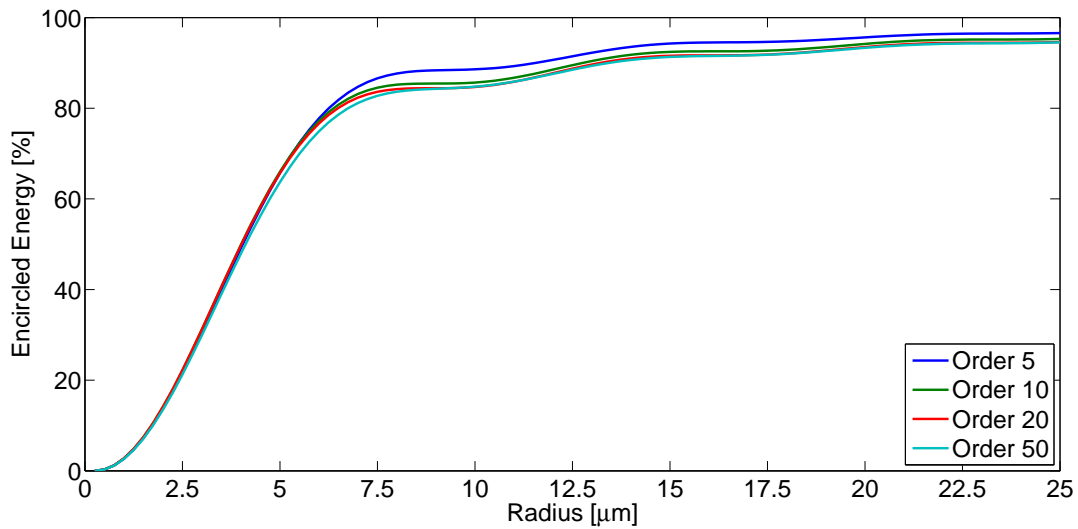


Figure 43: Encircled energy of the focused super-Gaussian beam of different orders with a circular hard aperture introduced (230 mm diameter).

By looking at these pictures it can be seen that the energy of all beam orders, regardless of the aperture diameter, encircled in a 5 μm radius is almost equivalent. By the size of the aperture the amount of energy between 5 and 25 μm can be adjusted to meet the specific demands on the focal spot.

Apodization

Finally, the influence of three diameters of apodization masks to the encircled energy

of the focal spot are investigated. Figs. 44-46 shows stepwise the encircled energy for the 270, 250 and 230 mm apodization mask sizes, respectively.

Compared with hard apertures, the apodization masks offer more precise control of the focal spot inside the $5\ \mu\text{m}$ radius, which is not possible with the hard aperture. The overall decrease of energy with decreasing apodization mask size is much smoother in comparison to hard apertures of same sizes.

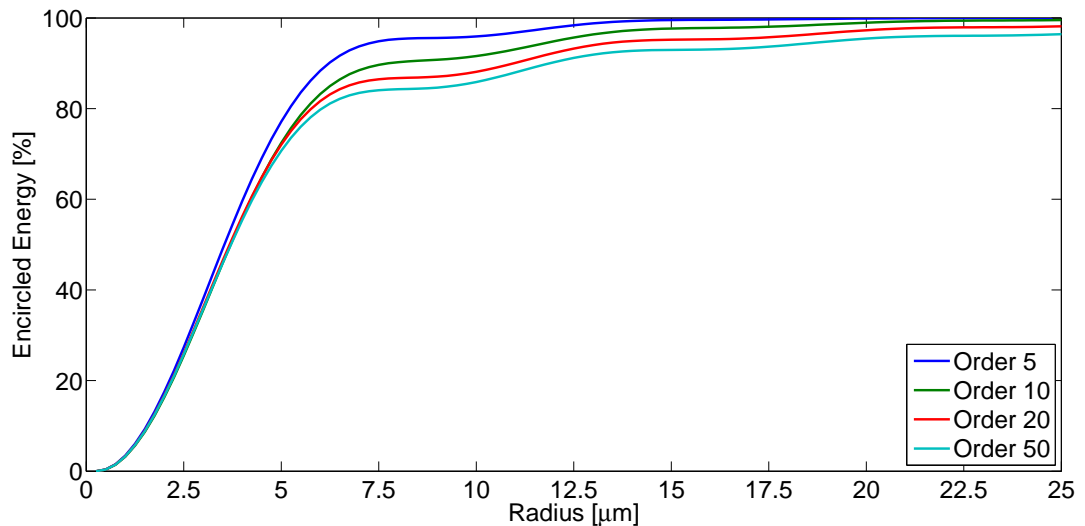


Figure 44: Encircled energy of the focused super-Gaussian beam of different orders with a circular apodization mask introduced (270 mm diameter).

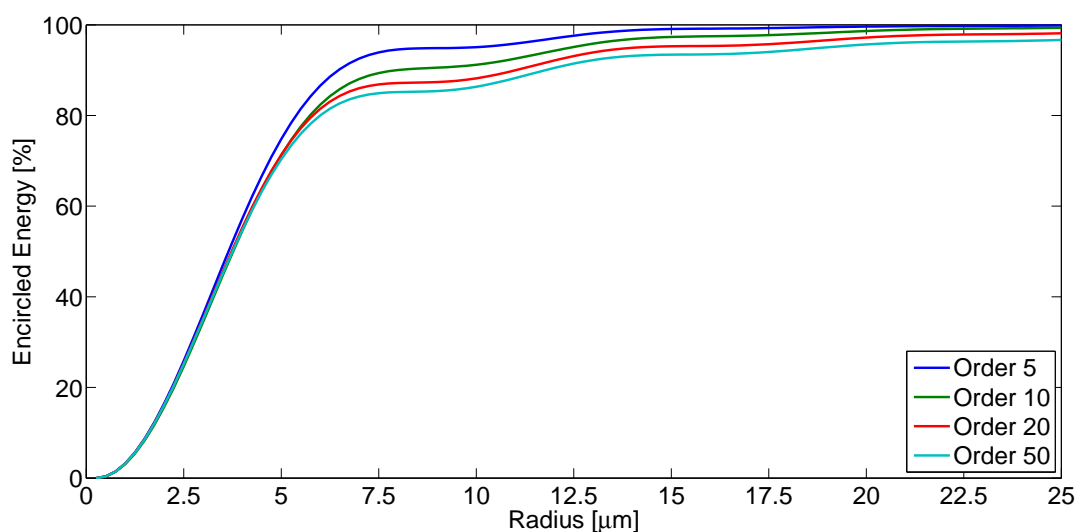


Figure 45: Encircled energy of the focused super-Gaussian beam of different orders with a circular apodization mask introduced (250 mm diameter).

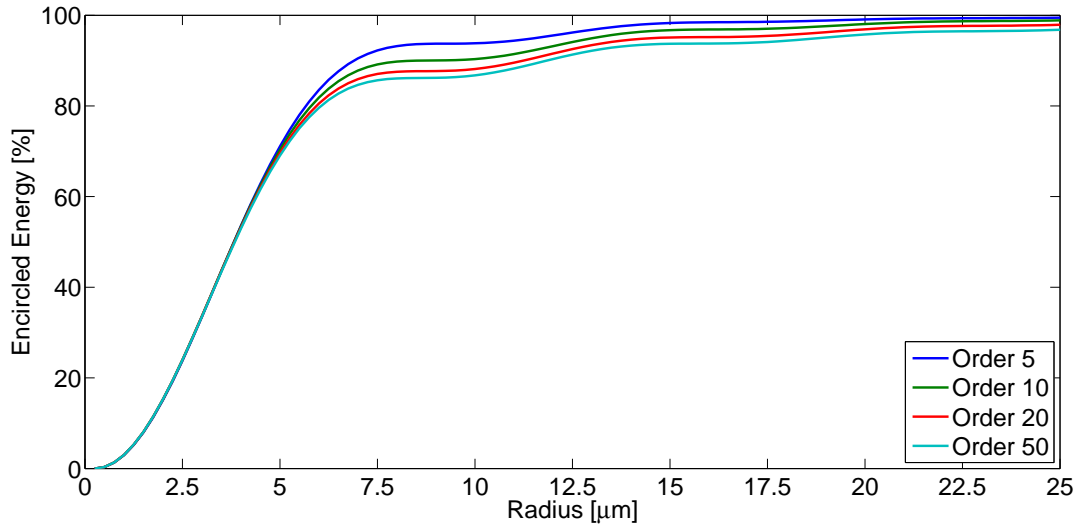


Figure 46: Encircled energy of the focused super-Gaussian beam of different orders with a circular apodization mask introduced (230 mm diameter).

Summary

In this subchapter the theoretical limitation of the super-Gaussian beam has been discussed. So far there is no clear agreement on the demanded focal spot shape or quality. Sometimes only the peak fluence is important. Therefore, it is complicated to define proper beam apodization if the requirements are not clearly defined by the laser users.

To quickly compare the resulting encircled energies, it is advantageous to choose some simple criterion. As an example, using the radius, inside of which 90 % of the focal spot's energy is encircled. Table 13 and Table 14 show these values separately for hard apertures and for apodization masks, respectively.

Table 13: Radius inside of which 90 % of the energy is contained (hard aperture).

Beam order	Without aperture [μm]	270 mm [μm]	250 mm [μm]	230 mm [μm]
5	5	7	9.25	11.75
10	6	10	11.5	13
20	7	11	12	13.25
50	10.5	11.25	12.5	13.5

Table 14: Radius inside of which 90 % of the energy is contained (apodizing mask).

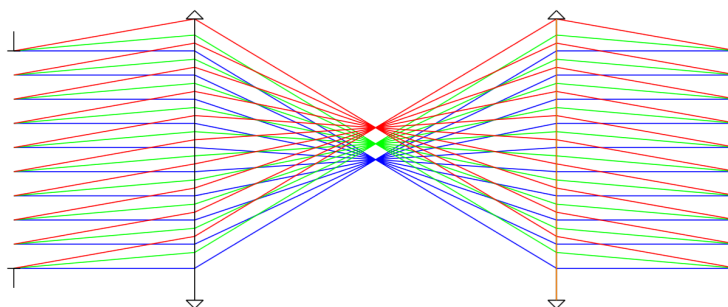
Beam Order	270 mm [μm]	250 mm [μm]	230 mm [μm]
5	6.25	6.5	7
10	7.75	8	8.5
20	11	11.25	11.25
50	12	12	12

8.4 Transmissive Optics

In this chapter various optical systems containing only refractive elements are investigated. There are several case scenarios related to the ELI-Beamlines facility. In the case of relay systems it has proceeded from the physically ideal (achromatic and without an aperture) $4-f$ system, to real systems comprising optical aberrations. Transmissive optics will probably not be the most used optics in the main beamlines of the ELI-Beamlines facility, due to the ultrashort (femtosecond) duration of the pulses. However, even within ELI-Beamlines, such systems may be used behind the leak mirrors to relay beams to diagnostic stations, or to change their sizes for imaging on the CCD sensors. The historical predecessors of ELI-Beamlines used transmissive relay telescopes for the main beamlines as well.

8.4.1 $4-f$ Relay Systems

The main motivation to use relay systems for a laser beam is to conserve its spatial profile over a long distance, which is typically being disturbed by the effects of diffraction and/or self-focusing, while the beam propagates. This was primarily investigated by Hunt [25, 26].

**Figure 47:** Ray-tracing of simple $4-f$ system created by two positive paraxial lenses (Zemax).

In the first example, the relay system does not exhibit any optical aberrations at all. The only limitation is beam diffraction. A practical example of such a system is

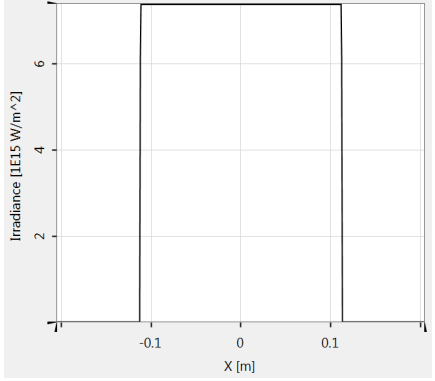
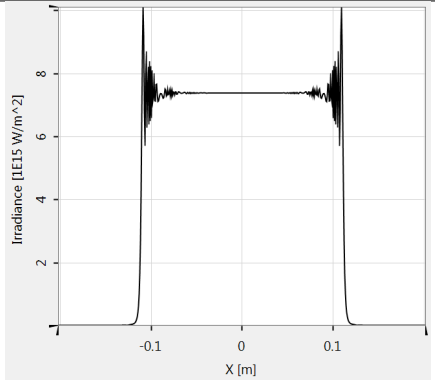
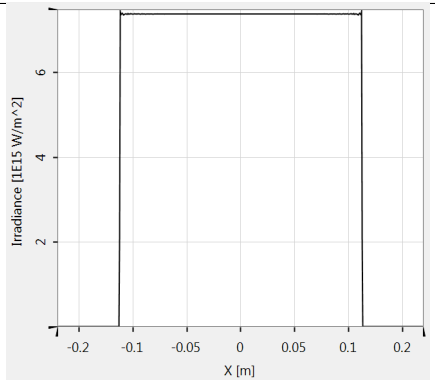
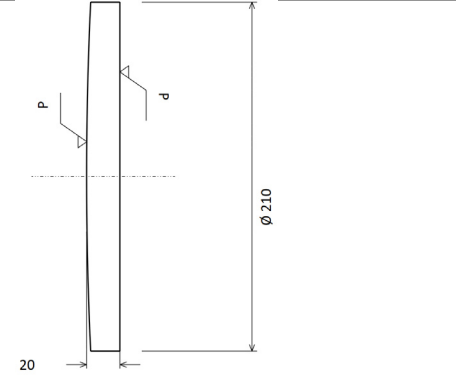
shown in Fig. 47. The system is built by two paraxial lenses (shown in the Zemax ray-tracing picture) with a common focal point and the same focal length, thus with magnification $M = 1$. Similar to that concept, two ideal lenses without an aperture are used within VirtualLab Fusion to create an optical system equal to that of Zemax.

From a technical point of view it makes sense to compare the free space propagation of super-gaussian beams with beams that were relayed by a $4-f$ system. Some examples of free space propagation of super-Gaussian beams are already described in 8.1. It was demonstrated that ideal super-Gaussians of orders of tens do not suffer by diffraction as do the beams with higher orders. Hence, it is only logical to show the advantage of relay systems for beams that suffer more by diffractive effects. In one example the super-Gaussian beam has an order of 1000, radius of 112.8 mm and wavelength of $\lambda = 820$ nm and its profile is shown in table 15.

Distances inside the ELI-Beamlines facility are typically within the magnitude of tens of meters. Therefore, the beam will most probably be relayed to a distance of around 20 m. To show the performance of such a $4-f$ system, two ideal lenses without an aperture of focal length $f = 5$ m were chosen. The beam is propagated from its source to the target plane with the use of a rigorous SPW operator. The reader can clearly see the difference between the beam propagated in free space and beam relayed by a $4-f$ system. High order, almost top-hat beams, exhibit spikes around the edges (in the community sometimes referred to as “ears”) after few meters of free space propagation, whereas the relayed beam is nearly the same as the original one. Such spikes can carry intensities larger than the mirror’s LIDT¹⁴ and lead to the mirror’s destruction. Therefore, it is desired to avoid these spikes, or at least precisely predict their magnitude to be sure that they will be within the mirror’s specified LIDT. There is also a case showing the use of a relay system with real plano-convex lenses. The material is fused silica, the lens thickness is 20 mm, diameter 210 mm and the surface radius is 2266.4 mm.

¹⁴Laser Induced Damage Threshold

Table 15: Beam free space propagation and relaying by an ideal and a real 4- f system.

	Spatial profile
Input beam (order 1000)	
Free space propagation (20 m)	
Ideal 4- f relay ($f = 5$ m)	
Relay with plano-convex lenses:	

8.4.2 Beam Expanders/Reducers

In the laser chain there is often a need to increase or decrease the beam size. For such purposes beam expanders or reducers are incorporated into the laser chain. There are two basic options for achieving this goal, depending on whether there is also a need to relay the wavefront, or if there is only a need to change the beam size. In the first case, similar systems to what we have seen previous subchapter are in use – Keplerian telescopes. Instead of a positive lens or group pairs of the same focal length, different focal lengths are chosen to achieve magnification $M \neq 1$. If the image or wavefront relay is not required, a pair of positive and negative elements or groups can be used in a so-called Galilean design. If optical doublets are used, then other combinations are possible depending on the negative lens position – Fraunhofer and Steinheil doublets.

Of course, transmissive expanders or reducers cannot be used in the main beamline for several reasons - mainly because of lower LIDT of lenses and high GVD¹⁵, caused by a large thickness of lenses needed for beams with a semi-diameter near 250 mm. However, they can be used behind leak mirrors for various diagnostic measurements, where the pulse duration is not as important. A feasibility assessment was also assigned to incorporate a transmissive reducer in a periscope for the L1-E1 beamline. The reducer should be designed as part of a periscope which serves to purpose of demagnifying the main beam to half of its original size¹⁶. There is a restriction to the proposed optical design (Fig. 48) – the distance between the lenses cannot exceed 350 mm. Therefore the degrees of freedom are restricted.

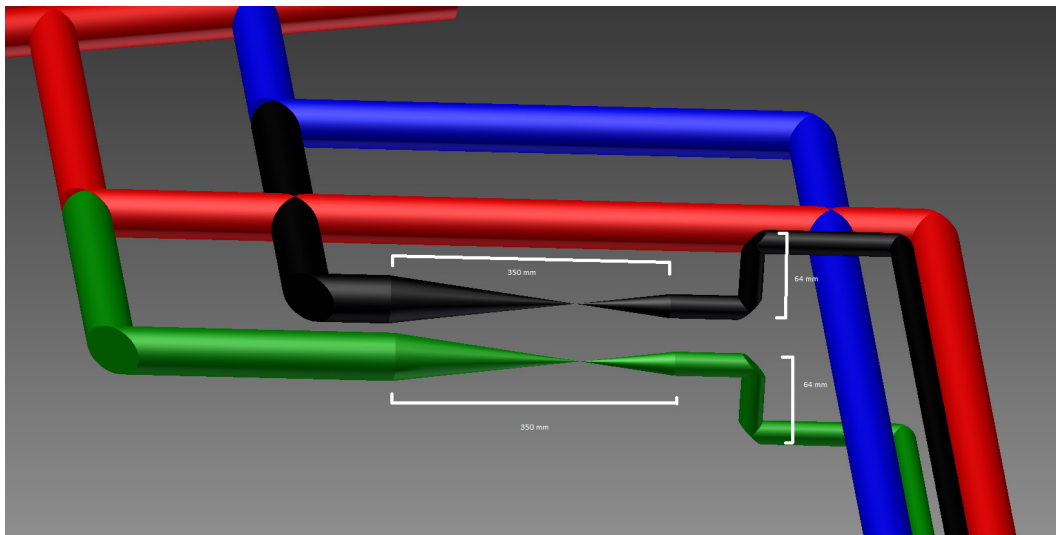


Figure 48: A mechanical engineer's (Colomer Real Pablo Ramón MSc.) visualization of a proposed location where the periscope should be placed inside the L1-E1 beamline.

¹⁵Group Velocity Dispersion

¹⁶ $1/e^2$ waist radius of the original Gaussian beam is 13.75 mm

In the first step, classical lens design is conducted by the Zemax OpticStudio. The merit function for the system's optimization in OpticStudio contains, among other things, an AMAG operand, which sets the proper angular magnification of the system, which is equal to -2 in the current example. Investigation of super-Gaussian beam transmission and pulse stretching caused by the lenses' GVD is aided in the second step by VirtualLab Fusion. Three specific possible solutions of the reducer's designs are shown in the next part of this chapter.

Keplerian Design

The Keplerian design comprises two positive lenses or groups with a common focal plane. The advantage of such a configuration is the capability of spatial filtering, if a pinhole is placed in the common focal plane. In addition, the image plane is being relayed, not only demagnified. However, it is also more difficult to correct for aberrations in Keplerian systems. Moreover, the space for the reducer's integration is restricted by the 350 mm length. Thus, the sum of the lenses focal lengths is 350 mm at most. The short length of the reducer makes the correction even more complicated.

As a starting point for designing the system, two commercially available doublets made by Thorlabs are used. These are combined in the second step and further optimized as a reducing optical system. One of the goals is to avoid any aspherical surfaces, hence only the surface radii are optimized. Due to the very short allowed total length of the reducing system, two additional menisci are included. These menisci contribute additional refracting power that leads to the compression of the total length of the system. The system is depicted in Fig. 49. The effective focal length of the first two groups is 233 mm, whereas the next two groups have a total effective focal length equal to 117 mm.

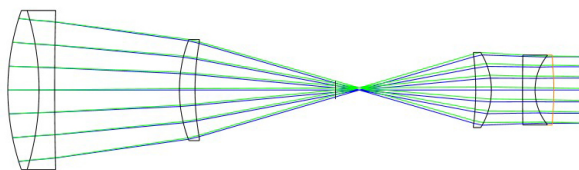


Figure 49: Ray-tracing of the Keplerian type reducer.

Thorough aberration analysis is conducted with the use of the standard geometrical optics approach. Spot diagrams shown in Fig. 50 demonstrate that the smallest achievable RMS radius for an axial field is almost $22\ \mu\text{m}$, in contrast to the Airy radius of $2.49\ \mu\text{m}$. For the off-axis field (0.5 degrees) the RMS radius is $250\ \mu\text{m}$. That makes the system very sensitive to any possible angular tilts of the incoming field. Longitudinal aberration analysis provided in Fig. 51 shows that the system is corrected for two wavelengths – $750\ \text{nm}$ and $850\ \text{nm}$. However, the aberration is still relatively large in comparison with the systems to be described in the next paragraphs.

As the last part of the geometrical analysis, the wavefront aberrations are also provided (see Table 16). Complementary to Fig. 51, the wavefront representing the field with a wavelength of 950 nm is much more distorted than the wavefront with a central wavelength of 850 nm. Also, similar to Fig. 51, the wavefront of the 750 nm wavelength is comparable to that of the 850 nm wavelength. The wavefront RMS of the central wavelength is equal to 0.1099λ , whereas the wavefront RMS of the $\lambda = 950$ nm is equal to 1.2949λ .

Another important thing that needs to be investigated is pulse stretching caused by the lenses' GVD. This is calculated with the use of VirtualLab Fusion's Field Tracing. For the input 30 fs pulse with an 850 nm central wavelength, the output reduced beam has a duration of 626 fs¹⁷.

¹⁷Situation with the reducer enclosed in a vacuum.

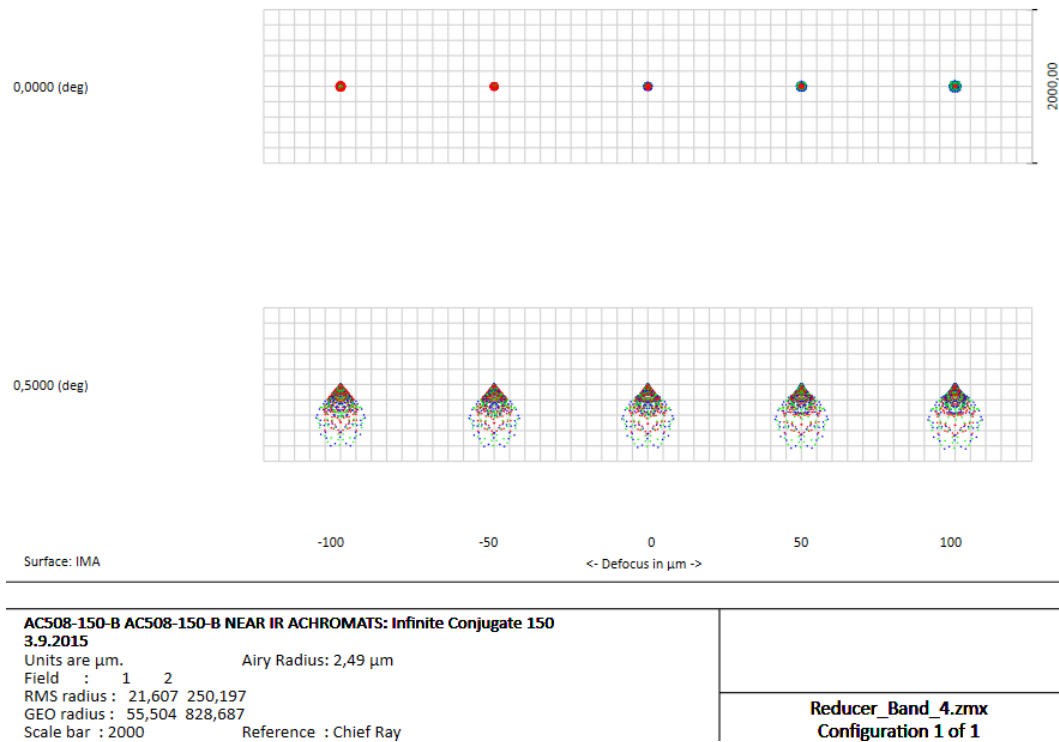


Figure 50: Spot diagrams of the Keplerian type reducer.

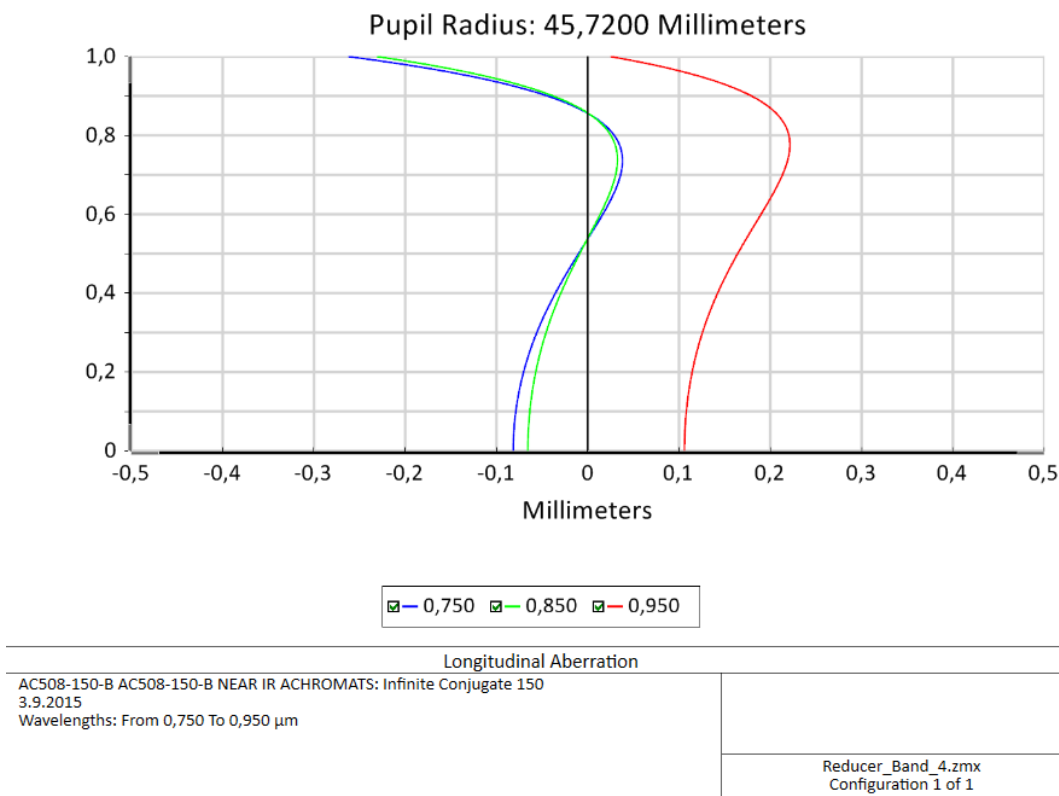
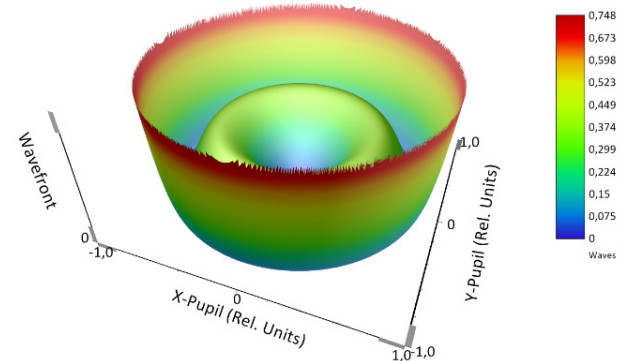
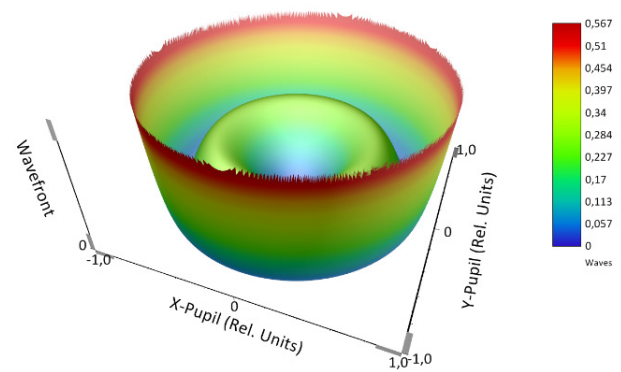
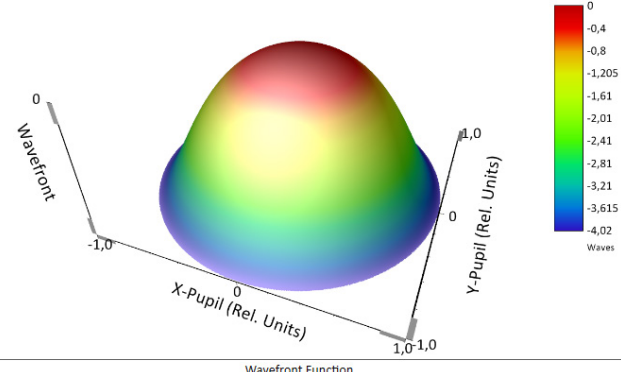


Figure 51: Longitudinal aberration of the Keplerian type reducer.

Table 16: The reducer’s wavefront maps for wavelengths within the desired pulse bandwidth.

Wavelength	Wavefront Map
$\lambda = 750 \text{ nm}$	 <p>Wavefront Function ACS08-150-B ACS08-150-B NEAR IR ACHROMATS: Infinite Conjugate 150 3.9.2015 0.7500 μm at 0.0000 (deg) Peak to valley = 0.7477 waves, RMS = 0.1445 waves. Surface: Image Exit Pupil Diameter: 4.5720E+001 Millimeters</p> <p>Reducer_Band_4.zmx Configuration 1 of 1</p>
$\lambda = 850 \text{ nm}$	 <p>Wavefront Function ACS08-150-B ACS08-150-B NEAR IR ACHROMATS: Infinite Conjugate 150 3.9.2015 0.8500 μm at 0.0000 (deg) Peak to valley = 0.5672 waves, RMS = 0.1099 waves. Surface: Image Exit Pupil Diameter: 4.5720E+001 Millimeters</p> <p>Reducer_Band_4.zmx Configuration 1 of 1</p>
$\lambda = 950 \text{ nm}$	 <p>Wavefront Function ACS08-150-B ACS08-150-B NEAR IR ACHROMATS: Infinite Conjugate 150 3.9.2015 0.8500 μm at 0.0000 (deg) Peak to valley = 4.0157 waves, RMS = 1.2949 waves. Surface: Image Exit Pupil Diameter: 4.5720E+001 Millimeters</p> <p>Reducer_Band_4.zmx Configuration 1 of 1</p>

Galilean Design

In contrast to the aforementioned case, the Galilean design is a combination of a positive and a negative lens, or a group, hence there is no common focal plane allowing spatial filtering of the beam. However, this system allows aberrations to be controlled in a better way. On the following pages, two specific configurations will be compared. One using a more common Fraunhofer doublet and another using a Steinheil doublet as a frontal lens group.

Galilean Design with Fraunhofer Doublet

Ray-tracing of the Galilean reducer with the Fraunhofer doublet is depicted in Fig. 52. The positive doublet with an effective focal length of 676 mm and the diverging lens effective focal length equal to -341 mm is needed in order to fit inside a 350 mm restricted length within the beamline.

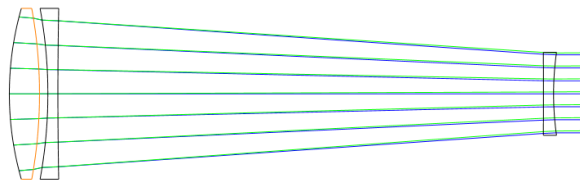


Figure 52: Ray-tracing of the Galilean type reducer with a Fraunhofer doublet.

Consistent with the case of the Keplerian telescope, the same aberration analysis follows. First of all, the spot diagrams are shown in Fig. 53. The smallest achievable RMS spot radius equals $1.313 \mu\text{m}$, which is more than ten times better than in the case of the Keplerian doublet. For a comparison, the Airy radius is $2.294 \mu\text{m}$. Thus the spot for the axial field is, in contrast to the Keplerian reducer, smaller than the Airy radius. The off-axis field (0.5 degrees) creates a spot with a $16.326 \mu\text{m}$ RMS radius. The optical system is corrected for only one wavelength of 750 nm (see Fig. 54). However, the overall result of this aberration is much better than in the case of the Keplerian reducer. Also the results of the wavefront errors (see Table 17) are superior to those achieved by the Keplerian reducer. The wavefront RMS error for the central wavelength (850 nm) is 0.1064 wavelengths. Whereas for the $\lambda = 750$ nm and 950 nm, the RMS errors are 0.0141λ and 0.0526λ , respectively. In opposition to the Keplerian reducer, all wavefront RMS errors are smaller than the wavelength.

For the input 30 fs pulse with an 850 nm central wavelength the output reduced beam has a duration of 152.95 fs^{18} .

The performance of the Galilean reducer is much better than that of the Keplerian one. However, the capability of spatial filtering is lost. The pulse is also stretched less than in the case of the Keplerian reducer, nevertheless the number is still large.

¹⁸Situation with the reducer enclosed in a vacuum.

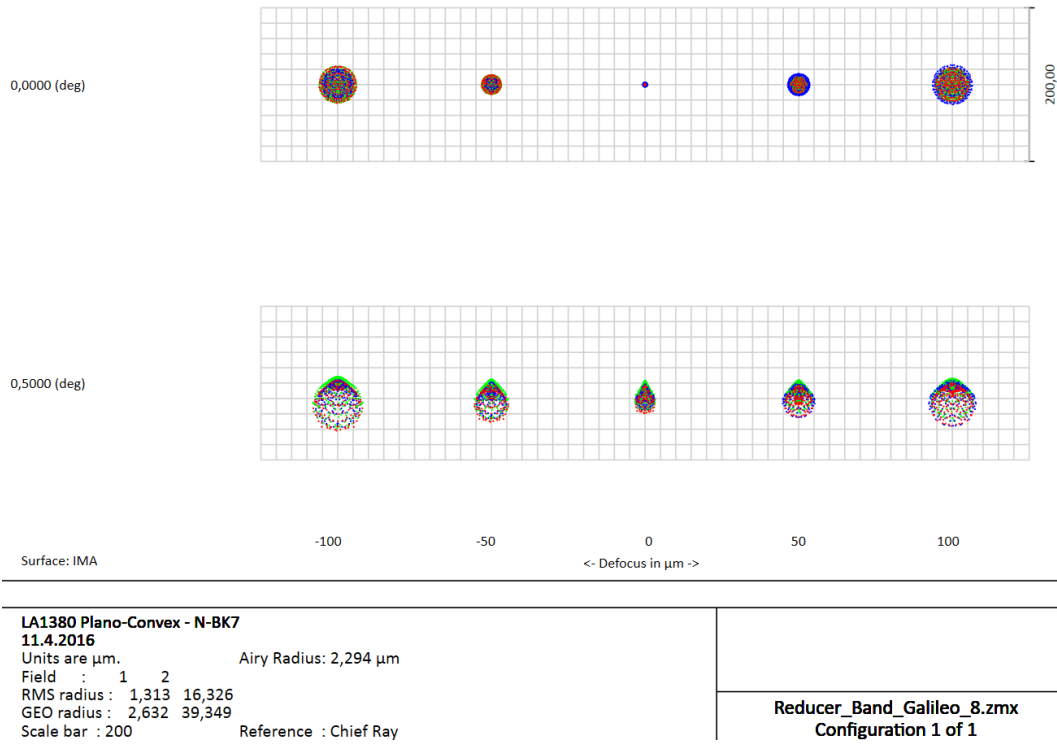


Figure 53: Spot diagrams of the Galilean type reducer with a Fraunhofer doublet.

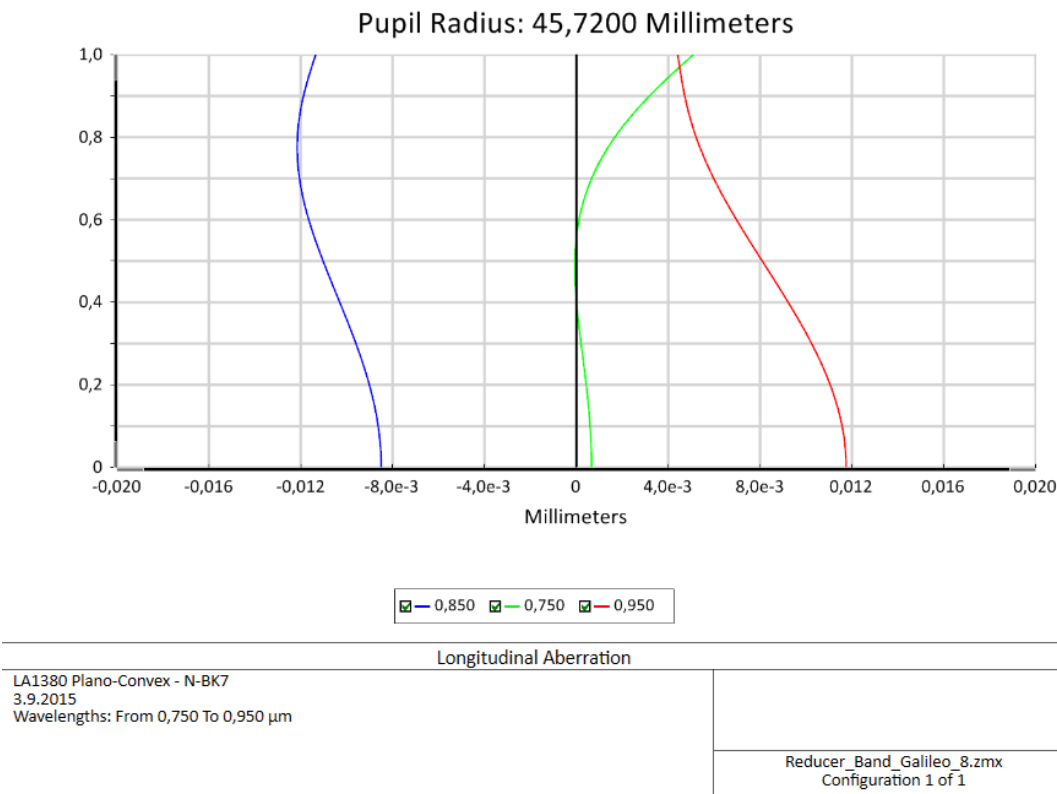
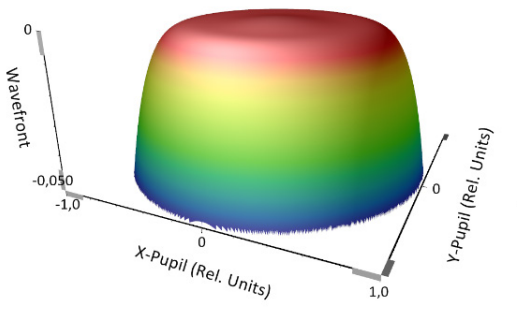
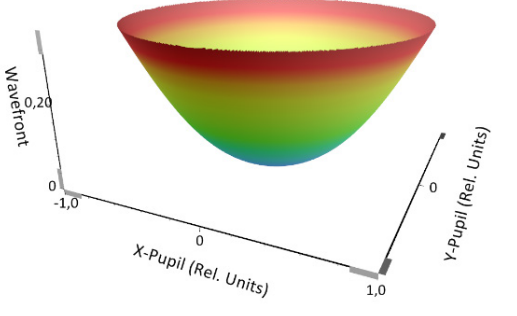
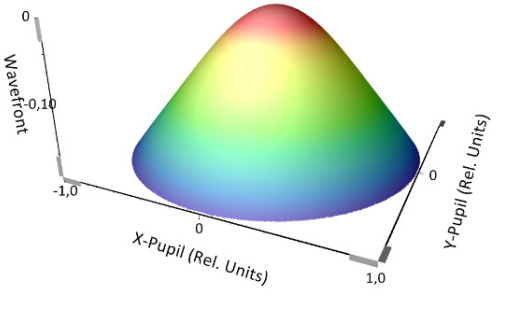


Figure 54: Longitudinal aberration of the Galilean type reducer with a Fraunhofer doublet.

Table 17: Reducer's wavefront maps for wavelengths within the desired pulse bandwidth.

Wavelength	Wavefront Map
$\lambda = 750 \text{ nm}$	 <p data-bbox="893 728 1013 750">Wavefront Function</p> <p data-bbox="598 750 861 817"> LA1380 Plano-Convex - N-BK7 3.9.2015 0,7500 μm at 0,0000 (deg) Peak to valley = 0,0524 waves, RMS = 0,0141 waves. Surface: Image Exit Pupil Diameter: 4,6104E+001 Millimeters </p> <p data-bbox="1117 795 1284 828">Reducer_Band_Galileo_8.zmx Configuration 1 of 1</p>
$\lambda = 850 \text{ nm}$	 <p data-bbox="893 1220 1013 1243">Wavefront Function</p> <p data-bbox="598 1243 861 1310"> LA1380 Plano-Convex - N-BK7 3.9.2015 0,8500 μm at 0,0000 (deg) Peak to valley = 0,3595 waves, RMS = 0,1064 waves. Surface: Image Exit Pupil Diameter: 4,6104E+001 Millimeters </p> <p data-bbox="1117 1288 1284 1321">Reducer_Band_Galileo_8.zmx Configuration 1 of 1</p>
$\lambda = 950 \text{ nm}$	 <p data-bbox="893 1713 1013 1736">Wavefront Function</p> <p data-bbox="598 1736 861 1803"> LA1380 Plano-Convex - N-BK7 3.9.2015 0,9500 μm at 0,0000 (deg) Peak to valley = 0,1888 waves, RMS = 0,0526 waves. Surface: Image Exit Pupil Diameter: 4,6104E+001 Millimeters </p> <p data-bbox="1117 1780 1284 1814">Reducer_Band_Galileo_8.zmx Configuration 1 of 1</p>

Galilean Design with Steinheil Doublet

The last possible option for the transmissive reducer is to use the Galilean reducer with the reversed Fraunhofer doublet, the so-called Steinheil doublet (see Fig. 55). Changes to the lens positions inside the doublet have a significant influence on geometric aberrations. To fit inside the same 350 mm length, the effective focal lengths of the doublet and the diverging lens are 578 mm and -293 mm, respectively.

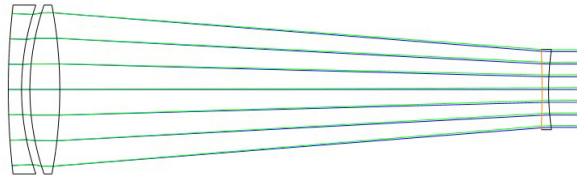


Figure 55: Ray-tracing of the Galilean type reducer with a Steinheil doublet.

Similar to the previously mentioned cases of the Keplerian and Galilean reducers with a Fraunhofer doublet, the same aberration analysis is conducted. The RMS spot radius (see Fig. 56) for the axial field is equal to $1.735 \mu\text{m}$. The spot radius for the axial field is smaller than the Airy radius, being $2.334 \mu\text{m}$. RMS spot radius of the off-axis field is $37.987 \mu\text{m}$. In this matter the reducer with the Steinheil doublet performs worse than the reducer with the Fraunhofer doublet. Longitudinal aberration (see Fig. 57) is relatively similar, in the sense of magnitude, to that achieved with the reducer incorporating the Fraunhofer doublet. Wavefront deviations, as seen in Table 18, feature RMS values of 0.1324λ for the central wavelength (850 nm), 0.0043λ for the 750 nm and 0.0558λ for the 950 nm. Regarding the wavefront errors, both Galilean reducers are comparable.

For the 30 fs input pulse with an 850 nm central wavelength, the output reduced beam has a duration of 167.11 fs ¹⁹, which makes the Steinheil variant reducer a little bit worse than the version incorporating the Fraunhofer doublet.

It is clear that even highly corrected transmissive reducers cannot be used for ultrashort pulses. In the best case scenario the pulse will be stretched approximately five times. The only possible application could be beam reduction for wavefront sensors, where the temporal distribution of the pulse is not so crucial.

The systems shown on the previous pages were examples. Other variations are possible as well. These were not the final designs of the reducer systems, but rather hypothetical examples.

¹⁹Situation with the reducer enclosed in a vacuum.

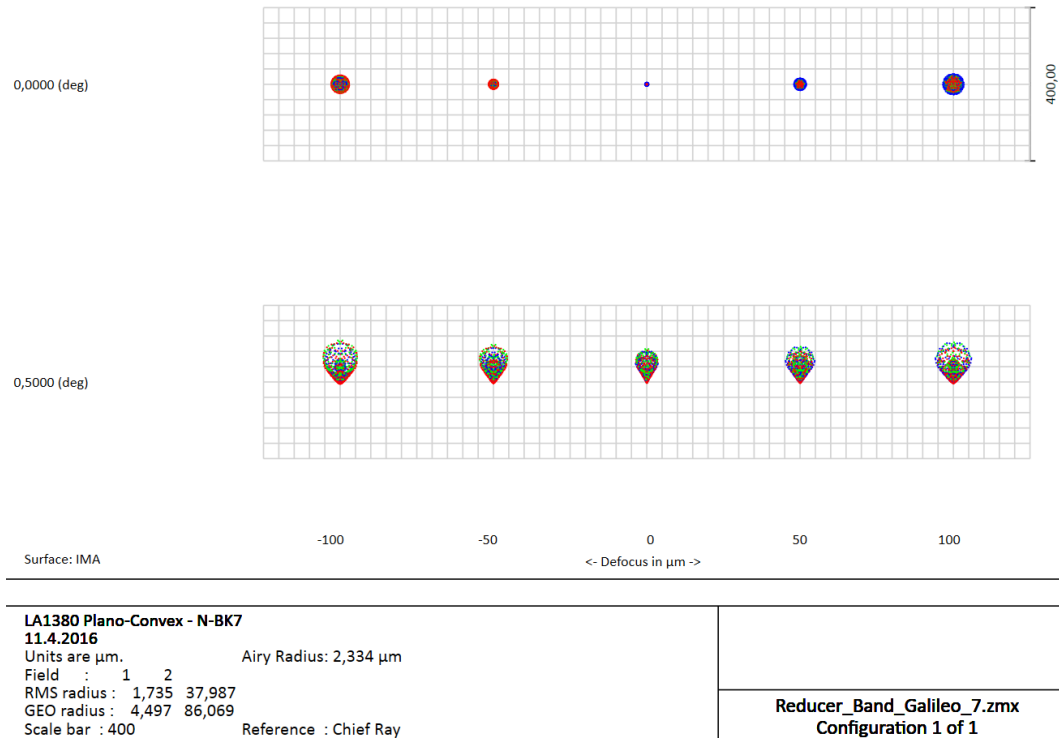


Figure 56: Spot diagrams of the Galilean type reducer with a Steinheil doublet.

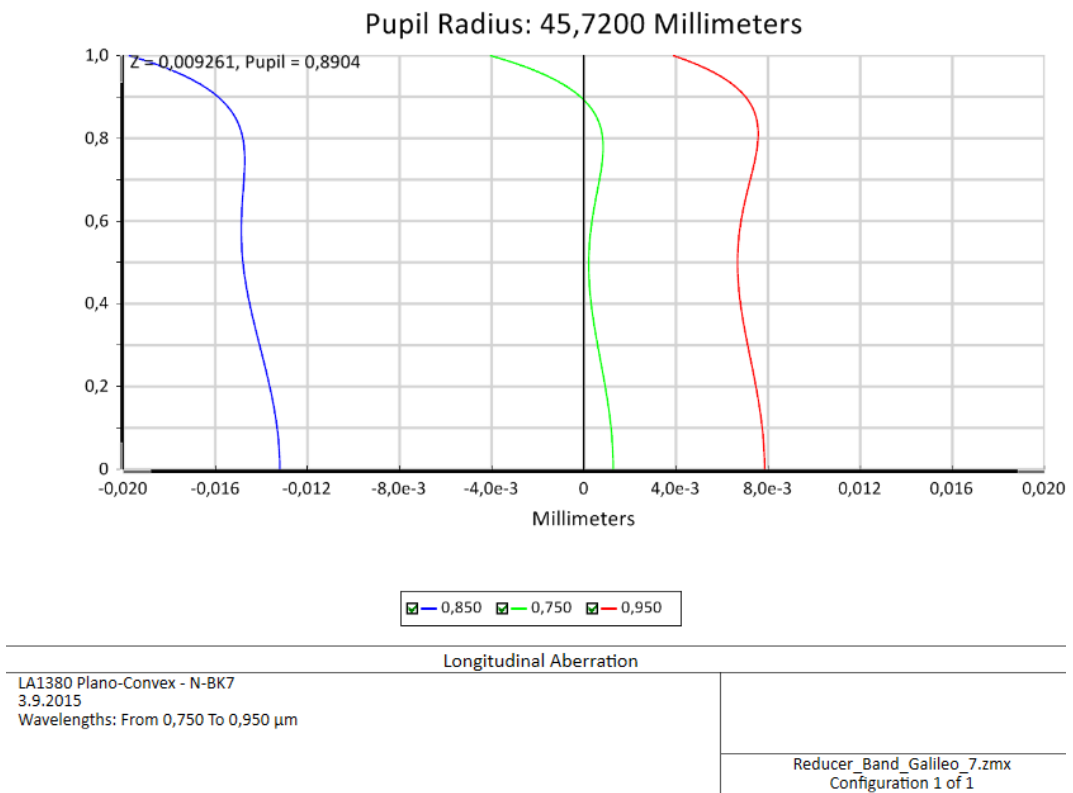
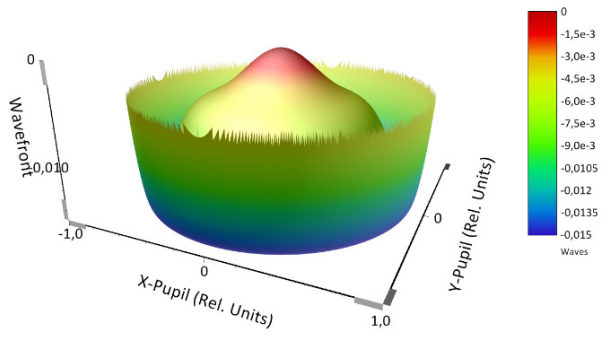
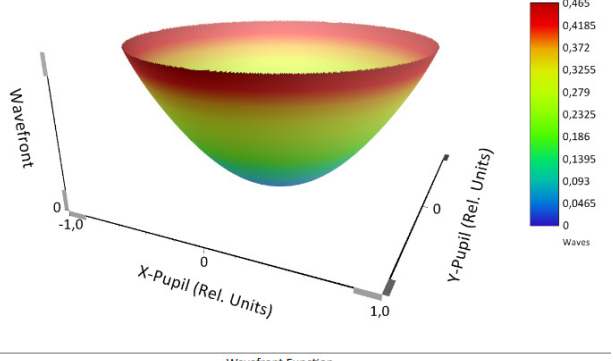
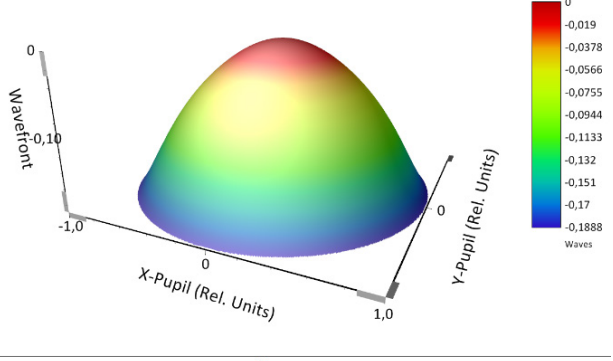


Figure 57: Longitudinal aberration of the Galilean type reducer with a Steinheil doublet.

Table 86: Reducer’s wavefront maps for wavelengths within the desired pulse bandwidth.

Wavelength	Wavefront Map
$\lambda = 750 \text{ nm}$	 <p style="text-align: center;">Wavefront Function</p> <p>LA1380 Plano-Convex - N-BK7 3.9.2015 0,7500 μm at 0,0000 (deg) Peak to valley = 0,0150 waves, RMS = 0,0043 waves. Surface: Image Exit Pupil Diameter: 4,6284E+001 Millimeters</p> <p style="text-align: right;">Reducer_Band_Galileo_7.zmx Configuration 1 of 1</p>
$\lambda = 850 \text{ nm}$	 <p style="text-align: center;">Wavefront Function</p> <p>LA1380 Plano-Convex - N-BK7 3.9.2015 0,8500 μm at 0,0000 (deg) Peak to valley = 0,4650 waves, RMS = 0,1324 waves. Surface: Image Exit Pupil Diameter: 4,6284E+001 Millimeters</p> <p style="text-align: right;">Reducer_Band_Galileo_7.zmx Configuration 1 of 1</p>
$\lambda = 950 \text{ nm}$	 <p style="text-align: center;">Wavefront Function</p> <p>LA1380 Plano-Convex - N-BK7 3.9.2015 0,9500 μm at 0,0000 (deg) Peak to valley = 0,1888 waves, RMS = 0,0558 waves. Surface: Image Exit Pupil Diameter: 4,6284E+001 Millimeters</p> <p style="text-align: right;">Reducer_Band_Galileo_7.zmx Configuration 1 of 1</p>

Summary

In the preceding paragraphs three examples of transmissive reducers were presented:

- Keplerian
- Galilean with Fraunhofer doublet
- Galilean with Steinheil doublet

These three reducers have an equivalent magnification ratio.

The design of the reducers described were made in Zemax OpticStudio.

From the geometric optics point of view, the poorest results were achieved by the Keplerian type reducer. The RMS spot radius of the Keplerian type reducer is more than ten times larger than the RMS spot radius achieved by each of the Galilean type reducers. Wavefront deviations for those other than the central wavelength are also better when the Galilean reducers are used.

In this task VirtualLab Fusion was only used to calculate the output beam pulse duration. The shortest output pulse duration is achieved by the Galilean type reducer with a Fraunhofer doublet (152.95 fs). The resulting duration with the Steinheil doublet is slightly bigger (167.11 fs). Consequently, there is no advantage in using Steinheil doublet in the case described. The longest output duration is achieved by the Keplerian type reducer, which is approximately four time longer (626 fs). These systems, even when enclosed in vacuum, have excess dispersion and thus they are not feasible for use with 10 fs pulses.

8.5 Reflective Optics

The previous chapter has shown possible optical systems configurations comprising lenses only. Systems in the following text are either catoptric or catadioptric. Several design concepts are discussed in the next few paragraphs. The basic problem to be solved within ELI-Beamlines how to relay the beam from the source to the experimental room, most likely with the use of either planar and/or off-axis parabolic mirrors. Several scenarios are discussed and assessed in the following subchapters. The feasibility of various system geometries are analysed. Also reflective reducers and telescopes for beam diagnostics are discussed.

8.5.1 Beam Relaying

The use of mirrors for beam relaying of high peak power ultrashort laser pulses is inevitable. Text in this subchapter assesses a few possible mirror configurations. The task is to define the feasibility of the following system configurations.

“U” and “Z” OAPs Configuration Comparison

One of the first tasks assigned to be analysed in VirtualLab Fusion was to assess various relaying systems containing two off-axis parabolas. A combination of parabolic surfaces can entirely eliminate spherical aberration and minimize influence of astigmatism as a consequence of optical surface tilt. These surfaces need to have an ideal or nearly ideal shape and they need to be perfectly aligned. A combination of two parabolas (and two planar mirrors) is the simplest solution for a relay telescope. There is no other solution that will be simpler than this one. Two spherical surfaces do not suffice for the required imaging quality. The solution is to use parabolic mirrors, which entirely eliminates the spherical aberration that is dominant in axial ray bundles.

Basic aberration of the telescope created by a pair of off-axis parabolas is logically caused by the aberration of each OAP (see Fig. 58). The parabolic mirror has zero spherical aberration. In the case of off-axis ray bundles (or surface tilts) there is coma and astigmatism. For a narrow ray bundle (in the case of high f -numbers), we can assume that the dominant off-axis aberration is astigmatism. Basic optical ray-tracing analysis of the “Z” and “U” OAP combinations have been conducted by Miroslav Palatka [75] (see Fig. 59 and Fig. 60). These analyses show that the dominant off-axis aberration is really an astigmatism (see Fig. 61). The main conclusion of these analyses is that the “Z” configuration enables the compensation of astigmatism due to the opposite sign of the aberration for both mirrors. Conversely, in the “U” configuration these astigmatism are not compensated, but rather their sum is the unfortunate result. It can clearly be seen that the “Z” type configuration is the only one that is satisfactory.

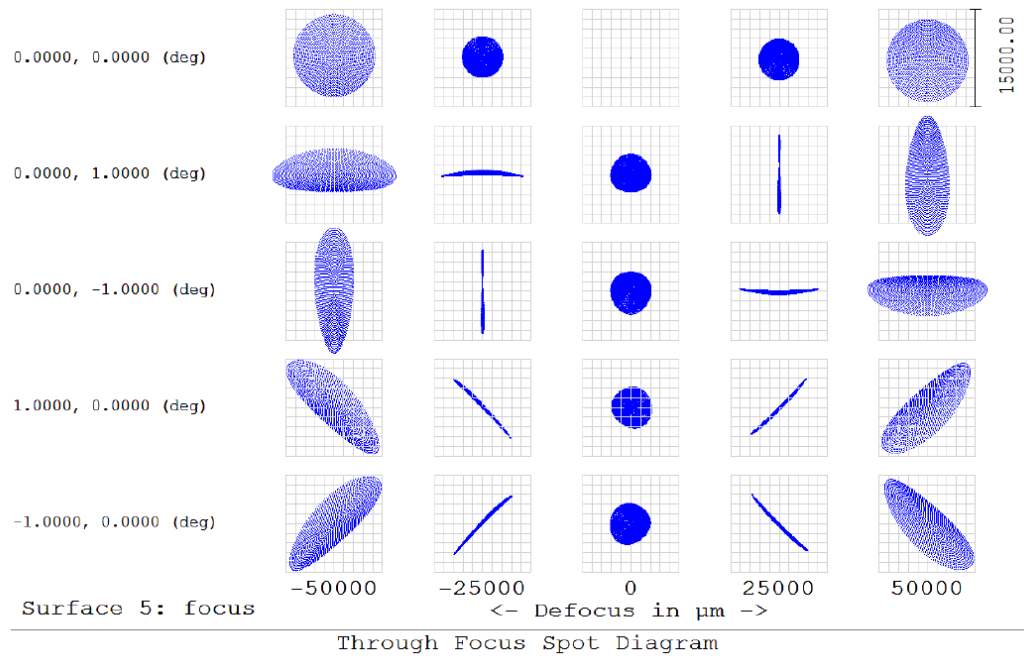


Figure 58: Spot diagrams of a single OAP [75].

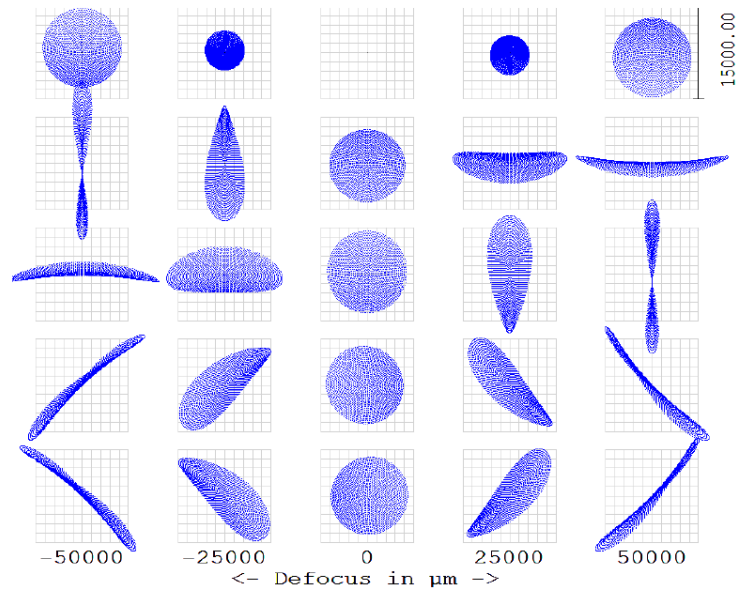


Figure 59: Spot diagrams of the “U” layout relay [75].

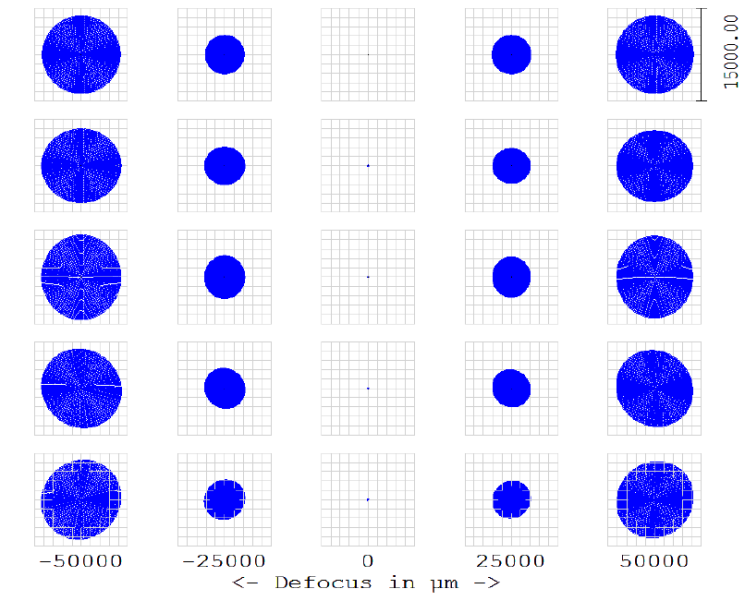


Figure 60: Spot diagrams of the “Z” layout relay [75].

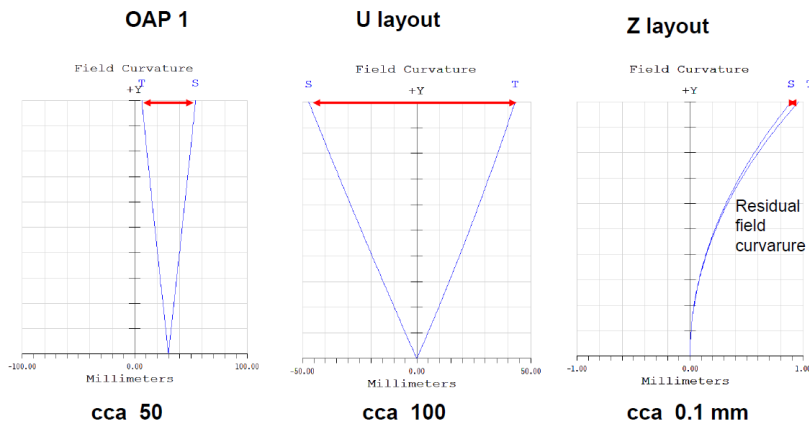


Figure 61: Astigmatism of a single OAP and the “U” and the “Z” layouts, respectively [75].

A similar investigation is conducted within VirtualLab Fusion. In contrast to Zemax OpticStudio, so-called smart rays are available. While using these smart rays, information concerning all components of the electromagnetic field is constantly available. Moreover, instead of the typical ray bundle (square, hexapolar or random), the super-Gaussian beam can be used directly. Thus, the shape of the relayed beam can be directly observed.

As usual, first the LPDs are prepared - particularly for the “U” and the “Z” shaped relay. Both geometries have a 90° off-axis angle (as seen in Fig. 62).

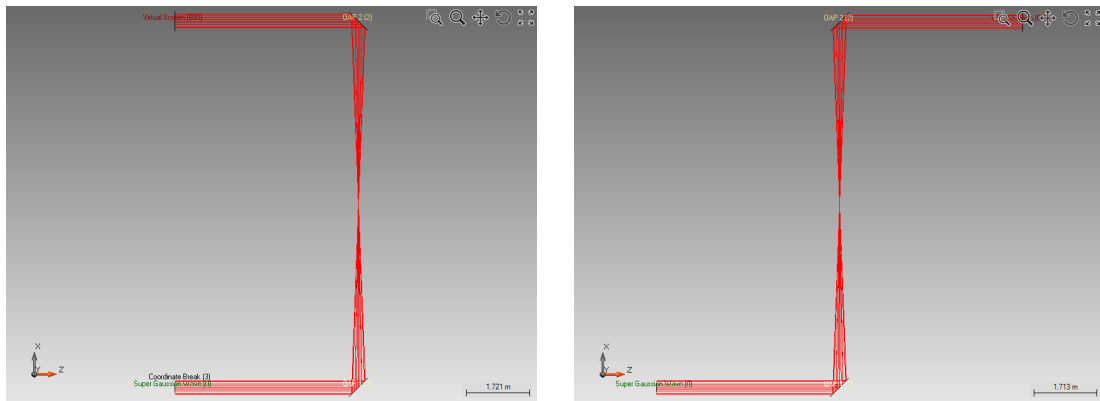


Figure 62: “U” (left) and “Z” (right) OAPs configuration – Ray Tracing (VirtualLab Fusion).

As the input, a super-Gaussian beam with a squared aperture is used. With the application of an optical relay system, a similar beam is the expected output as well. Based on the previously discussed ray-tracing information, it is expected that the “Z” shaped system should perform better than the “U” shaped, mainly because of the astigmatism. The simulation conducted within VirtualLab Fusion clearly confirms this finding. While the beam being relayed by the “U” shaped system is being distorted (Fig. 63), the beam relayed by the “Z” shaped system looks exactly like the input beam (Fig. 64). Geometric Field Tracing in VirtualLab Fusion is based on the use of meshes, which are shown in the left parts of the figures. From the meshes, the rest of the beam can be reconstructed.

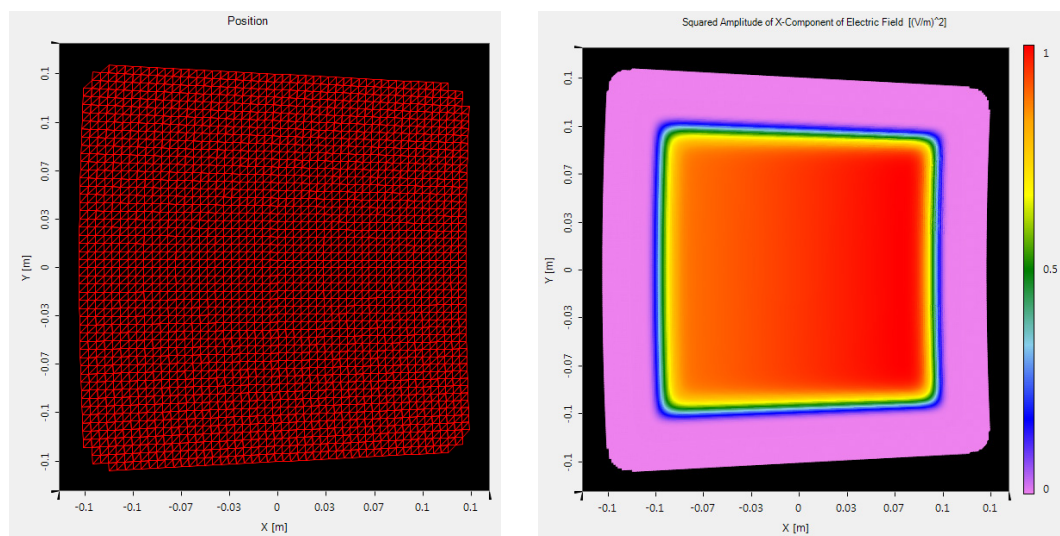


Figure 63: Super-gaussian beam relayed by “U” OAPs configuration – meshes (left) and the reconstructed field (right).

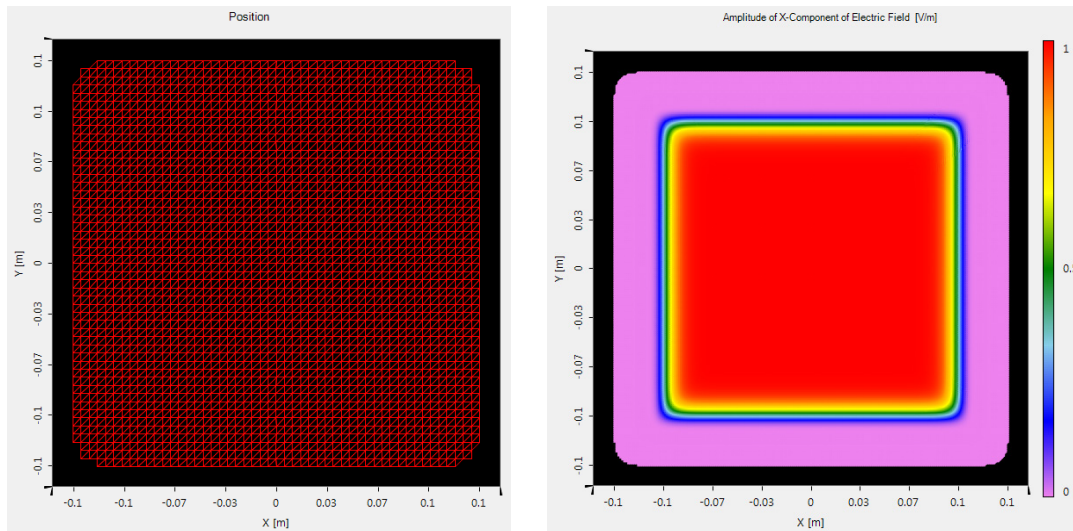


Figure 64: Super-gaussian beam relayed by “Z” OAPs configuration – meshes (left) and the reconstructed field (right).

It is obvious, that the “U” shaped system is absolutely unfeasible for the beam relaying. Conversely, the “Z” shaped system seems to work correctly. However, one question still remains – what is the influence of the off-axis angle to beam relaying?

Angle analysis of the “Z” OAPs Configuration

The previous paragraph demonstrated that the “Z”-like shaped configuration of OAPs is much more efficient in eliminating aberrations. However, in the previous case only the super-Gaussian beam has been traced. A correctly working $4-f$ relay system should transform planar wave into a planar wave, and the point source (spherical wave) into a point image. The following analysis is conducted with the intent to investigating whether or not two OAPs can be possibly used in such a regime. VirtualLab Fusion’s unique Geometric Field Tracing is exploited to aid in this task.

The input spherical wave is shown in Fig. 65.

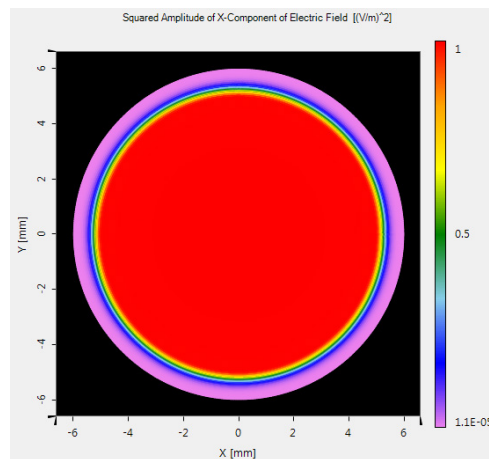


Figure 65: Input field to be relayed.

Then a similar system to the one already described is used to relay this spherical wave to the focus of the second OAP. Unlike the cases in Figs. 63 and 64, the off-axis angle is now only 5 degrees (see Fig. 66), in contrast to the 90 degrees originally used

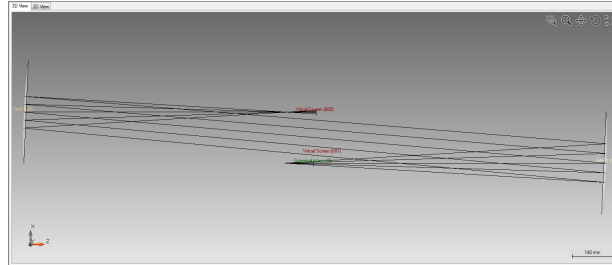


Figure 66: 5 degree “Z” OAPs configuration – Ray Tracing (VirtualLab Fusion).

The field being relayed from the focal point of the first OAP to the focal point of the second OAP is shown in Fig. 67. Fig. 67 illustrates the squared amplitude of the E_x , E_y and E_z components of the field in the focal plane. The reader will notice that the field is very similar to the input field, although there are non-zero values for the E_y and E_z components of the field.

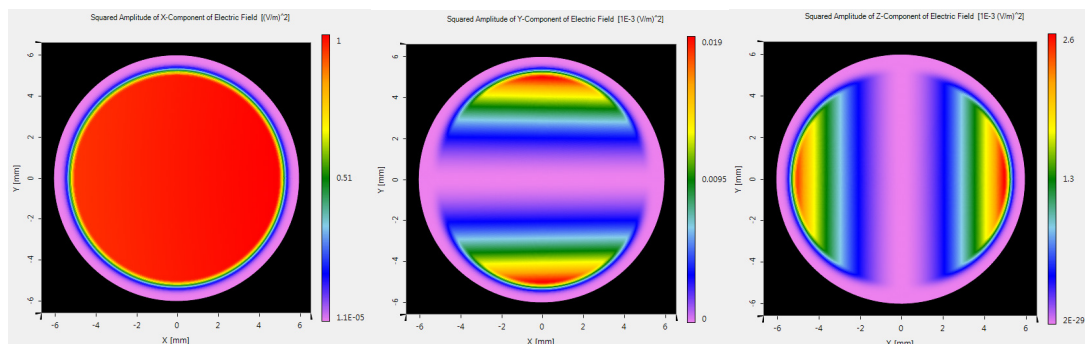


Figure 67: Comparison of the squared amplitude of the E_x , E_y and E_z components of the relayed electromagnetic field for the 5 degree angular tilt of the parabolic mirrors.

It is even more interesting to observe the field evolution while the off-axis angle is changing. On the following pages it is demonstrated how the relayed field is changed based on the off-axis angle from 10 to 90 degrees in 10 degree steps. The figures are organized in the following manner – the even figures between 68 and 84 are represent the ray-tracing of the system used to precisely display the system’s configuration, whereas the even figures between 69 and 85 show the squared amplitude of E_x , E_y and E_z components of the field in the focal plane, respectively.

Through all these pictures the reader can clearly distinguish the trend that with an increasing off-axis angle, more energy is transferred to the E_y component of the field. The E_x part of the field becomes more and more asymmetrical.

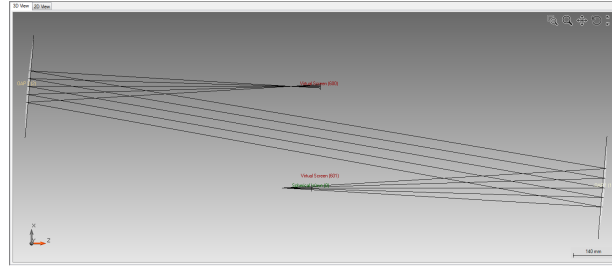


Figure 68: 10 degree “Z” OAPs configuration - Ray Tracing (VirtualLab Fusion).

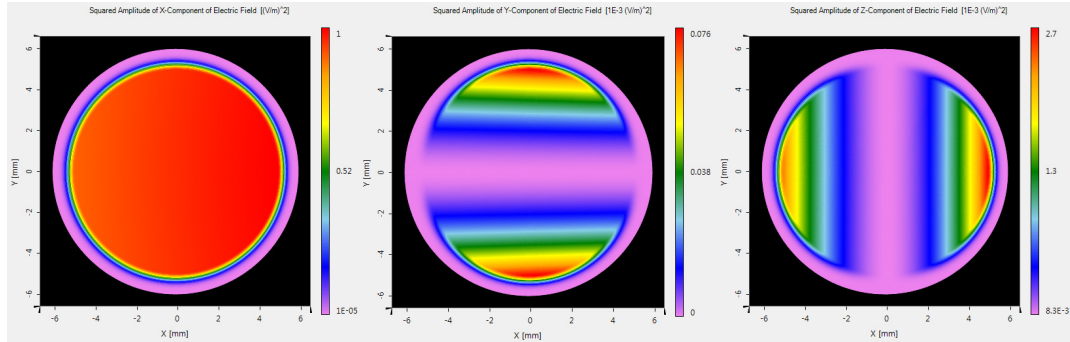


Figure 69: Comparison of the squared amplitude of the E_x , E_y and E_z components of the relayed electromagnetic field for the 10 degree angular tilt of the parabolic mirrors.

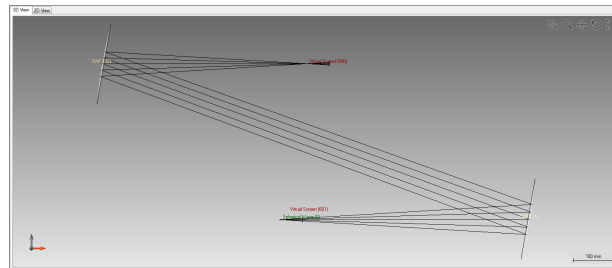


Figure 70: 20 degree “Z” OAPs configuration - Ray Tracing (VirtualLab Fusion).

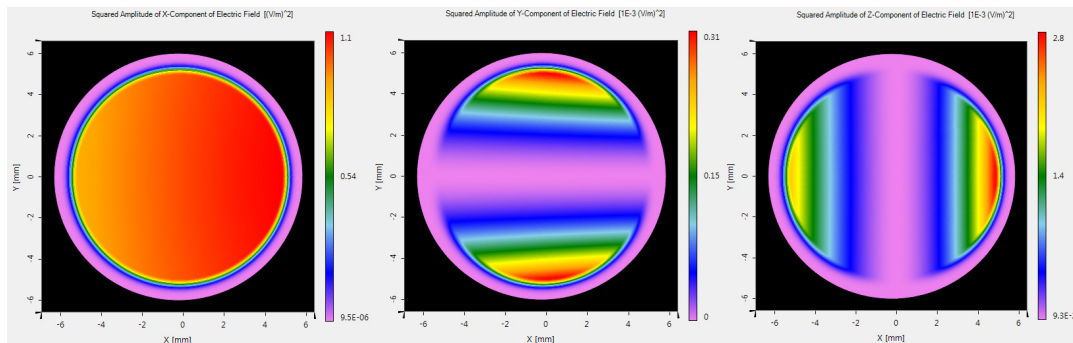


Figure 71: Comparison of the squared amplitude of the E_x , E_y and E_z components of the relayed electromagnetic field for the 20 degree angular tilt of the parabolic mirrors.

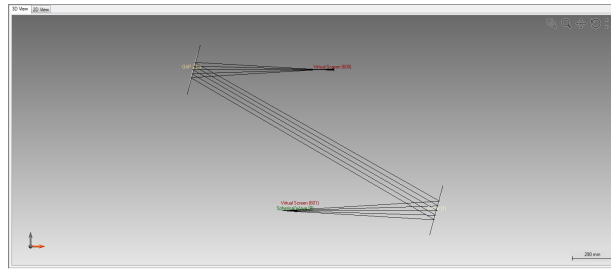


Figure 72: 30 degree “Z” OAPs configuration - Ray Tracing (VirtualLab Fusion).

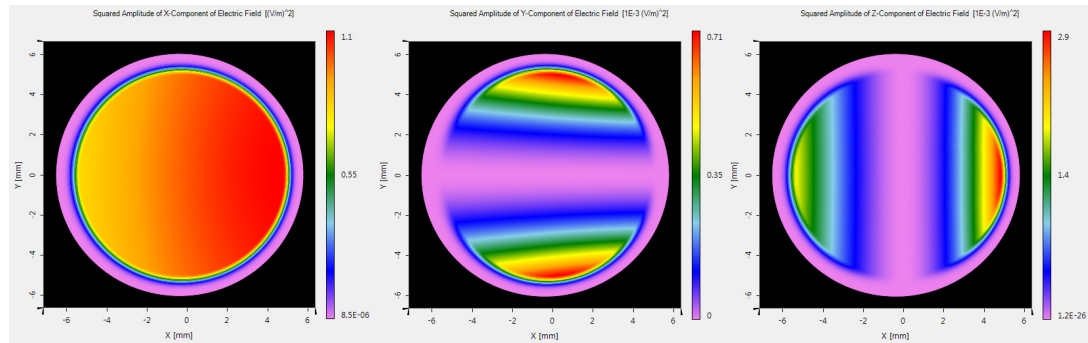


Figure 73: Comparison of the squared amplitude of the E_x , E_y and E_z components of the relayed electromagnetic field for the 30 degree angular tilt of the parabolic mirrors.

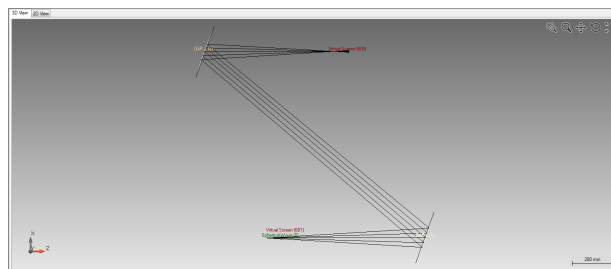


Figure 74: 40 degree “Z” OAPs configuration - Ray Tracing (VirtualLab Fusion).

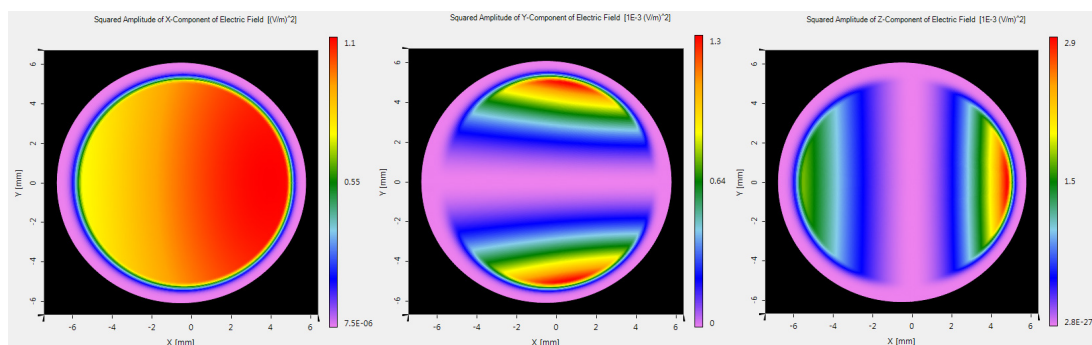


Figure 75: Comparison of the squared amplitude of the E_x , E_y and E_z components of the relayed electromagnetic field for the 40 degree angular tilt of the parabolic mirrors.

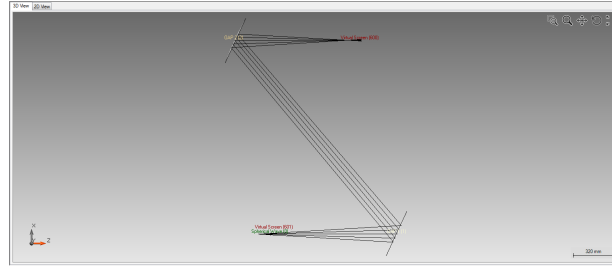


Figure 76: 50 degree “Z” OAPs configuration - Ray Tracing (VirtualLab Fusion).

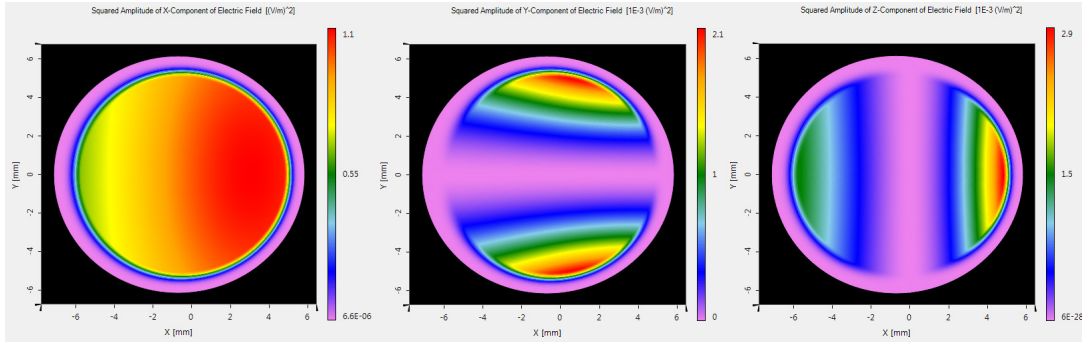


Figure 77: Comparison of the squared amplitude of the E_x , E_y and E_z components of the relayed electromagnetic field for the 50 degree angular tilt of the parabolic mirrors.

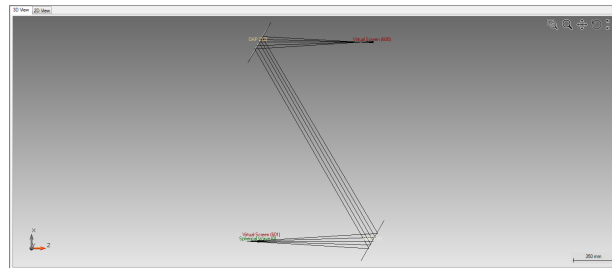


Figure 78: 60 degree “Z” OAPs configuration - Ray Tracing (VirtualLab Fusion).

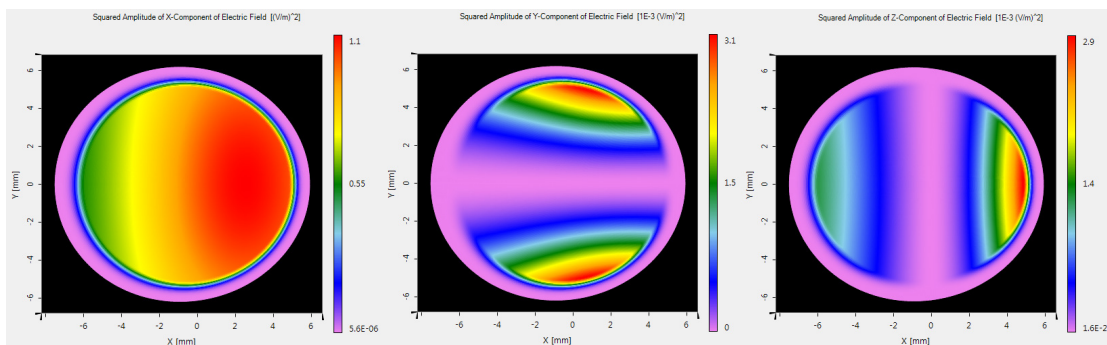


Figure 79: Comparison of the squared amplitude of the E_x , E_y and E_z components of the relayed electromagnetic field for the 60 degree angular tilt of the parabolic mirrors.

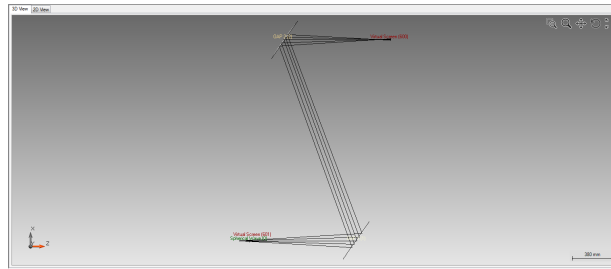


Figure 80: 70 degree “Z” OAPs configuration - Ray Tracing (VirtualLab Fusion).

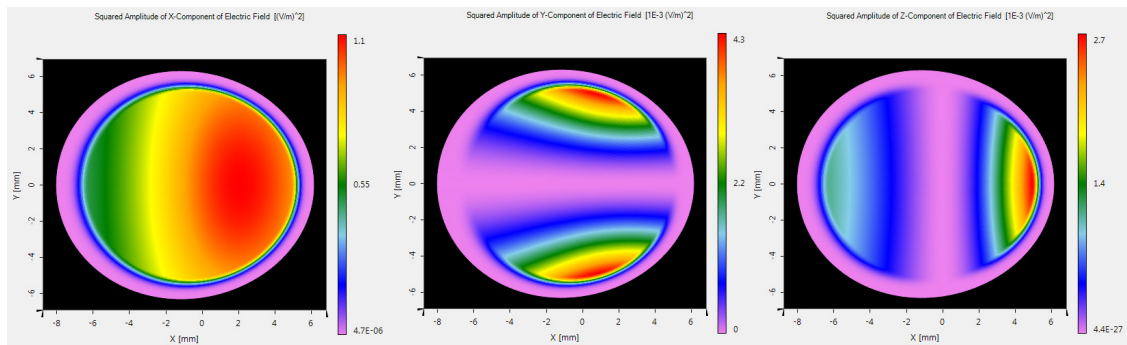


Figure 81: Comparison of the squared amplitude of the E_x , E_y and E_z components of the relayed electromagnetic field for the 70 degree angular tilt of the parabolic mirrors.

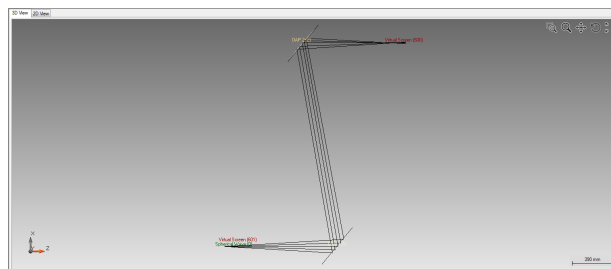


Figure 82: 80 degree “Z” OAPs configuration - Ray Tracing (VirtualLab Fusion).

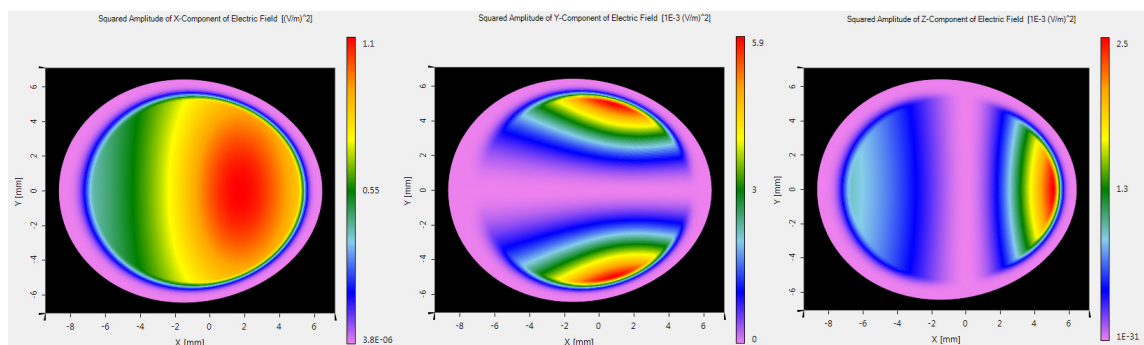


Figure 83: Comparison of the squared amplitude of the E_x , E_y and E_z components of the relayed electromagnetic field for the 80 degree angular tilt of the parabolic mirrors.

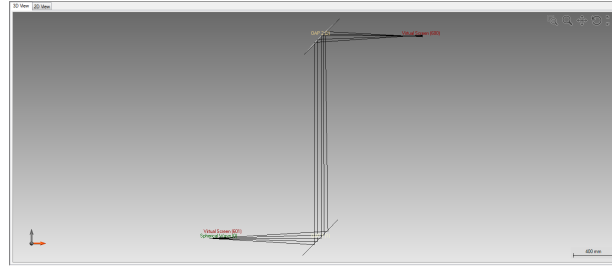


Figure 84: 90 degree “Z” OAPs configuration - Ray Tracing (VirtualLab Fusion).

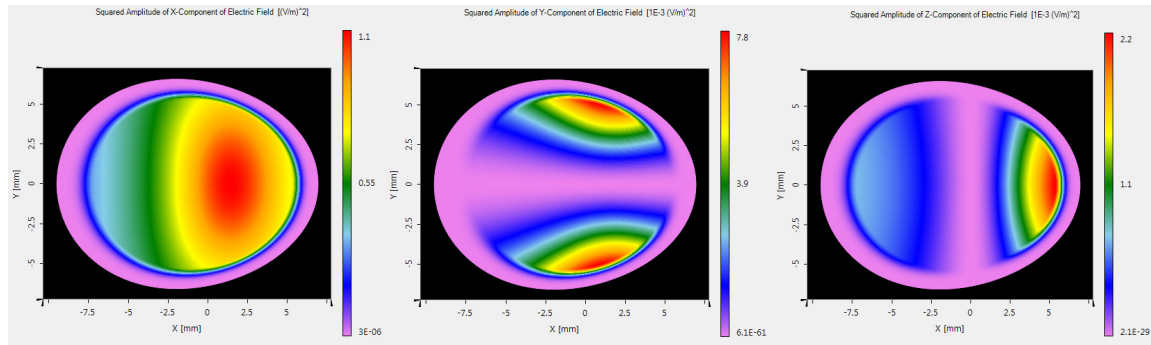


Figure 85: Comparison of the squared amplitude of the E_x , E_y and E_z components of the relayed electromagnetic field for the 90 degree angular tilt of the parabolic mirrors.

This conclusion demonstrates that the relay system with 90 degree off-axis angles actually does not do exact image relaying. If image relaying is required, the off-axis angle should be as small as possible. For example the already demonstrated 5 degrees.

8.5.2 Catoptric Reducers

Some reducer systems were already discussed in 8.4.2. However, for the main beam-line, only the reducers with reflective elements are feasible due to the laser induced damage threshold and GVD. Again, two basic system geometries are available for comparison, one with and one without the intermediate focal plane. These are equivalent to the aforementioned Keplerian and Galilean systems, but with the mirrors only.

The L3 laser parameters are extraordinary (see Table 19). Therefore, the laser induced damaged threshold needs to be briefly discussed.

Table 19: L3 source beam parameters.

Parameter	Value
FWHM	214 mm
$1/e^2$	225.6 mm
$1/e$	220
Order	20
Total Energy	30 J
Power	$1.5 \cdot 10^{15}$ W
Peak fluence	65 mJ

For our purposes it is assumed that the 1000 mJ/cm^2 is the fluence limit that a mirror can withstand without being damaged. There is a relation between the focal length, position and the fluence, as illustrated in Fig. 86 [73]. Any fluence in the figure that exceeds the 1000 mJ/cm^2 is set to 1000 mJ/cm^2 for illustration purposes. Thereby illustrating the “no-go zone”. The figure is related to the optical systems with a 45° incidence angle and to the ELI relay telescopes. That means 1:1 magnification ratio. In this paragraph a slightly different scenario is shown. However, the LIDT needs to be kept in mind as well. Here, the situation of incidence angles up to 5° are analyzed. The magnification ratio of the reducers described 2:1. The fluence on the secondary mirror of the reducers will not exceed 300 mJ/cm^2 . Nevertheless, it may be problematic to acquire large magnification ratios because of the excess fluence levels.

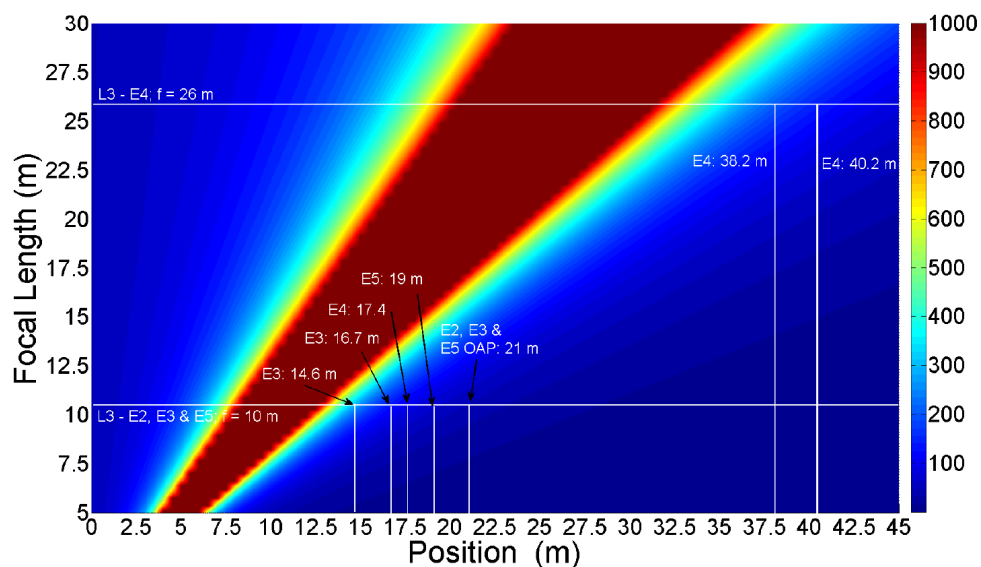


Figure 86: Provides the fluence (z -axis) as a function of position (x -axis) and focal length (y -axis) in the telescope for the L3 beam L3-E2, E3, E5 $\Rightarrow f = 10.5$ and for L3-E4 $\Rightarrow f = 26$. The positions of the mirrors are indicated. Calculation is performed for an incidence angle of 45 degrees to simulate impact on the mirrors [76].

Catoptric Reducers with an Intermediate Focal Plane

In the first case a reducer with an intermediate focal plane is analysed. The reducer contains two positive mirrors with a common focal plane as seen in Fig. 87 from Zemax OpticStudio. The first parabolic mirror has a focal length of 20 meters, whereas the second parabola has a focal length equal to 10 meters, thus reducing the beam size by half.

First the spot sizes are analyzed (see Fig. 88). Due to the use of this pair of parabolas, there are absolutely no aberrations in the focal plane. Fig. 89 depicts the amount of longitudinal aberration. This is mainly affected by the input field angle, which will be close to zero in the case described. Seidel coefficients clearly show how to compensate for the coma and the astigmatism of both mirrors (see Fig. 90). The residual aberrations are field curvature and distortion. In Table 20 there is a comparison of wavefront errors for the ray bundles near the axis. Due to the use of parabolas the performance observed is extremely good.

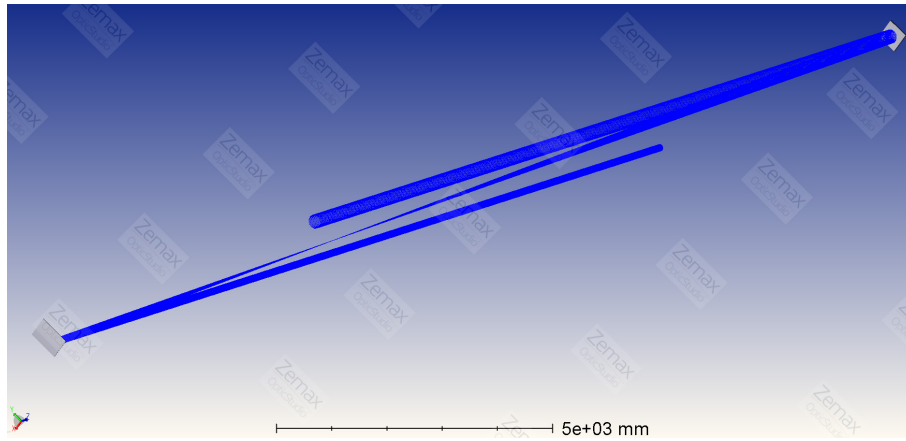


Figure 87: Ray-tracing of the reducer.

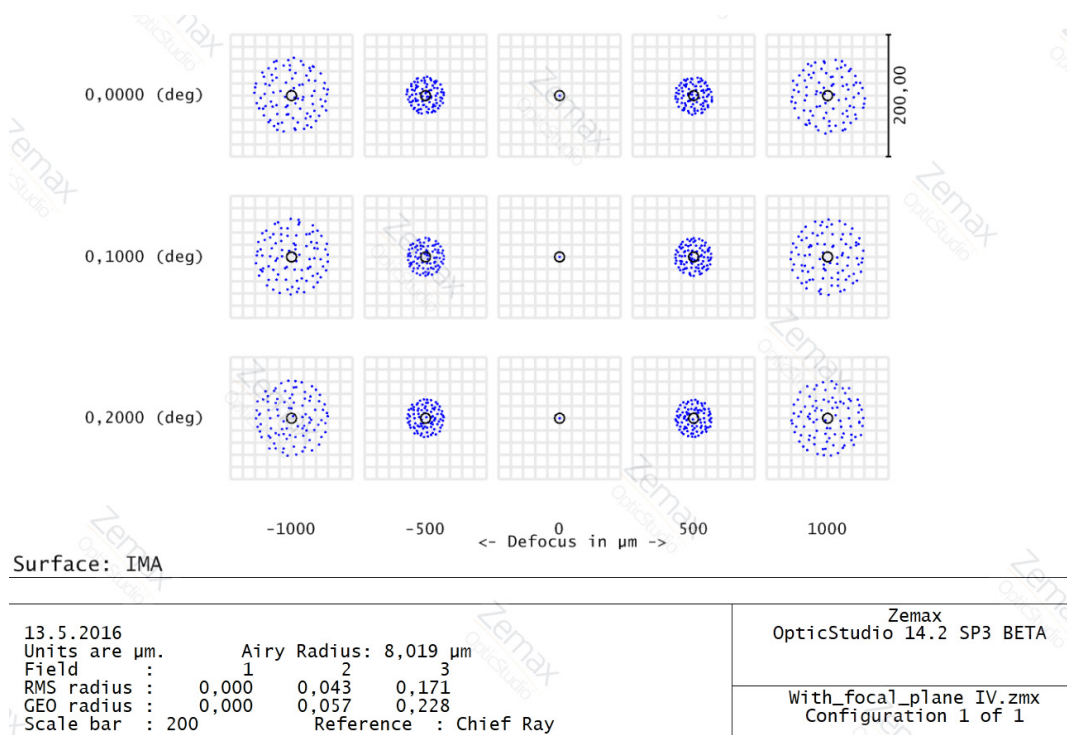


Figure 88: Spot diagrams of the reducer.

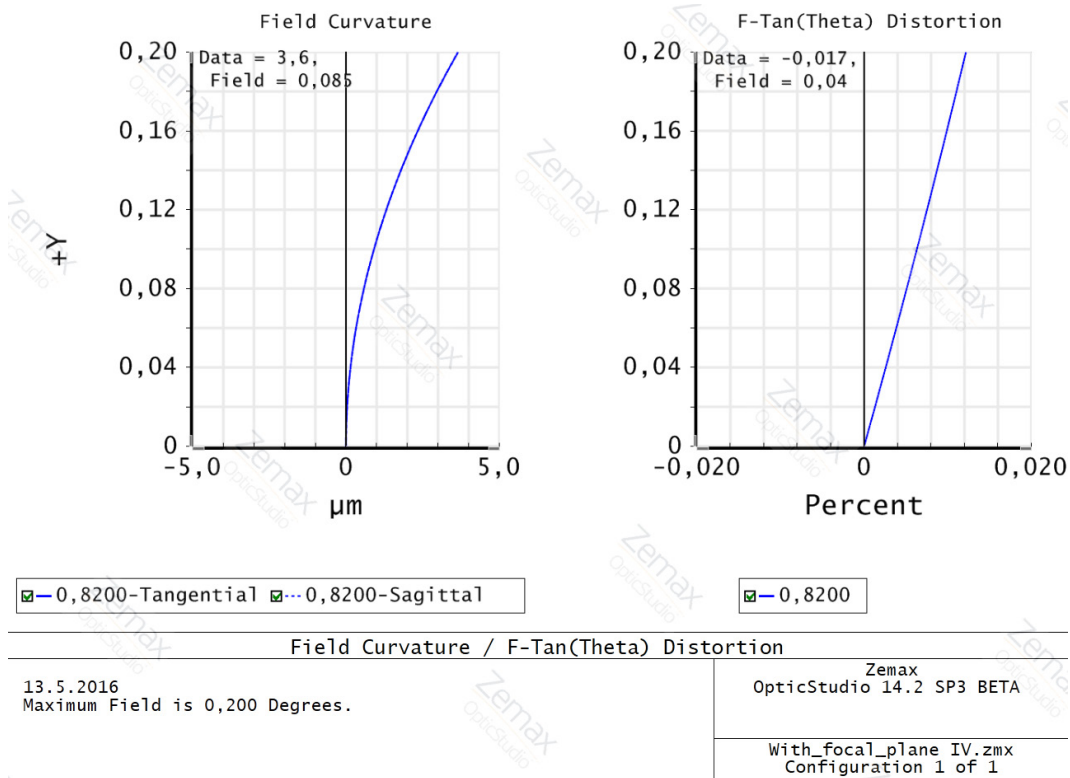


Figure 89: Longitudinal aberration of the reducer.

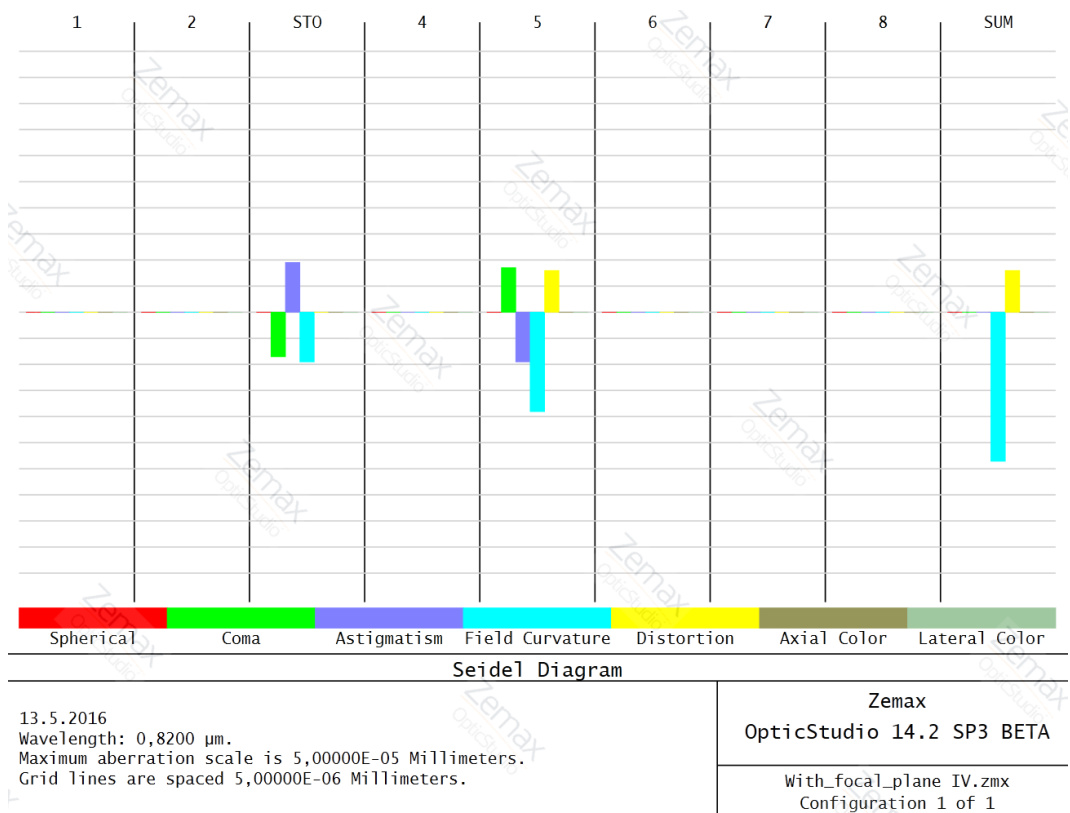
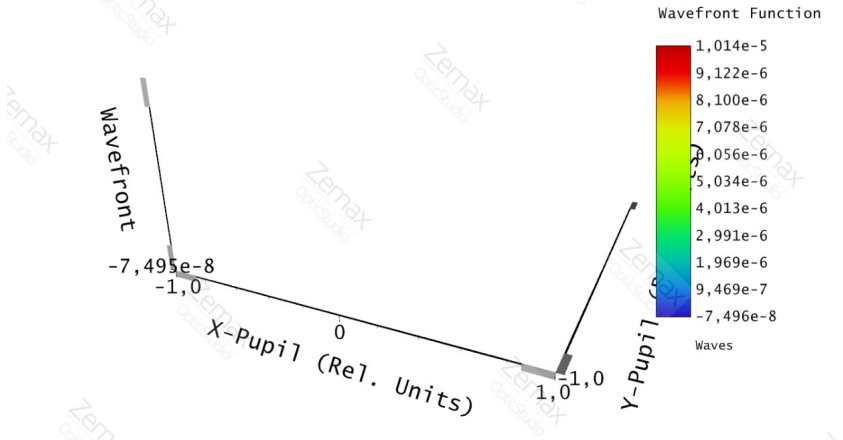
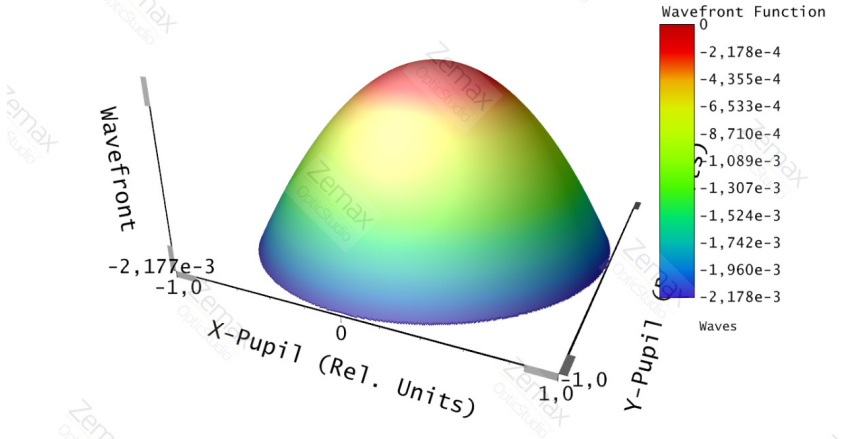
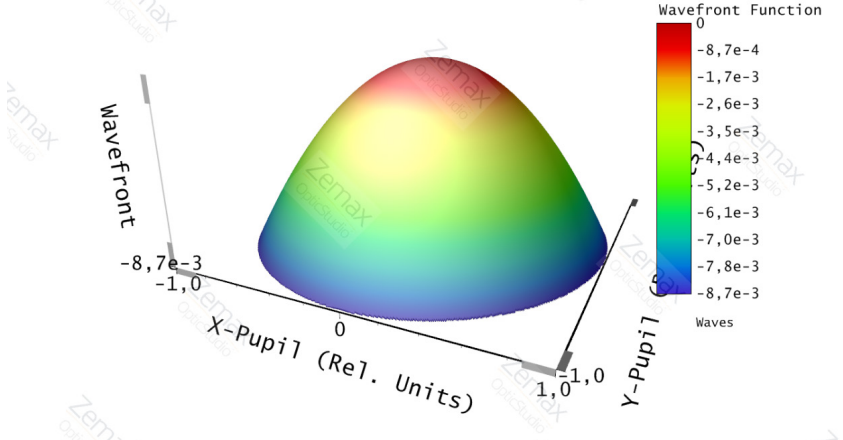


Figure 90: Seidel coefficients of the reducer.

Table 20: Reducer's wavefront maps for various field angles.

Field Angle	Wavefront Map
0°	 <p data-bbox="518 750 1364 795">Wavefront Function</p> <p data-bbox="518 795 1364 873">13.5.2016 0,8200 μm at 0,0000 (deg) Peak to valley = 0,0000 waves, RMS = 0,0000 waves. Surface: Image Exit Pupil Diameter: 2,5023E+01 Millimeters</p> <p data-bbox="1117 772 1364 873">Zemax OpticStudio 14.2 SP3 BETA With_focal_plane IV.zmx Configuration 1 of 1</p>
0.1°	 <p data-bbox="518 1339 1364 1384">Wavefront Function</p> <p data-bbox="518 1384 1364 1462">13.5.2016 0,8200 μm at 0,1000 (deg) Peak to valley = 0,0022 waves, RMS = 0,0006 waves. Surface: Image Exit Pupil Diameter: 2,5023E+01 Millimeters</p> <p data-bbox="1117 1361 1364 1462">Zemax OpticStudio 14.2 SP3 BETA With_focal_plane IV.zmx Configuration 1 of 1</p>
0.2°	 <p data-bbox="518 1928 1364 1973">Wavefront Function</p> <p data-bbox="518 1973 1364 2051">13.5.2016 0,8200 μm at 0,2000 (deg) Peak to valley = 0,0087 waves, RMS = 0,0025 waves. Surface: Image Exit Pupil Diameter: 2,5023E+01 Millimeters</p> <p data-bbox="1117 1951 1364 2051">Zemax OpticStudio 14.2 SP3 BETA With_focal_plane IV.zmx Configuration 1 of 1</p>

To check the reducer's performance with the super-Gaussian beam as the input, VirtualLab Fusion is used. To be sure that the LPD file is prepared correctly, ray-tracing is conducted (see Fig. 91). This simulation is sequential, thus the large size of the element does not obstruct the beam reflected on the preceding mirror.

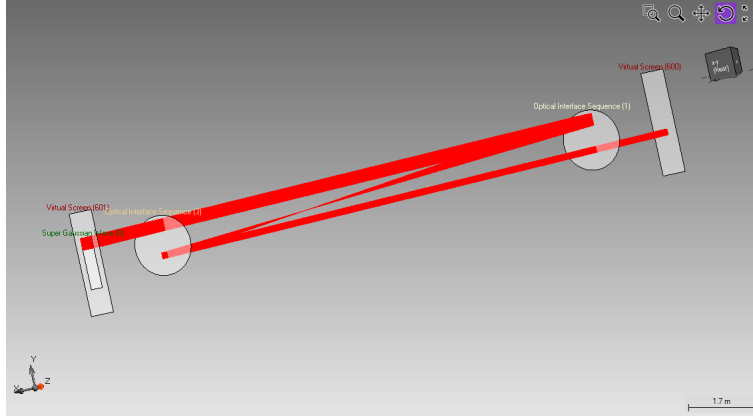


Figure 91: Ray-tracing of the reducer (VirtualLab Fusion).

There are two possible ways to demonstrate the reducers capability to correctly demagnify the input beam. The user can use both Classic Field Tracing (to include diffraction or temporal effects) or the new Geometric Field Tracing Plus (Beta). If only the monochromatic input beam is used and the output beam is observed far from the focus, the results should be similar. Fig. 92 illustrates the input and output super-Gaussian beams, respectively. The input beam radius in the direction of both axes is 120 mm. The resulting output beam radius for both axes is equal to 62 mm, hence fulfilling the initial requirement for the magnification ratio of the reducer.

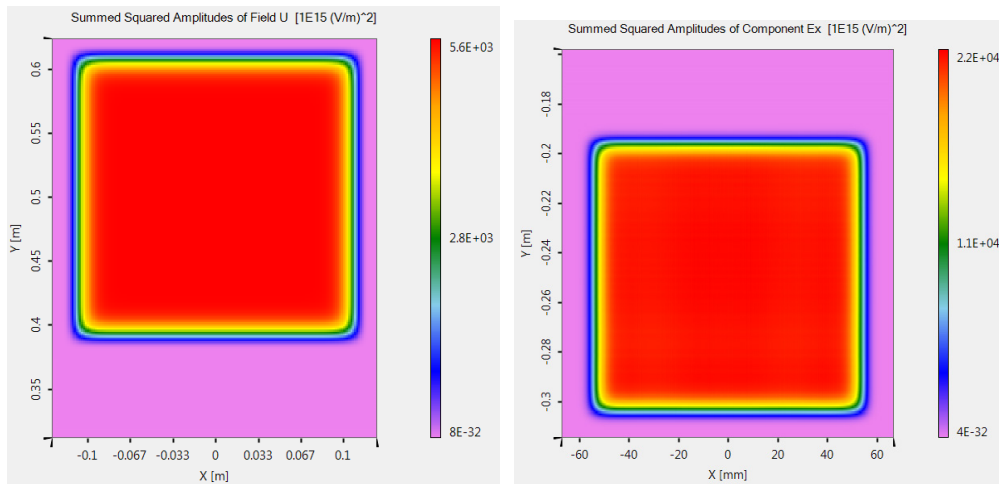


Figure 92: Input (left) and output beam (right) as calculated by Classic Field Tracing.

If there is no requirement to include diffraction as well, the use of the novel simulation technique called Geometric Field Tracing Plus (Beta) is possible. Fig. 93

shows the results acquired by this technique. Comparing Fig. 92 and Fig. 93 the reader can see that the results are similar in both size and in the value of squared amplitudes.

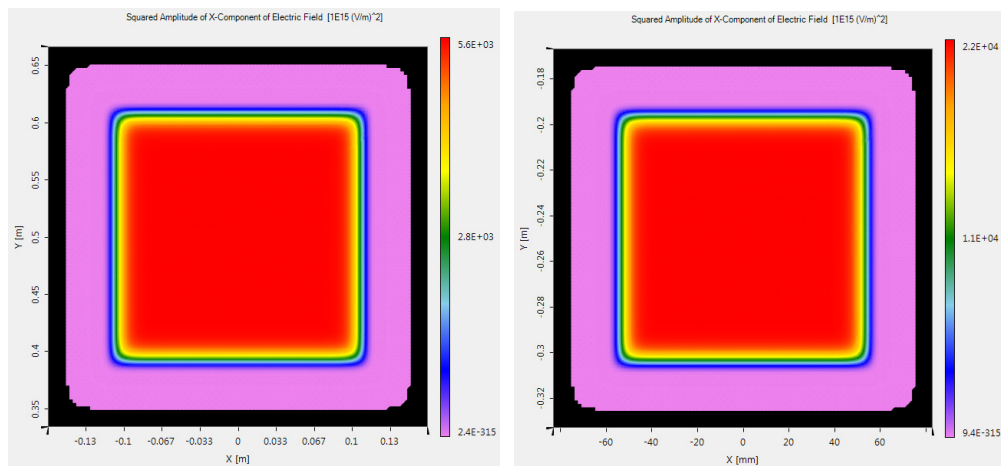


Figure 93: Input (left) and output beam (right) as calculated by Geometric Field Tracing Plus (Beta).

Catoptric Reducers without an Intermediate Focal Plane

In the current case, a reducer without an intermediate focal plane is analysed. The reducer contains one positive and one negative mirror. The focal length of the first concave mirror is 20 meters, whereas the second convex mirror has a focal length equal to -10 meters. The focal length of the first parabolic mirror has the same focal length as the first parabolic mirror in the previously described case. This makes the comparison of these two systems easier. Ray-tracing of the reducer is shown in Fig. 94.

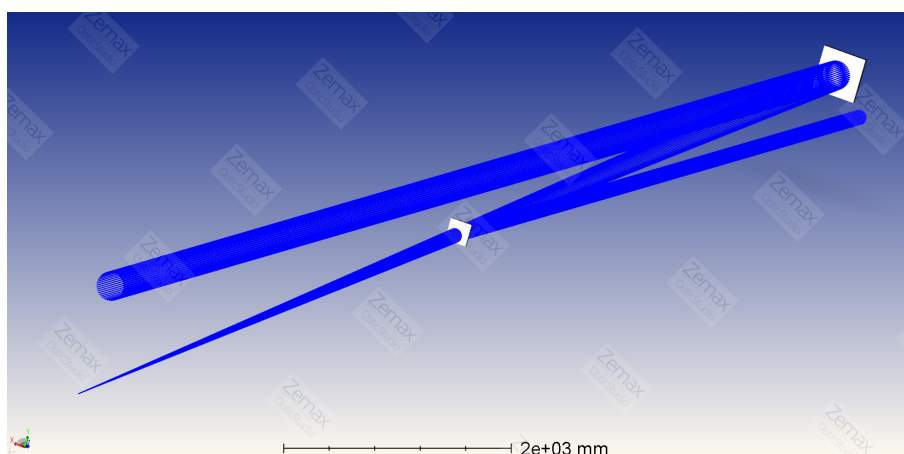


Figure 94: Ray-tracing of the reducer.

Similar to the previous reducer, the spot diagrams are observed first (see Fig. 95). Again, due to the use of a pair of parabolas, the focal spots lack any aberration.

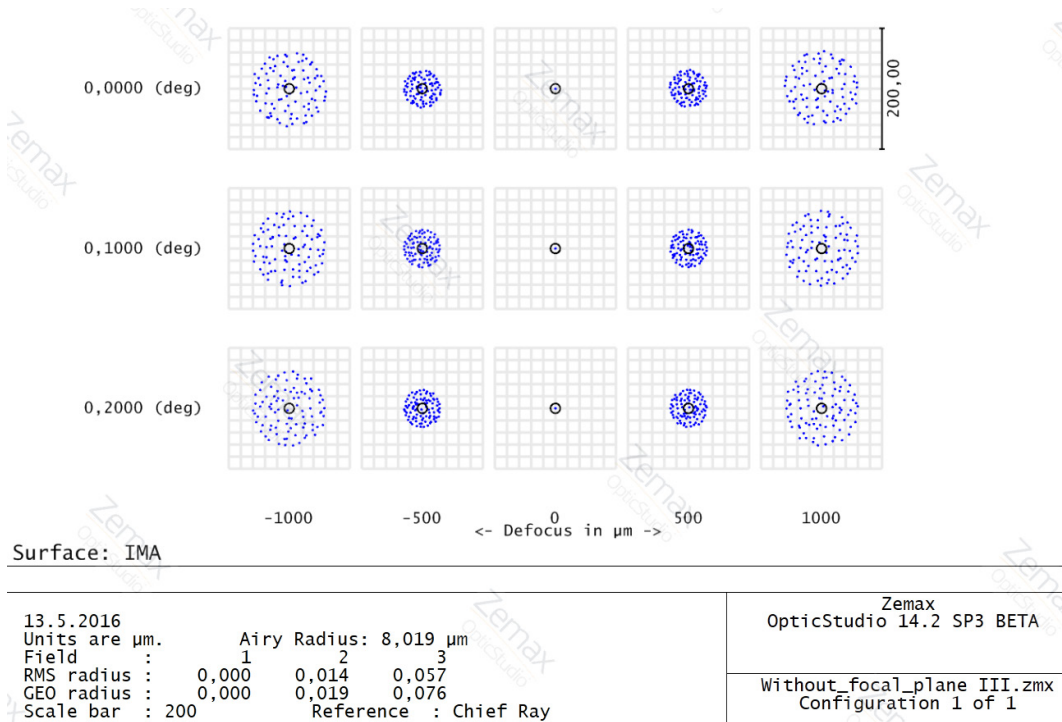


Figure 95: Spot diagrams of the reducer.

Fig. 96 illustrates the amount of longitudinal aberration. Both field curvature and distortion now have opposite values and are at half of the previous magnitude, which is caused by the use of a convex mirror in the reducer. Fig. 97 is showing all aberrations at a glance using the Seidel coefficients. Once again, the coma and the astigmatism are compensated. Also the field curvature is similar to the previous case. The only difference is in distortion, which is half of the previous amount. Table 21 summarizes the wavefront errors of the reducer for three fields, 0° , 0.1° and 0.2° , respectively. The performance is slightly better in comparison to the previous case. However both results are acceptable.

Also, similar to the previous case for this reducer type, a simulation within VirtualLab Fusion is conducted (see Fig. 98). There are input and output fields acquired by Classic Field Tracing and Geometric Field Tracing Plus (Beta) as well (compare Fig. 99 and Fig. 100).

Summary

Both reducer types perform very well based on the optical simulations conducted. The main reason to prefer one over the other depends on whether the intermediate focal plane (or re-imaging of the field) is needed. The main drivers are spatial filtering and ease of alignment. These two elements support the preference to use a reducer with an intermediate focal plane. Conversely, if the total length of the system is most important, then the reducer without the intermediate focal plane is more convenient.

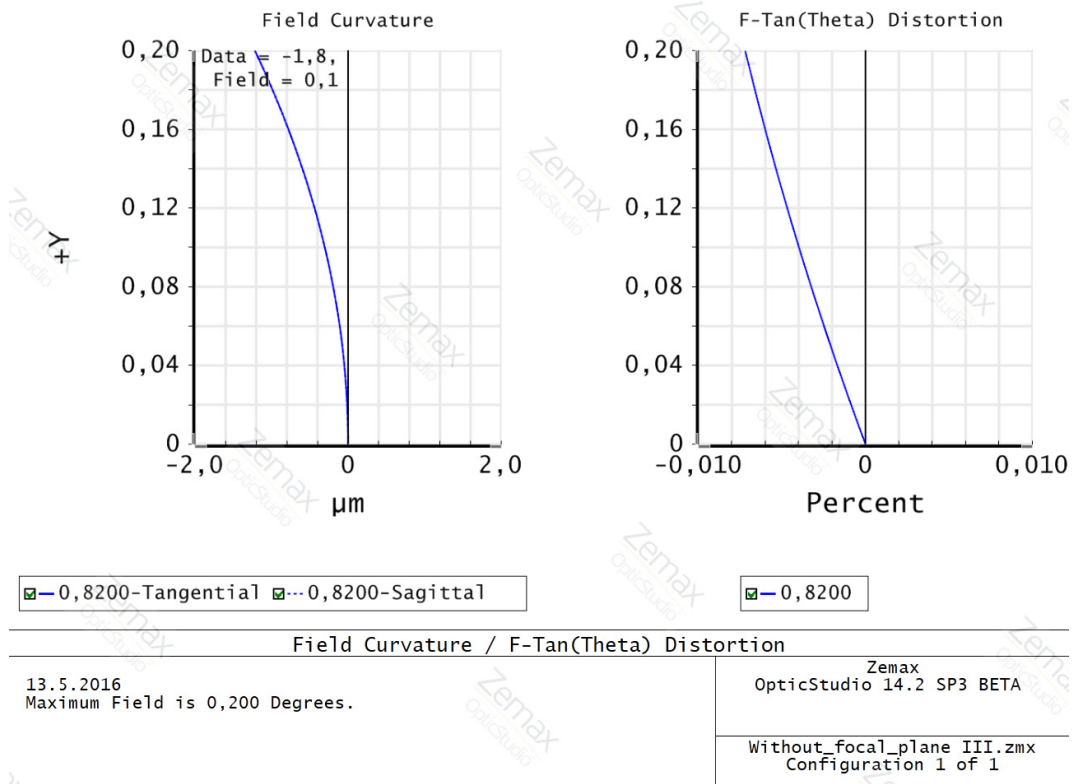


Figure 96: Longitudinal aberration of the reducer.

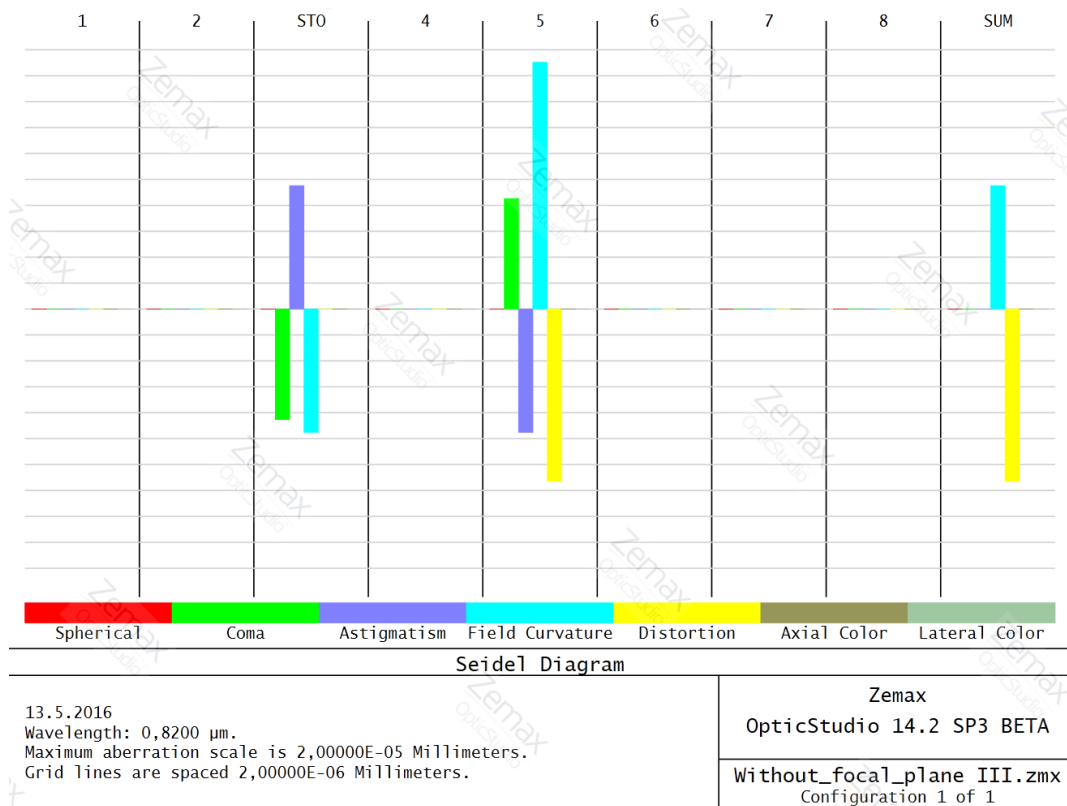


Figure 97: Seidel coefficients of the reducer.

Table 21: Reducer's wavefront maps for various field angles.

Field Angle	Wavefront Map
0°	
0.1°	
0.2°	

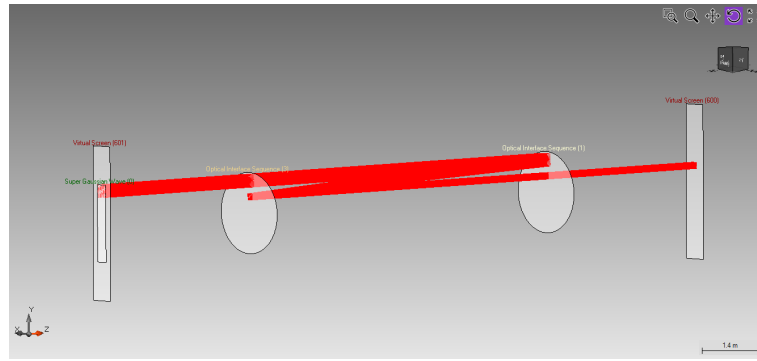


Figure 98: Ray-tracing of the reducer (VirtualLab Fusion).

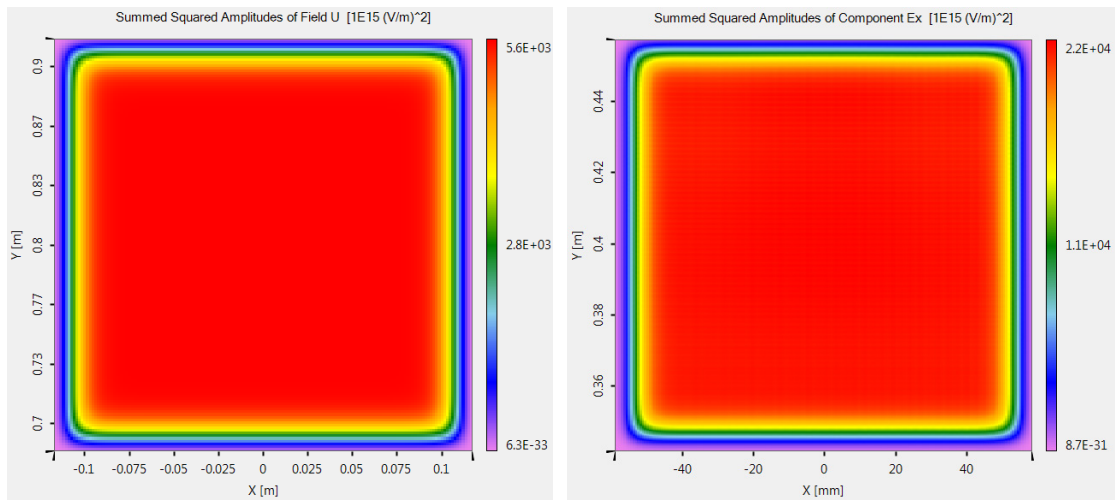


Figure 99: Input and output beam as calculated by Classic Field Tracing.

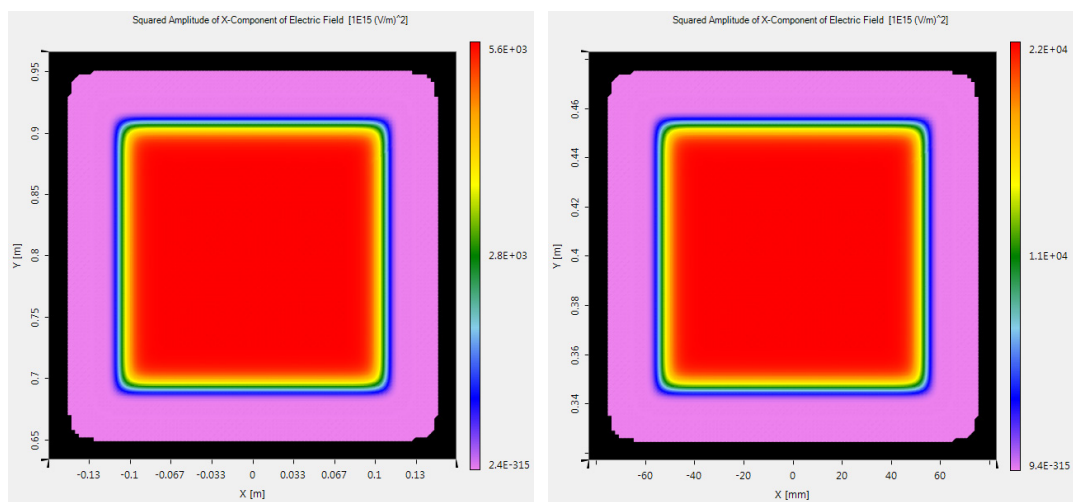


Figure 100: Input and output beam as calculated by Geometric Field Tracing Plus (Beta).

8.5.3 Telescopes for Beam Diagnostics

In the subchapter 8.4.2 transmissive reducers were discussed. A similar system is described in the current subchapter, with one main difference: telescopes for beam diagnostics (or beam monitoring) also contain a mirror. These systems are intended to be placed behind so-called leak mirrors. The main task of these telescopes is to reduce the beam size so it can be imaged on the CCD of a conventional Shack-Hartmann sensor made by Thorlabs [74] (see Fig. 101). The motivation for this system is to diagnose the beams' temporal and spatial properties across each beamline. However, there are some obstacles to achieving this goal. First of all, the power typically exceeds the damage threshold of most available diagnostic systems, and secondly the beam size is too big to be imaged on the majority of sensors. The combination of a leak mirror and the beam diagnostic telescope solves both problems. Behind the leak mirror only a fraction of the power is transmitted, then the beam can be reduced by the combination of reflective and transmissive elements to the desired size in order to match the sensor's dimensions. This system is commonly referred to as a telescope for beam diagnostics.



Figure 101: Shack-Hartmann sensor made by Thorlabs [77].

The inspiration for the telescope described in this dissertation comes from an achromatic beam diagnostic telescope for Astra Gemini [78] (Central Laser Facility, STFC Rutherford Appleton Laboratory).

The idea is to prepare a similar optical system out of commercially available components, especially the parabolic mirror, which is the most expensive component in the telescope. Such parabolas can be provided by companies like Edmund Optics Inc. (EO)[79] or Czech Astro Telescope Company (ATC), a. s. [80]. Both companies are capable of providing suitable parabolas with a focal length of 2 m and precision of $\lambda/8$. The current²⁰ price of EO's parabola is 7450 USD, whereas ATC's parabola costs 85 000 CZK (approximately 3500 USD).

Another important part of the system is a proper negative achromatic doublet working in the NIR part of the spectrum. Corresponding optical elements working

²⁰As of April 2016.

within the bandwidth of 650–1050 nm can be found in the catalogue of the Thorlabs company [81]. Suitable doublets include:

- ACN127-020-B with a -22.5 mm focal length and thus producing about hundred times demagnification and
- ACN127-025-B with a -27.7 mm focal length which produces about eighty times demagnification.

Both doublets are cost around 50 EUR, which makes them much cheaper than the parabolic mirror. Hence the design does not necessarily need to use the Thorlabs' doublets. However, they can be used to model the initial optical design used for further optimization in Zemax OpticStudio.

Based on the information presented above, the beam diagnostic telescope will look like the one presented in Fig. 102. The design is comprised of a parabolic mirror, a beam splitter and a doublet.

On the following pages there is a comparison of the telescopes' performance with the commercial only components and with the custom doublet. Customization of the mirror is not considered for fiscal reasons.

Of course, customization of the doublet will greatly increase the telescope performance. Furthermore, optimization of the doublet is much cheaper than optimization of the mirror. The first, most simple comparison is to compare the Seidel aberration coefficients drawn as bars. Fig. 103 compares the original telescope with commercial only components and a telescope with a customized doublet.

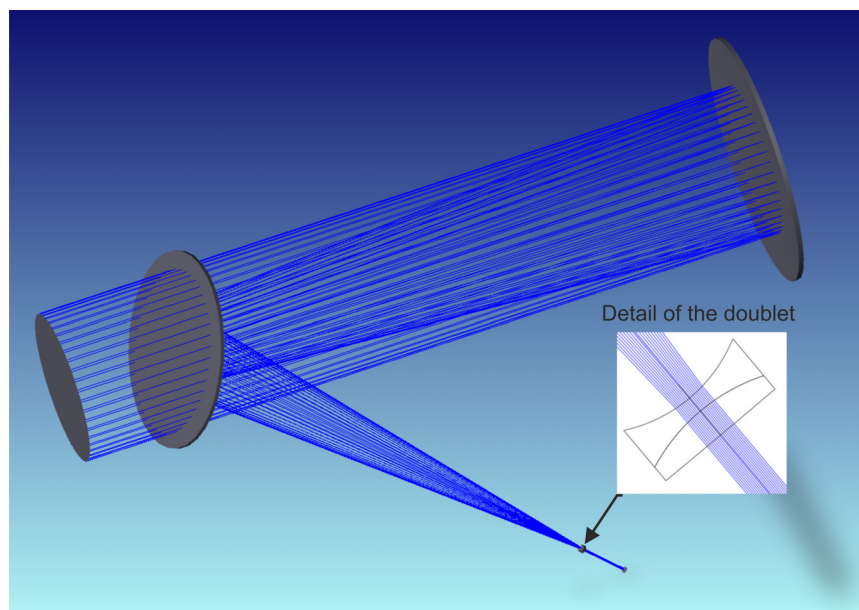


Figure 102: Ray-tracing of beam reducing telescope for diagnostics.

The most prominent aberration in the original configuration is the spherical aberration, followed by coma and astigmatism. Customization leads to major suppression of these aberrations.

The improvement introduced by the custom doublet is illustrated in the improvement of spot diagrams (see Fig. 104) and longitudinal aberration (see Fig. 105). The improvement delivered with the introduction of a custom doublet is clearly visible.

The last analysis uses the comparison of wavefront maps, which is provided in Tables 22 and 23, for a telescope with a commercial and a custom doublet, respectively. By comparing these wavefront maps it can be seen that the commercial doublet is increasing the telescope's performance by at least one order of magnitude.

Similar to the case of reducers for the main beamline, the simulation of super-Gaussian beam demagnification can also be conducted here in VirtualLab Fusion. Ray-tracing of the system is depicted in Fig. 106. As the numerical effort of Classic Field Tracing in this situation is too high, the Geometric Field Tracing Plus (Beta) technique can still be used without any problem (see Fig. 107). The size of the beam can clearly fit the size of the CCD sensor of Shack-Hartmann made by Thorlabs. The reader will notice exceedingly high values of the squared amplitude of the x -component of the electric field. However, these are the values corresponding to the main beamline. Behind the leak mirror there will be only a fraction of the beam's initial power, thus avoiding destruction of the Shack-Hartmann sensor in use.

Based on the results it is concluded that such beam diagnostic telescopes are feasible and easily optimized with the introduction of customized negative achromatic doublets, which are still reasonable from the fiscal point of view.

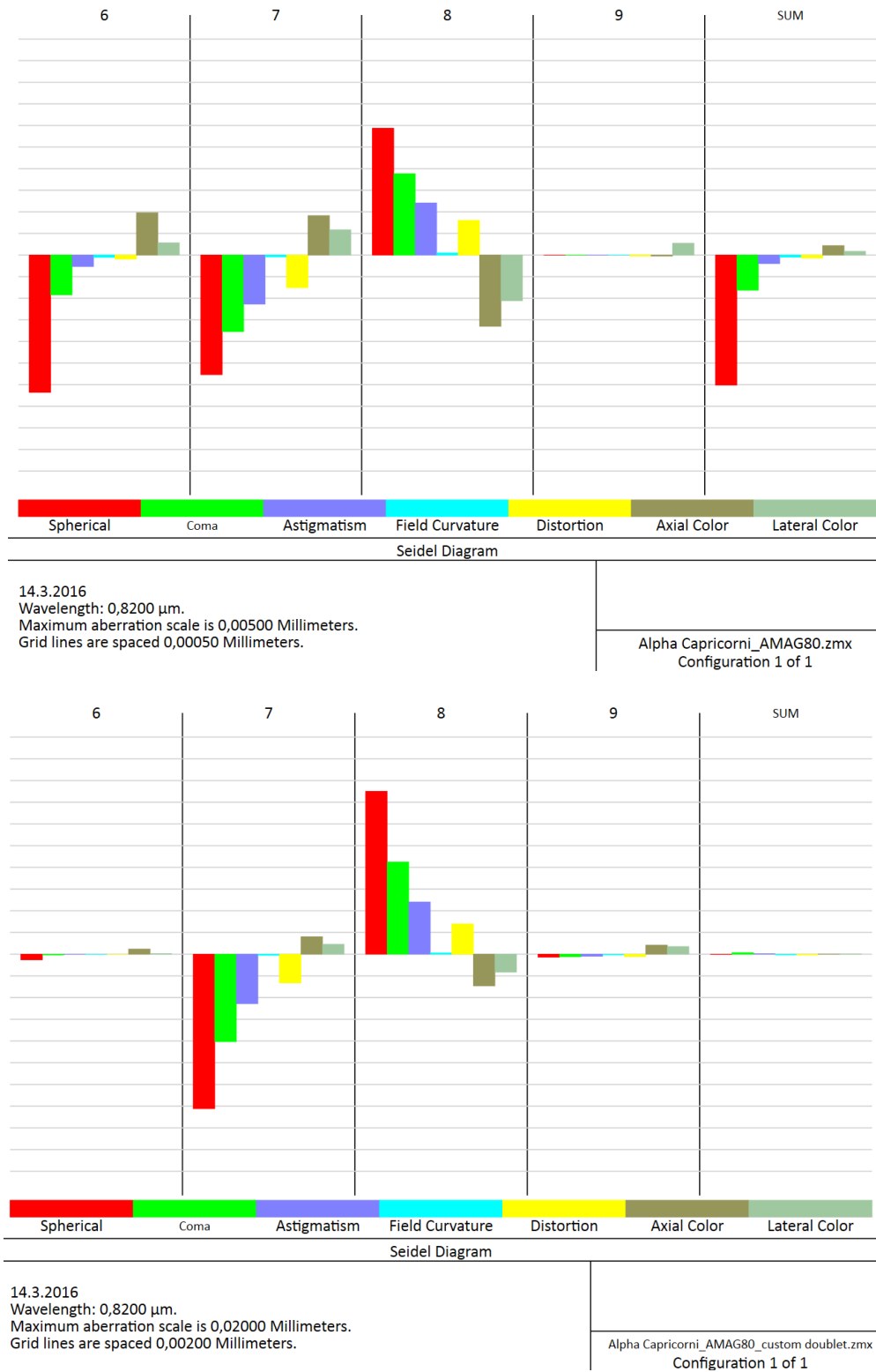


Figure 103: Seidel aberration comparison of a telescope with commercial (upper) and custom (lower) doublets.

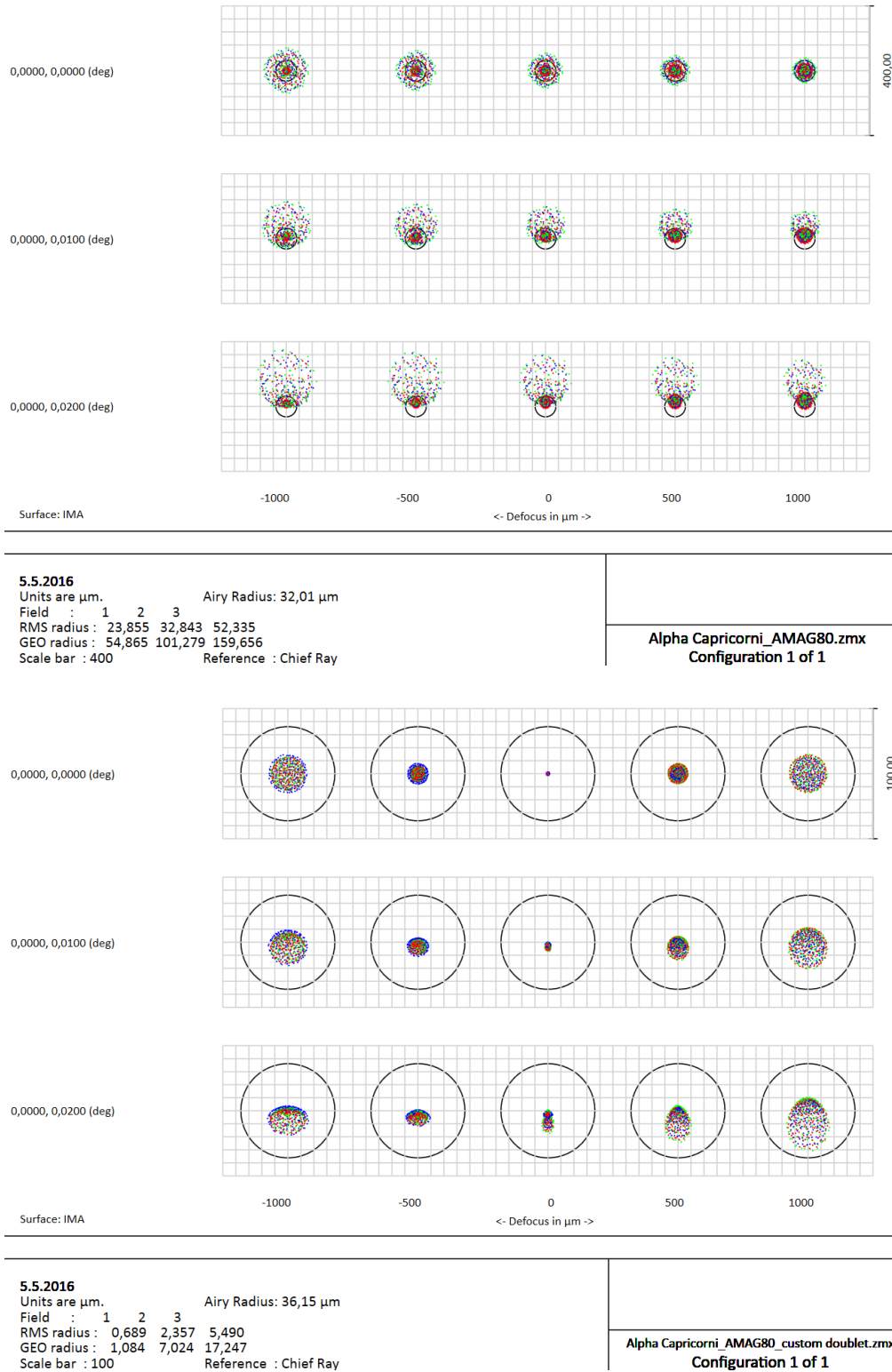


Figure 104: Spot diagram comparison of a telescope with commercial (upper) and custom (lower) doublets.

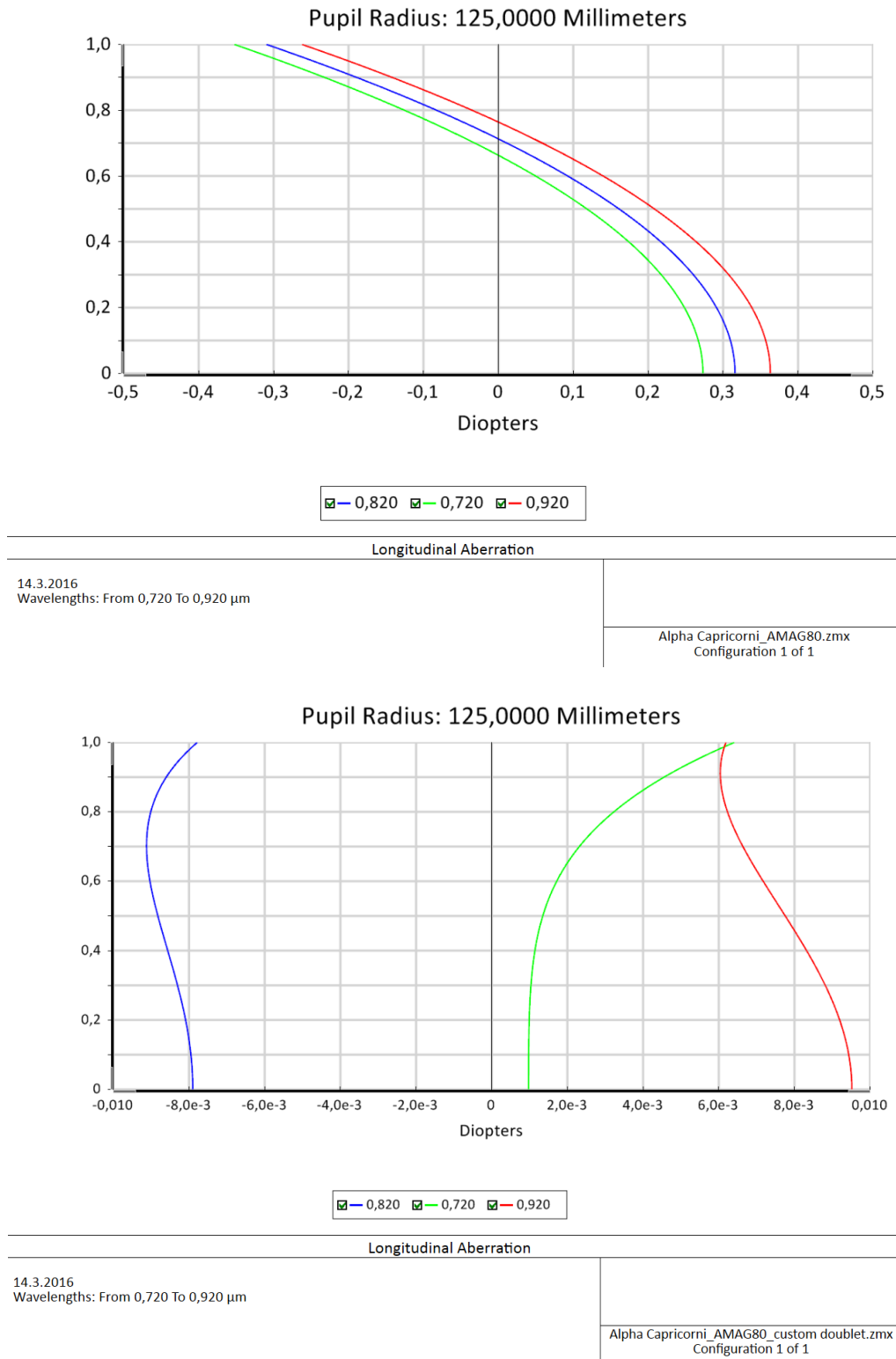


Figure 105: Longitudinal aberration comparison of a telescope with commercial (upper) and custom (lower) doublets.

Table 22: Reducer's (with a commercially available doublet) wavefront maps for wavelengths within the desired pulse bandwidth.

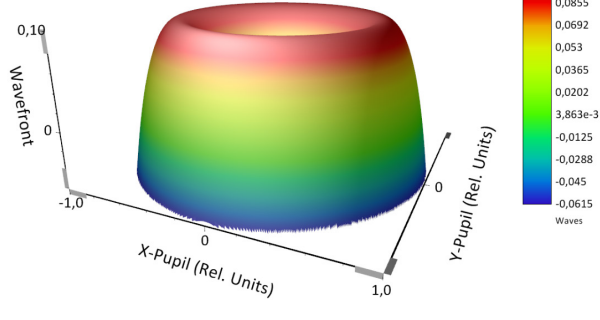
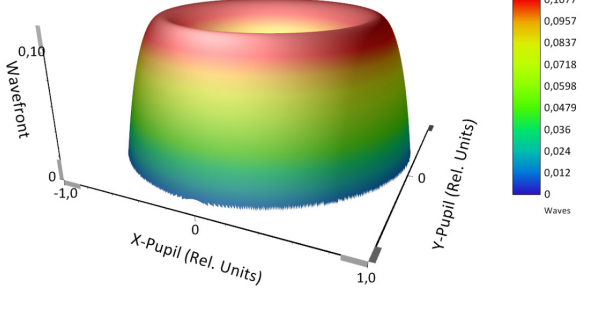
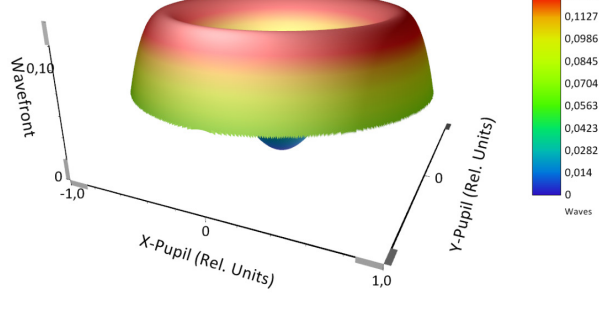
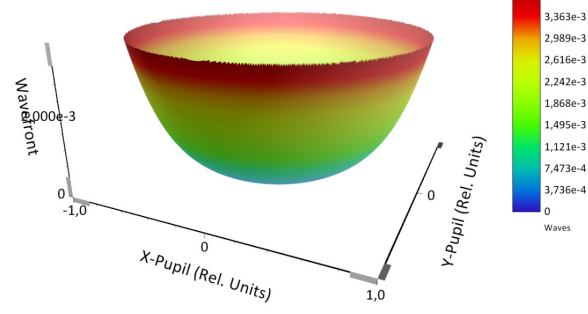
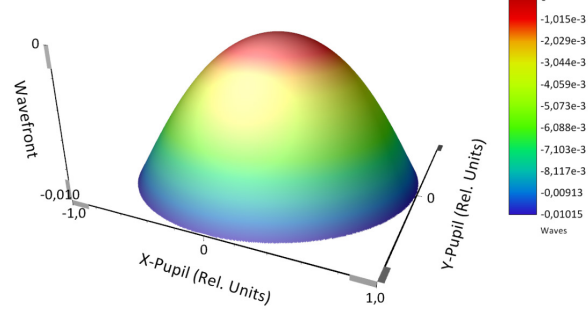
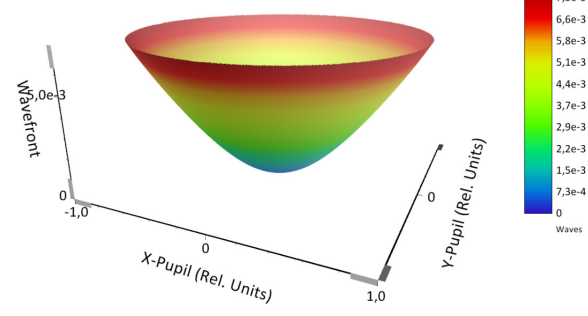
Wavelength	Wavefront Map
$\lambda = 720 \text{ nm}$	 <p style="text-align: center;">Wavefront Function</p> <p>14.3.2016 0,7200 μm at 0,0000, 0,0000 (deg) Peak to valley = 0,1633 waves, RMS = 0,0429 waves. Surface: Image Exit Pupil Diameter: 3,1312E+000 Millimeters</p> <p style="text-align: right;">Alpha Capricorni_AMAG80.zmx Configuration 1 of 1</p>
$\lambda = 820 \text{ nm}$	 <p style="text-align: center;">Wavefront Function</p> <p>14.3.2016 0,8200 μm at 0,0000, 0,0000 (deg) Peak to valley = 0,1196 waves, RMS = 0,0344 waves. Surface: Image Exit Pupil Diameter: 3,1312E+000 Millimeters</p> <p style="text-align: right;">Alpha Capricorni_AMAG80.zmx Configuration 1 of 1</p>
$\lambda = 920 \text{ nm}$	 <p style="text-align: center;">Wavefront Function</p> <p>14.3.2016 0,9200 μm at 0,0000, 0,0000 (deg) Peak to valley = 0,1408 waves, RMS = 0,0367 waves. Surface: Image Exit Pupil Diameter: 3,1312E+000 Millimeters</p> <p style="text-align: right;">Alpha Capricorni_AMAG80.zmx Configuration 1 of 1</p>

Table 23: Reducer's (with a custom designed doublet) wavefront maps for wavelengths within the desired pulse bandwidth.

Wavelength	Wavefront Map
$\lambda = 720 \text{ nm}$	 <p data-bbox="885 728 997 750">Wavefront Function</p> <p data-bbox="598 750 853 817">14.3.2016 0,7200 μm at 0,0000, 0,0000 (deg) Peak to valley = 0,0037 waves, RMS = 0,0010 waves. Surface: Image Exit Pupil Diameter: 2,7649E+000 Millimeters</p> <p data-bbox="1061 750 1284 817">Alpha Capricorni_AMAG80_custom doublet.zmx Configuration 1 of 1</p>
$\lambda = 820 \text{ nm}$	 <p data-bbox="885 1198 997 1220">Wavefront Function</p> <p data-bbox="598 1220 853 1288">14.3.2016 0,8200 μm at 0,0000, 0,0000 (deg) Peak to valley = 0,0101 waves, RMS = 0,0030 waves. Surface: Image Exit Pupil Diameter: 2,7649E+000 Millimeters</p> <p data-bbox="1061 1220 1284 1288">Alpha Capricorni_AMAG80_custom doublet.zmx Configuration 1 of 1</p>
$\lambda = 920 \text{ nm}$	 <p data-bbox="885 1668 997 1691">Wavefront Function</p> <p data-bbox="598 1691 853 1758">14.3.2016 0,9200 μm at 0,0000, 0,0000 (deg) Peak to valley = 0,0073 waves, RMS = 0,0021 waves. Surface: Image Exit Pupil Diameter: 2,7649E+000 Millimeters</p> <p data-bbox="1061 1691 1284 1758">Alpha Capricorni_AMAG80_custom doublet.zmx Configuration 1 of 1</p>

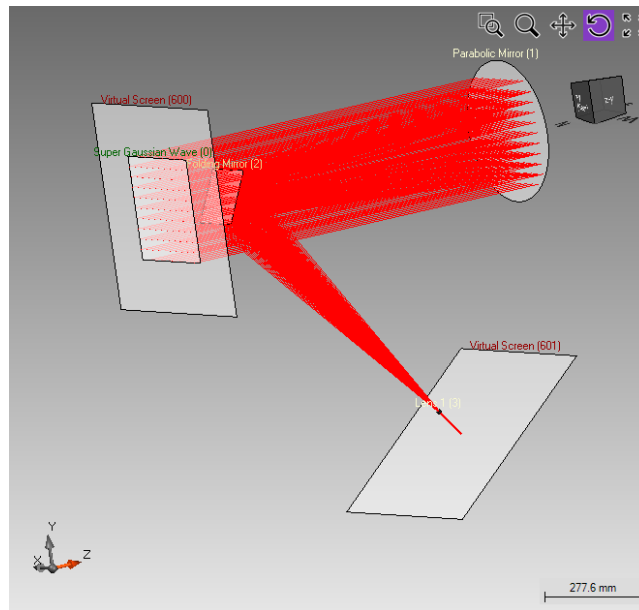


Figure 106: Ray-tracing of the beam reducing telescope for diagnostics (VirtualLab Fusion).

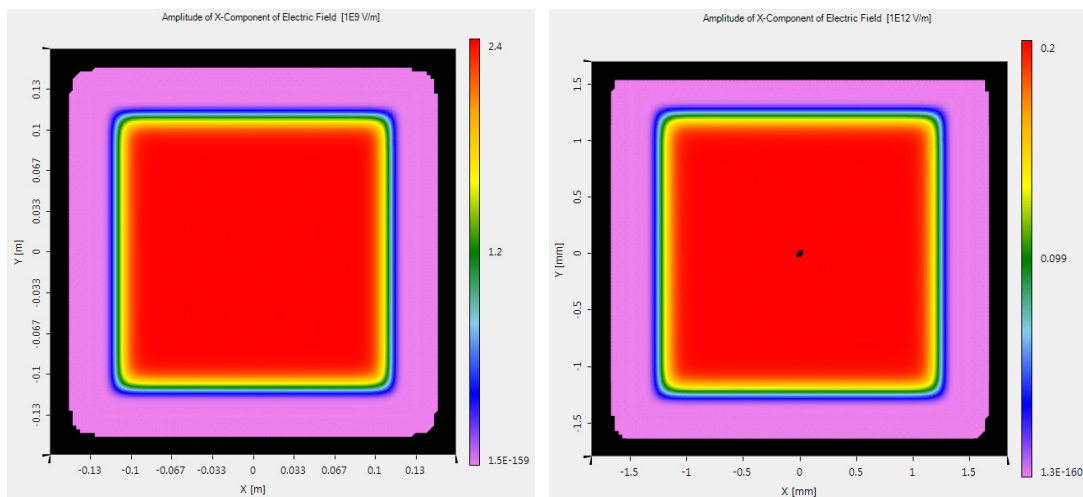


Figure 107: Input and output beam as calculated by Geometric Field Tracing Plus (Beta).

8.6 Beamlines

Unlike the previously written text showing only specific components of beamlines (for example, reducers), in this subchapter simulations of the entire beamlines' systems are described, containing several folding mirrors and final focusing optics. The ELI-Beamlines facility depicted in Fig. 108 contains several laser and experimental halls. Detail of the basement is shown in Fig. 109. One of the main purposes of each beamline is to steer the laser from the source to the target, while maintaining the prescribed requirements on the spatial and temporal quality of the beam.

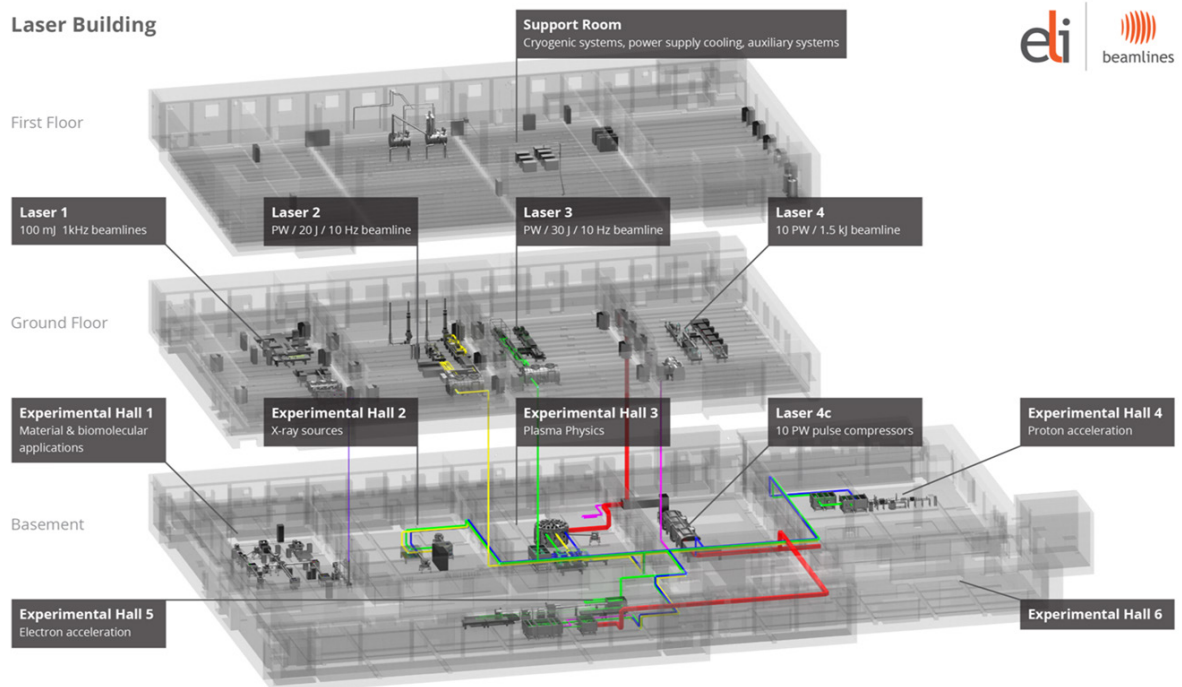


Figure 108: Laser and experimental halls visualization [82].

Among all beamlines within the ELI-Beamlines facility, this thesis focuses primarily on the L1-E1 and the L3-E3 beamlines. Both of these beamlines are subsystems of a larger system of beamlines as can be seen in Figs. 110 and 111, which present the complex L1 and L3 beamlines, respectively.

Analyses in the next few subchapters focuses especially on the tolerancing simulations (in the case of L1-E1) and the beam quality influenced by the hole inside the folding mirror (in the case of L3-E3).

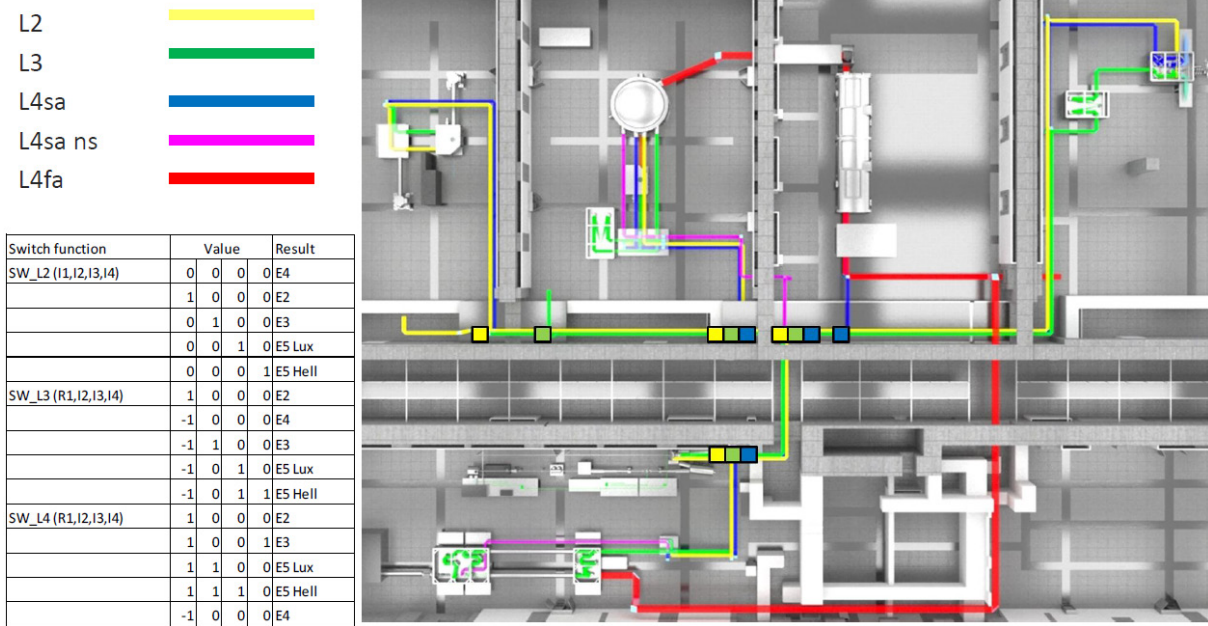


Figure 109: Detailed view of the basement from the previous visualization [83].

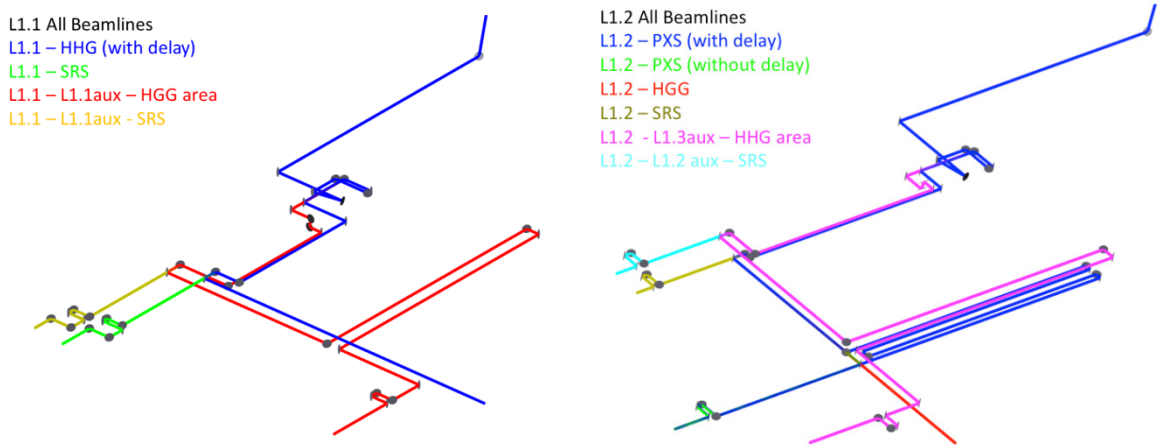


Figure 110: L1 Beamlines (in collaboration with Gashaw Melesse Fente MSc., Ing. Haris Zulic, Dr. Anita Thakur, Dr. Michael Morrissey and Dr. Danila Khikhlukha).

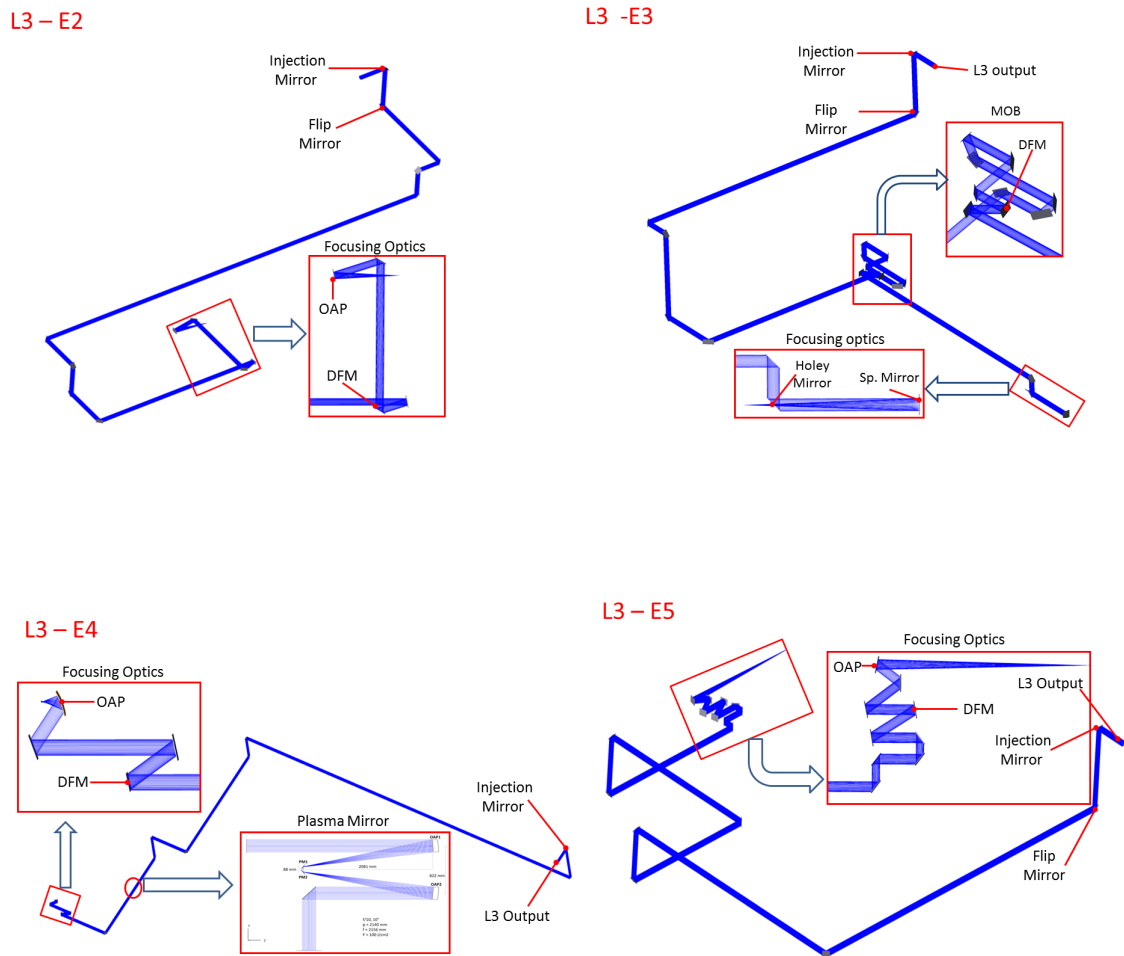


Figure 111: Four specific parts of the L3 Beamlines (in collaboration with Gashaw Melesse Fente MSc., Ing. Haris Zulic, Dr. Anita Thakur, Dr. Michael Morrissey and Dr. Danila Khikhlukha).

8.6.1 L1-E1

The reason for the following analysis is to demonstrate VirtualLab Fusion's capability to go beyond the classical tolerancing process that is usually conducted within the common ray-tracing software bundles like Zemax OpticStudio. Analysis with the use of ray-tracing has been conducted by other colleagues within the BPM team.

As usual, first the LPD of the L1-E1 (see the chamber visualization in Fig. 112) is built-up, so the ray-tracing can be conducted (see Fig. 113).

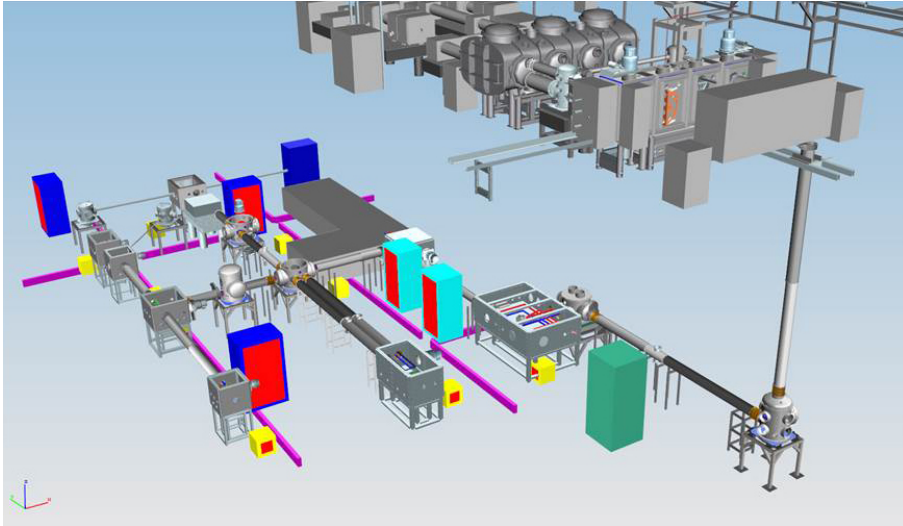


Figure 112: L1-E1 chamber visualization [82].

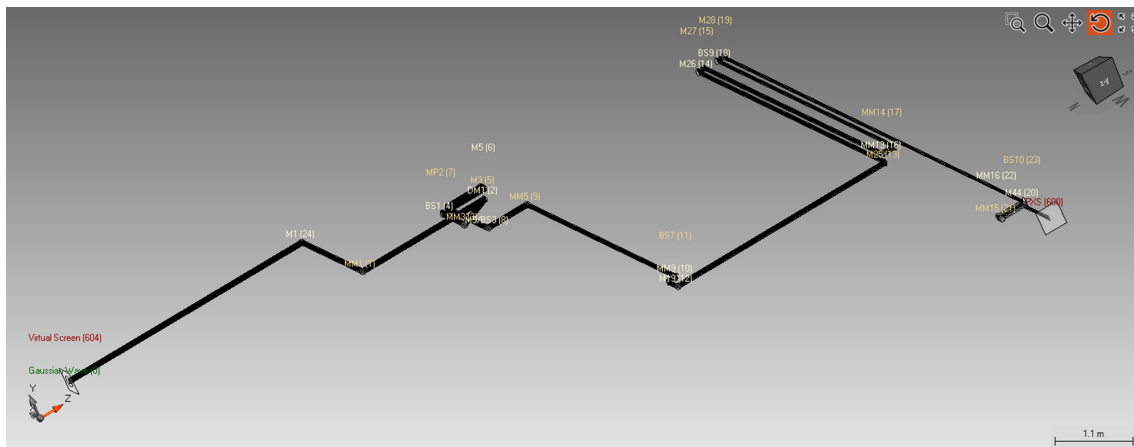


Figure 113: L1-E1 ray-tracing (VirtualLab Fusion).

Three specific tolerancing procedures are conducted:

- Investigation of the beam clipping by a mirror for various beam diameters
- Beam decentering
- Single mirror tilt

Note, that the L1-E1 incorporates a Gaussian, rather than a super-Gaussian beam.

Beam Clipping

Beam clipping was already discussed in 8.2, but only for the case of a single optical component and from the percentage of power loss point of view. In the current case, the beam transported by the entire L1-E1 beamline is directly observed. There are three Gaussian beam sizes that are tested – 25, 50 and 75 mm. The Unified Field

Tracing method within VirtualLab Fusion is used in order to examine diffraction effects as well.

From Fig. 114 the reader can see that only a 25 mm Gaussian beam is transferred by the L1-E1 system, without any clipping or edge diffraction effects.

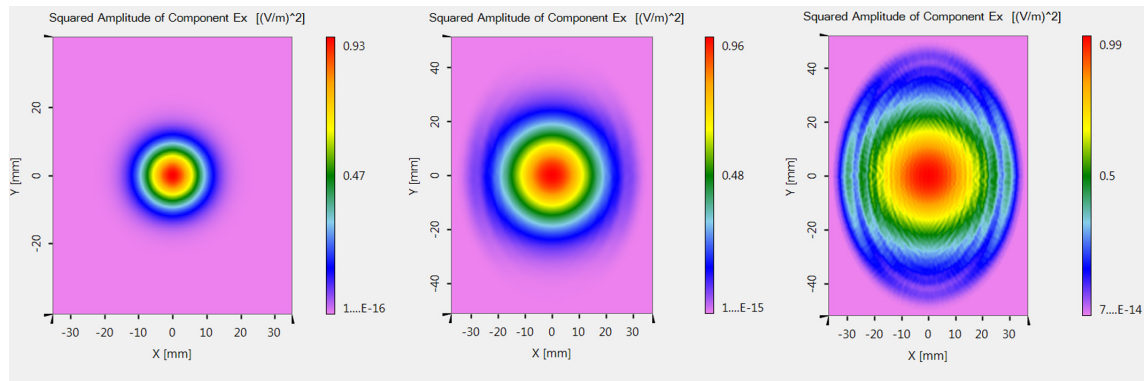


Figure 114: Beam clipping by a circular mirror with a 101.6 mm diameter. Beam diameters from left: 25, 50 and 75 mm, respectively.

Beam Decentering

Another tolerancing procedure is to observe the effects of beam decentering on the resulting beam. For that purpose three values of decentration were chosen – 5, 10 and 20 mm. Fig. 115 illustrates that even the smallest decentering will cause observable edge diffraction effects.

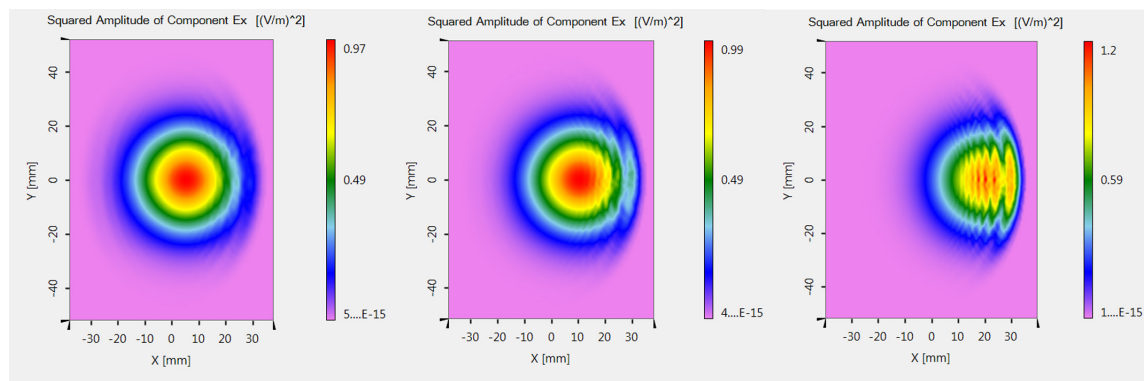


Figure 115: Beam decentering. From left: 5, 10 and 20 mm, respectively.

Single Mirror Tilt

The last tested tolerancing procedure was to observe the influence of a single mirror tilt on the beam quality. As expected, the beam quality is least resistant to mirror tilts. Even mirror tilt as small as 0.005° is clearly observable (see Fig. 116).

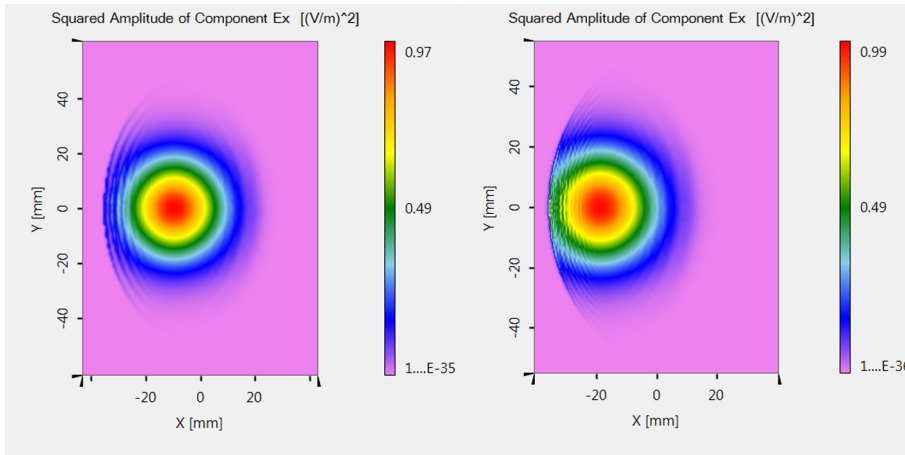


Figure 116: Tilt of a single mirror inside the beamline. From left 0.005° and 0.01° , respectively.

Summary

The conclusion is that VirtualLab Fusion is capable of bringing tolerancing procedures to another level with the use of Unified Field Tracing. It is possible to directly observe the diffraction effects caused by the tolerancing of different parameters of the beamline. The alignment of each single mirror has to be precisely controlled, especially for tilts. Most likely, it will be needed to control each optical component by other optical systems (alignment stations) in order to control their precise adjustment.

8.6.2 L3-E3

Unlike the aforementioned L1-E1 and all other beamlines, L3-E3 does not incorporate off-axis parabola as a final focusing optical element. The reader will see the ray-tracing of the system in the Fig. 117. In contrast to all beamlines, it uses a relatively cheaper spherical mirror. The use of an axial spherical mirror also makes it necessary to have a hole drilled in the middle of the last planar folding mirror, to allow the spherical mirror to focus the beam behind the folding mirror.

Since it is necessary to drill a hole in the mirror, several questions emerge. The most obvious and important ones are:

- How significant is the influence of the hole diameter on the transmitted beam power?
- What is the beam quality after passing the holed mirror, with respect to the M^2 factor and to the encircled energy?

Answers are revealed in the following paragraphs. First the ideal case is discussed, then the surface irregularities are also taken into account.

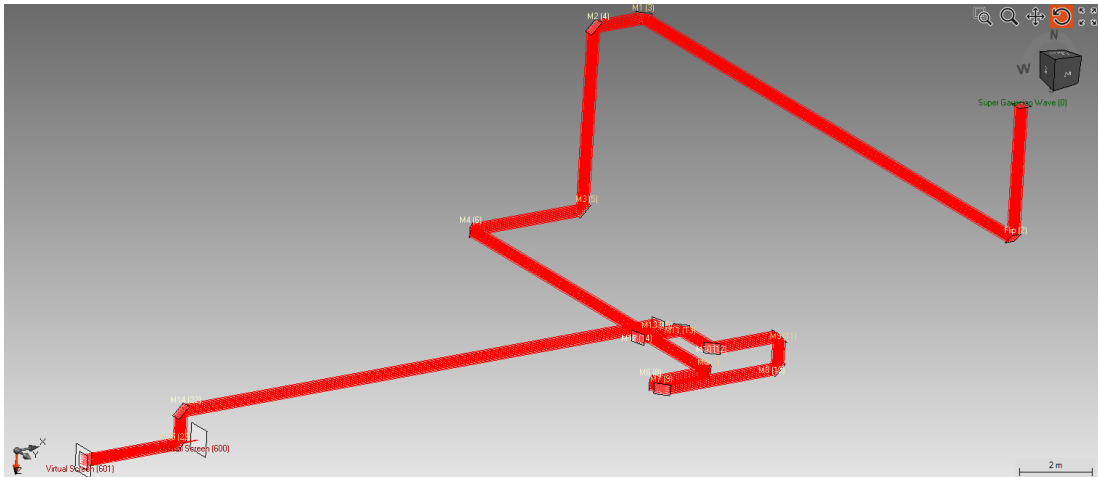


Figure 117: L3-E3 ray-tracing (VirtualLab Fusion).

Through the Hole Focus – Ideal Case

To know the physical limitations of the system, only the ideal components are considered. Either the planar folding mirrors and the spherical focusing mirror are free of any surface imperfections and the spectral reflectances are equal to 1 over the entire bandwidth. Also a simplification of the model, to save some computational time, has been done. The simplified system comprises the last two folding mirrors and the spherical focusing mirror ($f = 5$ m). The focal plane is 200 mm behind the folding mirror M2. This situation is depicted in Fig. 118.

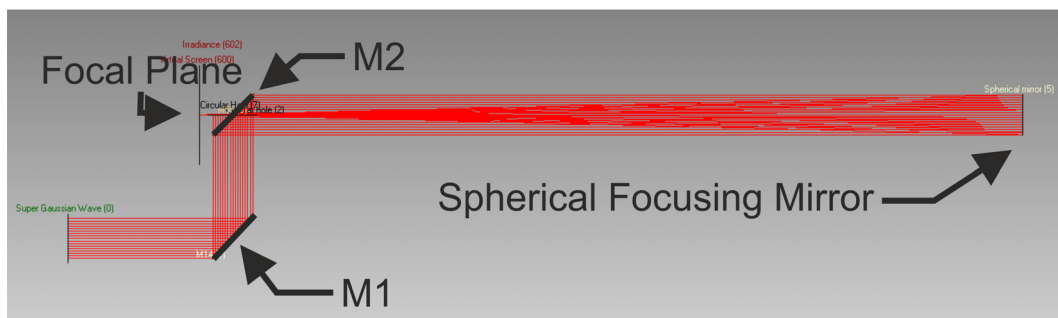


Figure 118: L3-E3 ray-tracing (VirtualLab Fusion).

First power is investigated, as focused power is the facility's main deliverable. The reader should understand that the hole inside the folding mirror actually plays two roles. Initially, the hole acts as a stop, while in the second step the same hole acts as an aperture. In other words – the hole (*the aperture*) needs to be large enough to transmit as much focused power as possible, while simultaneously the same hole (*the stop*) needs to be as small as feasible in order to block the minimum power of the original super-Gaussian beam with a square aperture. The expectation is that there should be some peak, representing an ideal trade-off between these two requirements.

The ideal hole size is investigated with the aid of VirtualLab Fusion and its feature called The Parameter Run. A Light Path Diagram is built for the simplified system and the hole size. The stop and aperture diameter is chosen as variables. While the power in the focus is being registered. The resulting plot of the focused power is shown in percentages in Fig. 119.

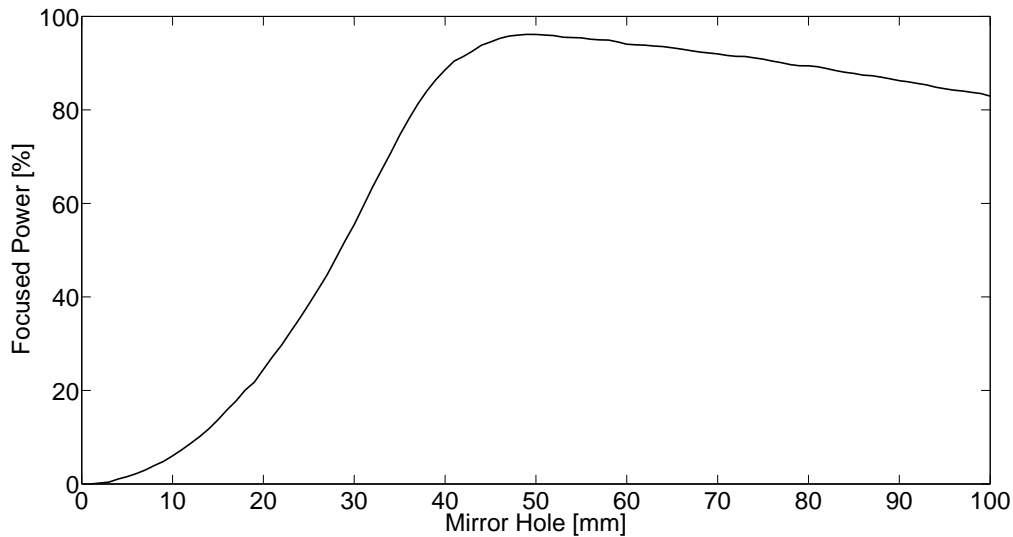


Figure 119: The percentage of focused power as a function of mirror hole diameter.

The plot clearly demonstrates that the ideal hole size for this specific geometry should be between 40 mm and 50 mm. This is only from the power transmission point of view. However, there can be other beam quality criterions. The simplest way to describe a beam quality is to use the so-called M^2 factor [84, 85], which is able to characterize the beam with a single number. Hence, it is also called a beam quality factor. Fig. 120 shows a plot of the M^2 factor for both beam axes as a function of mirror hole diameter. The lower the number, the better the beam. For the ideal TEM_{00} (Gaussian) beam, the $M^2 = 1$.

In the plot it can be seen that there are two minima, the first between 0 mm and 10 mm, which is not feasible from the transmitted power point of view. And the second one, which is near the 50 mm diameter of the mirror hole.

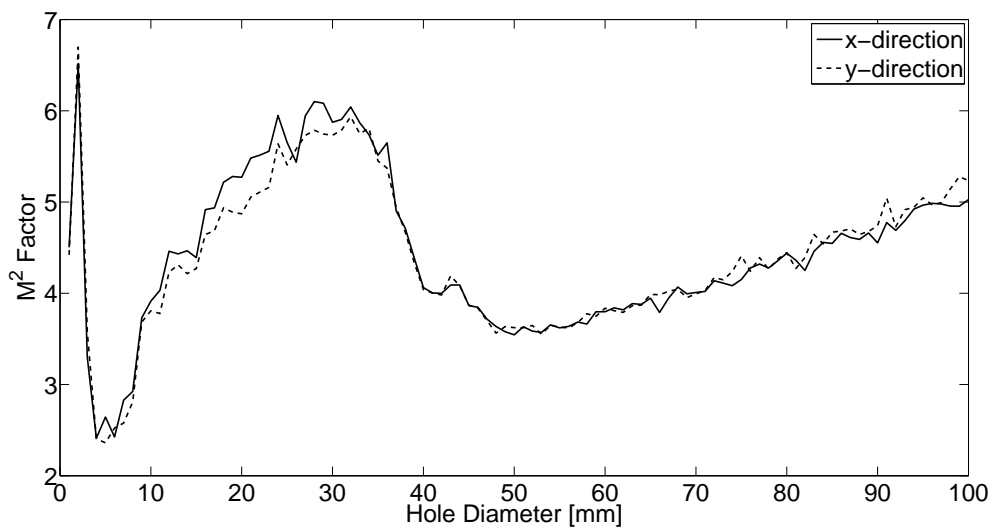


Figure 120: M^2 factor for both beam axes as a function of mirror hole diameter.

Another metric which illustrates beam quality is encircled energy. It is advantageous to compare the encircled energy of the real focal spots with the diffraction limited focal spot (see Fig. 121). Plots of encircled energies for both depicted hole sizes are very similar. However, the 40 mm hole size creates an encircled energy that is a little bit closer to the ideal state.

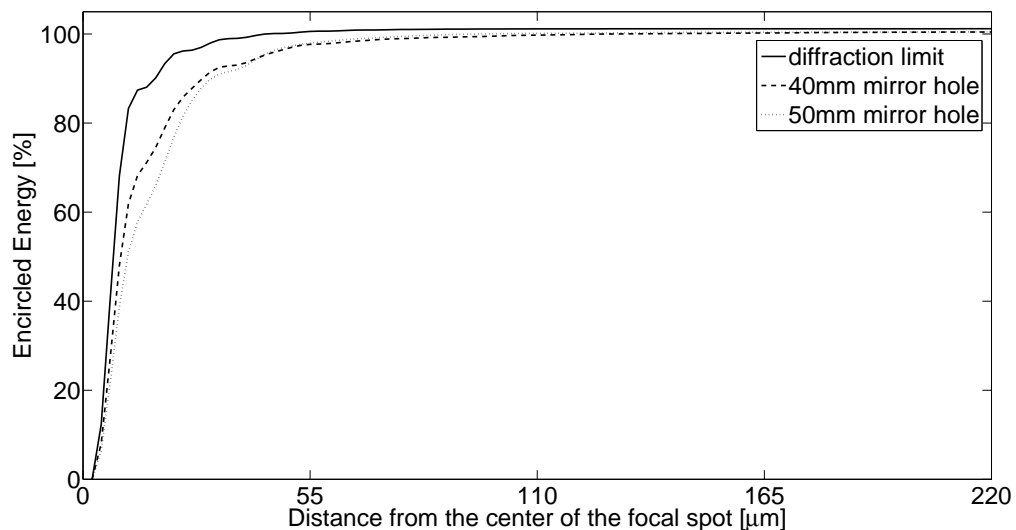


Figure 121: Encircled energy of the beam focused through the mirror hole (shown for a diffraction limited focusing and focusing through the hole with the two specific diameters).

From the previous comparisons, it is obvious that the ideal hole size should be between 40 and 50 mm in the case described. Nevertheless, it is worth demonstrating

the evolution of encircled energy distribution for various mirror hole sizes (as demonstrated in Fig. 122). Readers can see for themselves that these mirror hole sizes are close to the ideal state.

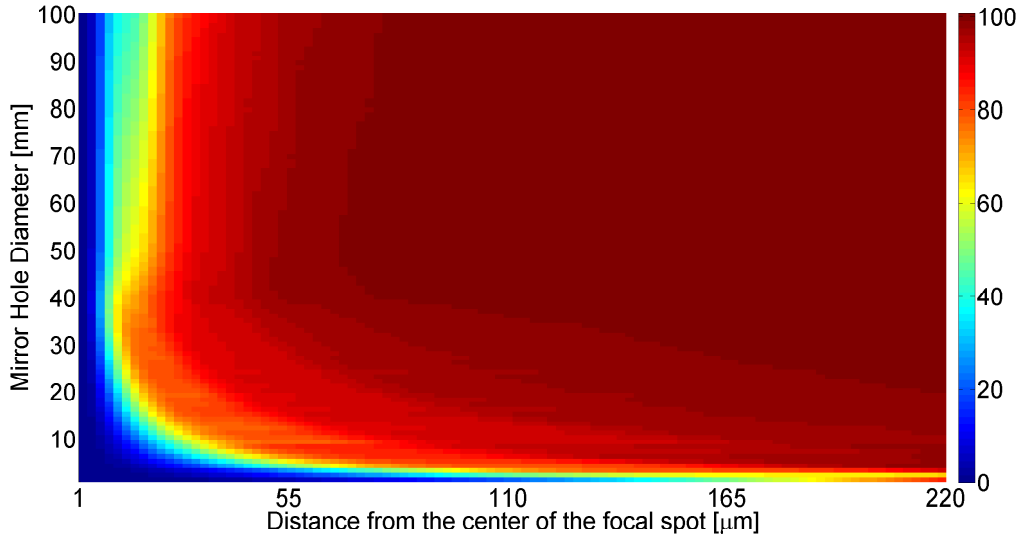


Figure 122: Encircled energies for various mirror hole diameters.

Through the Hole Focus - with Surface Irregularities

In the previous paragraph a limiting physically ideal situation, counting on ideal surfaces free of any surface irregularities was analyzed. However, in practice all optical elements have some amount of surface irregularities, which is proportional to the applied fabrication method. Consequently, the simulation must be extrapolated by introducing the presence of surface irregularities. Surface irregularities are described by the surface RMS, P-V²¹ [86] or slope error [87]. Optical manufacturers usually prepare several types of batches based on the surface RMS values – the typical range is $\lambda/4$, $\lambda/10$ and $\lambda/20$. Anything superior must be done using the custom fabrication process, thus causing additional financial expense.

To simulate the presence of surface irregularities the use of TEZI [47] operand²² within the Zemax tolerance feature is necessary. Provided that the surface RMS is

²¹Abbreviations for peak-to-valley.

²²An excerpt from the Zemax OpticStudio Manual: TEZI is used to analyze random irregular deviations of small amplitude on a surface that is either a Standard, Even Aspheric, or Toroidal surface. Analysis of irregularity on surface types other than these is not directly supported. The Int1 value indicates the number of the surface, Int2 defines the maximum Standard Zernike term (must be between 3 and 231), and Int3 defines the minimum Standard Zernike term (must be between 2 and the maximum term).

TEZI uses the Zernike Standard Sag surface (search the help files for “Zernike Standard Sag”) to model the irregularity on Standard and Even Aspheric surfaces, while Toroidal surfaces use the Zernike terms already supported by the Toroidal surface. When using TEZI, the max tolerance value is the exact RMS error of the surface in lens units. The min tolerance value is automatically set to the negative of the max value; this is done to yield both positive and negative coefficients for the

known, the TEZI operand will calculate the corresponding Zernike polynomial creating the matching surface sag. The user needs to determine the number of Zernike coefficients used to define the polynomial. In the case described, only coefficients up to 10 are chosen, thus the polynomial only represents the low spatial frequency errors. By implementing this procedure, surface roughness cannot be simulated to the extent that any diffraction effects caused by the single-point diamond turning mirror fabrication method are visible. It is obvious that there are infinite possible Zernike polynomials with corresponding surface RMS. Hence, the Monte Carlo simulation, which creates only a limited number of random Zernike polynomials, is used. After the Monte Carlo simulation, the best and worst cases are exploited for the follow-up simulation in VirtualLab Fusion.

Surface irregularities of the planar mirrors defined by the Zernike polynomial can be easily added to VirtualLab Fusion. Only the folding mirrors are affected by the surface irregularities in the simulations performed. The surfaces of the first and second mirrors are shown in Table 24. Surface errors generated by the Zemax TEZI operand have circular symmetry, however VirtualLab Fusion can extrapolate surface errors for the whole rectangle based on these data. A simple increase of the unit size radius within OpticStudio cannot correctly represent the surface irregularities of rectangular mirrors.

Several simulation analysis cases are created. Specifically, mirrors with surface RMS equal to the $\lambda/4$ and $\lambda/20$. For both surface RMS, values the best and the worst case scenarios are determined. Four distinct LPDs are then created in VirtualLab Fusion – the combination of the two worst case planar mirrors with $\lambda/4$ surface RMS, the

Zernike terms. The resulting RMS is of course always a positive number whose magnitude is equal to the max tolerance value.

For the sensitivity analysis, the surface is converted to a Zernike Standard Sag or Toroidal surface and all the coefficients of the Zernike polynomial for terms greater than #1 (the “piston” term) are set to a value so that the square root of the sum of the squares of the coefficients yields the specified RMS value. All coefficients are set to the same value.

For the Monte Carlo analysis, the surface is converted as for the sensitivity analysis, but each polynomial term is assigned a coefficient randomly chosen between -1.0 and 1.0 , and the resulting coefficients are then normalized to yield the exact RMS tolerance. The random value is chosen using the statistical model selected for the operand; search the help files for the STAT command for a discussion.

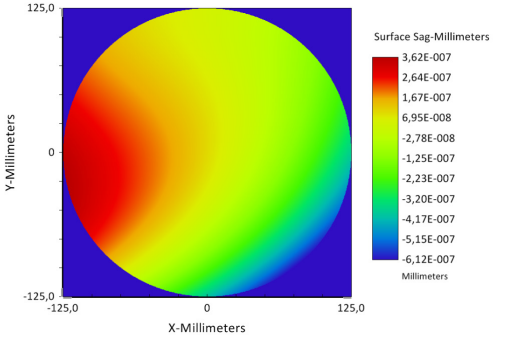
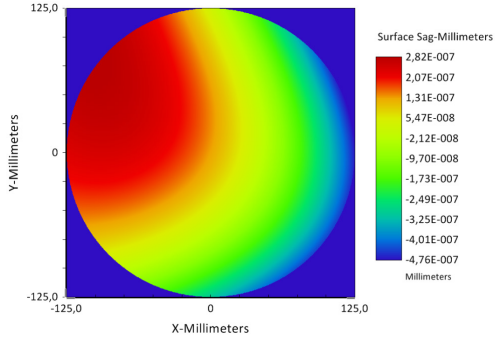
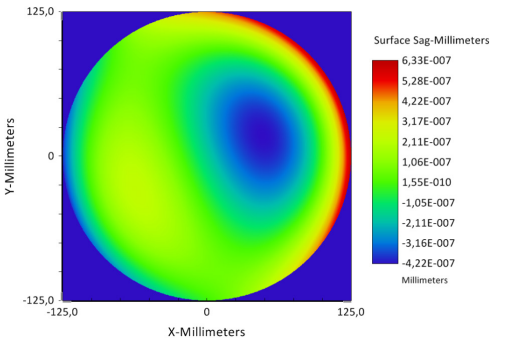
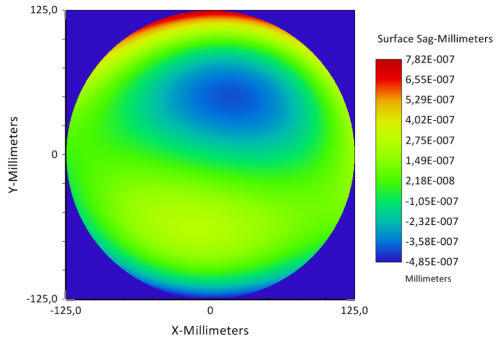
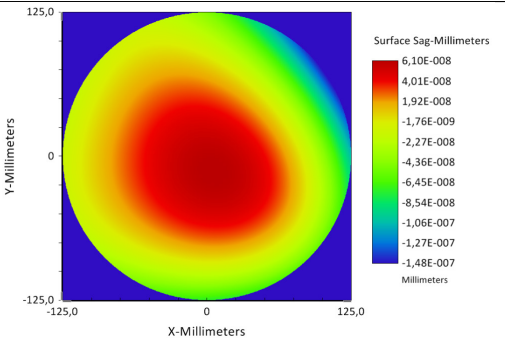
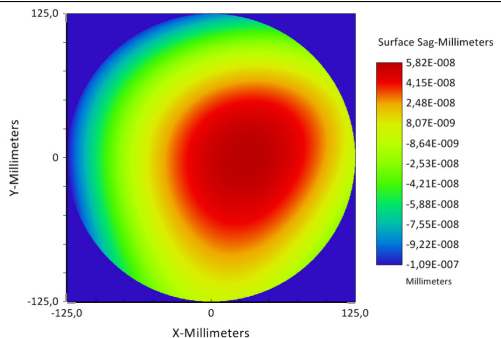
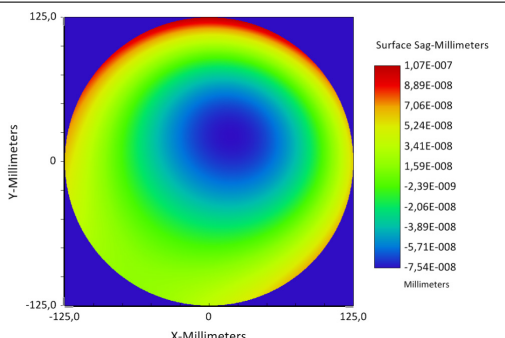
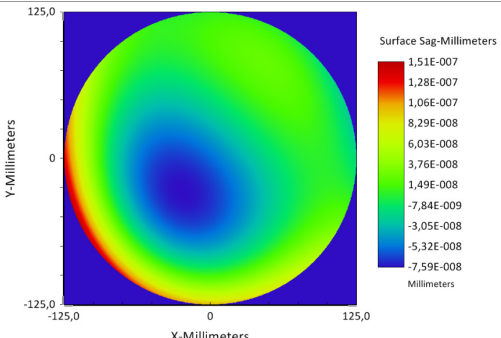
The number of terms is given by $\text{Int}2 - \text{Int}3 + 1$. Generally speaking, if lower order terms are used, the irregularity will be of low frequency, with fewer “bumps” across the surface. If higher order terms are used, there will be higher frequency irregularity, with more “bumps” across the surface. Note the TIRR irregularity operand models the lowest frequency form of irregularity, with just a quadratic and quartic deviation across the surface. TEZI can model much more irregular surfaces.

Because the Zernike Standard Sag surface sag expression contains portions of both the Standard and Even Aspheric surfaces, either of these surface types may be modeled by the Zernike Standard Sag surface created with the TEZI operand. If the surface is Toroidal, the Toroidal surface is retained since the Zernike terms are already supported with this surface type, however, the nominal value of all the Zernike terms must be zero if the nominal surface is Toroidal. The normalization radius for the Zernike terms is set to the semi-diameter of the surface.

TEZI always ignores Zernike term 1, the piston term, and sets this value to zero.

combination of the two best case planar mirrors with $\lambda/4$ surface RMS, the combination of the two worst case planar mirrors with $\lambda/20$ surface RMS and finally the combination of the two best case planar mirrors with $\lambda/20$ surface RMS. The resulting focal spots are shown in the Fig 123. Their sizes are in Table 25.

Table 24: Magnitude of surface irregularities on the first and the second planar folding mirror.

RMS Error	1st Mirror Surface	2nd Mirror Surface
$\lambda/4$ Best		
$\lambda/4$ Worst		
$\lambda/20$ Best		
$\lambda/20$ Worst		

The amount of allowable surface irregularities is mainly induced by the available deformable mirrors with sufficient LIDT. So far, the author has no information on the technical specifications of the deformable mirror that will be available for the beamline. As soon as the decision is made, a precise analysis of the allowable surface irregularities for all optical components can be conducted.

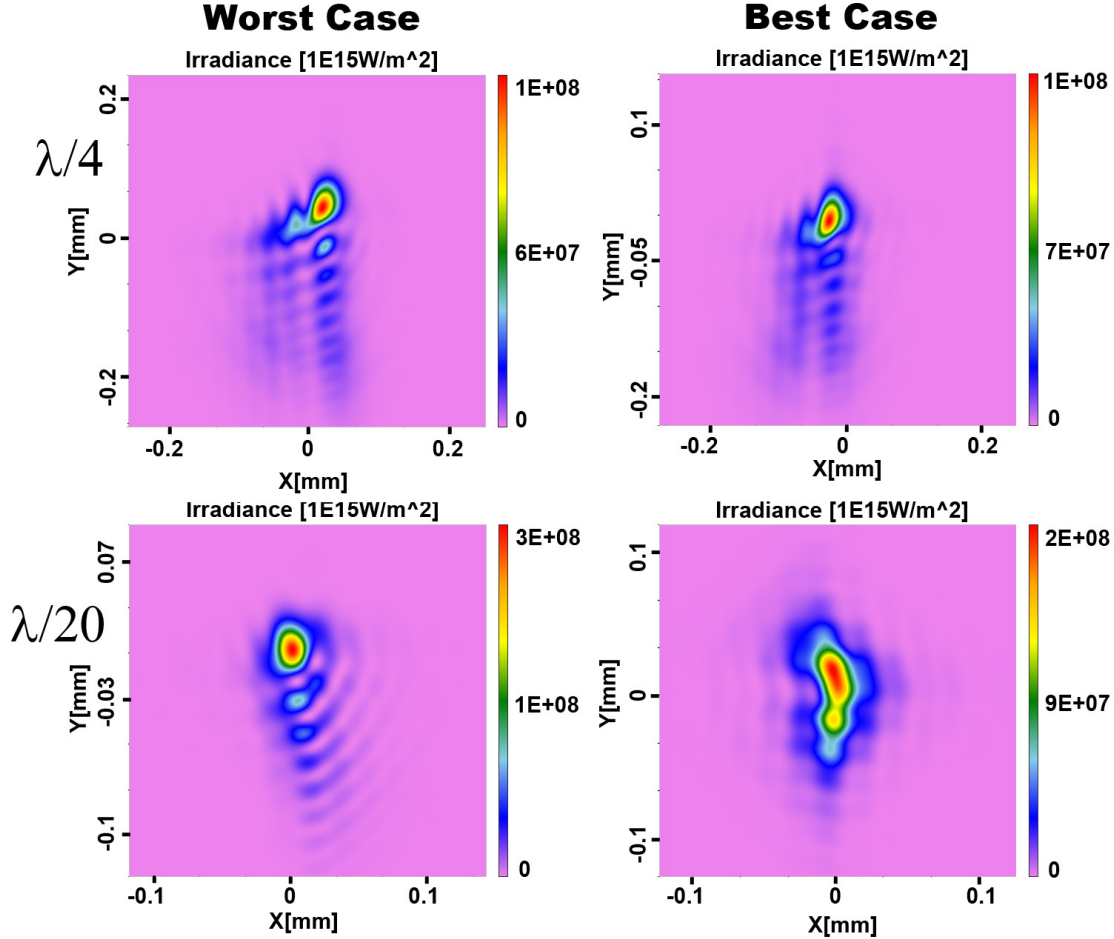


Figure 123: Resulting focal spots in the systems with surface irregularities on planar folding mirrors.

Table 25: Resulting focal spots sizes in the systems with surface irregularities on planar folding mirrors.

RMS error	Spot Size
$\lambda/4$ – Best	61.3 μm \times 135.3 μm
$\lambda/4$ – Worst	69.3 μm \times 141.2 μm
$\lambda/20$ – Best	43.3 μm \times 66.5 μm
$\lambda/20$ – Worst	41.8 μm \times 82.5 μm

Through the Hole Focus - with Coatings and fs Pulse

In the previous case, all of the mirrors used (either folding or spherical focusing) had ideal reflective surfaces. That means the reflectivity is equal to 1 over the entire bandwidth. The implication is that the temporal effects of the mirrors cannot be investigated. In reality, each mirror will have a stack of thin films deposited on their surfaces causing the pulse to stretch. Typically the high reflectivity coating stack is composed of two dielectrics with low and high refractive indices, which periodically alternate in this multilayer system. The layers used in the case described are created by a combination of SiO₂ and TiO₂ (as seen in VirtualLab Fusion's coating editor in Fig. 124). Prescriptions for these mirror stacks were kindly provided by Dr. Werner Moorhoff from LASEROPTIK GmbH [88].

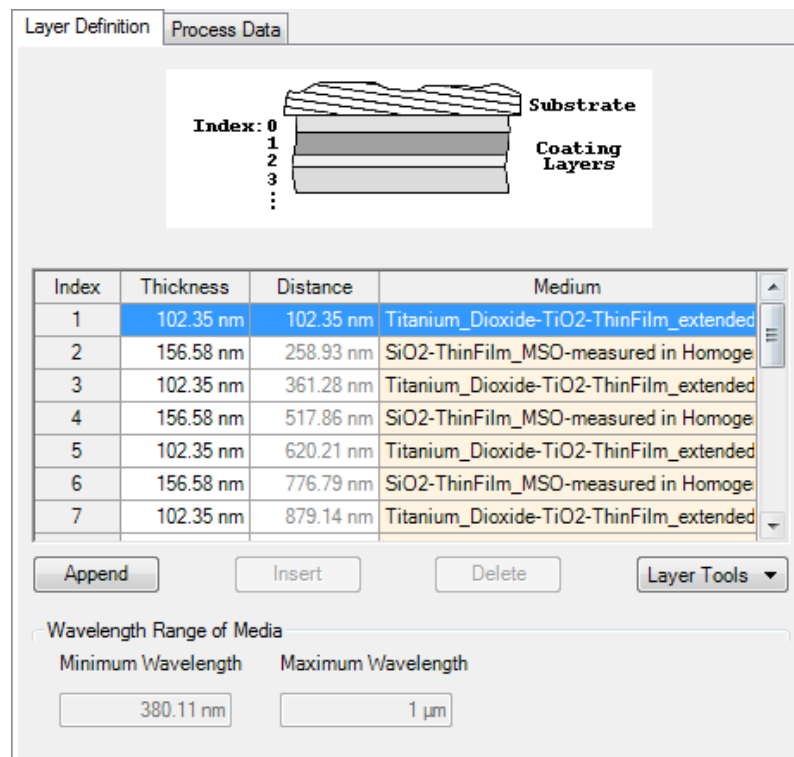


Figure 124: Coating editor within VirtualLab Fusion

The input pulse with $\lambda = 820$ nm has a Gaussian temporal profile and a duration of 31.34 fs. The duration of the pulse in the focal plane is equal to 36.79 fs. A comparison of the input and output profiles is depicted in Fig. 125.

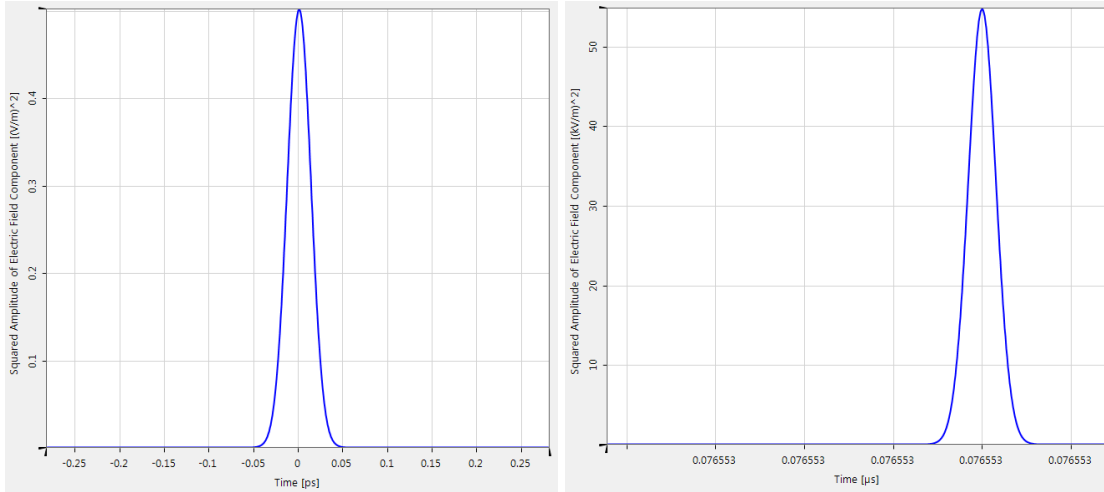


Figure 125: Comparison of input (left) and output (right) pulse components $|E_x|^2$ in the time domain.

It is worth analyzing the output pulse duration with respect to the incidence angle. For that purpose an LPD containing a single mirror was prepared. Both coating stacks used in the previous system were tested separately to analyze their influence on the duration of the output pulse. The resulting pulse durations for various incidence angles are shown in Fig. 126.

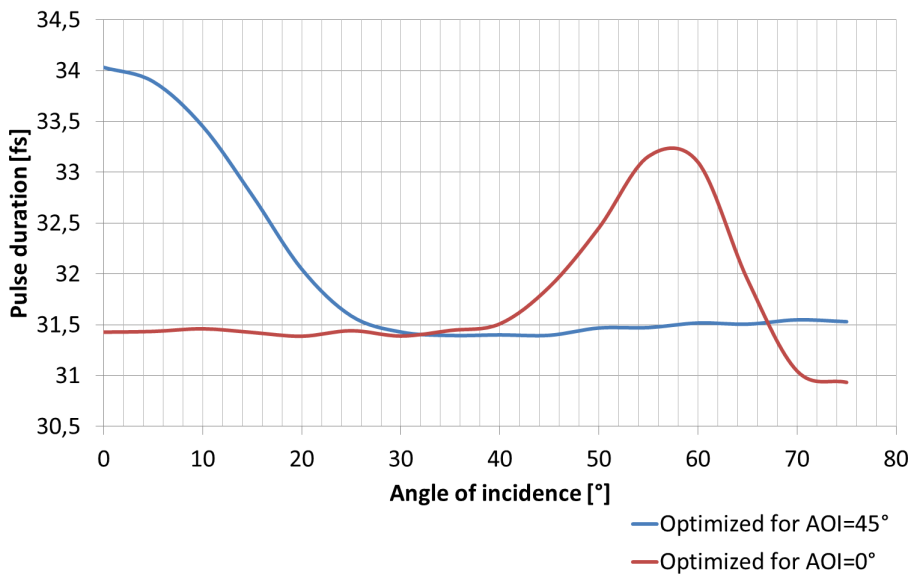


Figure 126: Pulse duration with respect to the angle of incidence.

The flat intervals of both resulting plots limit the ideal AOI range for each of the tested coatings.

Usually the output pulse duration is given with respect to the GDD as seen in Fig. 127, provided by one of the manufacturers [89]. The relation between the GDD, wavelength and incidence angle for one example of the manufactured mirrors is shown in Fig. 128. More on this topic can be found in [90].

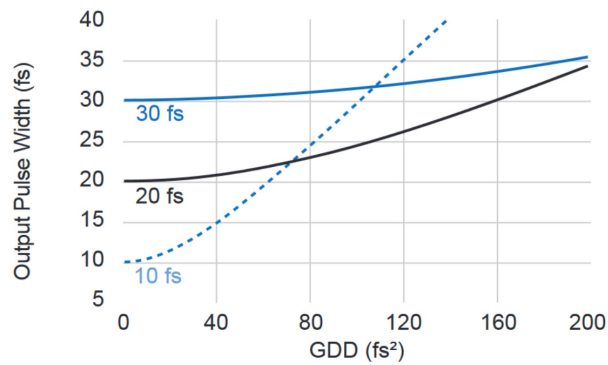


Figure 127: Output pulse duration with respect to the GDD, adopted from [89].

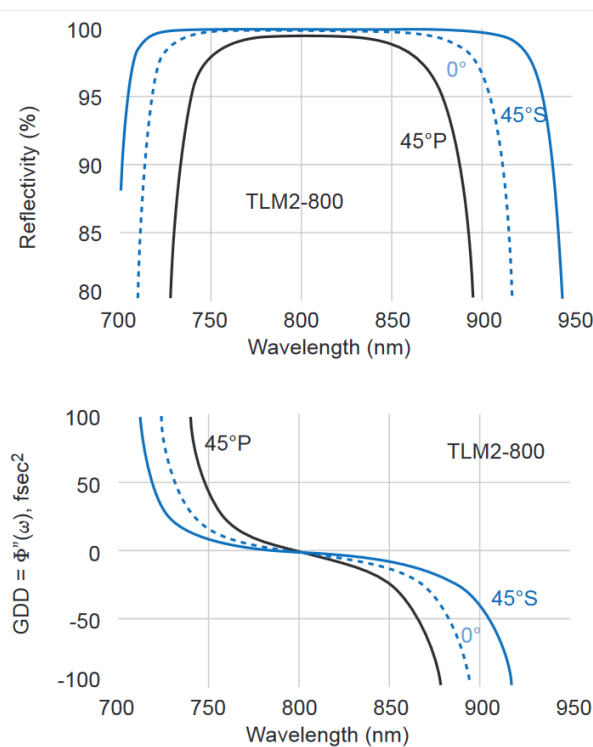


Figure 128: Dispersion and reflectivity for mirror TLM2-800-0, adopted from [89].

Summary

The E3 room serves for plasma physics experiments. The results shown in the previous text will help plasma physicists to prepare their experiments with betatrons, especially to determine the conditions for the optimum electron acceleration. Focal spots calculated by VirtualLab Fusion, are used in the next step for PIC (particle-in-cell) simulations. A paper showing the already finished optical, and forthcoming PIC simulations, has yet to be completed. Results are also shown in the research report contained within the appendix of this thesis.

9 Overall Discussion and Assessment

According to the actual needs of ELI-Beamlines, several case scenarios related to the operation of the lasers inside this facility were analysed within the preceding text. A short summary, with discussion and assessment of the acquired results follows.

Topics discussed in the presented dissertation were mainly:

Free space propagation

The basic element of every consequent simulation is free space propagation. The stress was put on the propagation of the squared super-Gaussian beams of higher orders. It was demonstrated that for beams with orders near 20 (similar to the one used in ELI-Beamlines), diffraction is not a major problem when the beam is propagating to a distance of 20 m, as shown in the text. However, the non-linear effects were not taken into account. Investigation of the non-linear effects on free space propagation is planned for the future. This simulation was completely conducted with the aid of VirtualLab Fusion and its rigorous Maxwell equations solver (*SPW* operator).

Beam clipping

Another important part of optical engineering is to deal with economic factors. The price of optics exponentially increases with the aperture size as both fabrication and metrology of large aperture optics is very expensive. Therefore, it is advantageous to know what aperture size is actually required. Or in other words, what are the possible power losses for various optical element sizes based on their beam size : element size ratio? Analyses were conducted for various beam orders and for both circular and square symmetry of the input beam. Also, this simulation was entirely accomplished within VirtualLab Fusion and Classic Field Tracing.

Beam focusability with the use of an ideal lens

To have an idea about the final focusing optics performance limits, it is helpful to know the physical limits of focusing the squared super-Gaussian beams of higher orders using an ideal lens. Several metrics were employed to support this objective – fitted values of logarithmed $|E_x|$, encircled energy and the Strehl ratio. The influence of hard apertures and apodizations of different diameters were demonstrated. The results will serve the experimental team's decision as to the feasibility of possible apodizing masks for their experiments with focusing a beam into a capillar tube. The acquisition of the resulting values were done by VirtualLab, post-processing of the data and plot generation was managed within MATLAB.

Transmissive optics

The feasibility of transmissive reducers was analyzed. Three example configurations were designed in Zemax OpticStudio – Keplerian and two Galileans (with Fraunhofer and Steinheil doublet as a frontal lens group). The total system length and magnification ratio was strictly limited by the mechanical design requirements, thus radically restricting the lens design of the required system. The proposed systems match these criteria. Nevertheless, the Keplerian system performance is not satisfactory. In the designs presented, all systems had only spherical surfaces. The aspherical surfaces would lead to the elimination of residual aberrations. They would also lead to a very high increase in fabrication and metrology expenses. Conversely, the performance of both Galilean systems is far superior. However, if spatial filtering is needed, then the Keplerian system is the only choice, because of the intermediate focal plane. All systems stretch the incoming 30 fs pulse. The shortest pulse stretching is achieved by the Galilean system with the Fraunhofer doublet (153 fs). The poorest result was attained by the Keplerian system (626 fs). Transmissive optics is, in this case, not feasible and similar reflecting alternatives are recommended. The temporal effects of the systems were investigated by VirtualLab Fusion.

Reflective telescopes and reducers

A slightly more complex analysis was conducted in the case of reflective optics. The use of reflective optics in the main beamline is inevitable due to the large aperture beams with fs pulse durations. First, comparison of the “U” and “Z” afocal OAP configurations was performed. Influence of aberrations was shown in both cases. It was demonstrated that the “U” configuration is not feasible due to output beam distortion. Both conventional methods (ray tracing within Zemax OpticStudio) and Geometric Field Tracing Plus (Beta) were used to achieve these results. In the next step the influence of the mirror’s off-axis angles in the “Z” configuration was examined for the case of a 1:1 relay. It was demonstrated how the electric field’s vectorial components change with this angle. Based on these results it is recommended to use the smallest angles possible to fulfill the conditions of image relaying. In the last case scenario, two reflective reducer configurations were demonstrated. The first one is a combination of two concave off-axis parabolic mirrors, whereas the latter one combines a concave and a convex off-axis parabolic mirror. From the geometric point of view the image for both reducers is perfect, without any aberrations. The only residual aberrations are field curvature and distortion. The choice for one reducer over the other is then mainly driven by the mechanical design restrictions and requirements for optical alignment. Convex surfaces are also more difficult to fabricate and control, thus increasing expenses. Demagnification of the input beam was also demonstrated

by both VirtualLab Fusion's techniques – Classic Field Tracing and Geometric Field Tracing Plus (Beta).

Telescopes for beam diagnostics

The main task of the optics in the ELI-Beamlines is, of course, to distribute the laser beam from the source to the target (focal plane). However, the beam needs to be inspected along its path. Thus there is a requirement for a special sort of optics called beam monitoring optics, or telescopes for beam diagnostics. In the case described a design inspired by the similar systems built for Astra Gemini was demonstrated. Economic efficiency was stressed. Thus the first proposed variant of the telescope is a combination of available stock optics. However, the acquired results were not satisfactory. Hence, the custom variant was designed with the aid of Zemax OpticStudio. Customization of the originally used doublet made by Thorlabs leads to far superior results. Correct demagnification of the input beam is demonstrated by using Geometric Field Tracing Plus (Beta) within VirtualLab Fusion.

Beamlines

Out of all the planned beamlines, the stress was put onto L1-E1 (Experimental Hall 1 – Material and biomolecular applications) and L3-E3 (Experimental Hall 3 – Plasma physics). In the case of L1-E1, the possibilities of physical optics based tolerancing were investigated. For example, beam clipping, decentrations and mirror tilting. Unlike traditional ray tracing methods the SPW operator within VirtualLab Fusion was used. In the case of the L3-E3 system, the focusing part of the beamline was analyzed. Unlike other beamlines, instead of the typically used off-axis parabola, a spherical focusing mirror is employed. This is allowed due to the longer focal length (f -number $\gg 1$), thus the need for a holed folding mirror arises. Calculation of the ideal hole size with respect to the focused power was conducted. Also the encircled energy and the M^2 factor for various hole sizes were determined. After the analysis of the ideal system condition, the influence of surface irregularities was studied. Focal spot sizes for various surface irregularity magnitudes were exposed. In the last step, the influence of the coating stacks was also taken into account. Pulse stretch caused by the coating stacks was calculated. All the results obtained in the beamline simulations were achieved using VirtualLab Fusion. Post-processing and the generation of some of the plots was done with the help of MATLAB.

Specific results of this PhD thesis to which the author contributed are as follows:

- Determination of VirtualLab Fusion's efficiency in order to fulfill the BPM requirements – the author tested the software on several case scenarios that he prepared. In the majority of cases VirtualLab Fusion provided a step up from previously used ray-tracing methods. The author also assessed the ability of the newly introduced Geometric Field Tracing Plus (Beta), especially in the case of reducers. With the use of this new technique, the exact values of all field components were determined without the numerical effort of diffractive techniques. Unfortunately the author was not able to conduct further simulations with high NA off-axis parabolas for final focusing. This was probably because of the extraordinarily large size of both optics and beams that lead to extraordinary numerical effort. The case scenario used for smaller sizes of the beam and optics performed well, but finally was not incorporated into the thesis.
- The author has shown the influence of diffraction on the high order super-Gaussian beams of square aperture and analyzed the influence of apodization on the focusing of these beams. He demonstrated that the order 20 beam does not suffer from the diffraction effects over the required optical path distance in comparison with higher orders. For this purpose a rigorous simulation technique was used (SPW operator), which is superior to those typically used by physical optics propagation techniques within common ray-tracing software bundles.
- The author prepared several optical design suggestions, especially for reducers/expanders. The author has shown the geometric aberrations of the systems, as well as the temporal effects implied by transmissive systems. While the geometric aberrations can be well controlled by a suitable optical design, as shown by the author, the behaviour in the temporal domain is mainly limited by the GVD of the glass used, and its necessary thickness. This field tracing technique allowed the author to control the influence of the system on the fs pulses and to determine the pulse stretching caused by transmissive systems. The author calculated the exact pulse duration of the pulses reduced by these optical systems. Based on this information, the author decided that transmissive systems are not feasible for the beamline. Transmissive systems stretch the pulse above the impermissible level. Access to the temporal domain is an improvement over the ray-tracing method, thus demonstrating new possibilities in the workflow of optical engineers. These new possibilities are characterized by access to all field components and to the temporal domain allowing the system to be tailored for the use with ultra-short pulses. The author also considered the specific requirements of the optical systems, like the total length of the system to fit inside the

beamline.

- The author analysed the influence of possible relay system shapes and their influence on image relaying and concluded that the off-axis angle needs to be minimized due to the acquired values of the electric field components in the output.. Also, the “U” shape of the relay system is not feasible at all due to the sum of both parabolas’ astigmatism.
- The author suggested a design for a beam diagnostic telescope based on the design of a similar system used with Astra Gemini. Two versions of the telescope were prepared by the author – one with commercial optical components only, and the second one with a custom doublet introduced, which highly improved the image quality of this demagnifying system. After the improvement, diagrams fit well inside the Airy disk radius. The system satisfies the requirement to demagnify the beam to the size of a standard CCD used inside the Shack-Hartmann sensor made by Thorlabs, thus allowing for the measurement of the wavefront error for the beam behind the leak mirror.
- The author used the method of Field Tracing for a tolerancing analysis of the beamline, and determined the proper hole size for the folding mirror inside the beamline in order to achieve the maximum peak fluence of the focused beam using the same approach. He also determined the amount of encircled energy and the beam quality factor. Such calculations are very important for finding the required precision of gimbals, linear stages and other opto-mechanical systems and devices. The author also considered the influence of surface irregularities and coatings.

10 Conclusions and Future Work

In the beginning of the author's work there was a question of which software could be used to aid in the endeavor of ELI-Beamlines. One of the software bundles being tested during the preparation of the author's master thesis was LightTrans VirtualLab, among others. Despite of the common use of Zemax OpticStudio, there are some case scenarios that cannot be investigated with the simple geometric optics approach. Hence the combined use of these software bundles seems like an excellent solution. Zemax OpticStudio is well established software used for optical design. VirtualLab Fusion is an advanced optical modeling software based on the physical optics approach. However, it lacks classical design features that optical engineers are used to handling. With their combined use shown in this dissertation, a new perspective on optical design is gained.

Since the first version of VirtualLab Fusion used within ELI-Beamlines, a lot of new features were added by the developers. Some of them are also inspired by the needs of ELI-Beamlines. The author also had the opportunity to be involved in the development process while working as an intern on Prof. Wyrowski's team in Jena, Germany.

The reader can consider this dissertation from two different perspectives. The first perspective is software related, while the second one is optical system related. It needs to be stressed that this dissertation shows the very first official application of VirtualLab Fusion inside a high peak power laser facility.

In this thesis a new optical workflow was established. All strengths and weaknesses of both software bundles were pinpointed and the workflow was adjusted accordingly. In the case of VirtualLab Fusion, many features were improved while this dissertation was being written. A part of the author's work on the team was the preparation of various case scenarios and the assessment of new features and improvements. Some of these case scenarios were described in this dissertation.

From the system perspective, the performance of various systems to be implemented within ELI-Beamlines were analyzed, mainly the reducers, both transmissive and reflective. Telescopes for beam diagnostics were also presented in this thesis. Thorough analysis using classical aberration theory, with a combination of physical optics approaches, was presented, thereby demonstrating the need for the parallel use of Zemax OpticStudio with VirtualLab Fusion. For investigation of temporal effects, VirtualLab Fusion was the leading analysis tool. Also, the newly introduced feature, Geometric Field Tracing Plus (Beta), proved to be useful in the situations where the numerical effort for Classic Field Tracing was too high, or when the diffraction effects did not need to be included. Still, all of the electromagnetic field components are,

even with this new technique, always available while the beam propagates through the system.

The first simulation, which was related to the focusability of the super-Gaussian beams, should serve as an insight for experimental teams, so that they will learn what the physical limit they should expect for focusing these beams onto their targets is.

Several optical design related recommendations emerge from the simulations described in the text of this dissertation. As demonstrated, transmissive reducers are not feasible for the L1 beamline due to the excessive pulse stretching they are causing, thus the design should lead to reflective systems only. Another recommendation is related to reflective relay telescopes and reducers. The “U” configuration of the OAPs is not recommended at all, since the output beam is distorted. For the “Z” configuration, the off-axis angles were analyzed. The optical design of such systems should lead to the minimalization of this value. An example was also presented of a beam diagnostic telescope that can be used practically. It is highly recommended to use customized negative NIR doublets in these telescopes because they improve the performance of the telescope drastically, without creating too much additional financial expense. Finally, the ideal size of the hole inside the folding mirror was calculated to achieve maximum power.

In the future, simulations should be step by step improvements towards more realistic models, including all system components and features. Also, the final focusing OAPs should be included in the simulations with femtosecond pulses. Some of these calculations will most likely require the computing power of supercomputers or clusters of computers, and are not expected to be done in the office workstation, like all the simulations presented throughout this dissertation.

It is not within the authority of this author to decide whether the VirtualLab Fusion will be permanently used within the ELI-Beamlines. The software proved its usefulness numerous times. However, the BPM project, which had the task of implementing the software has been officially cancelled by the director of Institute of Physics. Decision made was not to purchase the performance software, and especially its future custom development for the purposes of the ELI-Beamlines. Insufficient funds to cover this project were the reason for the decision. Nevertheless, a few licenses of the VirtualLab were bought and some employees still continue in their use, including the author.

Photo Attachment



Photo 1: Banners in front of the ELI-Beamlines facility saying “The Greatest Research Project in the History of our Country”.

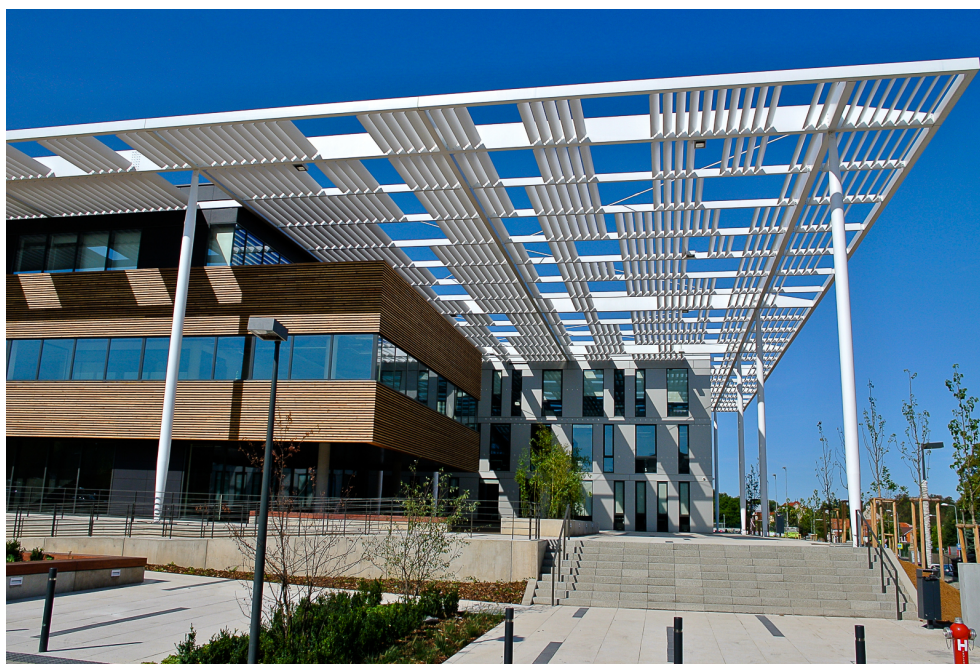


Photo 2: ELI-Beamlines facility (office building).



Photo 3: Author posing with the corner stone of the HiLASE project (ELI-Beamlines sister project).



Photo 4: Inside the forthcoming laser hall.



Photo 5: Laser hall under construction I.



Photo 6: Laser hall under construction II.



Photo 7: Grand opening ceremony I.



Photo 8: Grand opening ceremony II.



Photo 9: Author posing in front of a vacuum chamber (PALS facility, July 2013).

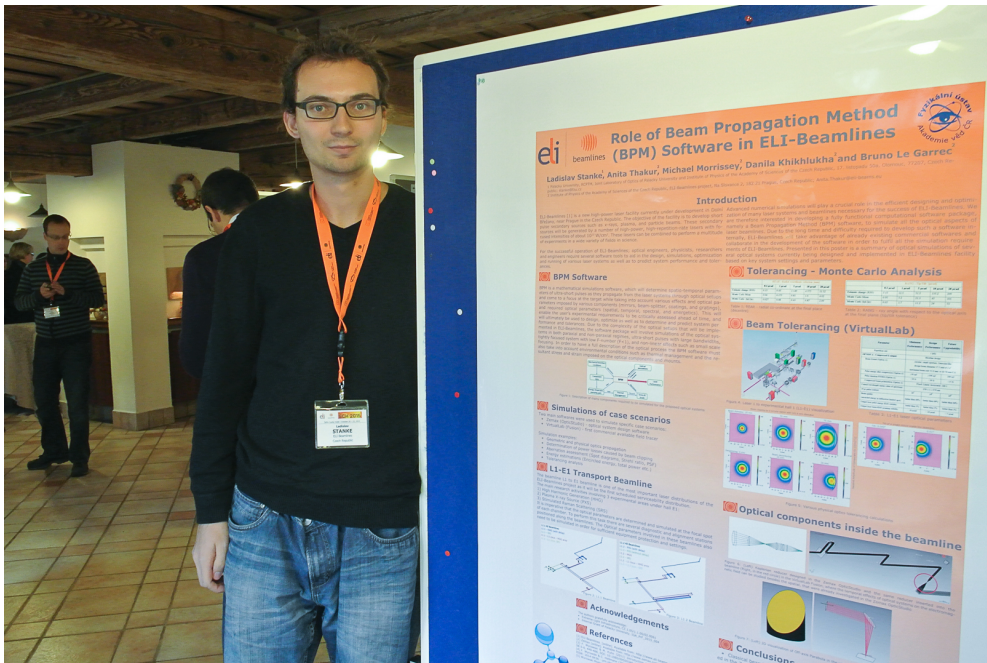


Photo 10: Author posing in front of the poster created by himself and members of the BPM team (presented at ELI Scientific Challenges 2015).



Photo 10: Author posing in front of Wyrowski Photonics UG with (from left) Christian Hellmann, Prof. Frank Wyrowski and Anita Thakur (Jena, July 2015).



Photo 11: Author posing with members of the Applied Computational Optics Group of Friedrich-Schiller-Universität Jena. From left: Site Zhang, Irfan Badar, Huiying Zhong, Olga Baladron-Zorita, Ladislav Stanke, Anita Thakur, Rui Shi, Dagmawi Berhanu Tadesse and Liangxing Yang. (Jena, July 2015).

References

- [1] ELI-Beamlines. [online]. [ref. 2015-09-14]. Available from:
<http://www.eli-beams.eu/>
- [2] MOUROU, G. A., KORN, G., SANDNER, W., COLLIER, J. L. (Eds.): ELI - Extreme Light Infrastructure Whitebook, Science and Technology with Ultra-Intense Lasers, THOSS Media GmbH, Berlin, 2011.
- [3] MORRISSEY, M.: ELI-Beamlines Requirements of a Beam Propagation Method Software [Adobe Acrobat slides], Workshop: Beam Propagation Method Softwares for Pulse Lasers, Prague, 2014.
- [4] STANKE, L.: Application of optical elements for temporal and spatial transformation of ultra-short and ultra-intense light pulses, Univerzita Palackého v Olomouci, Přírodovědecká fakulta, Olomouc, 2012.
- [5] Applied Computational Optics group. [online]. [ref. 2015-09-14]. Available from:
<http://www.applied-computational-optics.org>
- [6] LightTrans. [online]. [ref. 2015-09-14]. Available from: <http://www.lighttrans.com/>
- [7] Wyrowski Photonics. [online]. [ref. 2015-09-14]. Available from:
<http://www.wyrowski-photonics.com/>
- [8] WYROWSKI, F., HELLMANN, C.: Geometrical Optics Reloaded, DGaO Proceedings 2015. Available from:
http://www.dgao-proceedings.de/download/116/116_h2.pdf,
urn:nbn:de:0287-2015-H002-6, 2015.
- [9] International Committee on Ultra-High Intensity Lasers (ICUIL). [online]. [ref. 2015-09-14]. Available from: <http://www.icuil.org>
- [10] DAVIS, J. I., CLEMENTS, W. (Editors): Laser Program Annual Report 1974, Lawrence Livermore Laboratory, University of California, Livermore, 1975.
- [11] COLEMAN, L. W., STRACK, J. R. (Editors): Laser Program Annual Report 1979 Volume 1, Lawrence Livermore National Laboratory, University of California, Livermore, 1980.
- [12] COLEMAN, L. W., KRUPKE, W. F. (Editors): Laser Program Annual Report 1980 Volume 1, Lawrence Livermore National Laboratory, University of California, Livermore, 1981.
- [13] National Ignition facility User Guide. [online]. [ref. 2015-05-10]. Available from:
https://lasers.llnl.gov/for_users/pdfs/2012user_guide.pdf
- [14] LMJ-PETAL User Guide. [online]. [ref. 2015-05-10]. Available from:
http://www-lmj.cea.fr/docs/2014/LMJ_PETAL_Users_guide_v1.0.pdf

- [15] National Laser Users' Facility Users' Guide [online]. [ref. 2015-05-10]. Available from: http://www.lle.rochester.edu/media/about/documents/nluf_users_guide.pdf
- [16] PALS - Prague Asterix Laser System [online]. [ref. 2015-05-10]. Available from: <http://www.pals.cas.cz/cz/>
- [17] BAUMHACKER, H., BREDERLOW, G., FILL, E., VOLK, R., WITKOWSKI, S., WITTE, K. J.: Layout and performance of the Asterix IV iodine laser at MPQ, Garching, *Appl. Phys. B* 61 pp. 325-332, 1995.
- [18] SIMMONS, W. W., SPECK, D. R., HUNT, J. T.: Argus laser system: performance summary, *Applied Optics* **17**, pp. 999-1005, 1978.
- [19] PALATKA, M.: Historie NIF [Microsoft PowerPoint slides], Olomouc, 2011.
- [20] AHLSTROM, H. G.: Laser fusion experiments, facilities, and diagnostics at Lawrence Livermore National Laboratory, *Applied Optics* **20**, pp. 1902-1924, 1981.
- [21] MILLER, J. L., ENGLISH, R. E., Jr., KORNISKI, J. R., RODGERS, J. M.: Optical design of the National Ignition Facility main laser and switchyard/target area beam transport systems. *Proc. of SPIE* **3492**, Third International Conference on Solid State Lasers for Application to Inertial Confinement Fusion, 294, 1999; doi:10.1117/12.354140
- [22] BURKHART, S. C., BLISS, E., DI NICOLA, P., KALANTAR, D., LOWE-WEBB, R., MCCARVILLE, T., NELSON, D., SALMON, T., SCHINDLER, T., VILLANUEVA, J., WILHELMSSEN, K.: National Ignition Facility system alignment, *Applied Optics* **50**, pp. 1136-1157, 2011.
- [23] MALACARA, D., MALACARA, Z.: Handbook of Optical Design, Second Edition. Marcel Dekker, Inc., New York, 2004.
- [24] LAIKIN, M.: Lens Design, Third Edition, Revised and Expanded, Marcel Dekker, Inc., New York, 2001.
- [25] WALKER, B. H.: Optical Design for Visual Systems, SPIE, Bellingham, 2000.
- [26] LIANG, R.: Optical Design for Biomedical Imaging, SPIE, Bellingham, 2010.
- [27] TRÄGER, F. (Editor): Springer Handbook of Lasers and Optics, Springer Science+Business Media, LLC, New York, 2007.
- [28] HUNT, J. T., GLAZE, J. A., SIMMONS, W. W., RENARD, P. A.: Suppression of self-focusing through low-pass spatial filtering and relay imaging, *Applied Optics* **17**, pp. 2053-2057, 1978.
- [29] HUNT, J. T., RENARD, P. A. (1979). U.S. Patent No. 4,158,176.

- [30] EDWARDS, B. L., ISRAEL, D., WILSON, K., MOORES, J. D., FLETCHER, A. S.: The Laser Communications Relay Demonstration, *Proc. International Conference on Space Optical Systems and Applications (ICSOS) 2012*, 1-1, Ajaccio, 2012.
- [31] EDWARDS, B. L., ISRAEL, D. J., WHITEMAN, D. E.: A Space Based Optical Communications Relay Architecture to Support Future NASA Science and Exploration Missions, *Proc. International Conference on Space Optical Systems and Applications (ICSOS) 2014*, S6-1, Kobe, 2014.
- [32] WILSON, K. E., ANTSOS, D., ROBERTS Jr., L. C., PIAZZOLA, S., CLARE, L. P., CROONQUIST, A. P.: Development of the Optical Communications Telescope Laboratory: A Laser Communications Relay Demonstration Ground Station, *Proc. International Conference on Space Optical Systems and Applications (ICSOS) 2012*, 3-3, Ajaccio, 2012.
- [33] HARTMAN, M., RESTAINO, S. R., BAKER, J. T., PAYNE, D. M., BUKLEY, J. W.: EAGLE: relay mirror technology development. *Proc. of SPIE* **4724**, Laser Weapons Technology III, 110, 2002; doi:10.1117/12.472368
- [34] SCHNEIDER, W. Jr. (Editor): Defense Science Board Task Force on Directed Energy Weapons, Office of the Under Secretary of Defense For Acquisition, Technology, and Logistics Washington, D.C. 20301-3140, 2007. [online]. [ref. 2015-09-21]. Available from:
<http://www.acq.osd.mil/dsb/reports/ADA476320.pdf>
- [35] BASS, M. (Editor): Handbook of Optics, Volume I, Third Edition. McGraw-Hill, New York, 2010.
- [36] HOPKINS, H. H. (1966). U.S. Patent No. 3,257,902.
- [37] HOPKINS, H. H. (1979). U.S. Patent No. 4,168,882.
- [38] DOBSON, S. J., HOPKINS, H. H.: A new rod-lens relay system offering improved image quality, *J. Phys. E: Sci. Instrum.* **22** pp. 450-455, 1989.
- [39] KING, H. C.: The History of the Telescope, Dover Publications, Inc., Mineola, 2003.
- [40] WILSON, R. N.: Reflecting Telescope Optics I, Springer-Verlag, New York, 1996. doi: 10.1007/978-3-662-03227-5
- [41] MANLY, P. L.: Unusual Telescopes, Cambridge University Press, Cambridge, 1991.
- [42] STANKE, L., THAKUR, A., MORRISSEY, M., KHIKHLUKHA, D., LE GARREC, B.: Role of Beam Propagation Method (BPM) Software in ELI-Beamlines, Poster presented at the ELI Scientific Challenges 2015.

- [43] WARREN, W. E.: MALAPROP User's Guide, Lawrence Livermore Laboratory, 1977.
- [44] HUNT, J. T., RENARD, P. A.: ARTEMIS: A Diffraction Model for Laser Light Propagation, Lawrence Livermore Laboratory, 1977.
- [45] DONNAT, P., PORCHER, T., TREIMANY, C., MORICE, O., RIBEYRE, X., GALLICE, G., NASSIET, D., L'HULLIER, N., RIVOIRE, V.: MIRÓ V5.22 User guide
- [46] DONNAT, P., PORCHER, T., TREIMANY, C., MORICE, O., RIBEYRE, X., GALLICE, G., NASSIET, D., L'HULLIER, N., RIVOIRE, V.: MIRÓ V5.22 Reference manual
- [47] DONNAT, P., PORCHER, T., TREIMANY, C., GOUÉDARD, C., MORICE, O., RIBEYRE, X., GALLICE, G., NASSIET, D., L'HULLIER, N., RIVOIRE, V.: MIRÓ V5.22 Case studies
- [48] WYROWSKI, F., KUHN, M.: Introduction to field tracing, *Journal of Modern Optics* **58**, pp. 449-466, 2011. doi: 10.1080/09500340.2010.532237
- [49] Zemax LLC. [online]. [ref. 2015-11-09]. Available from: <http://www.zemax.com/>
- [50] OpticStudio 15 Help Files, Zemax, LLC, 2015.
- [51] GOODMAN, J. W.: Introduction to Fourier Optics, McGraw-Hill, New York, 1968.
- [52] LAWRENCE, G. N.: Optical Modeling, *Applied Optics and Optical Engineering* **11**, pp. 125-200, 1992.
- [53] LightTrans VirtualLab™ User's Manual. LightTrans GmbH, Jena, 2015.
- [54] Wyrowski VirtualLab User's Manual. Wyrowski Photonics UG (haftungsbeschränkt), Jena, 2015.
- [55] KUHN, M., WYROWSKI, F., HELLMANN, C.: Non-sequential optical field tracing. *Advanced Finite Element Methods and Applications* **66** of *Lecture Notes in Applied and Computational Mechanics*, pp. 257-273. Springer Berlin Heidelberg, 2013.
- [56] Wyrowski VirtualLab Fusion Release Notes. [online]. [ref. 2015-11-19]. Available from: <http://www.lighttrans.com/>
- [57] PEITGEN, H.-O., JÜRGENS, H., SAUPE, D.: Chaos and Fractals, New Frontiers of Science, Springer Science+Business Media New York, New York, 1992.
- [58] BEGLERIS, I., CHRISTIAN, J. M., McDONALD, G. S.: Fresnel diffraction at snowflake apertures: symmetries & boundary conditions, *4th CSE Doctoral School Postgraduate Research Conference*, University of Salford, Greater Manchester, 2013. [online]. [ref. 2016-01-29]. Available from: <http://www.cse.salford.ac.uk/physics>

- [59] HORVÁTH, P., ŠMÍD, P., VAŠKOVÁ, I., HRABOVSKÝ, M. Koch fractals in physical optics and their Fraunhofer diffraction patterns. *Optik* **121** (2), pp. 206–213, 2010. [online]. [ref. 2016-01-29].
- [60] VENTEON | PULSEAPPS vCHIRP Dispersion Calculation Software [online]. [ref. 2016-01-29]. Available from:
http://www.venteon.com/vCHIRP/vCHIRP_Manual_v1.0.pdf
- [61] vCHIRP software | Laser Quantum UK [online]. [ref. 2016-01-29]. Available from:
<http://www.laserquantum.com/products/detail.cfm?id=82>
- [62] SIEGMAN, A. E.: *Lasers*, University Science Books, Sausalito, 1986.
- [63] MAHAJAN, V. N.: *Optical Imaging and Aberrations, Part I, Ray Geometrical Optics*, SPIE Press, Bellingham, 1998.
- [64] MAHAJAN, V. N.: *Optical Imaging and Aberrations, Part II, Wave Diffraction Optics, Second Edition*, SPIE Press, Bellingham, 2011.
- [65] MAHAJAN, V. N.: *Optical Imaging and Aberrations, Part III, Wavefront Analysis*, SPIE Press, Bellingham, 2013.
- [66] MAHAJAN, V. N.: Strehl ratio for primary aberrations: some analytical results for circular and annular pupils. *J. Opt. Soc. Am.* **72** (9), pp. 1258–1266, 1982.
- [67] STREHL, K.: Über Luftschlieren und Zonenfehler, *Z. Instrumentenk.* **22**, pp. 213–217, 1902.
- [68] MAHAJAN, V. N.: Strehl ratio for primary aberrations in terms of their aberration variance. *J. Opt. Soc. Am.* **73** (6), pp. 860–861, 1983.
- [69] HERLOSKI, R.: Strehl ratio for untruncated aberrated Gaussian beams. *J. Opt. Soc. Am. A* **2** (7), pp. 1027–1030, 1985.
- [70] MARTIAL, G.: Strehl ratio and aberration balancing. *J. Opt. Soc. Am. A* **8** (1), pp. 164–170, 1991.
- [71] VAN DEN BOS, A.: Aberration and the Strehl ratio. *J. Opt. Soc. Am. A* **17** (2), pp. 356–358, 2000.
- [72] MAHAJAN, V. N.: Strehl ratio of a Gaussian beam. *J. Opt. Soc. Am. A* **22** (9), pp. 1824–1833, 2005.
- [73] CASTAÑEDA-OJEDA, J., MARTÍNEZ-CORRAL, M., ANDRÉS, P., PONS, A.: Strehl ratio versus defocus for noncentrally obscured pupils. *Applied Optics* **33** (32), pp. 7611–7616, 1994.
- [74] DRIGGERS, R. G. (ed.): *Encyclopedia of Optical Engineering, Volume 2: Las-Pho*, Marcel Dekker, Inc., Adelphi, 2003.
- [75] PALATKA, M.: OAP combination analysis, PDF slides, 2016.

- [76] MORRISSEY, M., DE LUIS DE BLANCO, D. M.: Initial Proposal for the Beamlines Telescope, PDF document, 2016.
- [73] MORRISSEY, M., DE LUIS DE BLANCO, D. M.: Initial Proposal for the Beamlines Telescope, PDF document, 2016.
- [77] Thorlabs Wavefront Sensor. [online]. [ref. 2016-05-28]. Available from: https://www.thorlabs.com/newgrouppage9.cfm?objectgroup_id=2946
- [78] HOOKER, C.: Achromatic Beam Diagnostic Telescopes for Astra Gemini, PDF document.
- [79] Edmund Optics Protected Gold, Parabolic Mirror. [online]. [ref. 2016-05-28]. Available from: <http://www.edmundoptics.com/optics/>
- [80] ATC Astro Telescope Company, a.s., ATC N 450/f2000. [online]. [ref. 2016-05-28]. Available from: <http://www.atc-astro.eu/eshop/atc-n-450f2000.html>
- [81] Thorlabs Unmounted Achromatic Doublets. [online]. [ref. 2016-05-28]. Available from: http://www.thorlabs.de/newgrouppage9.cfm?objectgroup_id=259
- [82] LE GARREC, B., THAKUR, A., MORRISSEY, M., STANKE, L., KHIKHLUKHA, D.: Role of Beam Propagation Method (BPM) in ELI-Beamlines, PPT slides, 2015.
- [83] VAZQUEZ-OTERO, A.: Extreme Light Infrastructure (ELI) Science and Technology at the ultra-intense Frontier, PDF slides, 2015.
- [84] ISO 11146-2:2005 Lasers and laser-related equipment – Test methods for laser beam widths, divergence angles and beam propagation ratios – Part 2: General astigmatic beams.
- [85] SIEGMANN, A. E.: How to (Maybe) Measure Laser Beam Quality, Tutorial presentation at the Optical Society of America Annual Meeting Long Beach, California, October 1997 [online]. [ref. 2016-05-28]. Available from: <http://web.archive.org/>
- [86] LAWSON, J. K., AIKENS, D. M., ENGLISH, R. E. Jr., WHISTLER, W. T., HOUSE, W., NICHOLS, M. A.: Surface figure and roughness tolerances for NIF optics and the interpretation of the gradient, P-V wavefront and RMS specifications. *Proc. of SPIE* **3782** Optical Manufacturing and Testing III, 1999.
- [87] KUMLER, J. J., CALDWELL, J. B.: Measuring surface slope error on precision aspheres. *Proc. of SPIE* **6671**, Optical Manufacturing and Testing VII, 2007.
- [88] LASEROPTIK GmbH. [online]. [ref. 2016-05-28]. Available from: <http://laseroptik.de/>
- [89] IDEX Optics & Photonics, Fundamental Optics, Ultrafast Theory. [online]. [ref. 2016-05-28]. Available from: https://marketplace.idexop.com/store/SupportDocuments/Ultra_Fast_TheoryWEB.pdf
- [90] PIEGARI, A., FLORY, F. (eds.): Optical thin films and coatings, From materials to applications, Woodhead Publishing, 2013.

List of Author's Publications

In reviewed journals with impact factor

STANKE, L., ŠMÍD, P., HORVÁTH, P., ESPI correlogram analysis by two stage application of wavelet transform with use of intensity thresholding, *Optik* (IF = 0.670), 2015, 7–8 (126), pp. 865–870. doi:10.1016/j.ijleo.2015.01.037

Available from: <http://www.sciencedirect.com/science/article/pii/S0030402615000716>

In preparation for *Rev. Sci. Instrum.*: STANKE, L., THAKUR, A., ŠMÍD, M., GU, Y., FALK, K., Optical simulations of laser focusing for optimization of laser-produced betatron

In reviewed journals without impact factor

STANKE, L., *ELI Scientific Challenges 2015*, *Jemná mechanika a optika*, 2015, 60 (11-12), pp. 336.

STANKE, L., *Seminář o výrobě přesné optiky [Workshop on the precision optics manufacturing]*, *Jemná mechanika a optika*, 2014, 59 (4), pp. 123.

STANKE, L., ŠMÍD, P., HORVÁTH, P., Dvoufázová aplikace vlnkové transformace pro filtraci šumu a fázovou analýzu ESPI korelogramů s využitím intenzitního prahování (II. část) [Two stage application of wavelet transform for denoising and phase analysis of ESPI corre-lograms with use of intensity threshold, part II], *Jemná mechanika a optika*, 2014, 59 (5), pp. 133–137.

STANKE, L., ŠMÍD, P., HORVÁTH, P., Dvoufázová aplikace vlnkové transformace pro filtraci šumu a fázovou analýzu ESPI korelogramů s využitím intenzitního prahování (I. část) [Two stage application of wavelet transform for denoising and phase analysis of ESPI corre-lograms with use of intensity threshold, part I], *Jemná mechanika a optika*, 2014, 59 (4), pp. 122–123.

STANKE, L., CHLUP, F., *Přehled technologie laserových dálkoměrů v AČR [Review of Laser Rangefinder Technology in the Czech Army]*, *Jemná mechanika a optika* 2013, 58 (5), pp. 152 – 157.

STANKE, L., *Aplikace optických prvků pro transformaci ultrakrátkých intenzivních světelných pulzů [Application of optical elements for transformation of ultrashort intensive light pulses]*, *Jemná mechanika a optika* 2012, 57 (9), pp. 256 – 257.

Research reports

THAKUR, A., STANKE, L., Simulation Results, L3-E3: Holey Mirror Simulations, 2016, ELI Beamlines Internal Technical Report, Institute of Physics of the Czech Academy of Sciences. (Included in an appendix)

FENTE, G. M., ZULIC, H., THAKUR, A., STANKE, L., MORISSEY, M., KHIKHLUKHA, D., Calculations, Summary of Ongoing Optical Simulations, 2016, ELI Beamlines Internal Technical Report, Institute of Physics of the Czech Academy of Sciences. (Included in an appendix)

IVANOV, G., STANKE, L., PAVLÍČEK, P., HRABOVSKÝ, M., Opticko-mechanická sestava měřicí triangulační jednotky k měření clonek reaktoru pro JE, Univerzita Palackého, Přírodovědecká fakulta, Olomouc, 2014, summary research report, RIV/61989592:15310/14:33151928.

SCHOVÁNEK, P., KITTLER, M., PECH, M., PALATKA, M., STANKE, L., Vývoj technologie frézování optických prvků pomocí materiálů firmy KGS, Univerzita Palackého, Přírodovědecká fakulta, Olomouc, 2013, summary research report, RIV/61989592:15310/13:33147617.

Conference contributions

BORNEIS, S. H., ACCARY, J.-B., BRABEC, L., BUCKA, M., CALDERON, S., de LUIS, D., EIMERL, D., KORN, G., HEILAND, D., HEJDUKOVÁ, J., HVĚZDA, R., KHIKHLUKHA, D., KOROUŠ, P., KRAMER, D., LAŠTOVIČKA, T., LAUB, M., LEVATO, T., MARGARONE, D., MORRISSEY, M. J., PEYROT, D. A., PUST, L., RUS, B., ŘÍDKÝ, J., SOKOL, M., STANKE, L., THAKUR, A., VACULÍK, J., WEBER, S., ZIANO, R., ELI-beamlines and its ultrahigh intensity beam transport system. (Plenary presentation, Mini-Symposium: Review of Large-Scale, High-Power Laser Facility Projects I, Laser-Induced Damage in Optical Materials 2016, Millennium Harvest House Hotel Boulder, Colorado, United States 25 - 28 September 2016).

STANKE, L., THAKUR, A., MORISSEY, M., KHIKHLUKHA, D., LE GARREC, B., Role of Beam Propagation Method (BPM) Software in ELI-Beamlines, ELI Scientific Challenges 2015, (October 19-22, 2015), Zámek Štířín, (poster).

STANKE, L., KŘEPELKA, J., PALATKA, M., SCHOVÁNEK, P., HRABOVSKÝ, M., Application of optical elements for temporal and spatial transformation of ultra-short and ultra-intense light pulses, Proc. SPIE 8697, 18th Czech-Polish-Slovak Optical Conference on Wave and Quantum Aspects of Contemporary Optics, 869702 (December 18, 2012); doi: 10.1117/12.2006163 (WOS:000319864100002) (poster and proceedings)

STANKE, L., HORVÁTH, P., ŠMÍD, P., HRABOVSKÝ, M., The use of 1-bit numerical correlation in the measurement of an object's translation by speckle correlation, OPTIMESS 2012, (April 4–5, 2012) Optical Measurement Techniques for Systems&Structures, eds. J. Dirckx, J. Buytaert, pp. 391 – 400 (poster and proceedings) (WOS:000319343800039)

Utility models

ŠMÍD, P., HORVÁTH, P., HRABOVSKÝ, M., STANKE, L., Zařízení pro bezkontaktní detekci absolutní polohy pohybujícího se předmětu s využitím jevu koherenční zrnitosti [Apparatus for contactless detection of moving object absolute position by making use of speckle], 2013-27545, 25644.

Patents

HORVÁTH, P., ŠMÍD, P., HRABOVSKÝ, M., STANKE, L., Způsob bezkontaktní detekce absolutní polohy pohybujícího se předmětu s využitím jevu koherenční zrnitosti a zařízení k provádění tohoto způsobu [Method of contactless detection of moving object absolute position by making use of speckle phenomenon and apparatus for making the same], 2013-164, CZ 304 207 (B6).

Others

STANKE, L., Metodika broušení optických elementů na CNC strojích Zeeko IRP-800G, rigorous thesis, Univerzita Palackého, Přírodovědecká fakulta, Olomouc, 2014.

STANKE, L., Elektronická interferometrie na bázi koherenční zrnitosti a její aplikace, master's thesis, Univerzita Palackého, Přírodovědecká fakulta, Olomouc, 2013.

STANKE, L., Aplikace optických prvků pro časovou a prostorovou transformaci ultrakrátkých intenzivních světelných pulsů, master's thesis, Univerzita Palackého, Přírodovědecká fakulta, Olomouc, 2012.

STANKE, L., Aplikace optických prvků pro časovou a prostorovou transformaci ultra-

krátkých intenzivních světelných pulsů, Annual student competition „O cenu děkana 2012“ (“The dean’s prize 2012”), VUP, Olomouc, 2012.

STANKE, L., Vliv typu numerické korelace struktur koherenční zrnitosti na měření translace zkoumaného předmětu metodou na korelace polí koherenční zrnitosti, bachelor’s thesis, Univerzita Palackého, Přírodovědecká fakulta, Olomouc, 2010.

STANKE, L., Vliv typu numerické korelace struktur koherenční zrnitosti na měření translace zkoumaného předmětu metodou na korelace polí koherenční zrnitosti, Annual student competition „O cenu děkana 2010“ (“The dean’s prize 2010”), VUP, Olomouc, 2010.

Index

Argus, 20

ARTEMIS, 37

Combined SPW/Fresnel Operator, 65

Cyclops, 19

Far Field Operator, 66

Fresnel Propagation Operator, 65

Janus, 18

Malaprop, 36

Miró, 42

NIF, 24

Nova, 22

OpticStudio, 48

PALS, 28

Rayleigh Sommerfeld Operator, 63

Shiva, 21

Spectrum of Plane Waves Operator, 63

Wyrowski VirtualLab Fusion, 61

Zemax, 48

Appendix

	Document No.:	00000XXX
	Edition:	1
	Process:	REP
	No. of pages:	77

Calculations

Summary of Ongoing Optical Simulations

	Position	Name	Signature	Date
Prepared	Optical Engineer	Gashaw Fente		
	Optical Engineer	Haris Zulic		
	Optical Engineer	Anita Thakur		
	Optical Engineer	Ladislav Stanke		
	Applied Physicist	Michael Morrissey		
	Theoretical Physicist	Danila Khikhlukha		
Approved				

Table of Contents

1. Introduction	3
2. Summary of L3 Beamlines	4
2.1 L3 Mirror Parameters	4
2.2 Implementation of Beamlines in Zemax	4
2.3 Comparison of Beamlines	5
3. L3 Source and Propagation	6
3.1 L3 Source Parameters	6
3.2 L3 Free Space Propagation	7
4. Beamline Analysis I3 - e3	10
4.1 Implementing Surface Irregularities	10
4.2 Beamlines Analysis	12
5. Case Study: Focusing Optics of L3 –E3	15
5.1 Focusing Optics: Parabolic Vs Spherical mirror	15
5.2 Preliminary Configurations and Simulations	16
6. Currently Ongoing Simulation Activities	20
6.1 Implementation of other beamlines in Zemax & VirtualLab	20
6.2 Focusing Regimes	20
6.3 Surface Irregularity	22
6.4 Phase and intensity Modulations	22
7. Summary and Outlook	24
The following a brief summary of the workload of the simulations:	24
7.1 Complete and Ongoing Work	24
7.2 Outlook – not too distance future	24
Temporal Profiles	24
Diagnostic stations:	24
7.3 Outlook – the distant future	25

1. INTRODUCTION

The primary objective of the ELI-Beamlines facility is to develop short pulse secondary sources such as x-rays, plasma, and particle beams. These secondary sources will be generated by a number of high-power, high-repetition-rate lasers with focused intensities of about 10^{23} W/cm², which can be combined to perform a multitude of experiments in a wide variety of field in science.

For the successful operation of ELI-Beamlines optical engineers, physicists, researchers and engineers alike require several software tools to aid in the design, simulations, optimization and running of various laser systems as well as to predict system performance and tolerances. This report deals with results obtained with the use of commercially available optical simulation softwares, namely Zemax – Optical Studio and VirtualLab – Fusion. These simulations are performed with the desire to aid in the successful design and implementation of the ELI-Beamlines facility as well as predict system performance and tolerances.

2. SUMMARY OF L3 BEAMLINES

Due to its current importance, this report deals mainly with the L3 Beamlines. We are essentially using L3 beamlines as a test-bed for simulations which can be applied to other beamlines once the procedures are developed and tested. The L3 laser propagates to experimental rooms E2 (Betatron - Compton), E3 (P3 - Plasma Source), E4 (ELIMAIA), and E5 (HELL).

2.1 L3 Mirror Parameters

All mirrors are assumed to be the same.

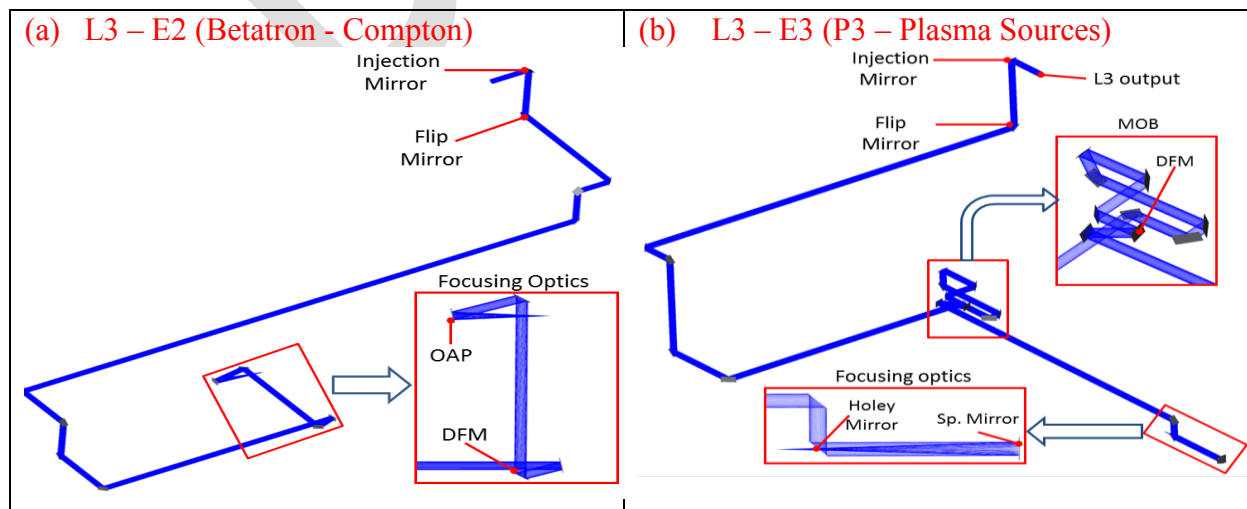
Table 1: Summary of mirror characteristics

Parameter	Value
Physical Dimensions	
Size (CA)	250 x 360 mm
Thickness	55 mm
Angle of incidence	45 degrees
Central Wavelength	820 nm
Surface quality	$\sim\lambda/10$
Coatings	
Central λ	820 nm
Bandwidth	>100 nm

Assumed Coating Spectrum

2.2 Implementation of Beamlines in Zemax

The coordinates for all the L3 beamlines were implemented in Zemax in order to simulate the beamlines. Schematic illustrations are shown below.



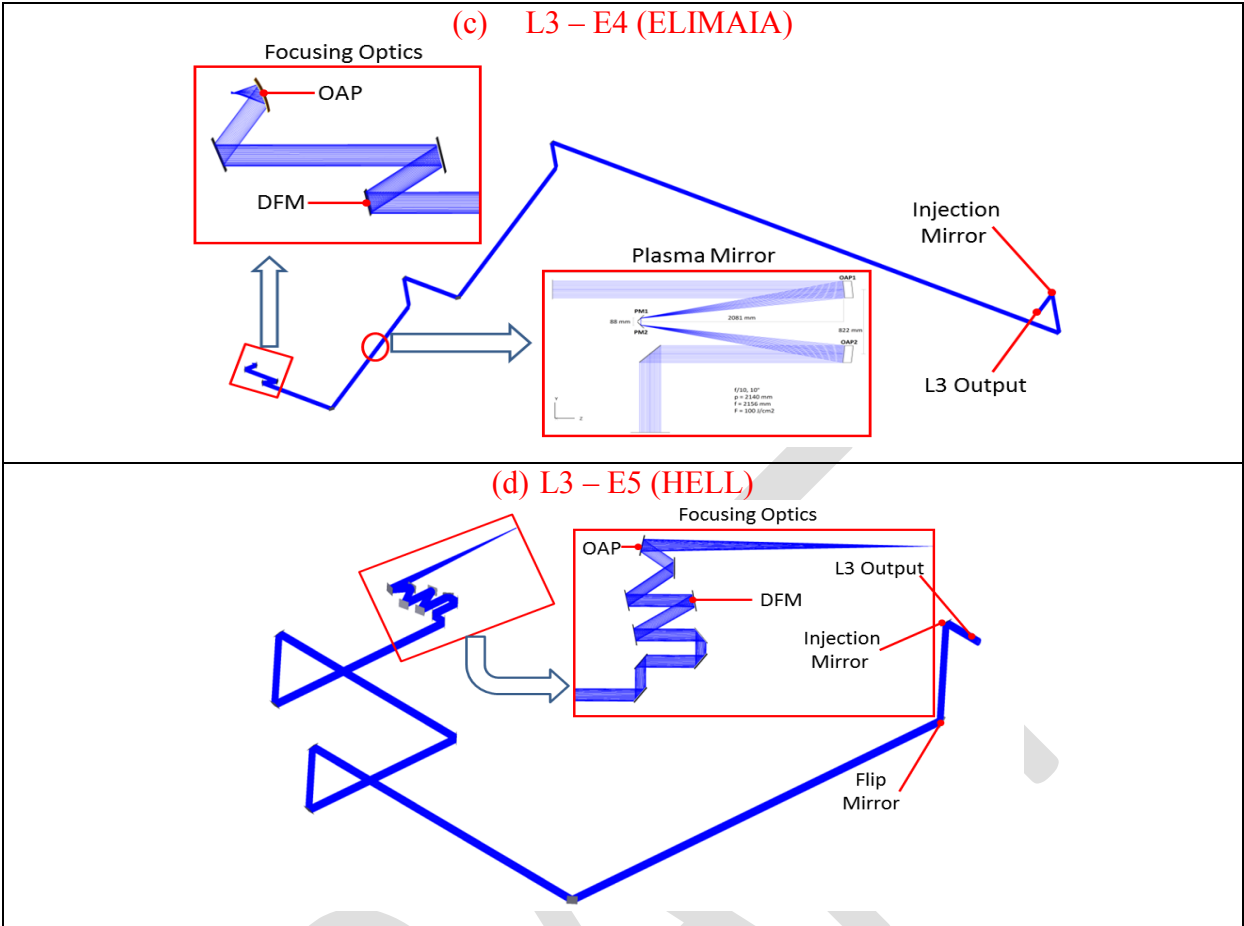


Figure 1: Schematic of L3 beamlines in Zemax

2.3 Comparison of Beamlines

Shown below are some of the main system parameters of the L3 beamlines.

Table 2: Summary of L3 Beamlines

	L3 - E2	L3 - E3	L3 - E4	L3 - E5
Beam Path (mm)	62687	65400	80773	69916
Mirrors (incl. DFM)	13	18	16*	17
DFM position	11	15	13	14
Focusing Optic	OAP f = 2 m $\theta = 10^\circ$ f# = ~6	Spherical mirror f = 3 m f# = ~9	OAP f = 375 mm $\theta = 50^\circ$ f# = ~1	OAP f = 6 m $\theta = 26^\circ$ f# = ~18

*Including the OAP's (M9 & M10) used in the plasma mirror setup.

3. L3 SOURCE AND PROPAGATION

3.1 L3 Source Parameters

The following are the assumed Laser parameter for the output of L3

$$I = \exp \left[-2 \left(\left(\frac{x}{w} \right)^G + \left(\frac{y}{w} \right)^G \right) \right]$$

Table 3: Summary of L3 Source beam

Parameter	Value	Parameter	Value
Spatial		Spectral	
FWHM	214 mm	Central λ	820 nm
1/e ²	225.6 mm	Bandwidth	100 nm
1/e	220		
Order (G)	20		
Divergence	5.37 μ rad		
Edge (10 - 90%)	16.2 mm		
Energetics			
Energy	30 J		
Power	1.5 x 10 ¹⁵ watts		
Peak Fluence	66 mJ/cm ²		

The figure below shows the ideal L3 source beam simulated using the above parameters

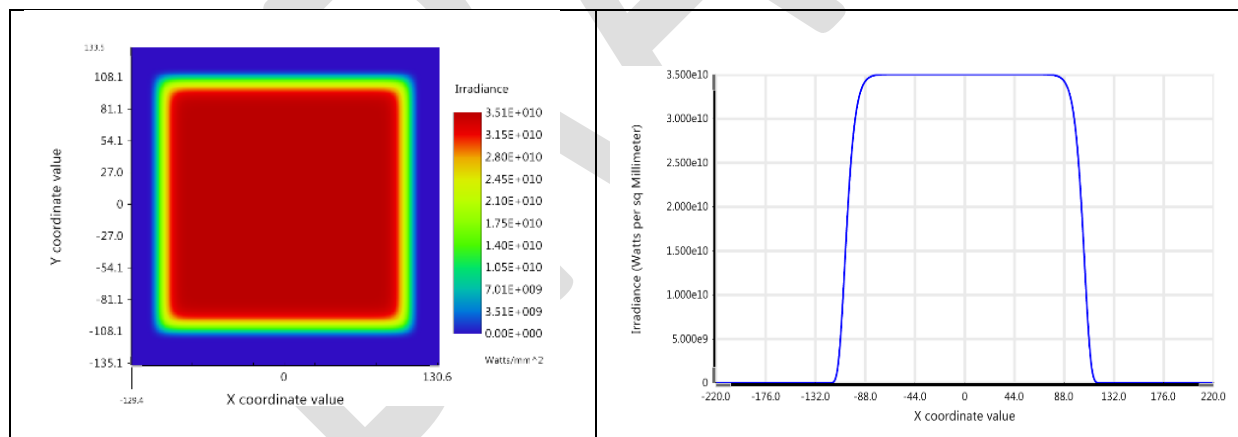


Figure 2: Ideal L3 source beam

A Python program has been written to create a representative L3 source beam which can produce a source with various characteristics such as diameter and super- Gaussian order. In reality, the output beam of the L3 laser will have some intensity and phase modulations due to the amplification and compression processes. To determine the response of the system on different types of initial beam imperfections several types of modulation have been implemented. They can be split into three groups which represent random Gaussian noise, random harmonic noise and patterned intensity modulations such as standing wave. The

properties of these modulations are also implemented in this script allowing us to control modulation pattern, spatial frequency, and amplitude. Described above are intensity modulations. However they may be applied to the phase as well.

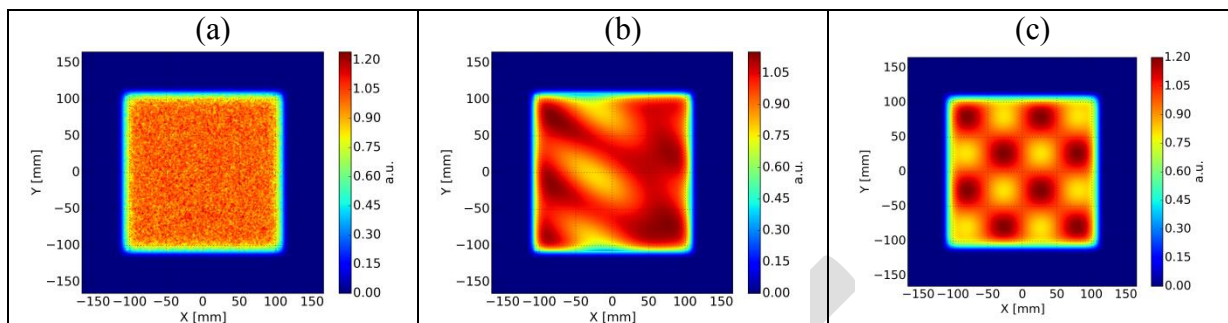


Figure 3: samples of some intensity modulated L3 beam profile (a) high frequency noise, (b) harmonic noise, (c) standing wave pattern

3.2 L3 Free Space Propagation

In this section the beam's free space propagation is discussed. The calculations were performed to estimate the amplitude of the diffraction ripples after certain propagation distance. The initial estimation was done using the Fresnel free space propagator implemented in Python. These calculations showed that for super-Gaussian beams of the order 20, after 100 m of free space propagation the amplitude of the diffraction ripples are small – below 1% of the maximum intensity amplitude.

To verify this number a rigorous simulation using Plane Wave Spectrum propagator (which doesn't employ Fresnel approximation) was performed in VirtualLab-Fusion. The results of these two calculations are in a good agreement. Below we discuss a VirtualLab simulation.

The simulation was performed for the L3 – E4 beamline, which is the longest beamline in ELI-Beamlines (80.7 m to the focal point). The following are super-Gaussian beam profiles over this distance for varying super-Gaussian orders ($G = 100$ and 20). The 2-D plots show the beam cross-section at various propagation distances. The 3-D plots show the accumulation of 2-D cross-sections as a function of propagation distances.

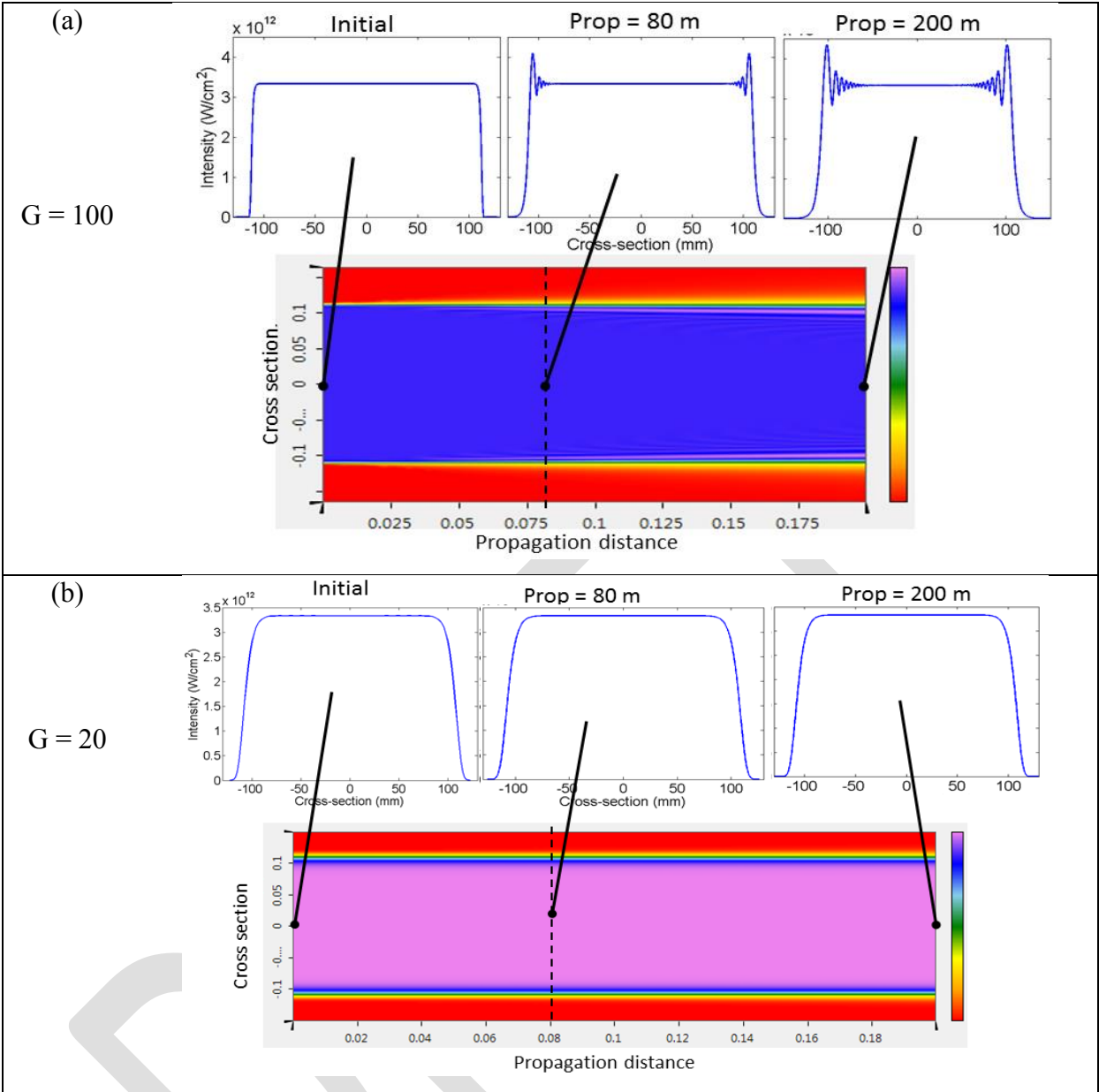


Figure 4: Intensity plots (2-D and 3-D) of L3 beam after propagating distances of 0, 80 and 200 m (a) $G=100$ (b) $G=20$.

It can be seen that for larger orders of a super-Gaussian beam ($G = 100$), large scale intensity modulations at the edge of the beam are evident after the beam has propagated a distance in the range of the largest beamline (80 m). These modulations increase as the beam propagates further. Clearly these modulations are due to diffraction during propagation. These effects can be eliminated by increasing the effective Rayleigh range by choosing a large beam radius (and/or an appropriate low order) or including a relay imaging system. When the simulation was repeated for $G = 20$ (which is the envisaged L3 super-Gaussian order), these diffraction ripples did not persist. Although the diffraction ripples are not visible on the intensity scale of

the beam, smaller ripples are expected as can be seen from the following plots for a beam propagation of 80 m and only viewing the flat-top part of the beam (120 x 120 mm).

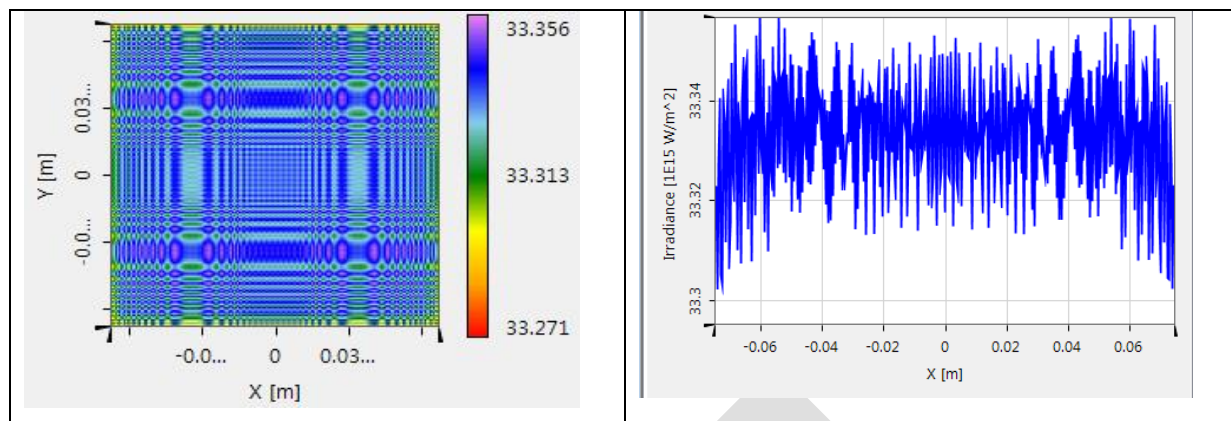


Figure 5: Central region of propagated L3 beam

The above image represents the profiles for the L3 source beam after 80 m of propagation. It can be seen that there are in fact modulation. This modulation however, is in the order of 1% of the maximum intensity.

DRAFT

4. BEAMLINER ANALYSIS L3 - E3

In order to specify optical components, parameters should be simulated and bench-marked to assess their performance in the optical system. Currently there are several beamline characteristics that are of concern and require analysis; wavefront error, focal spot parameters, aberrations etc.

4.1 Implementing Surface Irregularities

The surface irregularity (SI) of the optical components becomes critical when considering the parameters of the focal spot. Therefore, these SI's need to be implemented to have a better understanding of the expected parameters and to be able to determine what SI is sufficient to preserve suitable beam characteristics. These are implemented using the TEZI operand which generates random irregular deviations of small amplitude on the mirror surfaces. These irregularities are produced using the Zernike Standard Sag surface. In the simulations performed here, Zernike coefficient to the 2nd – 5th orders are implemented allowing only low frequency irregularities across the surface. The Surface RMS value is entered and Zemax then generates a surface profile which corresponds to this RMS value and can be described by the specified Zernike coefficients. Clearly there are many variations of Zernike coefficients that can have the same RMS value. Thus a Monte Carlo simulation is performed (~500 cycles) whereby the worst case (in terms of WFE or focal spot) of all calculated Zernike polynomials is determined.

There is however a problem using the TEZI operand in Zemax. This operand uses a unit circle, of user defined radius, to define the area in which to apply the surface irregularities. Given that our mirrors are rectangular in shape there are several options as to the circular implementation of the SI.

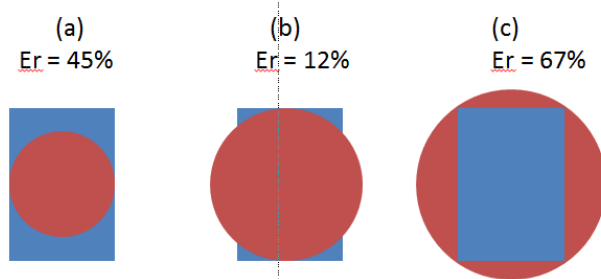


Figure 6: illustration of SI implementation (red) compared to actual mirror (blue)

In the cases illustrated in Figure 6, the surface irregularity will be applied to part of the mirror ((a) and (b)) or only part of the SI will be applied to the mirror (c). Options (a) and (b) will create a sharp edge in the mirror surface where it goes from flat to irregular. The sum of all

these sharp edges has a negative effect in focal spot calculations. Option (c) removes the sharp edges on the surface profile but induces a large error due to the mirror-IS area mismatch. There are several solutions to this which are currently being developed and will be implemented in the future.

- Perform the SI calculations externally for rectangular surfaces and import them into Zemax. To rescale the Zernike polynomials to a rectangular area one has to apply Gramm-Schmidt orthogonalisation process and rescale the normalisation coefficients. As a result the coefficients for new polynomial series will give an RMS of balanced aberrations.
- Use interferometric data obtained from the mirrors (mirrors not available yet) and import into Zemax.

There are three cases of surface irregularity considered

Table 4: Applied values of surface irregularities

Irregularity	P-V (nm)	RMS (nm)	Comments
$\lambda/10$	82	16	Recommended
$\lambda/6$	137	27	Mid-range
$\lambda/4$	205	41	Worst case

In order to show some results, option (c) from Figure 6 was implemented. The RMS values were implemented in Zemax using the TEZI function, and 500 Monte Carlo simulations were run for Zernike coefficients Z2 –Z5 and the worst cases (in terms of focal spot radius) for each irregularity setting were extracted. The amount of tip/tilt, defocus, astigmatism etc in the wavefront can be deduces from the values of the Zernike polynomial coefficients.

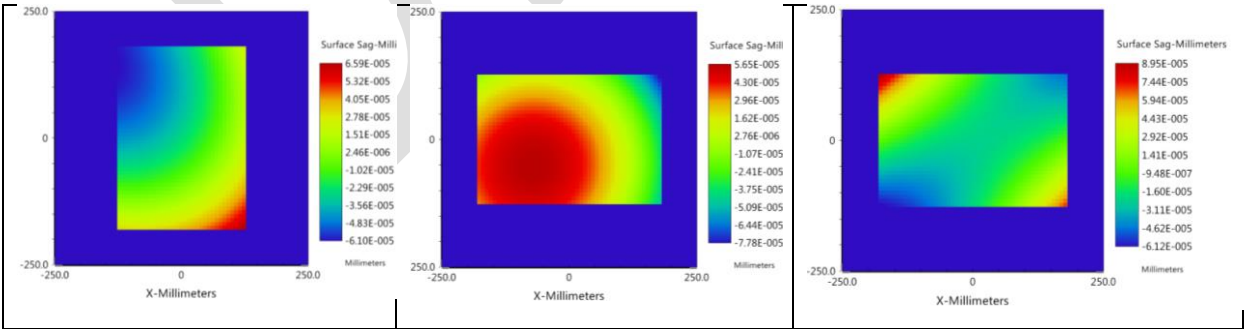


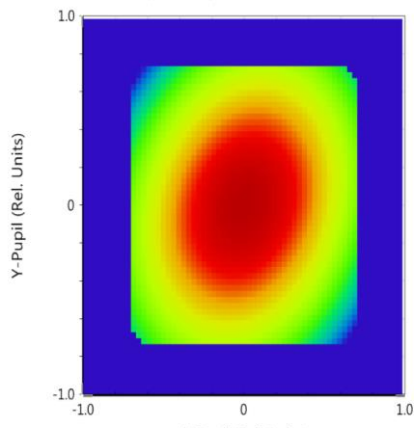
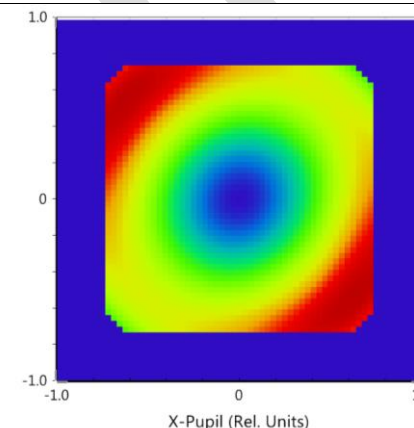
Figure 7: Sample surface profile of 3 different mirrors with a surface irregularity of 41 nm RMS ($\lambda/4$ P-V) implemented using Zernike polynomials

4.2 Beamlines Analysis

The L3 - E3 beamlines was used for analysed. The following are some results that were achieved using the ideal L3 beam which is described in Figure 2. It should be noted that the SI's were implemented using option 3 in Figure 6. This will obviously induces an error caused by using circular Zernike polynomials for the rectangular mirrors. The following are some of the typical analysis that will be performed for each surface irregularity criteria (once the correct implementation of SI is devised) and the results compared to determine the optical setups which provide adequate results for ELI-Beamlines.

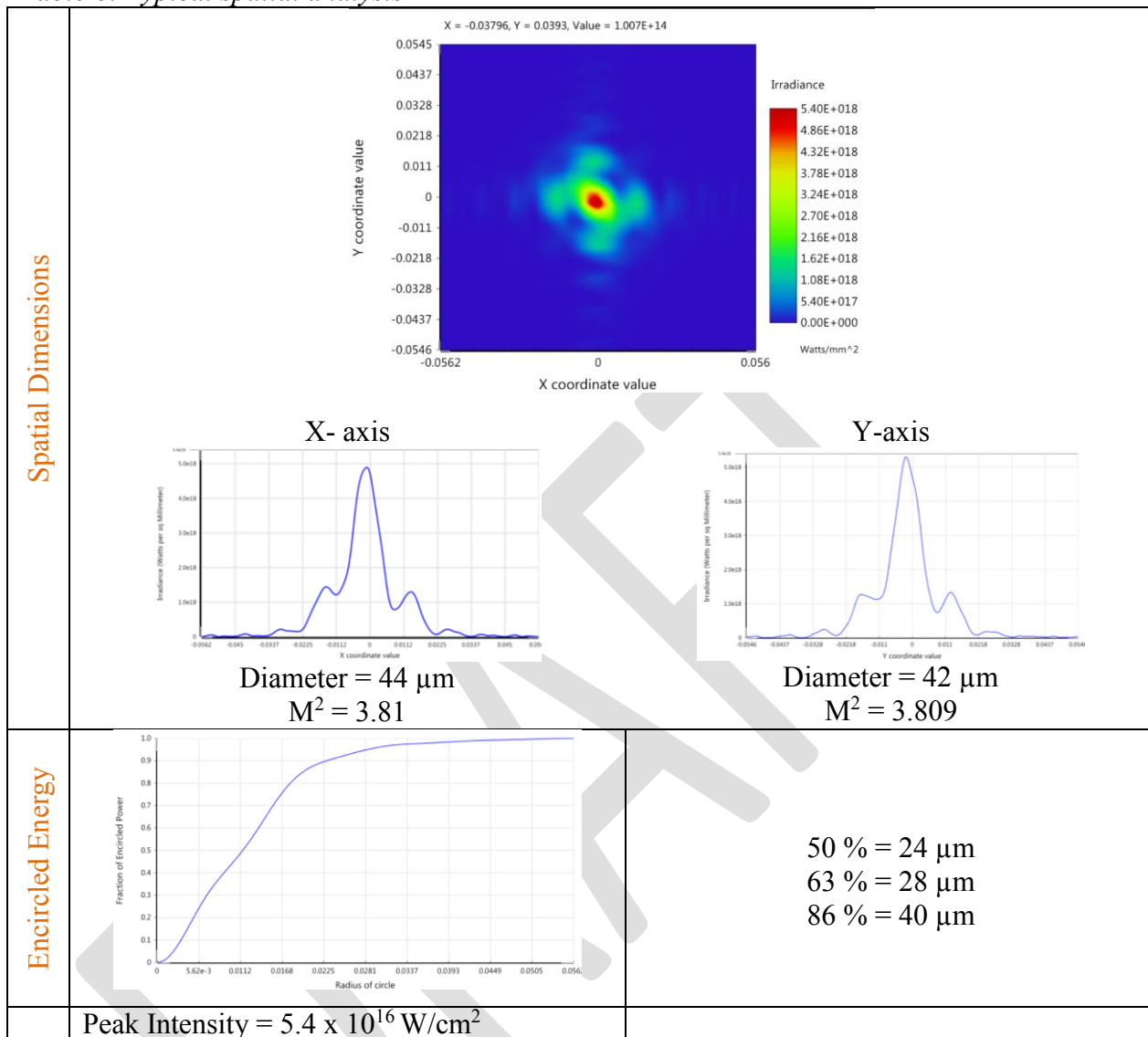
Wavefront Error:

Table 5: Typical Wavefront analysis

Deformable Mirror	 <p style="text-align: center;"> $PV = 0.378\lambda$ or 310 nm $RMS = 0.075\lambda$ or 61.5 nm </p>	Z1 -0.11174722 Z2 -0.00000001 Z3 -0.00000007 Z4 -0.06451729 Z5 -0.05117207 Z6 0.02099013 Z7 -0.00000003 Z8 0.00000000 Z9 0.00000000 Z10 0.00000002 Z11 0.00000000 Z12 0.00000000 Z13 0.00000000 Z14 0.00000000 Z15 0.00000000
Focal Spot	 <p style="text-align: center;"> $PV = 0.5602\lambda$ or 460 nm $RMS = 0.146\lambda$ or 120 nm </p>	Z1 0.34804002 Z2 0.00003154 Z3 -0.00006178 Z4 0.10058725 Z5 -0.05537999 Z6 0.00779007 Z7 -0.00002225 Z8 0.00001143 Z9 -0.00000002 Z10 0.00000007 Z11 -0.07809859 Z12 -0.00001371 Z13 -0.00005368 Z14 -0.00000016 Z15 -0.00000006

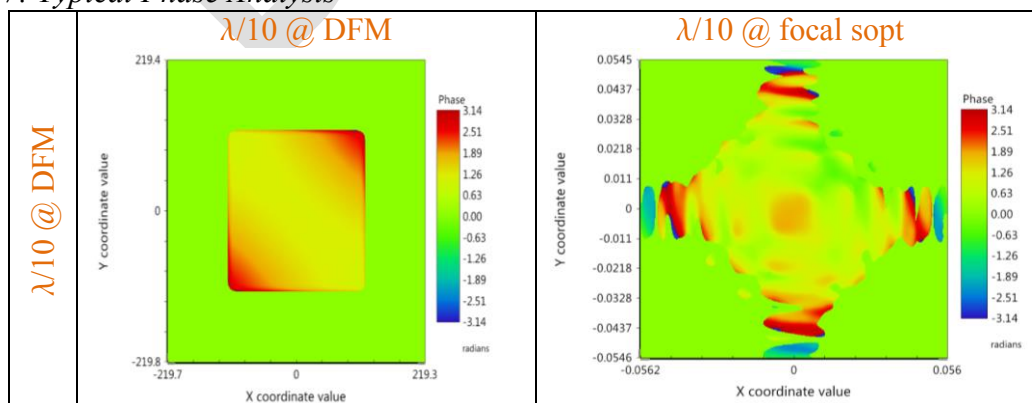
Spatial

Table 6: Typical spatial analysis



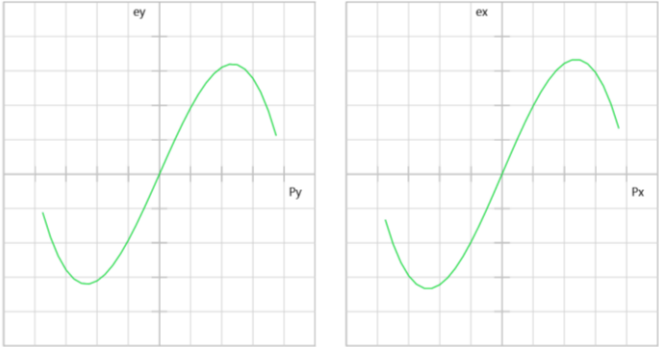
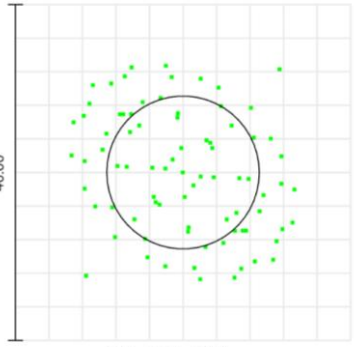
Phase:

Table 7: Typical Phase Analysis



Aberrations:

Table 8: Typical aberration analysis

	<p>OPD Diagram</p> 	<p>Ray Spot Diagram</p> <p>OBJ: 0.0000 (deg)</p>  <p>IMA: 0.001, 0.001 mm</p>	
	<p>Tilt Defocus Spherical Coma Astigmatism Curvature Distortion</p>		

DRAFT

5. CASE STUDY: FOCUSING OPTICS OF L3 –E3

Due to spatial constraints in the E3 target chamber the following focusing system, c.f. Figure 8(a) for the L3 – E3 was proposed. The optical component before the spherical mirror is a standard L3 mirror (as described above) with a hole in the centre (i.e. nicknamed “holy mirror”). Once the L3 beam is reflected from this surface, a portion of the incident beam will be cut from the centre of the L3 beam, the cross-sectional profile of which can be seen in Figure 8(b). This is then reflected off the spherical mirror, counter propagated and focused through the holy mirror to the focal point. For this case study, VirtualLab was used.

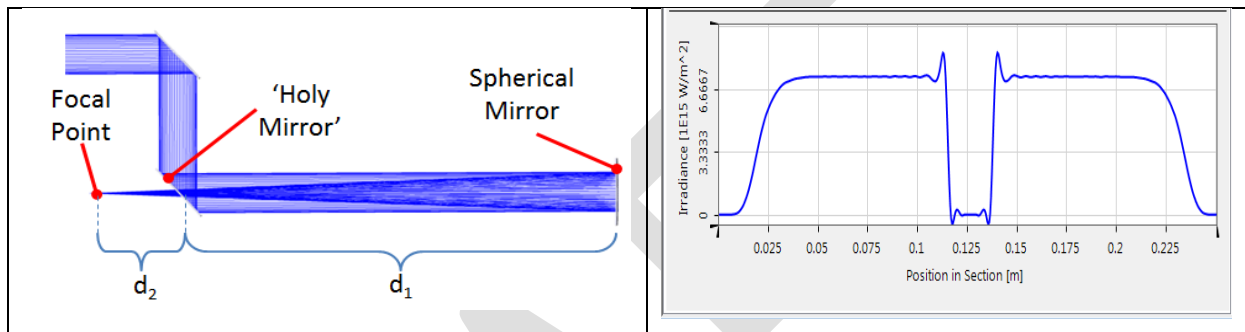


Figure 8 (a) focusing optics of L3 – E3 (b) cross-section after holey mirror

From Figure 8(b), it can be clearly seen that there are intensity ripples induced by the holy mirror. The effect of this hole on reflection and transmission (during focusing) of the holy mirror need to be simulated.

5.1 Focusing Optics: Parabolic Vs Spherical mirror

Initially, simulations were performed for the above system whereby results (M^2 , encircled energy and radius) for two different focusing optics, axial parabolic mirror and spherical mirror, were compared. It could be seen that the parabolic mirror eliminates spherical aberration which results in higher peak intensity. For the system with incorporated parabolic mirror, the vicinity of the focal plane is symmetrical whereas it's not the case with spherical one.

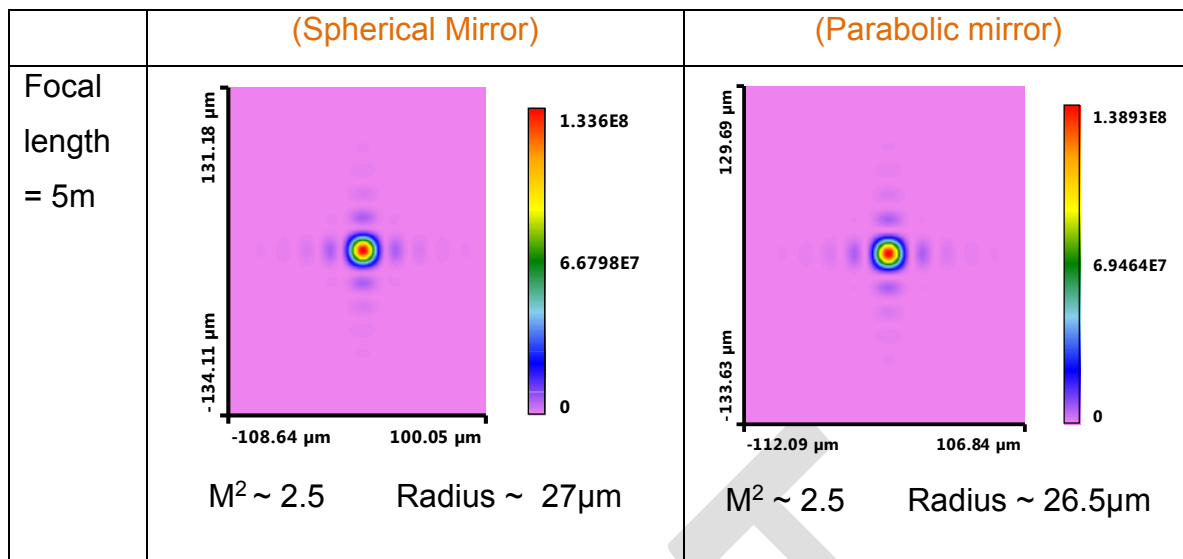


Figure 9: Focal spot for spherical and parabolic mirrors

5.2 Preliminary Configurations and Simulations

In fact there are several proposed dimension of this setup

Table 9: list of L3-E3 focusing configurations

Focal Length (mm)	Hole Diameter [mm]	f/#
3000	20	f/10
3000	50	f/10
5000	20	f/15
5000	50	f/15

By the means of so called parameter run within the VirtualLab-Fusion, a set of general experiments were conducted. The acquired results were then exported to the MATLAB for further processing. The study focused on the investigation of the power throughput for various hole sizes (Figure 10). Also, the quality of obtained encircled energy values were compared to the diffraction limited encircled energy for the beam focused by an ideal lens of the same focal length (Figure 11). Ideal size of the hole for the experimental geometry with the 3 m focal length of the spherical mirror can be derived from the figure showing the evolution of the encircled energy while changing the hole size (Figure 12).

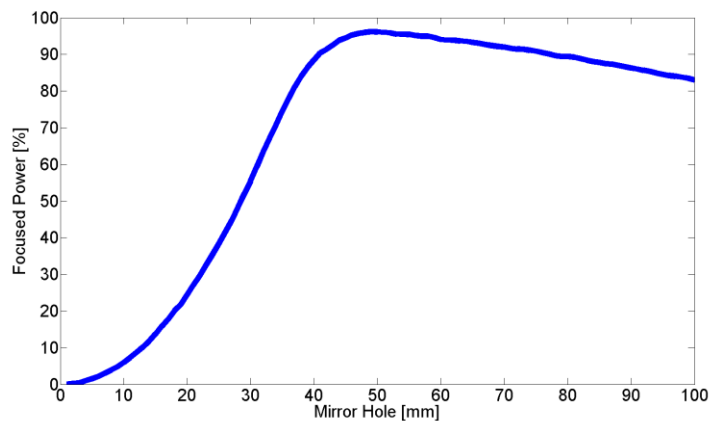


Figure 10: Percentage of power at the focal point as a function of hole diameter (for the focal length $f=3$ m of the spherical mirror)

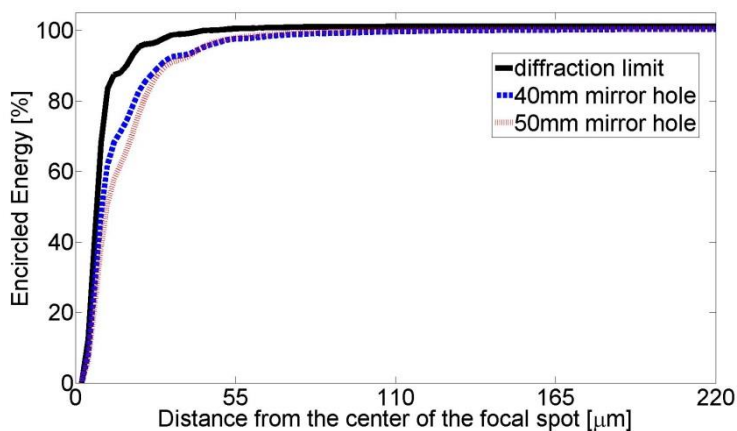


Figure 11: Encircled energy comparison for three different cases (for $d_1 = 40$ mm and $d_2=50$ mm and diffraction limited focus without the influence of any hole) for $f=3$ m

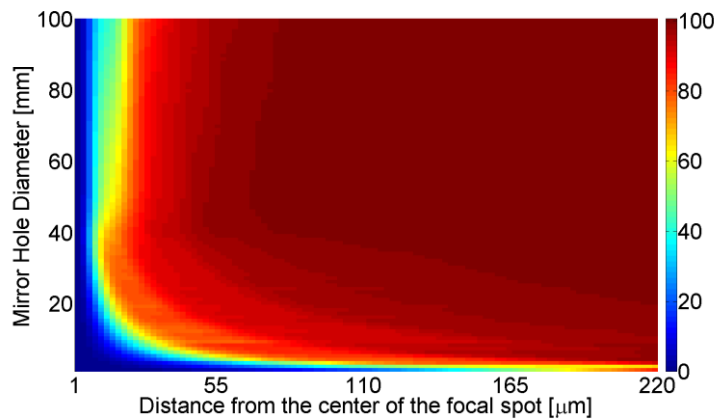


Figure 12: Encircled energies reachable at the focal length $f=3$ m of the spherical mirror for various hole sizes

Since the L3 beam will not be Gaussian, a set of simulations for a square beam with supergaussian profile were performed. A spherical mirror with focal length of 3 or 5 m was used as the focusing element, and the influence of the hole in the mirror was studied. The results are shown and discussed in following plots:

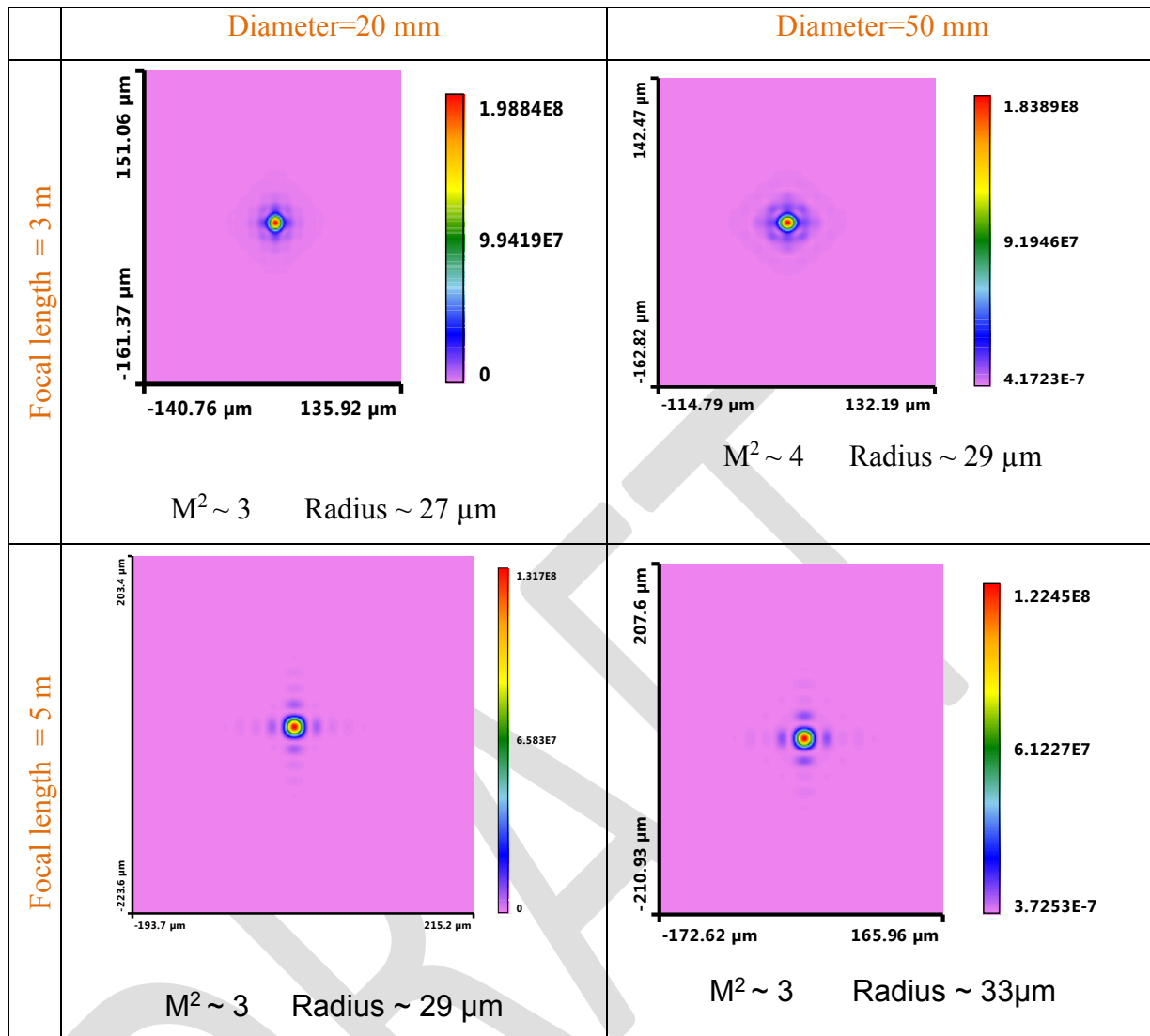


Figure 13: Focal spot results for given focal lengths and hole diameters.

Comparing the above outcomes of focus spots, it is obvious that due to the spherical aberration; it is far better to use mirrors with longer focal lengths as high NA mirrors are prone to spherical aberration more than those with low NA. Also, the beams with larger hole have typically worse M^2 factor and lower peak intensity. Moreover, greater the hole diameter means larger focal spot radius, as well.

Although surface and beam's phase irregularities are not included but still few important conclusions can be drawn. Shorter focal length means higher peak intensity, but on the expense of the spot size quality. So, the priority between the focal spot quality and the peak intensity needs to be clearly defined and discussed. Another important conclusion is that the hole helps to suppress the effects of square beam diffraction, at least to some extent.

From analysis of the above scenarios, it was evident that, it is much better to use mirrors with longer focal lengths as high NA mirrors are prone to spherical aberration more than those with low NA. Also, larger the hole diameters typically have worse M^2 factor (as per the Figure – for the sizes between 5 and 30 mm), larger focal spot and thus lower peak intensities.

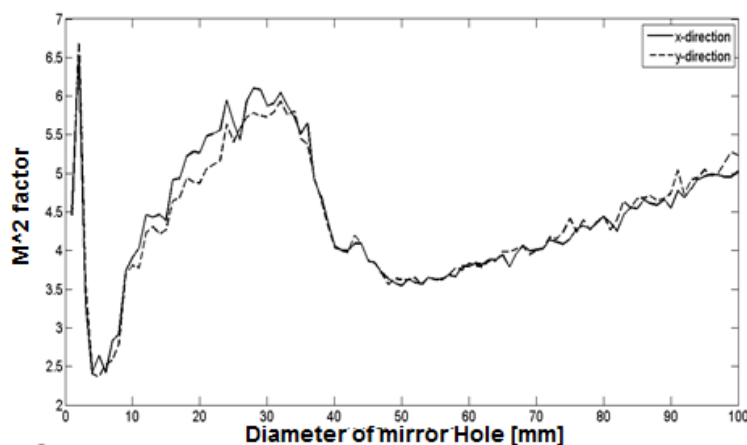


Figure 14: M^2 value as a function of hole diameter

It should be noted that these simulations are not counting for phase irregularities of the input beam, only aberrations and diffraction are included. The detailed report on Holey mirror simulations can be found in a separate report which can be provided on request ([S:\Control systems Team\4.5 Performance Group Share\4.5.1 BPM\Optical Simulations\Simulation Reports](#)). This includes several case studies with different focal length, hole diameters and mirror positions.

The preceding tests will be improved with added surface irregularities on the planar mirrors and the phase irregularities of the input beam (with dummy glass phase plate). Unfortunately, with the current state of the Virtual Lab software, we cannot apply the surface irregularities on the spherical mirror.

6. CURRENTLY ONGOING SIMULATION ACTIVITIES

6.1 Implementation of other beamlines in Zemax & VirtualLab

This report shows the implementation of L3 beamlines only. Other beamlines are also being implemented. In particular, L1 – E1 which has 9 main beam paths, including two identical lasers, three target chambers, 2 auxiliary beams, and several delay lines. We are however using L3 beamlines as a prototype/benchmark to implement and develop all techniques required for accurate simulations and which can then be applied to other beamlines.

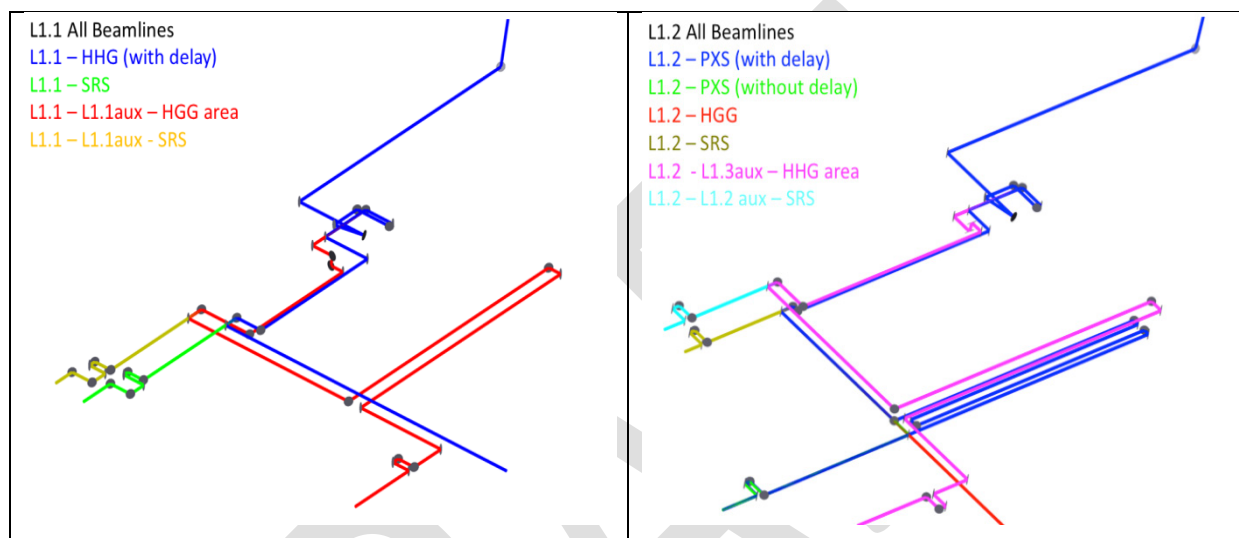


Figure 15: Implementation of L1 beamlines in Zemax

6.2 Focusing Regimes

As can be seen from Figure 1 and Table 2, even for L3 there are several focusing regimes. The surface roughness of the focusing optics (spherical mirrors and off-axis parabolas) is thought to be critical regarding the quality of the focal spot. This has already been observed with some initial preliminary calculations. In all the focusing systems shown below, the effect of the surface irregularity of the focusing optics on the focal spot was compared to the effect of the SI for flat mirrors. In all cases it was observed that the focal spot is more susceptible to aberrations due to SI on the curved surface (focusing optics) than in flat surfaces. This means that the SI for the focusing optics will require a much higher specification. This requires a more intensive study. The WFE will also need to be investigated for SI of the focusing optics under these conditions

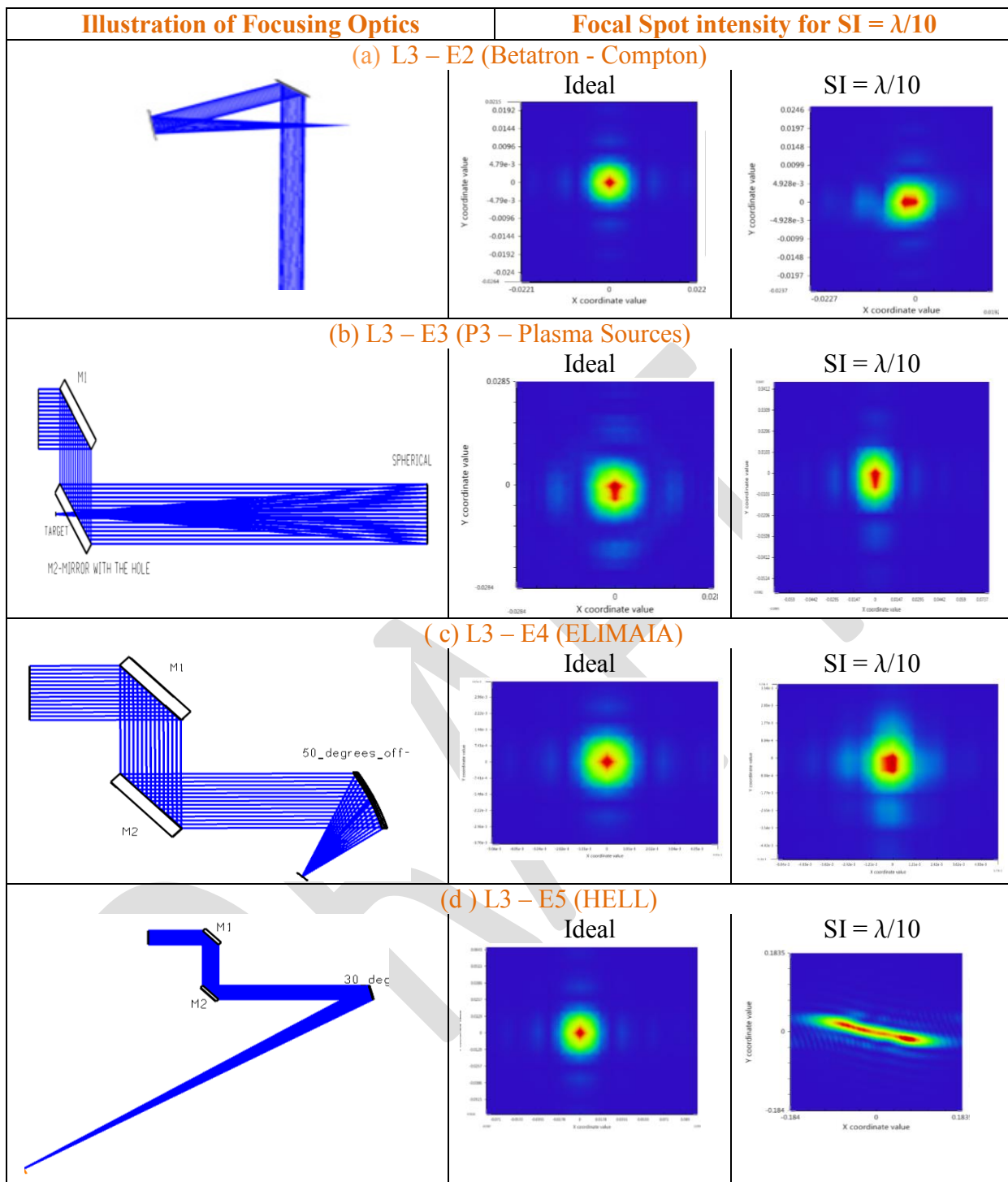


Figure 16: Focusing regimes for the L3 beamlines as well as some focal spot analysis S_i implemented in the focusing optics

A thorough investigation needs to be performed in order to determine the suitable surface irregularity of the focusing optics. A direct comparison of the parameters of the focusing optics ($f\#$, surface irregularity) will be compared to the parameters of the focal spot (M^2 , Strehl ratio, diameter, encircled energy, peak intensity, spot diagram etc.). By doing this we will determine the focusing parameter which create the most appropriate focal spot. The

minimum requirement of the curved surfaces needs to be determined due to the difficult and expensive procedure required to polish them

6.3 Surface Irregularity

Rectangular Polynomial

Using a Python code, we are developing a method to implement surface irregularities using Zemax polynomials and importing them into Zemax.

Gravitational sag and mounting stresses

Mechanical simulations are being performed with the aid of a CAD software, whereby surface deformations due to long-term gravitational sag and mechanical stress caused by mounting apparatus are being implemented and added to the already existing surface irregularity. These deformations will be added to the standard surface irregularities and imported into Zemax for further optical analysis of the system.

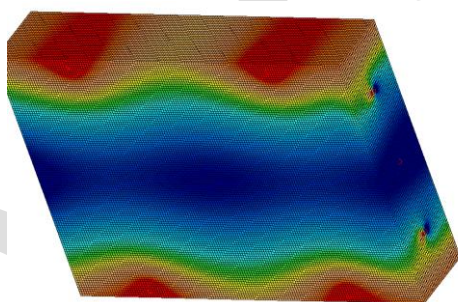


Figure 17: CAD generated surface deformations resulting from gravitational sag and mounting apparatus

Interferometric Data

Eventually we aim to use interferometric data as a source of surface irregularities and roughness for more realistic simulations. Currently the mirrors for most beamlines have not been ordered. We are thus contacting other ELI pillars and institutes to obtain interferometric data regarding the typical irregularity profiles.

6.4 Phase and intensity Modulations

As is mentioned in section 3.1, we have developed numerical tools to simulate source beam parameters and import the resultant profile into Zemax and VirtualLab. We are currently creating modulated beams (phase and intensity) and determining their effect on the overall system (focal spot, WFE, etc.). These modulated beams will be propagated through the perfect system (without any SI on the mirror) and the resultant focal spot compared to the ideal source beam. By doing so, it gives us a benchmark for our future simulation with

realistic parameters. It also provides an insight into controlling the modulation of the laser output in order to improve focus performances.

These simulations will allow us to determine the characteristics of the focal spot in the worst case scenario (modulated intensity and phase, SI on mirrors, tip/tilt and decentre etc). We can then determine whether the target focal spot is within the limits of expected performance. In addition it will highlight the necessity, or lack thereof, for correctional optics such as relay telescopes.

DRAFT

7. SUMMARY AND OUTLOOK

The following a brief summary of the workload of the simulations:

7.1 Complete and Ongoing Work

Things are done:

- Clipping of beam: the effect of having mirrors too small or large tip/tilt or decentre.
- Beamlines: Implementation of L1 – E1 as well as the L3 beamlines in VirtualLab and Zemax
- Implemented surface roughnesses on mirror (although not numerically correct)
- Wavefront and focal spot analysis as a function of surface irregularity
- Free space propagation analysis of L3 beam over distance of beam line
- Python script to generate laser profiles with phase and intensity modulations exported to Zemax and VirtualLab
- Development of Zernike polynomial generator
- Started Case study of focusing optics
- Case study of holey mirror
- Development of a “Propagator” based on standard analytical solutions to be used as bench marking tool

7.2 Outlook – not too distance future

Temporal Profiles: Presented here are only results for a single wavelength. However, the systems need to be simulated for temporal profiles with a larger BW. This will be investigated with the aid of VirtualLab.

Diagnostic stations: Every beamline has dedicated diagnostic station to measure, energy, pulse duration, profile etc. these diagnostic stations will also be simulated in order to have an idea of what parameters to expect.

Power spectral density: Although the surface irregularities have been implemented, midrange and high frequency modulations have not been implemented

System Tolerancing

7.3 Outlook – the distant future

Thermal Effects: these will be performed in the distant future. Due to the high intensity and power of the beams, as well as the high repetition rate of the lasers, clearly there will be some thermal effects involved in the system. These will need to be investigated.

Non-linear Physics: non-linear effect (mainly the Kerr effect) will be investigated with the aid of VirtualLab

DRAFT

	Document No.:	00000XXX
	Edition:	1
	Process:	REP
	No. of pages:	77

Simulation Results

L3 – E3: Holey Mirror simulations

	Position	Name	Signature	Date
Prepared	Applied Physicist	Anita Thakur		
	Optical Engineer	Ladislav Stanke		
Approved				

Table of Contents

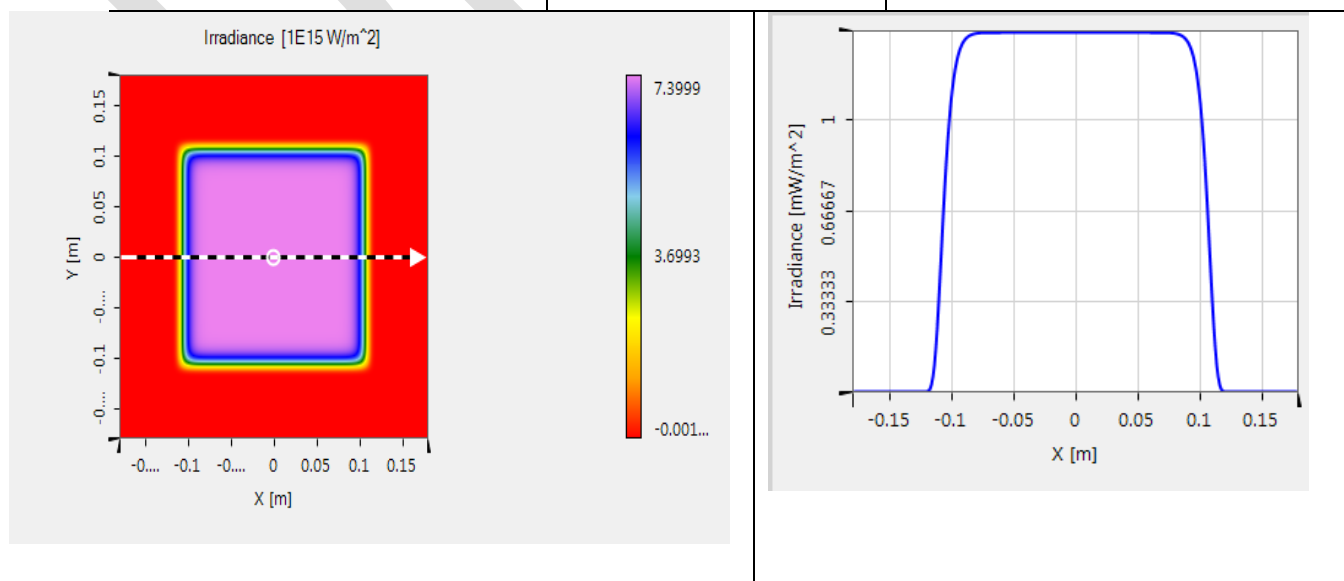
1. Setup for Simulations	3
1.1 Assumed Laser Output Beam Parameters for L3:.....	3
1.2 Assumed Beam Transport Mirror Parameters for L3:.....	4
1.3 Beamline Transport System (L3 – E3)	5
2. Scenario 1: Super Gaussian source with hole	6
2.1 Aim.....	6
2.2 Conclusion	8
3. Scenario 2: With $D=2\text{cm}$, $f=5\text{m}$, Initial Intensity =333 TW and distance between Holey mirror and focus= 200mm	8
3.1 Aim.....	8
3.2 Conclusion	11
4. Scenario 3: Comparison between Spherical and Parabolic mirror	11
4.1 Aim.....	11
4.2 Conclusion	12
5. Scenario 4: With Holey mirror corresponding to different focal length and diameter.....	Error! Bookmark not defined. 13
5.1 Aim.....	13
5.2 Conclusion	18
6. With Holey mirror in case of Gaussian source	
6.1 Aim.....	19
6.2 Conclusion.....	20
7. With Surface irregularities	
7.1 Aim.....	21
7.2 Conclusion.....	23
8. Implementation of Optical coatings	
8.1 Aim.....	23
8.2 Conclusion.....	24
9. Summary and Prospective work	Error!
defined.....	Bookmark not defined. 25

1. SETUP FOR SIMULATIONS

1.1 Assumed Laser Output Beam Parameters for L3:

The following are the assumed Laser parameter for the output of L3 (S:\Control systems Team\4.5 Performance Group Share\4.5.1 BPM\Optical Simulations\Beamline Specifications\Beam Profiles\L3\From Daniel Kramer\Beam size L3_214mmFWHM_v2)

Parameter	Value	Comment
Physical Dimensions		
FWHM	214 mm	
1/e ²	225.6 mm	
1/e	220	estimated
Order	20	
Optical Parameters		
Energy	30 J	
Power	333 TW	
Central Wavelength	820 nm	



1.2 Assumed Beam Transport Mirror Parameters for L3:

For the simulations of the beamlines it is assumed that all mirrors have the same characteristics (S:\Control systems Team\4.5 Performance Group Share\4.5.1 BPM\Optical Simulations\Beamline Specifications\Beamline mirrors\ELI-BL-4300-TSP-00000111-E)

Parameter	Value	Comment
Physical Dimensions		
Size	360 x 250 mm	clear aperture
Shape	Rectangular	
Angle of incidence	45 degrees	
Central Wavelength	820 nm	

1.3 Beamline Transport System (L3 – E3)

For the following simulations the L3 – E3 Beam transport system is considered. The beamline is shown in Figure 2 where the first two mirrors are the “injector mirror” and the “Flip mirror” respectively.

Property	Value	Comment
Total Length	64.4 m	
Total number of mirrors	18	Including spherical mirror
Number of mirrors to DM	13	Excluding DM
Propagation length to focus	47.835	
Focusing optic	Spherical Mirror	f = 3 and 5 m
Diameter of Hole	2 or 5 cm	

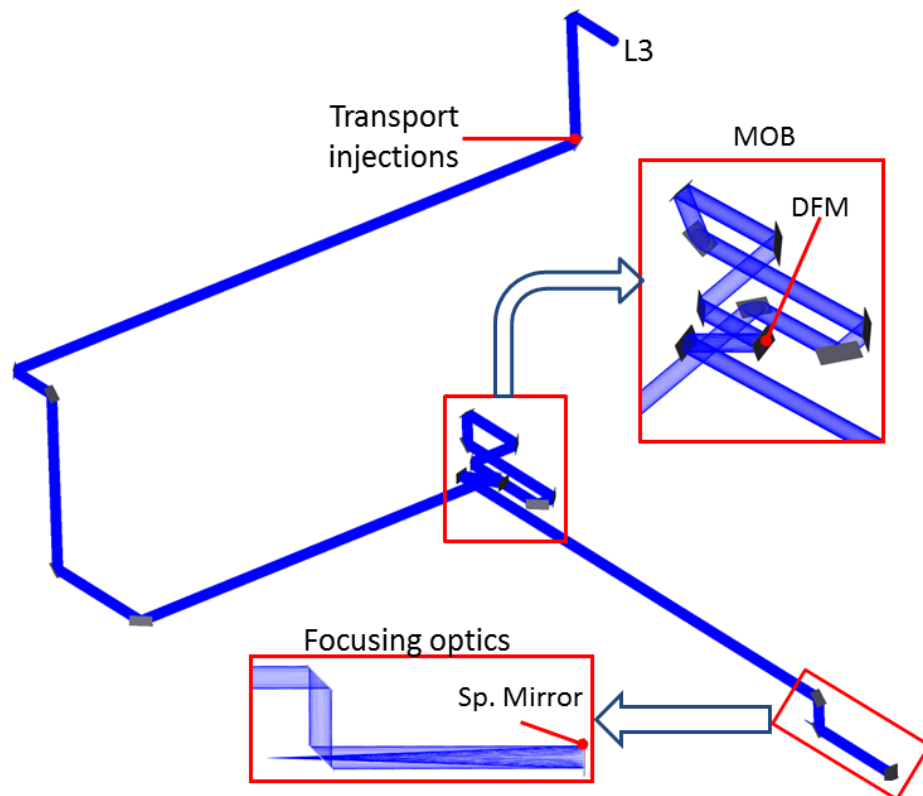
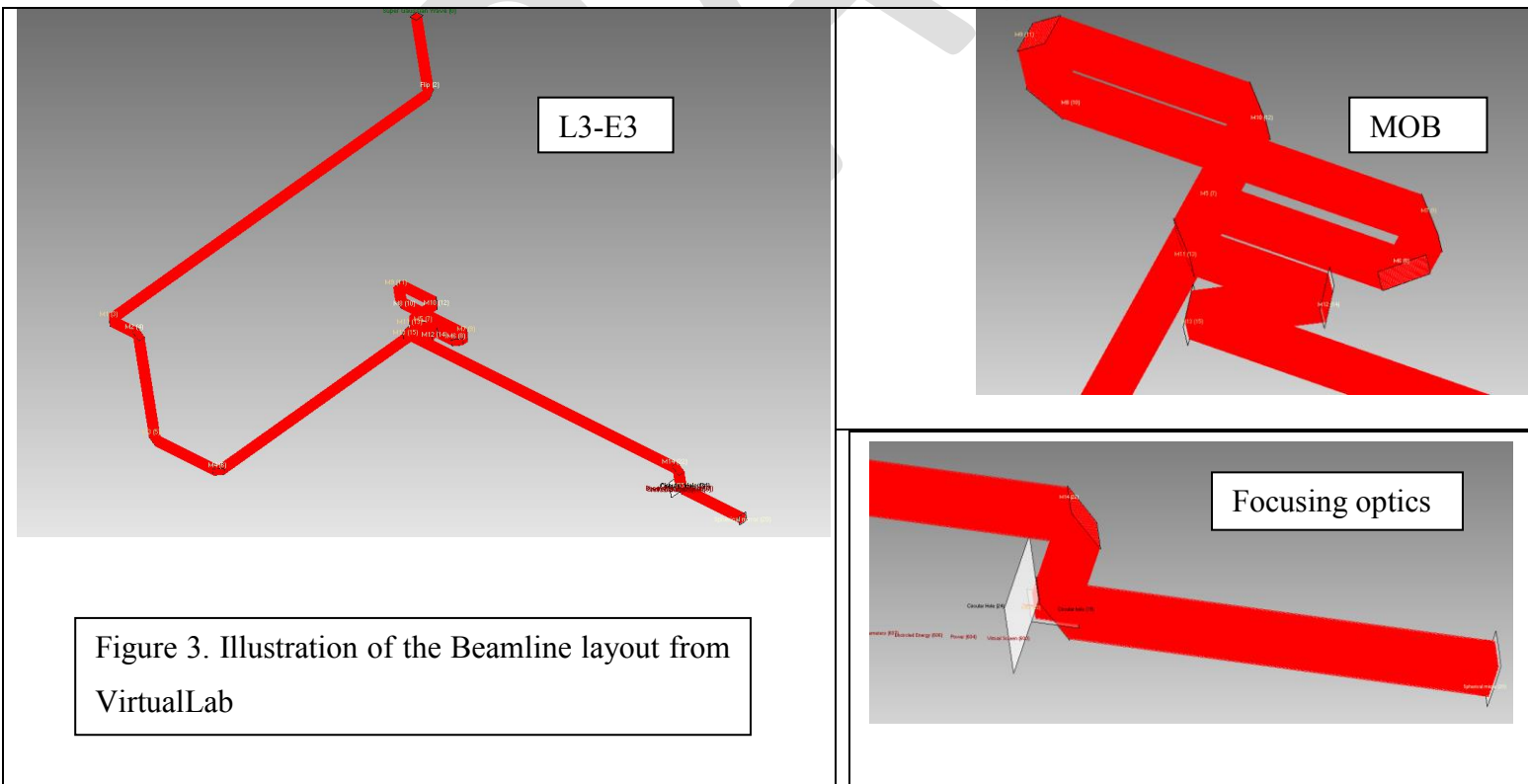
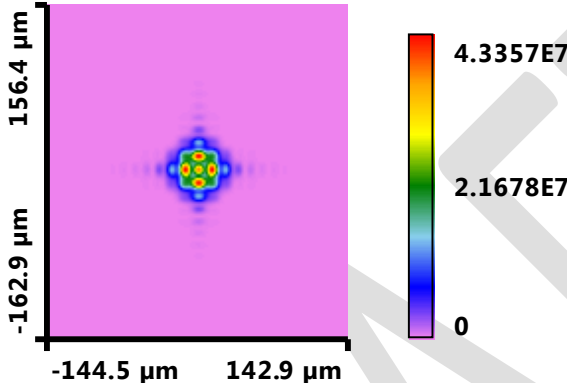
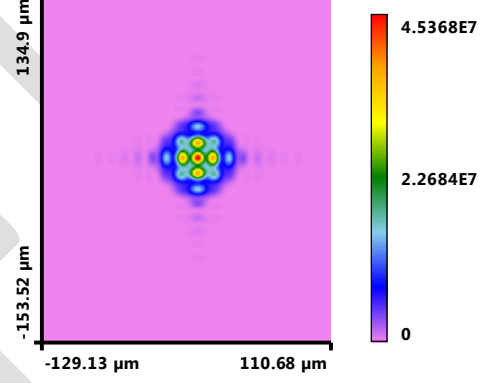
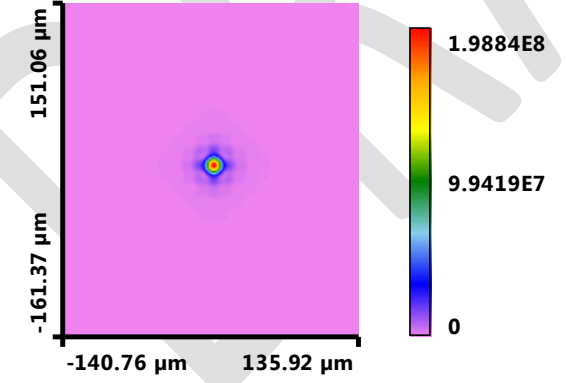
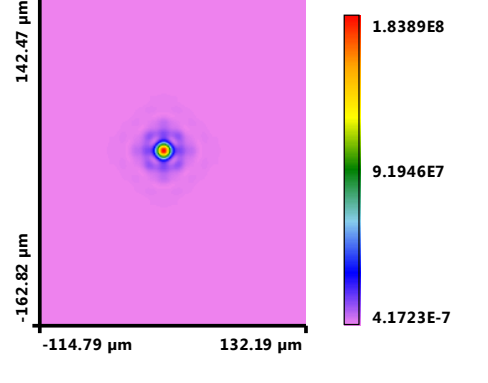


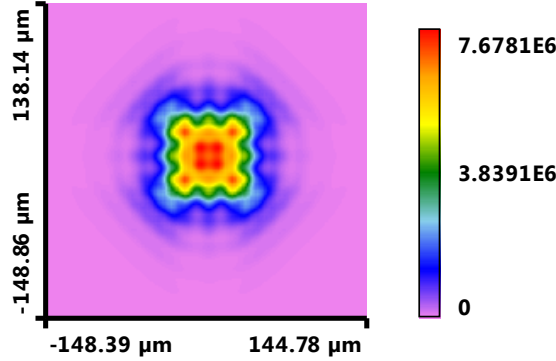
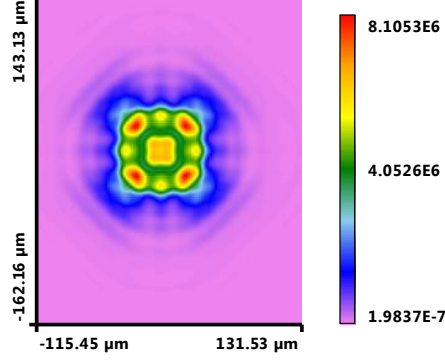
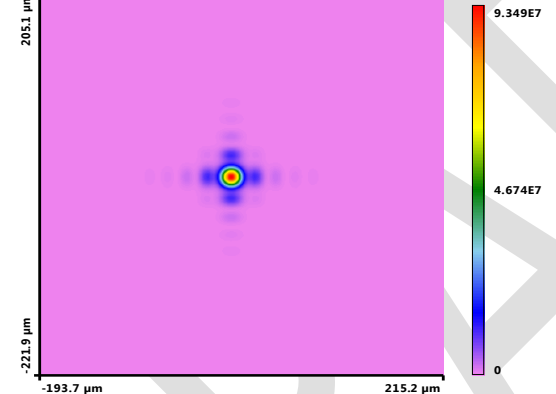
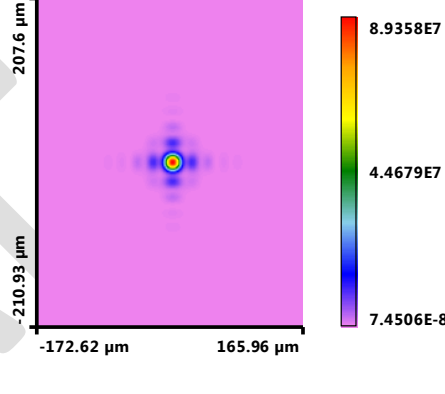
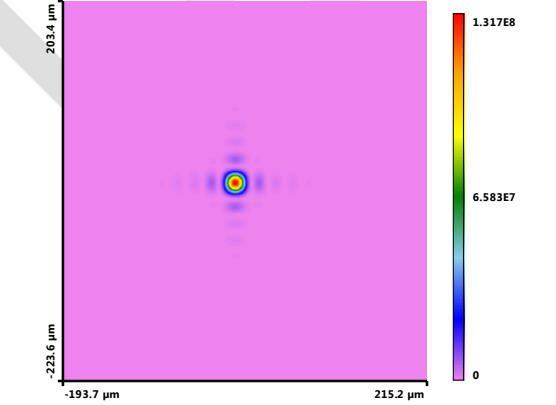
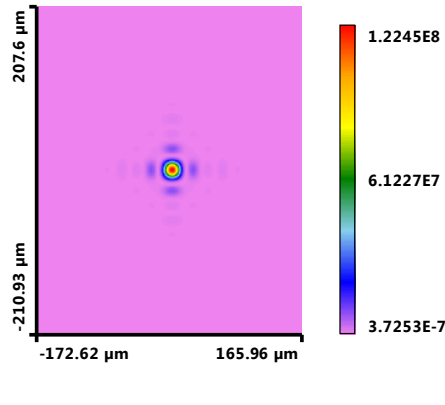
Figure 2: Illustration of Beamline layout (from Zemax) also showing the location of the deformable mirror

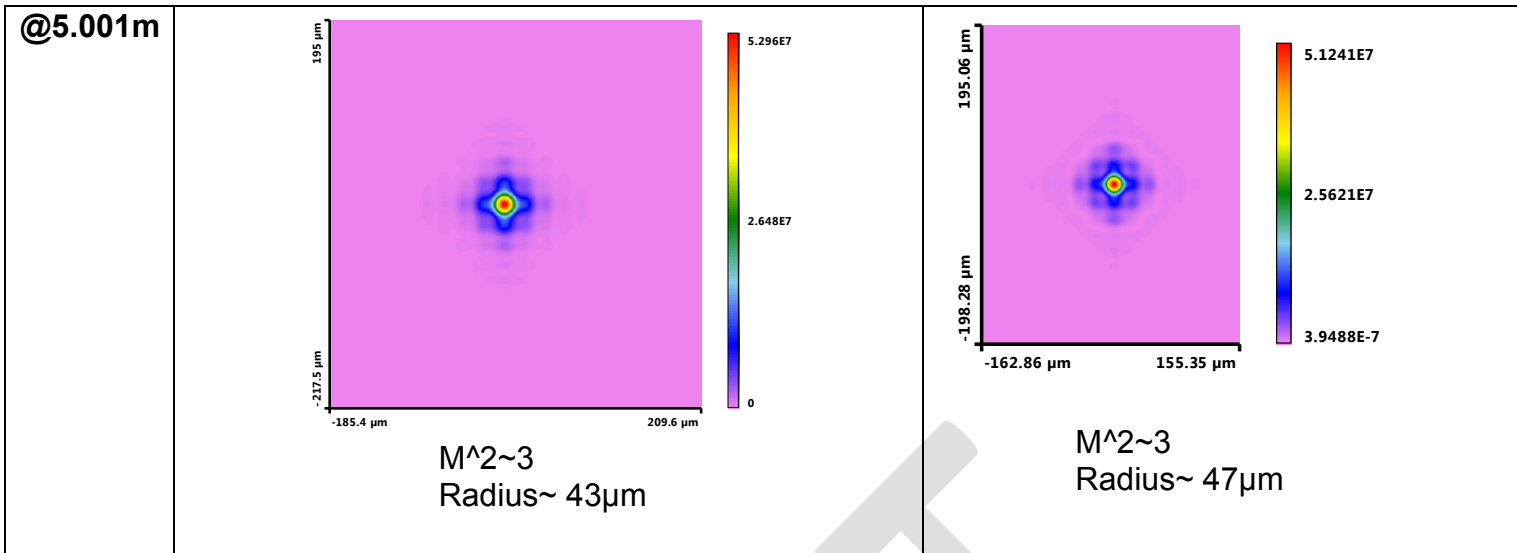


Scenario 1: Super Gaussian Source with Hole for different focal length and diameter

Aim: Since the L3 beam will not be Gaussian, a set of simulations for a square beam with supergaussian profile were performed. A spherical mirror with focal length of 3 or 5 m was used as the focusing element, and the influence of the hole in the beam was studied. The results in different scenarios are shown and discussed below:

<u>Case 1</u>	<u>Diameter=2cm, Focal length=3m</u>	<u>Diameter=5cm, Focal length=3m</u>
@2.999m	 <p>$M^2 \sim 3$ Radius $\sim 30 \mu\text{m}$</p>	 <p>$M^2 \sim 4$ Radius $\sim 33 \mu\text{m}$</p>
@3m	 <p>$M^2 \sim 3$ Radius $\sim 27 \mu\text{m}$</p>	 <p>$M^2 \sim 4$ Radius $\sim 29 \mu\text{m}$</p>

<p>@3.001m</p>	 <p>M²~3 Radius~63μm</p>	 <p>M²~4 Radius~66μm</p>
<p><u>Case 2</u></p>	<p><u>Diameter=2cm, Focal length=5m</u></p>	<p><u>Diameter=5cm, Focal length=5m</u></p>
<p>@4.999m</p>	 <p>M²~3 Radius~34μm</p>	 <p>M²~3 Radius~ 38μm</p>
<p>@5m</p>	 <p>M²~3 Radius~ 29μm</p>	 <p>M²~3 Radius~ 33μm</p>



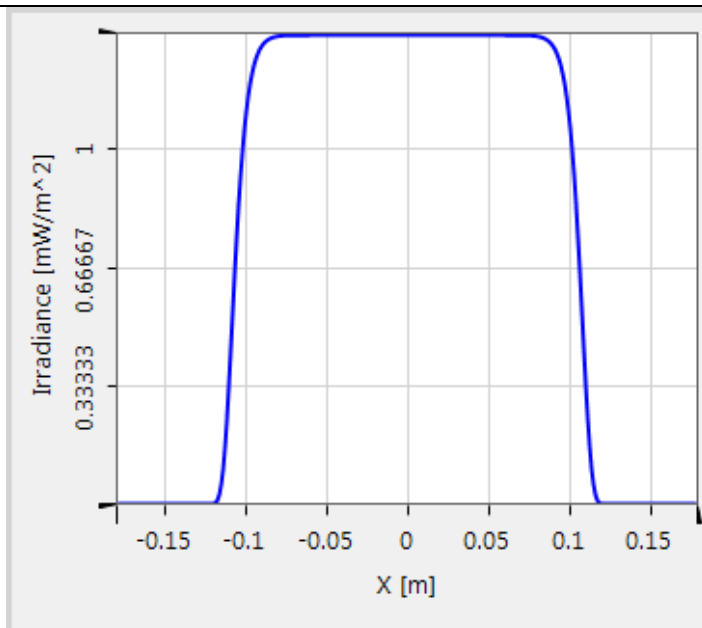
Conclusion:

Comparing the outcomes of focus spots, it is obvious that due to the spherical aberration; it is far better to use mirrors with longer focal lengths as high NA mirrors are prone to spherical aberration more than those with low NA. Also, the beams with larger hole have typically worse M² factor and lower peak intensity. Moreover, greater the hole diameter means larger focal spot radius, as well. It needs to be stated that these simulations are not counting for phase irregularities of the input beam, only aberrations and diffraction are included.

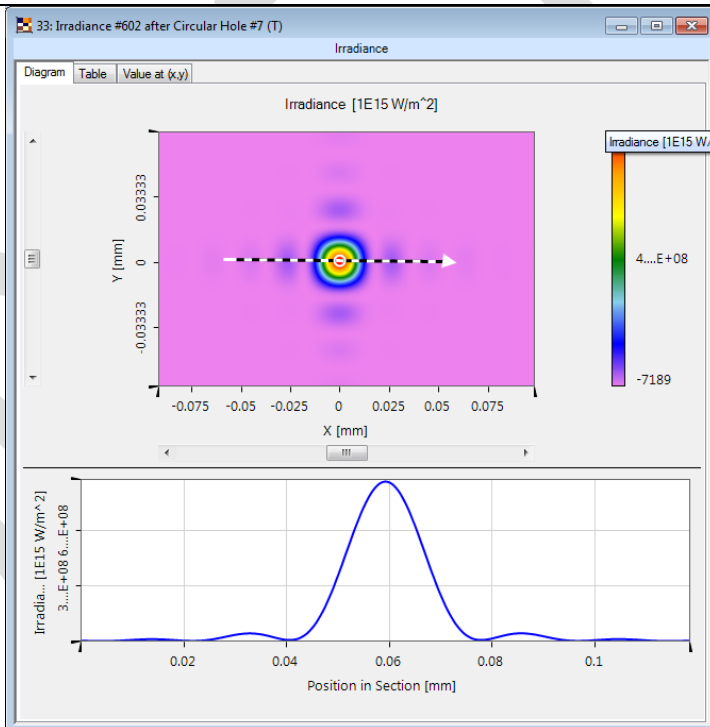
Scenario 2: With D=2cm, f=5m, Initial Intensity =333 TW and distance behind the Holey mirror d= 200mm (S:\Control systems Team\4.5 Performance Group Share\4.5.1 BPM\Optical Simulations\Simulation Reports)

Aim: In this set of simulation, we have studied the Output Irradiance profile and shape of focal spot produced at initial intensity equals to 333TW

**Input Irradiance at
333TW**

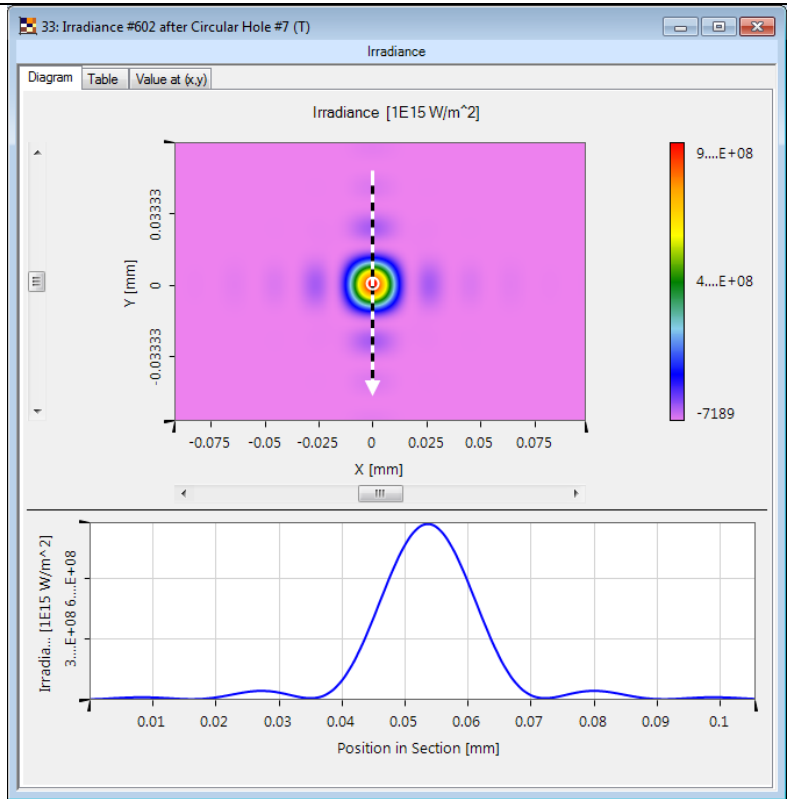


**Output Irradiance
 $I_x = 10^{18} \text{W/cm}^2$**



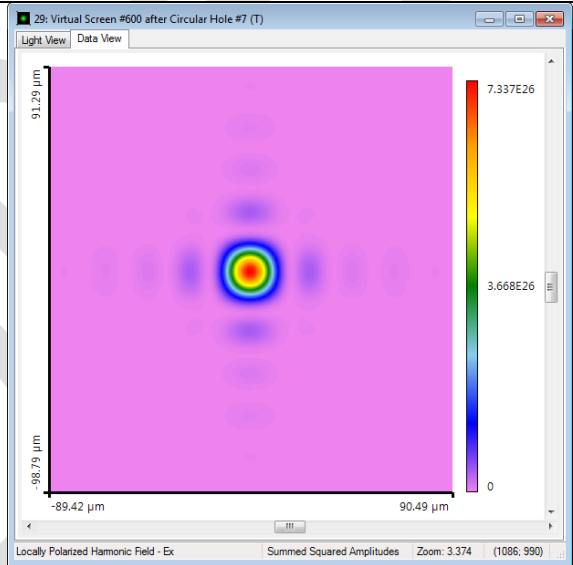
Output Irradiance

$I_y = 10^{18} \text{ W/cm}^2$



Shape of focal spot @

200mm



Radius of airy disc at $1/e^2 = 29.431 \mu\text{m}$

$M^2 = 2.72$

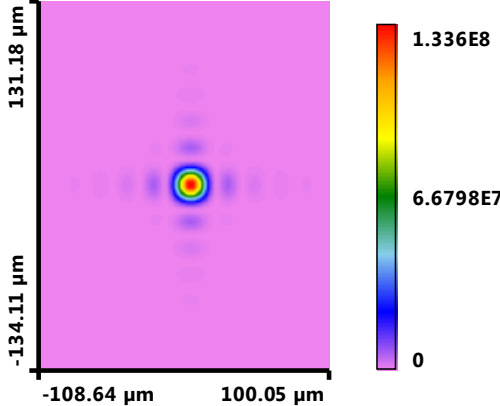
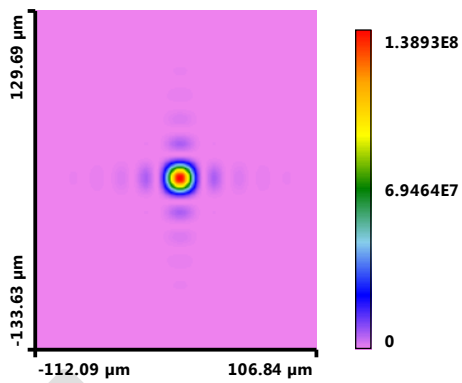
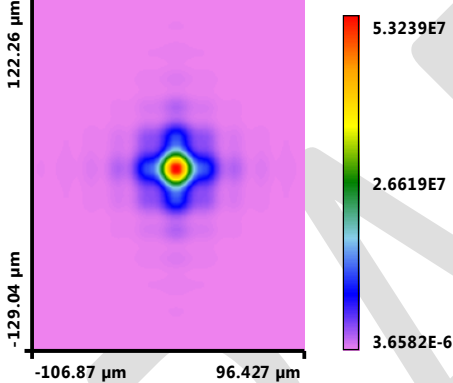
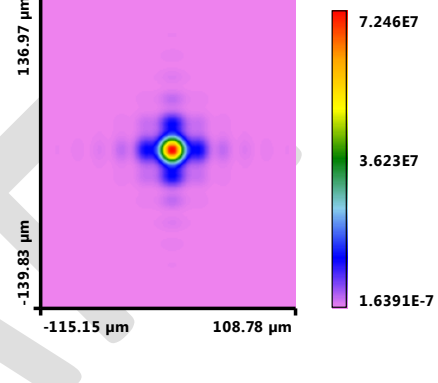
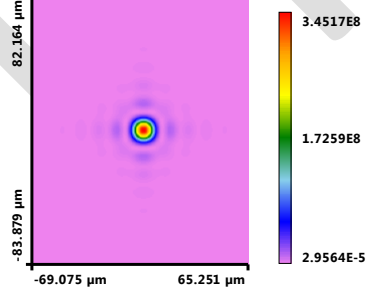
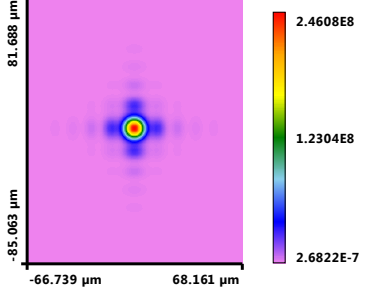
Conclusion:

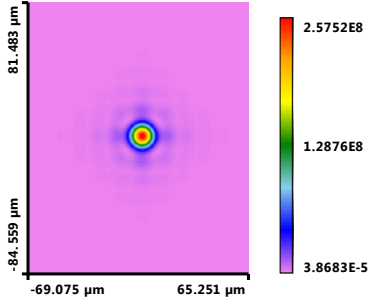
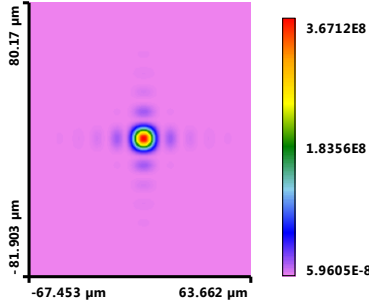
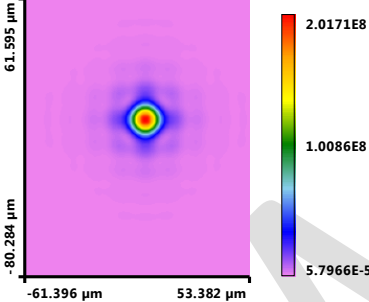
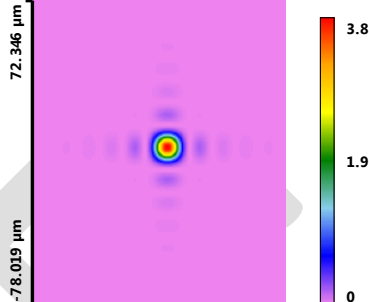
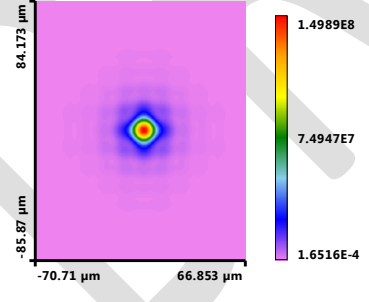
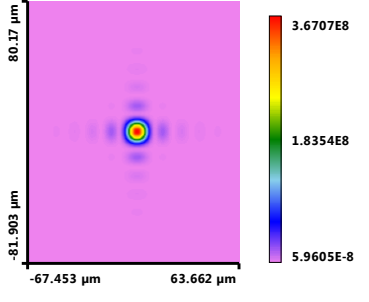
In the above scenario, it was demonstrated how accurately the VirtualLab can trace the input high peak power super-Gaussian square aperture beam through the setup with the holey mirror. The irradiance profile in the focal spot is calculated, for a single specific geometry of the set up without taking surface irregularities and phase errors of the input beam into consideration. The obtained results are also found comparable with Zemax OpticStudio by another group. The symmetrical and typical cross nature of the output beam is caused by the square symmetry of the input beam.

Test 3: Comparison between Spherical and Parabolic mirror

Aim: Here, in this case, we tried to find out which mirror would be a better choice in the setup with respect to the produced intensity of the focal spot

	<u>Diameter=0, Focal length=5m</u> <u>(Spherical Mirror)</u>	<u>Diameter=0, Focal length=5m</u> <u>(Parabolic mirror)</u>
@4.999m	<p>M²~2.5 Radius~32μm</p>	<p>M²~2.5 Radius~ 36μm</p>

<p>@5m</p>	 <p>$M^2 \sim 2.5$ Radius $\sim 27 \mu\text{m}$</p>	 <p>$M^2 \sim 2.5$ Radius $\sim 26.5 \mu\text{m}$</p>	
<p>@5.001m</p>	 <p>$M^2 \sim 2.5$ Radius $\sim 41 \mu\text{m}$</p>	 <p>$M^2 \sim 2.5$ Radius $\sim 36 \mu\text{m}$</p>	
<p><u>Diameter=0, Focal length =3m</u></p>		<p><u>Diameter=0, Focal length =3m</u></p>	
<p>@2.9997m</p>	 <p>$M^2 \sim 2.8$ Radius $\sim 18.5 \mu\text{m}$</p>	 <p>$M^2 \sim 2.5$ Radius $\sim 20.107 \mu\text{m}$</p>	

<p>@2.9999m</p>	 <p>$M^2 \sim 2.8$ Radius $\sim 22.5 \mu\text{m}$</p>	 <p>$M^2 \sim 2.5$ Radius $\sim 16.4 \mu\text{m}$</p>
<p>@3m</p>	 <p>$M^2 \sim 2.8$ Radius $\sim 25.3 \mu\text{m}$</p>	 <p>$M^2 \sim 2.5$ Radius ~ 15.9</p>
<p>@3.0001m</p>	 <p>$M^2 \sim 2.8$ Radius $\sim 28.5 \mu\text{m}$</p>	 <p>$M^2 \sim 2.5$ Radius $\sim 16.41 \mu\text{m}$</p>

Conclusion:

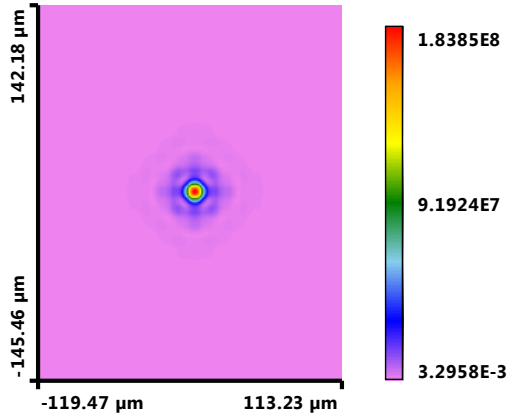
In the third scenario, the performance of a spherical and parabolic mirror is shown. It is well known that the parabolic mirror eliminates spherical aberration which results in higher peak intensity. It can also be seen that for the system with incorporated parabolic mirror, the vicinity of the focal plane is symmetrical whereas it's not the case with spherical one.

Test 4: With Holey mirror

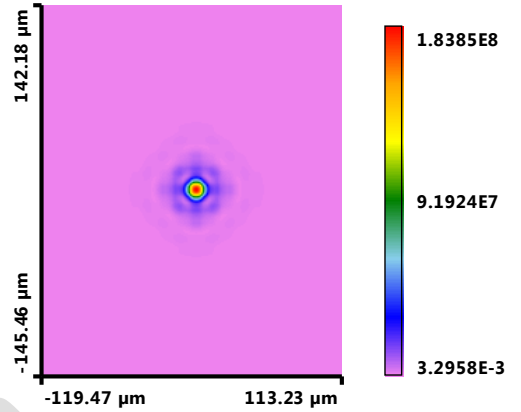
Aim: The following simulations are performed with a beam traced through a system with 2 cm and 5 cm hole, respectively in order to observe the shape of focal spots in different cases and to estimate the decrease of intensity

	<u>Diameter=2cm, Focal length=3m</u>	<u>Diameter=5cm, Focal length=3m</u>
@-1mm	<p>M²~3 Radius~30μm</p>	<p>M²~3.7 Radius~ 33μm</p>
@-500μm	<p>M²~3 Radius~ 19μm</p>	<p>M²~3.4 Radius~ 21μm</p>

@focus

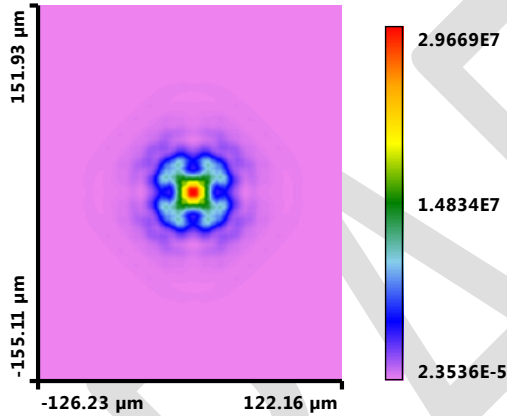


$M^2 \sim 3$
Radius $\sim 26 \mu\text{m}$

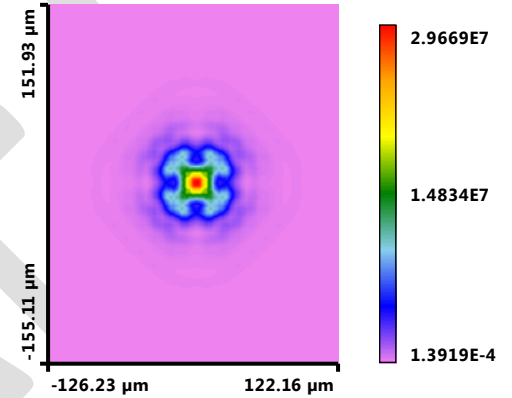


$M^2 \sim 3.5$
Radius $\sim 29 \mu\text{m}$

@500µm

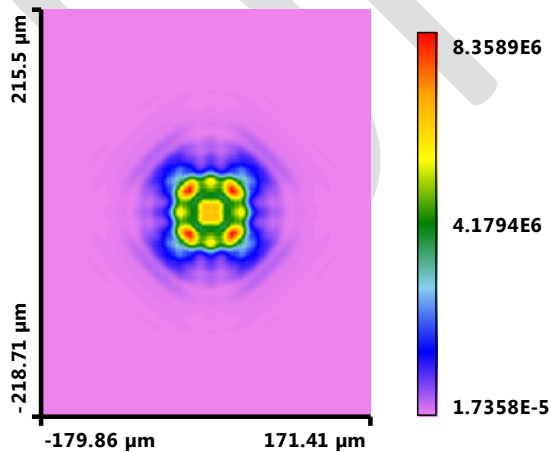


$M^2 \sim 3$
Radius $\sim 44 \mu\text{m}$

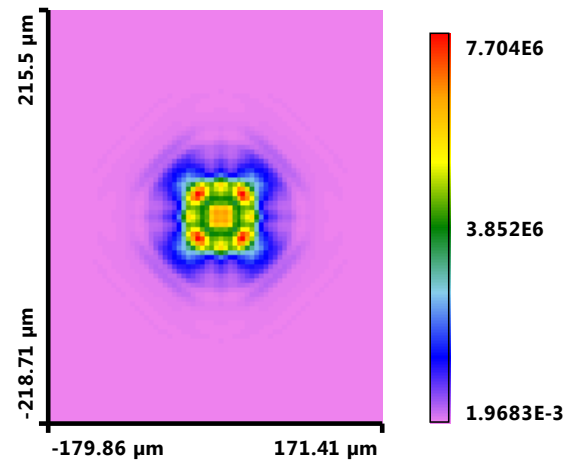


$M^2 \sim 4$
Radius $\sim 47 \mu\text{m}$

@1mm

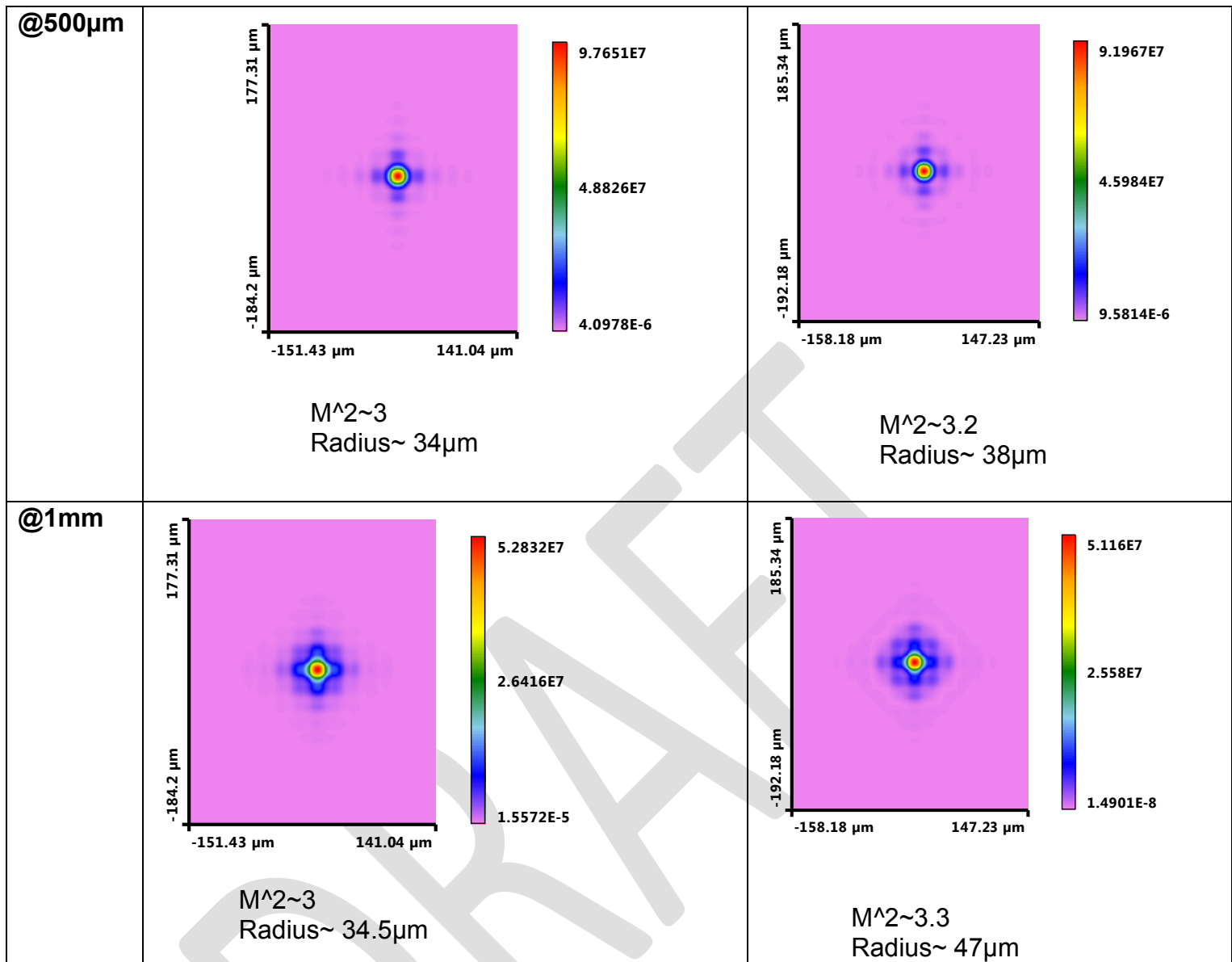


$M^2 \sim 3.4$
Radius $\sim 64 \mu\text{m}$



$M^2 \sim 4$
Radius $\sim 67 \mu\text{m}$

	<u>Diameter=2cm, Focal length=5m</u>	<u>Diameter=5cm, Focal length=5m</u>
@-1mm	<p>M²~3 Radius~34μm</p>	<p>M²~3.2 Radius~ 38μm</p>
@-500μm	<p>M²~3 Radius~ 29μm</p>	<p>M²~3 Radius~ 33μm</p>
@focus	<p>M²~3 Radius~ 29μm</p>	<p>M²~3 Radius~ 33μm</p>



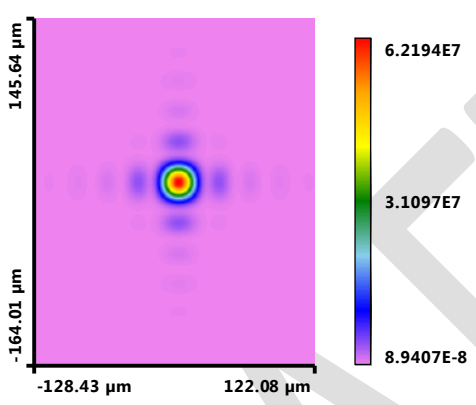
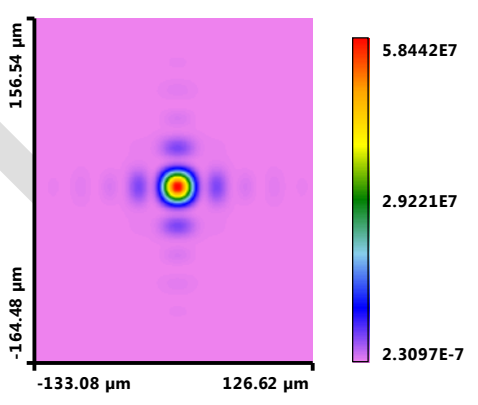
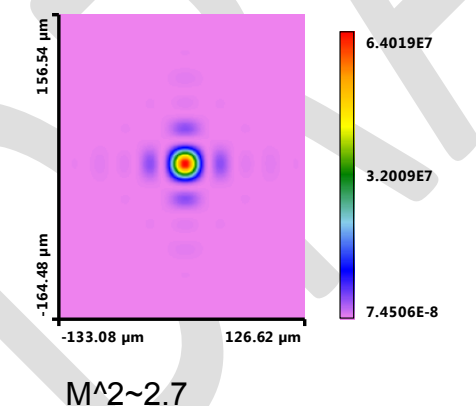
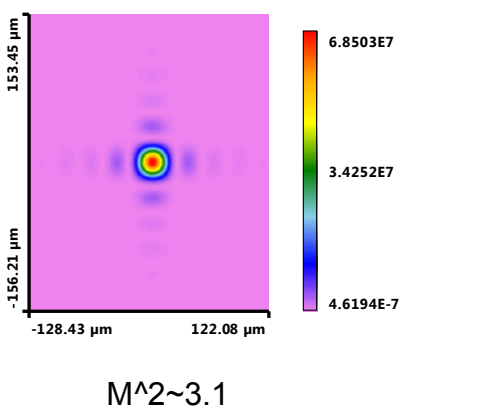
Conclusion:

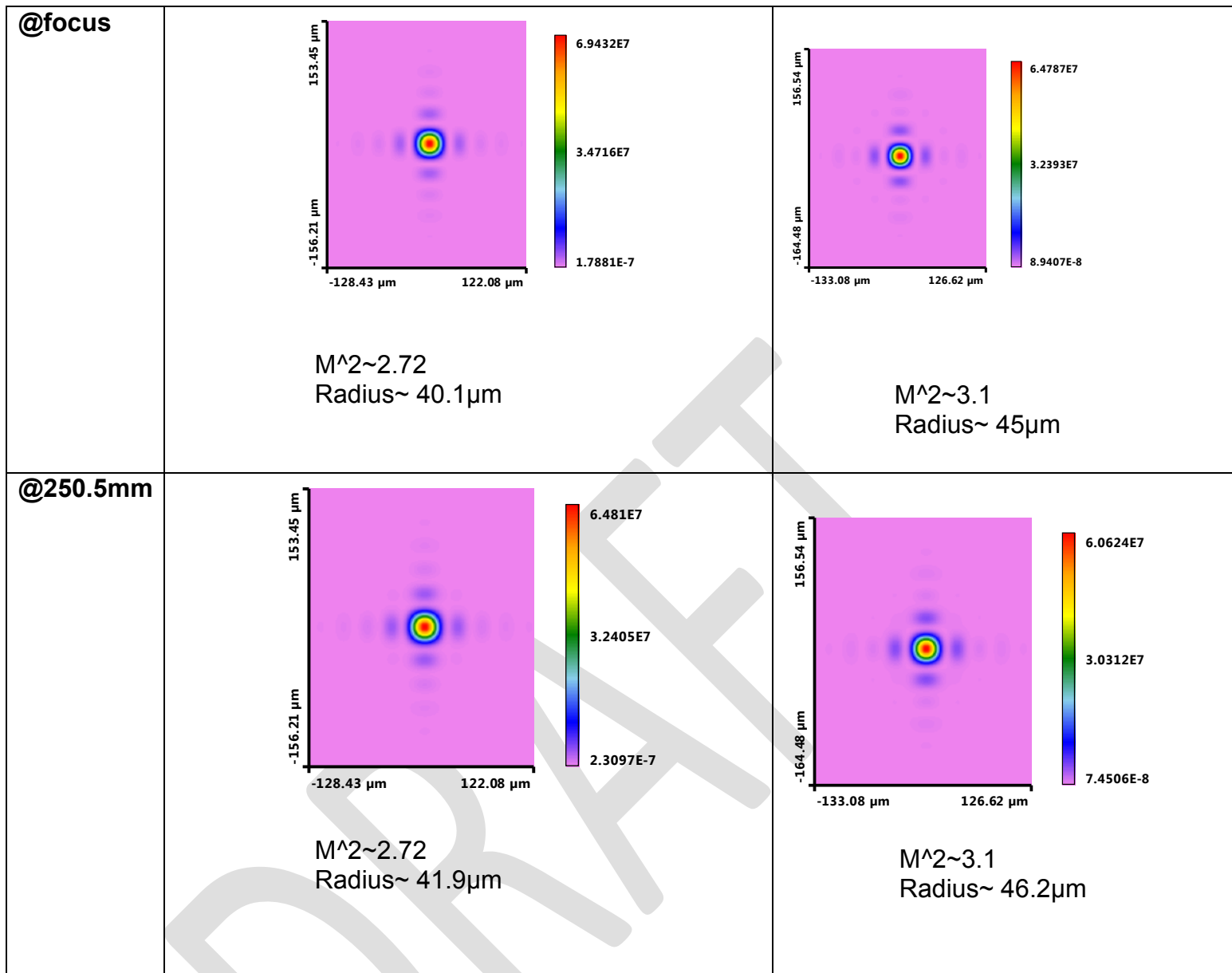
The last scenario is the most complex one although surface and beam's phase irregularities are not included but still few important conclusions can be drawn. Shorter focal length means higher peak intensity, but on the expense of the spot size quality. So, the priority between the focal spot quality and the peak intensity needs to be clearly defined and discussed. Another important conclusion is that the hole helps to suppress the effects of square beam diffraction, at least to some extent.

Test 5: With Holey mirror

Aim: The following simulations are performed with a beam traced through a system with 2 cm and 5 cm hole, respectively in order to observe the shape of focal spots in different cases and to estimate the decrease of intensity.

Note: The distance between holey mirror and focal point is 250 mm

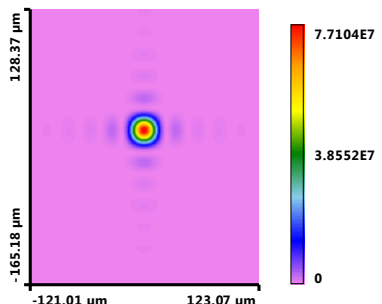
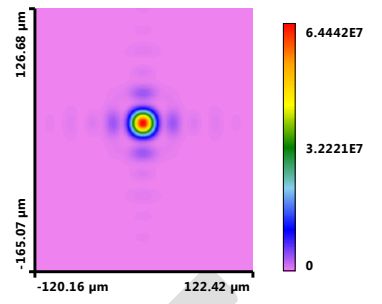
	<u>Diameter=2cm, Focal length=7m</u>	<u>Diameter=5cm, Focal length=7m</u>
@249mm	 <p>Intensity map for a 2cm hole at 249mm. The plot shows a central focal spot with a color scale from 8.9407E-8 to 6.2194E7. The x-axis ranges from -128.43 μm to 122.08 μm, and the y-axis ranges from -164.01 μm to 145.64 μm.</p> <p>$M^2 \sim 2.7$ Radius $\sim 42.62 \mu\text{m}$</p>	 <p>Intensity map for a 5cm hole at 249mm. The plot shows a central focal spot with a color scale from 2.3097E-7 to 5.8442E7. The x-axis ranges from -133.08 μm to 126.62 μm, and the y-axis ranges from -164.48 μm to 156.54 μm.</p> <p>$M^2 \sim 3.1$ Radius $\sim 47 \mu\text{m}$</p>
	 <p>Intensity map for a 2cm hole at 250mm. The plot shows a central focal spot with a color scale from 7.4506E-8 to 6.4019E7. The x-axis ranges from -133.08 μm to 126.62 μm, and the y-axis ranges from -164.48 μm to 156.54 μm.</p> <p>$M^2 \sim 2.7$ Radius $\sim 40.3 \mu\text{m}$</p>	 <p>Intensity map for a 5cm hole at 250mm. The plot shows a central focal spot with a color scale from 4.6194E-7 to 6.8503E7. The x-axis ranges from -128.43 μm to 122.08 μm, and the y-axis ranges from -156.21 μm to 153.45 μm.</p> <p>$M^2 \sim 3.1$ Radius $\sim 45 \mu\text{m}$</p>



Test 6: With Holey mirror in case of Gaussian source

Aim: The following simulations are performed with a Gaussian beam traced through a system with 2 cm and 5 cm hole, respectively in order to observe the shape of focal spots in different cases and to estimate the decrease of intensity.

Note: The distance between holey mirror and focal point is 250 mm

	<u>Diameter=2cm, f=7m</u>	<u>Diameter=5cm, f=7m</u>
@focus	 <p>7.7104E7 3.8552E7 0</p> <p>128.37 μm -165.18 μm -121.01 μm 123.07 μm</p> <p>$M^2(X) \sim 2.7, M^2(Y) \sim 2.6$ $R(X) \sim 47.5\mu\text{m}, R(Y) \sim 44.9 \mu\text{m}$</p>	 <p>6.4442E7 3.2221E7 0</p> <p>126.68 μm -165.07 μm -120.16 μm 122.42 μm</p> <p>$M^2(X) \sim 7.8, M^2(Y) \sim 7.6$ $R(X) \sim 104.7\mu\text{m}, R(Y) \sim 101.65 \mu\text{m}$</p>

Conclusion: The beam focus is little bit asymmetrical in the case of Gaussian beam as source due to the size of the rectangular mirror size used in the set up cause the beam clipping at the edges (shown below) which leads to the different radius in x and y directions in the above scenario.

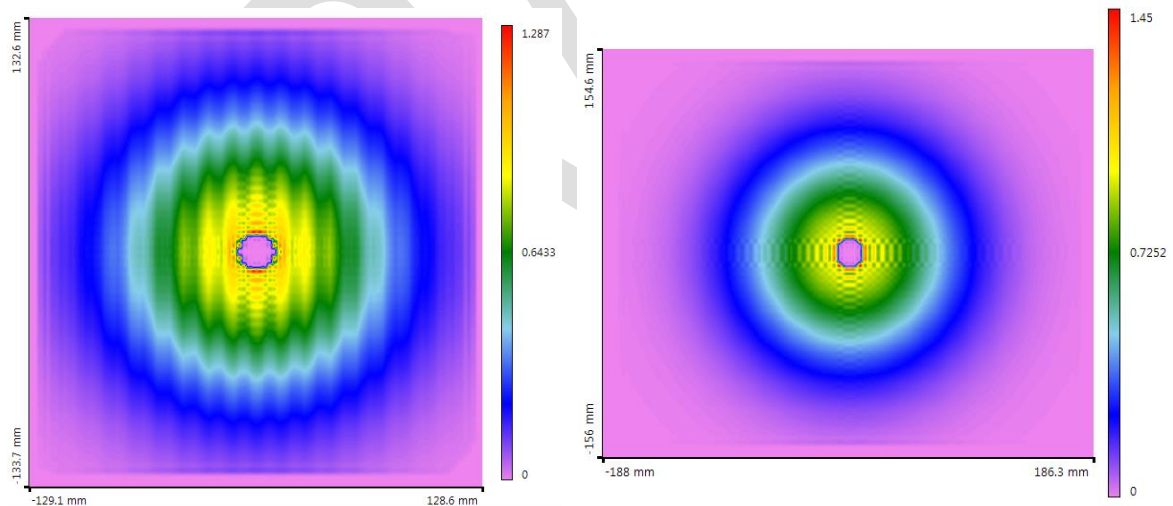


Fig: Left image – original, for the Gaussian beam improperly sized mirrors causing beam clipping and additional edge diffraction (picture showing the field impinging spherical mirror)

Right image – folding mirror with increased size allows to properly transporting the beam (picture showing the field impinging spherical mirror)

Test 7: With Surface Irregularities

Aim: The following simulations are performed with a Super-Gaussian beam traced through a system with 2 cm hole and spherical mirror with focal length=5m, in order to observe the shape of focal spots in different scenarios. In this case, the spherical mirror is free from surface irregularities.

Note: The distance between holey mirror and focal point is 200 mm

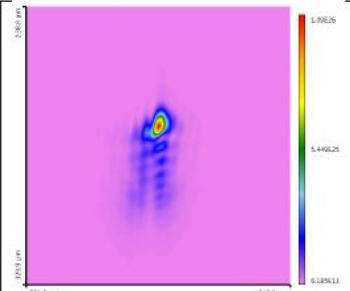
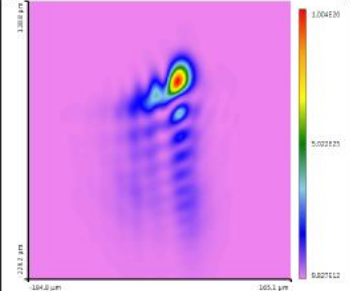
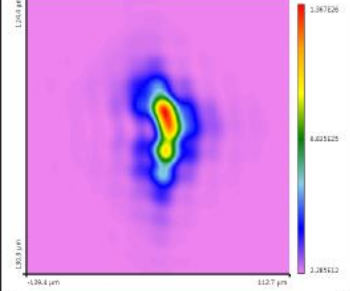
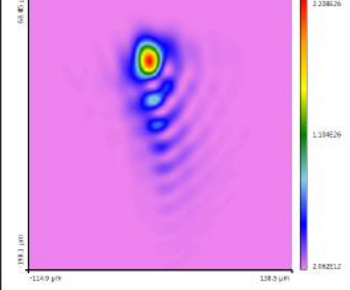
RMS error	Resulting Focal Spot	Spot Size
$\lambda/4$ - Best		61.3 μm \times 135.3 μm
$\lambda/4$ - Worst		69.3 μm \times 141.2 μm
$\lambda/20$ - Best		43.3 μm \times 66.5 μm
$\lambda/20$ - Worst		41.8 μm \times 82.5 μm

Table: Focal spots in different scenarios after implementing surface irregularities on the folding mirrors only (spherical mirror has surface without any irregularities).

RMS Error	1st Mirror Surface	2nd Mirror Surface
$\lambda/4$ - Best		
$\lambda/4$ - Worst		
$\lambda/20$ - Best		
$\lambda/20$ - Worst		

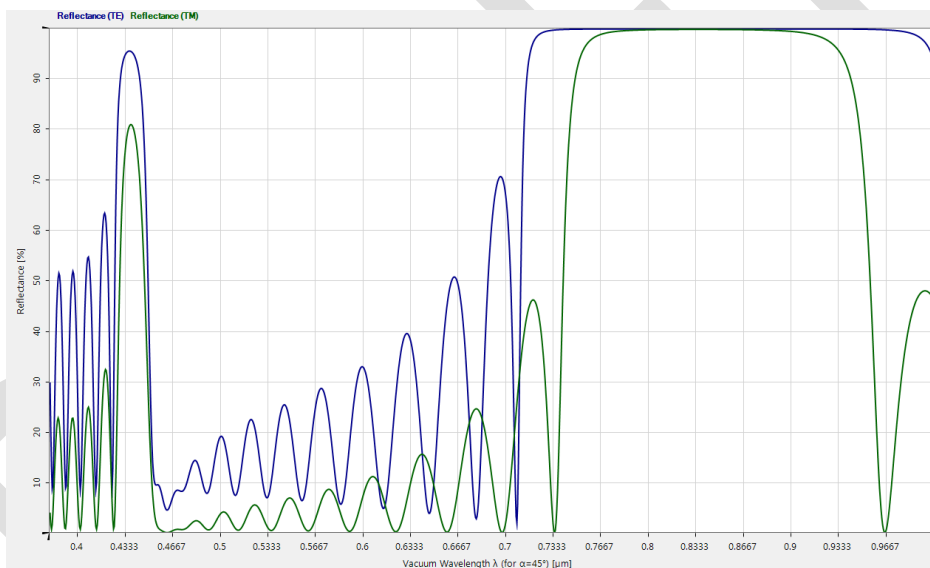
Table: It shows surface irregularities on the folding mirrors in each scenario.

Conclusion: Study of surface irregularities largely depends on statistical calculations. Surface irregularities are generated in the Zemax with use use of Monte Carlo simulation and the implemented to the VirtualLab. Above simulations are showing that the surface quality is critical either to the peak intensity or to the spot radius, as well. As there are many possibilities to have a same Zernike with the same RMS, two scenarios (best and worse) from the statistical ensemble (20 000 possible variants of Zernike polynomial) are always taken. Generally speaking even the $RMS = \lambda/20$ do not have to be sufficient for the beamline folding mirrors, as it can be seen from the table. Moreover, in the above scenario only a part of the beamline is taken into consideration. Of course the surface irregularity can be applied to each

and every single mirror into the beamline, requiring to generate several original Zernike polynomials in the Zemax. In reality the beam will be already disturbed while entering presented part of the beamline. Question that arises is, whether additional deformable mirror will be able to correct the wave-front. So far no technical data is available to consider also the deformable mirror. Number of actuators, piston and the geometry of considered deformable mirror needs to be provided.

Test 8: With Optical Coatings

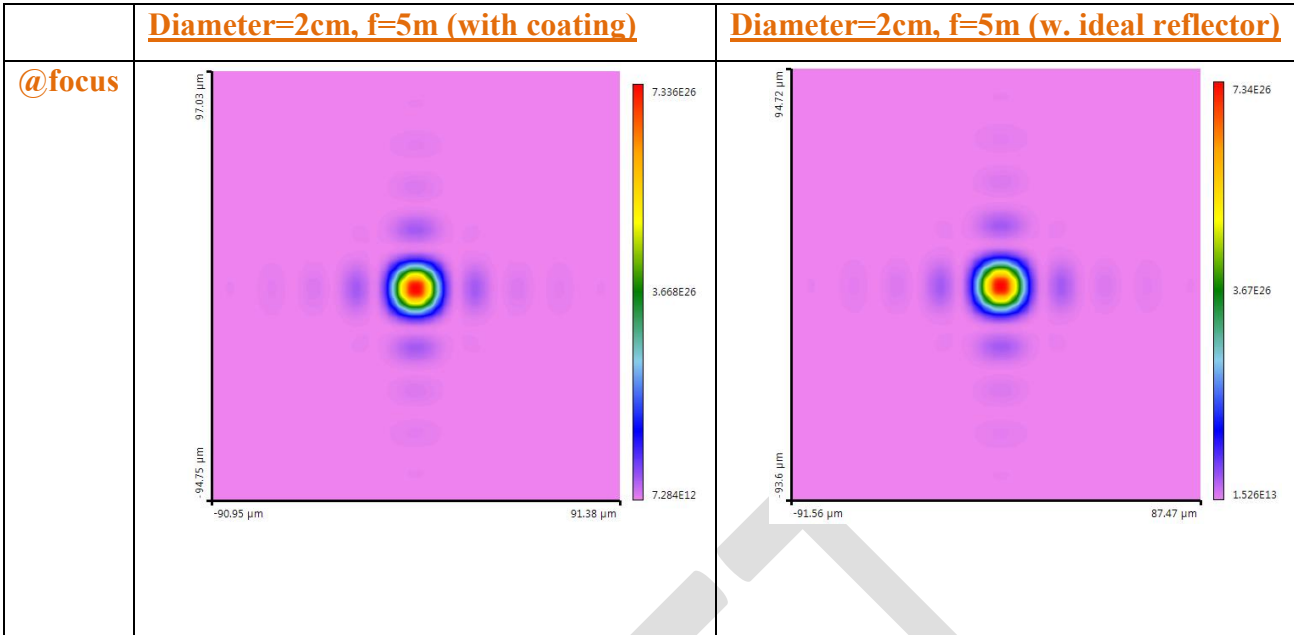
Aim: The following simulations are performed with a Super-Gaussian beam traced through a system with 2 cm hole and spherical mirror with focal length=5m. Coating is applied to planar folding mirrors only. These coatings has been specifically calculated for peak wavelength of 820 nm (combination of SiO₂ and TiO₂), broadband spectrum that should match 10 fs pulse duration and AOI=45°.



Just to test the coating implementation in the VirtualLab a monochromatic 820 nm source is used. No temporal effects are hence produced. The only effect user should expect is of course slight intensity drop. In comparison with ideal reflector, applied coating stack has a reflectivity equal to 0.9998 for TE and 0.9988 for TM.

Test Parameters		
Vacuum Wavelength	820 nm	
Angle of Incidence	45°	
Intensity Coefficients		
	TE	TM
Reflectance	0.9998	0.9988
Transmittance	3.249E-05	0.00113

Note: The distance between holey mirror and focal point is 200 mm



Conclusion:

Coating stack has been successfully implemented to the VirtualLab simulation. As expected, coating work flawlessly with the monochromatic source and only a slight intensity drop is observed. A pulsed beam simulation should follow to observe temporal effects.

Summary:

Here, in this report, we have concluded main four cases with a common goal to investigate the beam’s interaction with the circular-like hole. The comparison of a spherical and conical (parabolic) focusing mirror was also executed.

The preceding tests will be improved with added surface irregularities on the planar mirrors and the phase irregularities of the input beam (with dummy glass phase plate). Unfortunately, with the current state of the VirtualLab software, we cannot apply the surface irregularities on the spherical mirror.

The theoretical studies by Michal Smid on different size focal spots (derived from above simulation results) can be summarized in the following table:

Focusation type	hole diameter [cm]	focal length [m]	energy in central spot [%]	central spot FWHM [μm]
theoretical (Airy disk)	-	5	83.9	20.4
simulation	-	5	84	20
simulation	2	5	74	20
simulation	5	5	66	20
theoretical Gaussian (Airy disk)		3	83.9	12.2

From the above table, it is concluded that the simulation with the square beam focused by a spherical mirror provides comparable results as a theoretical limit of Airy disk focusation. The introduction of 2 cm hole decreases the energy by 10%, and increasing this hole to 5 cm diameter decrease the energy in the focal spot further to 66% of laser energy.

Prospective work:

The above simulation results are also being used for the forthcoming publication in close collaboration with Stephan Weber's group with a special involvement of Katerina Falk (Senior Scientist) and Michal Smid (Junior Reseacher). We are intended to submit this article either in Rev. Sci. Instrum. or J. Instrumentation.

DRAFT

PALACKÝ UNIVERSITY

OLOMOUC

FACULTY OF SCIENCE

DEPARTMENT OF EXPERIMENTAL PHYSICS



SUMMARY OF DOCTORAL DISSERTATION

**Design and Analysis of Optical Elements and Devices for PW Laser
Systems**

Author: RNDr. Mgr. Ladislav Stanke

Supervisor: Ing. Jaromír Křepelka, CSc.

OLOMOUC 2016

Doctoral thesis was carried out under the full-time doctoral program Physics in specialization Applied Physics in 2012 - 2016. The research institute at which the thesis was prepared was the Joint Laboratory of Optics in Olomouc. The program was maintained by the Department of Experimental Physics at Faculty of Science at Palacký University in Olomouc.

Ph.D. candidate: **RNDr. Mgr. Ladislav Stanke**

Supervisor: **Ing. Jaromír Křepelka, CSc.**
Joint Laboratory of Optics
of Palacký University and Institute of Physics
of the Czech Academy of Sciences

Reviewers: **prof. Ing. Miroslav Jelínek, DrSc.**
Institute of Physics
Czech Academy of Sciences

doc. RNDr. Libor Mrňa, Ph.D.
Brno University of Technology
Faculty of Mechanical Engineering
Dept. of Welding Technology and Surface Treatment

pplk. doc. Ing. Teodor Baláž, CSc.
University of Defence
Faculty of Military Technology
Dept. of Weapons and Ammunition

The summary of the thesis has been sent to distribution on

Defence will take place on at Joint laboratory of Optics in front of the committee for Ph.D. study of Physics program and specialization Applied Physics, room, 17. listopadu 50a, Olomouc.

The Ph.D. thesis is available in the library at Faculty of Science of Palacký University.

Abstract

ELI-Beamlines is a unique forthcoming high-power laser facility in Dolní Břežany near Prague, Czech Republic. This facility is comprised of several laser and experimental halls. The main goal of the ELI systems engineering team is to design, build and maintain the beamline systems from both a hardware and a software point of view.

The design of optical systems to steer laser beams from the source to the target area is closely related to BPM (Beam Propagation Method) software. In the scope of this thesis, Wyrowski VirtualLab Fusion serves as the BPM software enabling the physical optics simulations, with access to all field components and to the temporal domain as well.

The author of this thesis shows the use of Wyrowski VirtualLab Fusion serving as BPM software on several ELI-Beamlines case scenarios. These scenarios include: free space propagation, focusing by ideal lens, image relaying, demagnifying the beam, tolerancing of beamline systems, etc.

Specific optical system designs are described and assessed within this thesis. These are primarily beam relaying or reducing systems. Both transmissive and reflective systems are designed and assessed. Design of a special beam diagnostic telescope to analyze a beam's wavefront irregularities is also demonstrated.

Throughout this thesis the combined use of Zemax OpticStudio and Wyrowski VirtualLab Fusion is applied to show new possibilities in the workflow of optical engineers, allowing physical optics phenomena to be taken into account, thanks to the Field tracing technique incorporated within Wyrowski VirtualLab Fusion.

Several recommendations for the ELI-Beamlines facilities arose from the analyses of the acquired results.

Contents

1	Introduction	5
2	Theoretical background	7
3	Hypothesis	10
4	Contribution to Knowledge	12
5	Optical Simulation Software	13
5.1	Zemax OpticStudio	13
5.2	Wyrowski VirtualLab Fusion	14
6	Suggested Workflow	17
7	Optical Modeling and Design	18
7.1	Free Space Propagation	18
7.2	Focusing by an Ideal Lens	20
7.3	Transmissive Relay Optics	23
7.4	Reflective Optics	25
7.5	Beamlines	36
8	Overall Discussion and Assessment	44
9	Conclusions and Future Work	48

1 Introduction

Extreme Light Infrastructure (ELI) Beamlines [1] is a highly challenging project in terms of both scientific and engineering aspects. These two specific aspects are also characteristic for the two distinct phases of the project. While the preparatory stage should be handled by means of various engineering approaches, the latter, operational phase, will mostly be the domain for the application of miscellaneous experimental scientific methods.

In the first stage, optical engineering plays one of the vital roles in the ELI-Beamlines project. The two main tasks to be solved in this dissertation are the two main tasks of optical designers and engineers, beam transport and beam focustion. Both of these tasks have also been somewhat solved by ELI predecessors, but ELI represents a whole new level of laser intensities and ultra short pulse durations, which can be accessed by this new facility. According to the ELI Whitebook [2], ELI will be the first infrastructure to achieve intensities $I > 10^{24} \text{ W} \cdot \text{cm}^{-2}$. Huge surface power will be obtained by producing kJ of energy over 10 fs and focusing of such energy over a micrometer size spot will lead to the achievement of highest intensity, including extraordinary beam sizes. The L4¹ top-hat beam is inside a $400 \times 400 \text{ mm}^2$ aperture, and if the misalignments are considered, the simulation area for such a beam should be at least $600 \times 600 \text{ mm}^2$ [3]. It is obvious that not only the fabrication of optical elements for such a laser facility will be challenging, but also simulation of the optical systems themselves. Due to the high peak power, diffraction effects and extreme short pulse duration, these simulations are not typically solved by common optical designer's software, like Zemax. According to the author's master thesis [4] LightTrans VirtualLab seems like a good tool for simulations of optical systems – mainly relaying and focusing optics for large aperture pulsed beams of top-hat intensity profile.

On September 8 and 9 of 2014 a *Beam propagation method workshop* took place in the ELI office building in Harfa, Prague. It was agreed that VirtualLab represents one of the most sophisticated tools for solving this significant task that was commercially available at that time, which also meets the requirements of ELI facility.

The author was given a unique opportunity to stay for an internship (April – July 2015) in the Applied Computational Optics group [5], lead by professor Frank Wyrowski, at the Institute of Applied Physics of the Friedrich-Schiller-Universität, Jena. Moreover, the author was directly connected with all of the creators of VirtualLab in Jena, Germany, where LighTrans International UG (haftungsbeschränkt) [6], and Wyrowski Photonics UG (haftungsbeschränkt) [7] are also located. These companies were founded personally by the professor Frank Wyrowski. His PhD students in the Applied Computational Optics group not only use VirtualLab for innovative simulations, but also maintains a close relationship with the developers and steadily improve the software.

Before this research internship could happen numerous minor, but also important, problems were addressed and solved via electronic communication during earlier years of study. This tight relationship and collaboration of the dissertation author with the creators of VirtualLab enabled the software creators to tune this software exactly to meet the highly specific expectations of ELI Beamlines. Besides all of this, the author was invited to become an alpha tester working on the early version of the brand new Wyrowski VirtualLab Fusion.

Wyrowski VirtualLab Fusion is a powerful optical simulation software bundle of the new generation that is not based on ray-tracing methods. The concept of so-called *Field tracing*, first introduced in LightTrans VirtualLab, evolved into two specific approaches for solving Maxwell's equations. One of these approaches is called *Geometric field tracing* [8], which can be summarized as “smart” ray tracing and it is useful in all wavefront dominated simulation scenarios. The latter

¹One of the beams. Beams are designated L1, L2, L3 and L4.

one, called *Diffraction field tracing*, is especially advantageous in all situations where focusing of the field occurs. In these cases, the transverse dimensions of the electromagnetic field are too small to be wavefront dominated, and the fusion of these two methods create so called *Unified field tracing*.

Unfortunately, on November 13, 2015 the tendering process for the public contract “Performance Software: Beam Propagation Method (BPM)” was officially cancelled by the director of the Institute of Physics. Resultingly, this thesis cannot show the designs of all optical systems and their simulations within the BPM software. Rather, it demonstrates all possible scenarios and workflows within the ELI-Beamlines facility that can be solved by VirtualLab Fusion. With the persistent technical support from Wyrowski Photonics, the author continues to conduct the majority of tasks originally assigned to the whole BPM group, which was also dismantled during February of 2016.

This thesis will show how this software can solve typical ELI Beamlines’ simulation scenarios and how this software can entirely change the optical designer’s thinking.

The main method used throughout this thesis is to apply a brand new and more advanced approach to optical systems’ analysis and their design, employing a more sophisticated and physically precise technique than just ray-tracing. The original goal of analyzing optical systems was based on the solution of two specific tasks. Firstly, assessment and assistance with improving VirtualLab Fusion before its implementation to the BPM (*Beam Propagation Method*) within the frame of the VBL (*Virtual Beamline*). Secondly, designing optical systems specifically created for ELI-Beamlines specifications and their modelling and simulation in VirtualLab Fusion. The main point of this thesis focused on the temporal effects of optical systems and their thin film optical structures applied to ultra-short pulses, and diffraction effects caused either by finite dimensions of optical systems, or by beam propagation itself. These aspects are typically not the center of interest for most designers developing visual systems for non-coherent light conditions.

As of 2016, the author also aids other subgroups with optical simulations needed to solve their own specific tasks - for example, calculation of focal spots for betatron simulations (in collaboration with Dr. Anita Thakur, Dr. Kateřina Falk and Dr. Michal Šmíd), which are included instead of some previously planned simulations.

2 Theoretical background

According to the ELI Whitebook [2], today's top specifications of high power laser systems are characterized by a peak power between one and two petawatts at very low (sub Hz) repetition rates, this being unchanged for over a decade now. The majority of high power systems, however, still rest at the 100 TW level. ELI and its national predecessor projects, like ILE and Vulcan 10 PW, will boost the peak power of single lasers (modules) into the 10 PW or multi-10 PW regime at much higher repetition rates, constituting an evolution of more than one order of magnitude in both of these parameters. ELI will be the first laser research infrastructure, which is the result of a co-ordinated effort of the multi-national scientific laser community. Other communities (high energy physics, synchrotrons, astronomy etc.) have long standing traditions in the operation of international user facilities. Lasers, having evolved 50 years ago from small table-top devices, are only now at the edge of such a mode of operation, and ELI is the first world-wide installation to take that step.

A critical part of ELI-Beamlines are optical relay systems [9–12]. Top-hat beams, unlike Gaussian, change their profiles while propagating. Therefore it has to be relay imaged [13] to successive optical elements of the laser system to avoid hot spots and laser damage [14]. In high-power laser systems relay imaging is often combined with other optical systems, such as beam expanders and spatial filters [15]. The most common relays are 4f systems.

Several factors are important in designing relay trains [16]. First, it is preferable to minimize the number of relay stages in the relay train, both to maximize transmittance and to minimize the field curvature induced by the large number of positive lenses. Second, the outside diameter of the relay train is typically restricted, so the choice of image and pupil diameter inside the relay is critical. Third, economic considerations make it desirable to use as many common elements as possible, while minimizing the total number of elements. Fourth, it is preferable to keep internal images well clear of optical surfaces where dust and scratches can obscure portions of the image. Fifth, the number of relay stages must be either odd or even to provide the demanded output image orientation.

Afocal lenses can be designed with powered mirrors or combinations of mirrors and refractors. Several such designs have been developed in recent years for use mainly in the photolithography of microcircuits. All-reflecting afocal lenses are classified in the following text accordingly to the number of powered mirrors they contain, in the order of increasing complexity.

The simplest reflecting afocal lenses are the variants of the Galilean and Keplerian telescopes [16] shown in Figs. 1a and 1b. They may also be thought of as afocal Cassegrainian and Gregorian telescopes. The Galilean/Cassegrainian version is often called a Mersenne telescope. In fact, both Galilean and Keplerian versions were proposed by Mersenne in 1636, so his name should not be associated solely with the Galilean variant. More information about the Mersenne telescope design can be found in the literature [17–19]. Making both mirrors parabolic corrects all third-order aberrations except field curvature. This property of confocal parabolas has led to their periodic rediscovery and to subsequent discussions of their merits and shortcomings. The problem with both designs, in the forms shown in Figs. 1a and 1b, is that their eyepieces are buried so deeply inside the design that their usable field of view is negligible. The Galilean form is used as a laser beam expander where field of view and pupil location is not a factor, and where elimination of internal foci may be vital. Eccentric pupil versions of the Keplerian form of confocal parabolas, have proven useful as lens attachments. Being all-reflecting, confocal parabolas can be used at any wavelength, and such attachments have seen use in infrared designs. Especially when dealing with ultra-intense ultra-short optical pulses these designs are superior. Also for the purposes of transport telescopes within the ELI-Beamlines systems like Mersenne or Cassegrain are considered

for implementation.

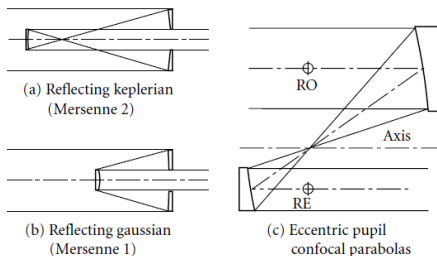


Figure 1: Reflecting Afocal Systems, adopted from [16].

For the successful operation of ELI-Beamlines optical engineers, physicists, researchers and engineers alike require several software tools to aid in the design, simulation, optimization and running of various laser systems as well as to predict system performance and tolerances. Advanced numerical simulations will play a crucial role in the efficient design and optimization of the many laser systems and beamlines necessary for the success of ELI-Beamlines. Development of a fully functional computational software package, namely a Beam Propagation Method (BPM) software, to simulate all the optical aspects of laser beamlines is therefore demanded [20]. Due to the long time and difficulty required to develop such software internally, ELI-Beamlines will take advantage of already existing software bundles and collaborate in the development of these bundles in order to fulfil all the simulation requirements of ELI-Beamlines.

The BPM is a mathematical simulations program, which will determine spatio-temporal parameters of ultra-short pulses as they propagate from the laser systems through optical setups and come to a focus at the target while taking into account the effect imposed by various components (mirrors, beam-splitter, coatings and gratings), and required optical parameters (spatial, temporal, spectral and energetics). This will enable the user's experimental requirements to be critically assessed ahead of time, and will ultimately be used to design, optimize as well as to determine and predict system performance and tolerances. Due to the complexity of the optical setups that will be implemented in ELI-Beamlines, the software package will involve simulations of the optical systems in both paraxial and non-paraxial regimes, ultra-short pulses with large bandwidths, tightly focused system with low f -number ($f < 1$), and non-linear effects such as small scale focusing. In order to have a full description of the optical process, the BPM software must also take into account environmental conditions such as thermal management, and the resultant stress and strain imposed on the optical components and mounts.

In the context of this thesis the most relevant item is the development of the so-called Beam Propagation Method (BPM) itself (see the flowchart in Fig. 2). It is important to be able to determine all the parameters of the beam at various points of alignment, transport, diagnostics and target systems. Comparing the results of the simulations with experimental data will allow understanding of the behaviour of the systems which can be optimized. Several BPM software bundles already exist: Malaprop and Prop92 LLNL, USA; Fresnel at the GPI, Moscow, Russia; *Miró* at CEA, Bordeaux, France. Similar software to run the ELI facility is required.

The intensity at the focal spot is the main deliverable. ELI staff must be able to tell the user the laser energy, pulse duration, power, size, beam quality and pulse duration. The BPM method will start with this information: 2-D spatial intensity profile $I(x, y)$, 2-D wavefront profile $\vartheta(x, y)$. Additional dimensions providing: spectral (λ) parameters, temporal (t) parameters.

A pseudo dimension is added through the propagation of the beam along its axis (z). Thus the required software system will be a 7-D solution.

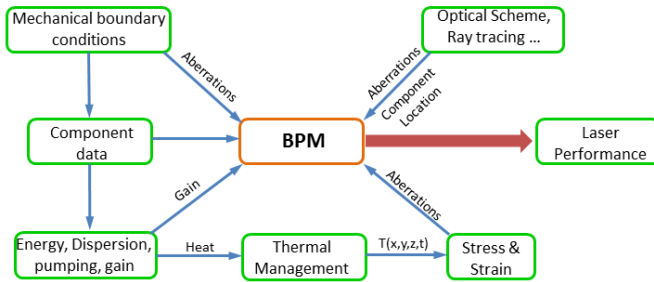


Figure 2: The BPM schematic diagram (adopted from [3]).

3 Hypothesis

Most of the high power laser facilities rely on the combination of standard ray-tracing software and some kind of beam propagation method or specialized software, typically designed in-house specifically for the purposes of these facilities. Examples of such software bundles include Malaprop, ARTEMIS and *Miró*.

In the author’s previously written master thesis [4] it was described how advantageous it can be to exploit more advanced methods and software packages for free-space propagation simulations and designing optical systems for the ELI-Beamlines facility. The strong potential of Field tracing [21], first introduced by LightTrans VirtualLab, can be exploited to solve the task of the BPM.

The aims and objectives of this thesis are to define the potential capability of VirtualLab’s Field tracing to improve the way optical designers think and to put more stress on the physical propagation methods that make tracing through the optical systems “smarter”. Ray-tracing offers very limited field information to be useful for the extreme conditions of ELI-Beamlines. Conversely, Field tracing offers the fully vectorial description of electromagnetic fields.

The overall goal of this thesis is to demonstrate that VirtualLab Fusion can offer more detailed information about the propagated fields and improve the optical designer’s workflow, while showing these capabilities on ELI-Beamlines’ test case scenarios.

The ability to propagate such extreme fields through the beamlines highlights the capability of VirtualLab Fusion. This ability is exploited for tasks that are normally solved by simple ray-tracing methods. Also a new possibility of simulating high numerical aperture systems arises with the introduction of Field tracing.

The author collaborated with the systems engineering team lead by professor Bruno Le Garrec. The systems engineering team’s goal at the facility level is to develop the technology to either describe or construct the laser’s path from its source to the target area (focal point).

The aim of the this PhD study is to use the means of optical simulations and modeling to design and assess performance of relay telescopes and other optical systems necessary to transport, magnify and demagnify, or focus large aperture top-hat, super-Gaussian or Gaussian beams of femtosecond duration. A part of this aim is to collaborate with LightTrans International UG (haftungsbeschränkt), Wyrowski Photonics UG (haftungsbeschränkt) and the Applied Computational Optics group at the Institute of Applied Physics of the Friedrich-Schiller-Universität Jena. The collaboration with professor Wyrowski’s teams should ensure fast and effective development of VirtualLab Fusion in accordance with ELI-Beamlines’ required specifications. VirtualLab Fusion could play the following role in the Virtual Beamline Model – beam propagation simulation and time domain analysis.

The specific aims and objectives are given below:

Aims

- Find strengths and weaknesses of Wyrowski VirtualLab Fusion in comparison with Zemax OpticStudio.
- Help with creating the missing user scenarios and to identify typical ELI-Beamlines simulation tasks and assign proper simulation methods.
- Discuss possible improvements of VirtualLab Fusion with professor Wyrowski and his co-workers.

- Assist with testing of the new VirtualLab Fusion improvements to check if they match the ELI-Beamlines criteria.
- Design the author's own optical systems and assess existing systems by means of optical simulation in VirtualLab Fusion and/or Zemax OpticStudio.

Objectives

- Simulate a free space propagation of Gaussian, super-Gaussian and/or top-hat beams.
- Explore the possibility to scale commercially available doublets and assess the performance of scaled optical systems.
- Analyse the proper aperture size of the mirrors for beam transportation systems.
- Design and assess performance of the relay telescopes and/or reducers or expanders.
- Test the optical systems' resistance to mirror tilts and decentrations by means of tolerancing.
- Test the influence of form deviations to beam properties using the optical systems described in this thesis.
- Simulate the beamlines of the ELI-Beamlines facility by means of Field tracing.

4 Contribution to Knowledge

The contributions to knowledge produced by this PhD thesis are as follows:

- Use of VirtualLab Fusion for the purposes of the high power laser facility ELI-Beamlines and determination of the software's efficiency to fulfill the BPM requirements.
- Assessment and reporting of relay telescopes, beam reducers, expanders and other optical systems' feasibility and performance.
- Analyses and optimisation of the optical systems for the needs of ELI-Beamlines.
- Beamlines simulations and their performance analyses.
- Recommendations based on the information gathered by the aforementioned analyses and optimisations.

5 Optical Simulation Software

There are two specific optical simulation software bundles used to aid in fulfilling the aims of this thesis. Namely Zemax|OpticStudio 15 [22] and Wyrowski VirtualLab Fusion [6, 7].

5.1 Zemax|OpticStudio

OpticStudio [22] is the industry standard for optical system design software, combining sequential lens design, analysis, optimization, tolerancing, physical optics, non-sequential optical system design, polarization, thin-film modeling and mechanical CAD Import/Export in a single, easy-to-use package.

This software is typically used by the optical designers for ray-tracing simulations. However Professional and Premium editions of this software also contain the means of physical optics propagation.

An excerpt from the OpticStudio 15 manual follows [23].

Geometrical optics is the modeling of optical systems by tracing rays. However, rays are not well suited to modeling certain important effects, primarily diffraction. Zemax does have some ray based diffraction computations, such as the diffraction MTF or PSF. These diffraction computations make a simplifying approximation: that all the important diffraction effects occur going from the exit pupil to the image. This is sometimes called the “single step” approximation. Rays are used to propagate the beam from the object, through all the optics and intervening spaces, all the way to the exit pupil in image space. The ray distribution in the exit pupil, with transmitted amplitude and accumulated OPD used to compute the phase, is used to form a complex amplitude wavefront. Then, in a single step, a diffraction computation is used to propagate this complex amplitude wavefront to the region near focus. Geometrical optics and the single step approximation work quite well for the majority of traditional optical designs, where the beam is not near focus anywhere except the final image. However, the model breaks down for several important cases: (1) When the beam comes to an intermediate focus, especially near optics that truncate the beam (rays by themselves do not predict the correct distribution near focus). (2) When the diffraction effects far from focus are of interest (rays remain uniform in amplitude and phase, wavefronts develop amplitude and phase structure). (3) When the propagation length is long and the beam is nearly collimated (collimated rays will remain collimated over any distance, real beams diffract and spread).

Physical optics is the modeling of optical systems by propagating wavefronts. The physical optics model is generally more accurate at predicting the detailed amplitude and phase structure of the beam away from focus than conventional ray tracing. However there are some disadvantages to the physical optics propagation analysis: (1) Physical optics computational method is generally slower than geometrical optics. Because the entire beam array must be stored in computer memory at once, the required RAM may be quite large for large sampling arrays. (2) The sampling limits the amount of aberration in the beam that can be accurately modeled. For highly aberrated systems, geometrical optics should be used.

The methods used in Zemax are based upon references [24, 25]. The electric field may be represented in three dimensions as [23]

$$\vec{E}(x, y, z) = E_x \hat{x} + E_y \hat{y} + E_z \hat{z} \quad (1)$$

where the E values are all complex and \hat{x} , \hat{y} , and \hat{z} are the Cartesian unit vectors. The coordinate system used by Zemax is that the beam propagates primarily down a local z axis. The z axis used to represent the beam is aligned with a reference chief ray in each optical space, and therefore this z axis is not generally the same as the z axis defined by the Lens Data Editor which is used to position optics. Because the beam is propagating along the local z direction, the first approximation made is to neglect the E_z component. Since the electric field must always be normal to the ray propagation direction, E_z can be reconstructed from other data when required, as will be described later. By keeping track of the electric field components along both the x and y axes, effects due to polarization may be studied, such as transmission and reflection losses, polarization aberrations, and of course the polarization state of the beam. If polarization effects are not required, the y component of the field may be ignored, speeding the computations.

Statements presented above are very important when later comparing the OpticStudio to the VirtualLab Fusion.

5.2 Wyrowski VirtualLab Fusion

VirtualLab Fusion [6, 7] is the latest step in the development of the first available commercial field tracing [21] software bundle. LightTrans VirtualLab [26], which brought the concept of Field tracing to the optical community, has changed its name to VirtualLab Fusion [27] and delivered yet another unique concept for optical simulations. This new concept is called Geometric Field Tracing [8]. By the unification of these two specific concepts, Unified Field Tracing has been created.

As per the creator’s paper [21]: Field tracing is the generalization of ray tracing and enables electromagnetic system modeling. Harmonic fields are traced through the optical system instead of ray bundles. This allows the smooth combination of different modeling techniques in different subdomains of the system, e.g. to use the rigorous spectrum-of-plane-wave operator for homogeneous media, geometrical optics to trace through a lens and finite element methods to include the effect of scatterers. All modeling techniques are formulated for vectorial harmonic fields.

Field tracing considers [28] a decomposition of an optical system into subdomains. Contrary to ray tracing, electromagnetic harmonic fields are traced through the system. This approach provides three fundamental advantages: (1) Field tracing enables unified optical modeling. Its concept allows the utilization of any modeling technique that is formulated for vectorial harmonic fields in different subdomains of the system. (2) The use of vectorial harmonic fields as a basis of field tracing permits a great flexibility in light-source modeling. By propagating sets of harmonic field modes through the system, light that is partially both temporally and spatially coherent, as well as ultrashort pulses can be investigated. (3) In system modeling and design, the evaluation of any type of detector function is essential. The use of vectorially formulated harmonic fields enables unrestricted access to all field parameters, and therefore it allows the introduction and evaluation of any type of detector. In field tracing, local Maxwell problems for subdomains are solved. These local problems often have properties that give rise to solutions in certain subspaces of all admissible functions. Then, approximate Maxwell solvers are accurate enough and are typically much cheaper than rigorous Maxwell solvers. The goal of field tracing is to construct a problem dependent solver, which is as fast as possible and as accurate as needed by combining different subdomain solvers [28].

In 2014, Wyrowski Photonics [29] took over the development of the next generation of VirtualLab in order to provide the simulation technologies required for the challenges of modern optics. VirtualLab Fusion introduces the new geometric field tracing engine using smart rays

which carry complete light field information. The user of VirtualLab Fusion builds up the optical system once, and has three optical modeling engines available.

- Ray Tracing: this engine provides a fast analysis of the performance of optical system based on conventional ray tracing technology. It delivers 2D ray information including position, direction, optical path length and absorption.
- Geometric Field Tracing Plus: this engine delivers complete electric and magnetic field information. It solves Maxwell's equations in its geometric approximation. It is as fast as ray tracing but includes amplitude, phase, polarization, spatial and temporal coherence, interference, and speckles. It delivers 2D ray information on the detector surface including all ray tracing quantities, the electric field (E_x, E_y, E_z) and the magnetic field (H_x, H_y, H_z).
- Classic Field Tracing: this engine combines geometric modeling techniques with numerous diffractive modeling techniques. More wave-optical effects, in particular diffraction, are included in the simulation.

Geometric field tracing presents the newest technique introduced within the Wyrowski VirtualLab Fusion. The principles of this latest improvement to VirtualLab were also presented during the DGaO conference in Brno, 2015 [8].

Until now, geometric and wave optics were commonly understood as two opposite branches. Often, scientists and engineers expect that phenomena like diffraction, interference, coherence and polarization cannot be included in geometrical optics. However, Prof. Wyrowski and his team propose another view on geometrical optics. They applied geometrical-optics based arguments for the development of a fast Maxwell equation solver in its geometric field approximation.

In order to overcome limitations of geometrical optics/ray-tracing, optical modeling and design must be based on physical optics. Therefore Maxwell's equations need to be solved. However, typical Maxwell solvers like FEM or FDTD cannot be used in most optical system due to their extraordinarily high numerical effort. Of course these solvers are important for simulations that consider very small features, but they are not practical for common lens systems. Consequently, there are two contradictory demands - the need to solve the Maxwell's equations and a reasonable numerical effort. The result is that specialized and/or approximated approaches need to be applied to solve Maxwell's equations. There are already several of these methods like Rayleigh integral for homogeneous media, or Fresnel integral for paraxial light. These methods are being combined within the physical optics modeling concept referred to as Field tracing [21].

An interesting point to make is how geometrical optics can be used to achieve similar results. Huygens already used the ray concept in the context of wavefronts. Prof. Wyrowski in his paper refers to Born and Wolf's Principles of Optics, where the geometrical approximation to solve the Maxwell's equations is already suggested. Wyrowski Photonics further developed and implemented this concept to obtain a geo-metric field tracing technique, which solves Maxwell's equations in its geometric approximation [8]. The geometric approximation leads to Maxwell's equations for local plane waves, which deliver accurate solutions in regions in which the spatial evolution of a field is dominated by its wavefront. In practice, the solution to Maxwell's equations in geometric approximation is obtained by a ray tracing algorithm with smart rays [8]. Smart rays have the following properties: (1) Smart rays know the full electromagnetic field information at their position. That includes amplitudes and phases of the electric and magnetic field components, and because of that, also polarization. (2) Smart rays know and remember their neighbors on the wavefront in the source plane. This is done by an appropriate ray index concept (wavefront indices). This method is combined with different lateral interpolation techniques for all field quantities which are allocated to a ray. Interpolation techniques include spline interpolation and mesh-based interpolation with barycentric coordinates. (3) Smart rays come with another index concept (spatial coherence indices), which enables their association to mutually coherent and incoherent modes, and their combination. That allows the modeling of partially spatially

coherent light, including the special cases of fully coherent and incoherent light. (4) In order to include color, temporal coherence, and ultrashort pulses, the frequencies which are allocated to a ray also come with an index to distinguish frequency contributions to stationary and pulsed light (frequency indices).

By tracing smart rays they obtained a solver for Maxwell's equations, which overcomes most of the limitations of conventional ray tracing, but delivers the results just as fast as ray tracing.

6 Suggested Workflow

Currently², VirtualLab Fusion does not contain a lens designing toolbox or environment similar to Zemax OpticStudio. In practice, that means the classical (pre)design process needs to be conducted by ray tracing in Zemax OpticStudio. This is caused by the lack of specific plot generators (e.g. ray fans, field curvatures, chromatic aberrations etc.) and other evaluating tools that are needed for a classical lens design task. For example, in the case of reducers, the system will be prepared in Zemax OpticStudio, where it can be optimized with the use of a common merit function and then evaluated using conventional aberration theory. After this step, the system can be transferred into VirtualLab Fusion for further simulations with the use of the physical optics approach. Transferring the system to VirtualLab Fusion does not necessarily mean the automated importing of Zemax files supported by VirtualLab Fusion. This is due to the fact, that by importing the Zemax file to VirtualLab, only a single OIS (Optical Interface Sequence) subdomain is created. Quite often it is better to prepare the whole system manually, while maintaining only a single lens per OIS subdomain. The main advantage of this procedure is that physical optics propagation between the components is accessible. In that case, an aperture can be added to provide spatial filtering as well.

Conversely, systems containing only folding mirrors³ can be easily implemented directly into VirtualLab Fusion due to more flexible manipulation of axes, that do not require the use of coordinate breaks. The frequent presence of coordinate breaks is often unavoidable in Zemax OpticStudio. This causes the beamlines' lens data sheet to be exceedingly long. Coordinate breaks actually form a bigger part of the lens data sheet than the optical elements themselves.

In the case of each beamline, mechanical design requirements and constraints are typically available. Such input data is provided by mechanical engineers. Based on this data a proper light path can be modeled.

The aim of this workflow is to show the advantage of stepping up from common ray tracing to physical optics represented by so-called Field tracing [21]. Physical optics is required to simulate the effects of diffractive beam propagation, aperture or stop diffraction. To some extent physical optics is also presented in the Zemax OpticStudio. The Field tracing approach is far more advantageous when temporal effects have to be shown. This will also be exploited to assess the effects of group velocity dispersion of reducers and expanders, since the temporal broadening caused by these systems can be directly investigated within VirtualLab Fusion.

In situations where the numerical effort to use Classic Field tracing will be too high, the latest Geometric Field Tracing Plus (Beta) will be employed to solve the demanded task.

²As of fall 2015

³A large portion of the beamline is typically comprised of folding mirrors (approximately 15–20 mirrors), beamsplitters and some focusing element (typically an off-axis parabola) in the end.

7 Optical Modeling and Design

Optical modeling and design represents a core chapter of this doctoral dissertation showing the author's results, either conducted independently or in collaboration with colleagues from the Joint Laboratory of Optics of Palacky University and the Institute of Physics of the Academy of Sciences of the Czech Republic and/or ELI-Beamlines facility. It contains the case scenarios being solved within the ELI-Beamlines facility, including:

- Free space propagation – which is a basic element of every consecutive simulation.
- Determination of the physical restrictions of ideal beams – influence of hard apertures and apodizations.
- Focusing by an ideal lens – physical limit of beam focusing.
- Design and simulation of transmissive optics for beam relaying or demagnification.
- Design and simulation of reflective optics for beam relaying or demagnification.
- Beamline simulations and performance analyses.

The beams used throughout the presented dissertation are either circular Gaussians or squared super-Gaussians. Only a part of all acquired results are shown in this summary of doctoral dissertation.

7.1 Free Space Propagation

From the geometrical optics point of view, free space propagation is not very interesting to investigate. Rays pass the homogenous free space without any change at all – rays in homogeneous media are straight [16]. This is typically not a limiting simplification when considering an optical setup for imaging purposes only.

When the designer wants to create an optical system for transmitting or reflecting coherent laser beams, it is also highly desirable to take into account diffraction effects, at least for beams that are diffraction dominated (e.g. near the focus). In reality this means that the optical designer needs to step up from ray-tracing to more precise physical optics methods. In such situations the optical designer normally switches Zemax from ray-tracing to Physical Optics Propagation (POP), which is described in the previous chapter. There are, of course, many other methods than those already contained in the POP. Some of them were described in the author's master thesis [4]. POP cannot be understood as a general nor rigorous method, however, for many cases this method can be used. Usually for the Gaussian laser beams of common dimensions, when there is none or very tiny inclination of the field, this method has sufficient results. The main drawback of POP is, that it completely neglects the longitudinal E_z component of the field. This is not a problem as long as the field propagated through free space is not being transported by high NA off-axis parabolas or being focused by the same type of optical element.

The free space propagation topic can be understood as self-contained, but in this dissertation it is merely shown as a basic building block for more complex simulations, and also for comparison of the output spatio-temporal shape of the beams propagated with and without use of a relaying optical system.

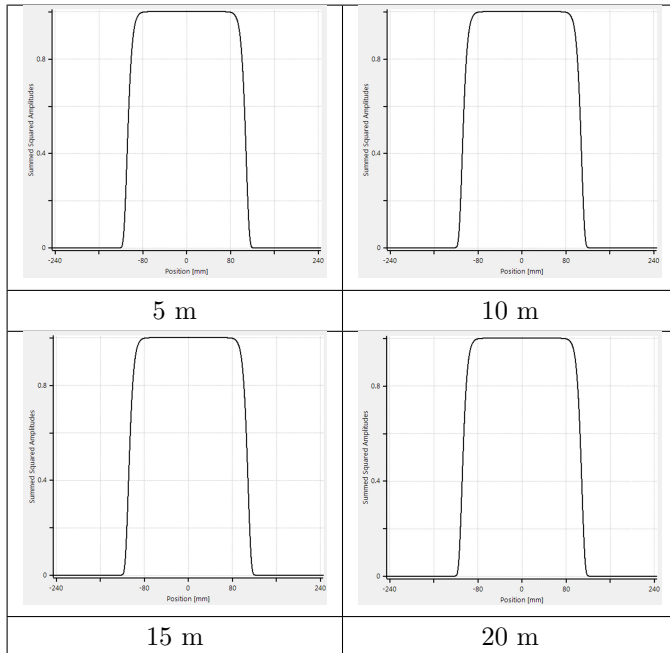
Propagation of ultra-short fs pulses is a key element in the simulation portfolio conducted for the ELI-Bamlines facility. This is also another important reason to step-up to Unified Field Tracing, since the ray-tracing software bundles (like the Zemax OpticStudio, OSLO and others) do not contain any feature to propagate ultra-short pulses.

For the purposes of this dissertation it will be advantageous to simulate a free space propagation for a super-Gaussian beam to a distance of 20 m. This is also a distance to which the considered relay optical systems should transport the input beam. The reader can later compare the free space propagation of these beams and their relaying by optical systems. Propagation of super-Gaussian beams is also much more interesting from the simulation point of view, since the diffraction effects are becoming more pronounced and are also causing other effects than just beam spreading.

The purpose of the following beam propagation study is to show the amount edge diffraction effects on the beam, and eventually demonstrate the need for optical relaying systems.

A reference distance of 20 m has been chosen to describe the beam's diffraction effects. This distance is similar to the length of the proposed 4- f systems. It is anticipated that such simulations should demonstrate whether there is a need to optically relay super-Gaussian beams of specific orders by transport telescopes. To compare the diffraction effects, beams are observed at distances of 5, 10, 15 and 20 meters. The beam orders used are m equals to 20, 100 and 500. The lowest order $m = 20$ is closest to the real situation.

Table 1: Propagation of order 20 super-Gaussian beam with 107 mm radius (5 m, 10 m, 15 m and 20 m propagation distance, respectively).



Results in Table 1 clearly demonstrate that a beam of order $m = 20$ does not exhibit diffraction effects at any of the shown target planes. However, it needs to be stressed that all beams used in the simulations described in this dissertation are ideal, i.e. without any intensity, phase distortions or modulations.

The beam of order $m = 500$ manifests strong diffraction effects at all distances. Such edge spikes can be higher than the LIDT and can consequently cause damage to the optics.

If we only consider diffraction effects, the following conclusion can be made: A beam that has an equal shape at the 20 m distance as an initial beam has less need to be optically relayed than a beam that exhibits pronounced diffraction effects.

Summary

Simulations in this subchapter are limited to cases of ideal beams only (i.e. without phase irregularities). These can be extrapolated to include artificial phase irregularities as shown in the Zemax simulations inside the research report contained within the appendix of this thesis. However, the exact data of the input HAPLS beam delivered by the LLNL was not available to the author. When the measurement of the HAPLS (The High-Repetition-Rate Advanced Petawatt Laser System) becomes available, it will be possible to improve the precision of the simulations by importing real world phase irregularities. Also the influence of non-linear effects was not considered, as they are not yet included in the VirtualLab Fusion engine.

7.2 Focusing by an Ideal Lens

The following simulations were envisioned by an experimental team preparing the experiments for focusing the beam onto a capillary tube. In these experiments it is advantageous to know what the limitations caused by diffraction are when focusing squared super-Gaussian laser beams of various orders. Knowing the diffraction limit of the focused squared beams will help with several experiments conducted within the ELI-Beamlines facility.

In the practice of optical engineering, there exist numerous metrics for image or beam quality assessment. These metrics can be divided into two basic groups – geometric and diffraction. The most simple one is spot size. However, even determining the spot size can be complicated due to aberrations and/or the eccentricities in the optical system. Another widely used criterion in lens design is wavefront distortion. Generally, if the distortions are smaller than one wave, it is far better to use diffraction metrics. These comprise PSF⁴ [30–32], MTF⁵ [16] or the Strehl ratio [31–34]. In contrast to the common approach for accessing these metrics, Maxwell’s equations are directly solved in the cases presented in the dissertation. These can be solved either approximately or in a rigorous way by the application of the spectrum of the plane waves (*SPW*) operator that is used to propagate the field in the vicinity of the focal plane in order to investigate the Strehl ratio evolution of defocused beams. This is conducted in Wyrowski VirtualLab Fusion with the use of the Unified Field Tracing concept. The influence of the squared super-Gaussian beam order and its apodization is also considered. Results of the acquired metrics are plotted.

It is very important to know how the aperture or apodizing mask will change the diffraction pattern in the focal plane. In Fig. 3 there are three cases (270 mm, 250 mm and 230 mm diameter) for a hard aperture (1 % edge width). For each of the input beams, its diffraction pattern is shown in the focal plane. If the hard aperture is used to clip the input square beam, a

⁴Point spread function

⁵Modulation transfer function

typical star-like shape appears in the focal plane. This is caused by the polygon-like shape of the input field. If the only homogenous part of the beam is selected, the beam behaves like a top-hat beam, thus the focal spot more resembles the Airy disk.

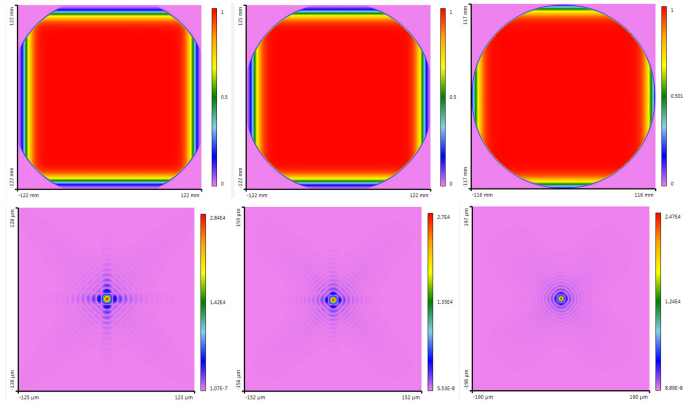


Figure 3: Beams after a hard aperture (upper part of the figure) and diffraction patterns in the focal plane (lower part of the figure). Aperture diameters are from the left 270 mm, 250 mm and 230 mm, respectively.

According to the preliminary information on one of the facility’s beamlines (abbreviated L3), the source to be tested has expected properties that are as follows: FWHM size 214 mm, beam order 20, wavelength 820 nm. These parameters are used for defining the first LPD subdomain – a super-Gaussian wave. Another subdomain is the aperture. With this subdomain, either hard apertures or gradient apodizations can be set based on the aperture width. In this case we are specifically interested in four cases. Without an aperture, and also with 270 mm, 250 mm and 230 mm circular apertures, respectively. These values were proposed by the experimental team. The width of the aperture edge is set to 1 % or 10 % - defined relatively to the smaller of both values of diameter [27]. That means that in the first case scenario the aperture can be considered as a hard aperture, whereas the latter scenario simulates an apodizing mask. The next subdomain in the simulation sequence is a $2f$ -Setup that embodies an ideal lens. In the scenario presented, a 2 m focal length is chosen. For visualization purposes Virtual Screens are added to the light path wherever the field distribution is of interest.

Fig. 4 consists of apodized input beams and corresponding diffraction patterns in the focal planes. If an apodizing mask of the same diameter is applied instead of a hard aperture, the star-like diffraction is suppressed, while achieving higher values of amplitude in the spot’s center. The quality of all these diffraction patterns is assessed by application of various metrics. Here, in this summary, only encircled energy calculations are presented.

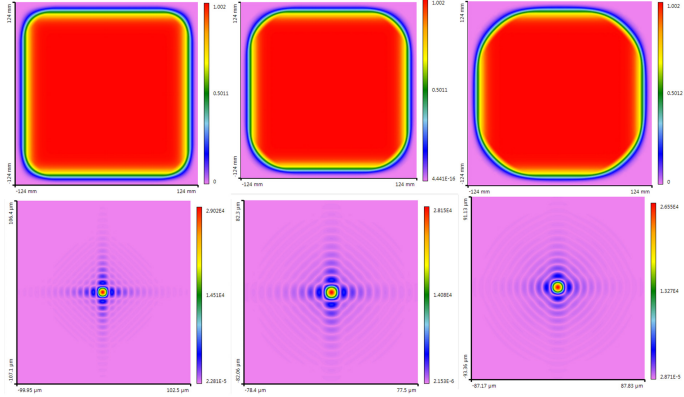


Figure 4: Beams after a 10 % apodization (upper part of the figure) and diffraction patterns in the focal plane (lower part of the figure). Aperture diameters from the left are 270 mm, 250 mm and 230 mm, respectively.

Summary

In this subchapter the theoretical limitation of the super-Gaussian beam has been discussed. So far there is no clear agreement on the demanded focal spot shape or quality. Sometimes only the peak fluence is important. Therefore, it is complicated to define proper beam apodization if the requirements are not clearly defined by the laser users.

To quickly compare the resulting encircled energies, it is advantageous to choose some simple criterion. As an example, using the radius, inside of which 90 % of the focal spot's energy is encircled. Table 2 and Table 3 show these values separately for hard apertures and for apodization masks, respectively.

Table 2: Radius inside of which 90 % of the energy is contained (hard aperture).

Beam order	270 mm [μm]	250 mm [μm]	230 mm [μm]
5	7	9.25	11.75
10	10	11.5	13
20	11	12	13.25
50	11.25	12.5	13.5

Table 3: Radius inside of which 90 % of the energy is contained (apodizing mask).

Beam Order	270 mm [μm]	250 mm [μm]	230 mm [μm]
5	6.25	6.5	7
10	7.75	8	8.5
20	11	11.25	11.25
50	12	12	12

7.3 Transmissive Relay Optics

In this chapter various optical systems containing only refractive elements are investigated. There are several case scenarios related to the ELI-Beamlines facility. In the case of relay systems it has proceeded from the physically ideal (achromatic and without an aperture) 4- f system, to real systems comprising optical aberrations. Transmissive optics will probably not be the most used optics in the main beamlines of the ELI-Beamlines facility, due to the ultrashort (femtosecond) duration of the pulses. However, even within ELI-Beamlines, such systems may be used behind the leak mirrors to relay beams to diagnostic stations, or to change their sizes for imaging on the CCD sensors.

The main motivation to use relay systems for a laser beam is to conserve its spatial profile over a long distance, which is typically being disturbed by the effects of diffraction and/or self-focusing, while the beam propagates. This was primarily investigated by Hunt [11, 12].

In the first example, the relay system does not exhibit any optical aberrations at all. The only limitation is beam diffraction. The system is built by two paraxial lenses with a common focal point and the same focal length, thus with magnification $M = 1$. Similar to that concept, two ideal lenses without an aperture are used within VirtualLab Fusion to create an optical system equal to that of Zemax.

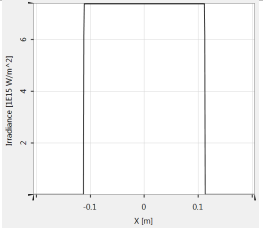
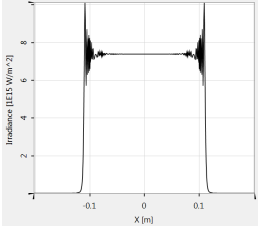
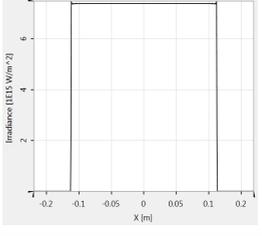
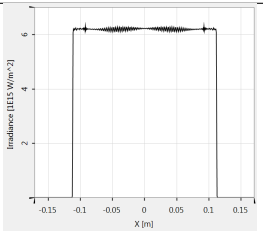
From a technical point of view it makes sense to compare the free space propagation of super-gaussian beams with beams that were relayed by a 4- f system. Some examples of free space propagation of super-Gaussian beams are already described. It was demonstrated that ideal super-Gaussians of orders of tens do not suffer by diffraction as do the beams with higher orders. Hence, it is only logical to show the advantage of relay systems for beams that suffer more by diffractive effects. In one example the super-Gaussian beam has an order of 1000, radius of 112.8 mm and wavelength of $\lambda = 820$ nm and its profile is shown in table 2.

Distances inside the ELI-Beamlines facility are typically within the magnitude of tens of meters. Therefore, the beam will most probably be relayed to a distance of around 20 m. To show the performance of such a 4- f system, two ideal lenses without an aperture of focal length $f = 5$ m were chosen. The beam is propagated from its source to the target plane with the use of a rigorous SPW operator. The reader can clearly see the difference between the beam propagated in free space and beam relayed by a 4- f system. High order, almost top-hat beams, exhibit spikes around the edges (in the community sometimes referred to as “ears”) after few meters of free space propagation, whereas the relayed beam is nearly the same as the original one. Such spikes can carry intensities larger than the mirror’s LIDT⁶ and lead to the mirror’s destruction. Therefore, it is desired to avoid these spikes, or at least precisely predict their magnitude to be sure that they will be within the mirror’s specified LIDT. There is also a case showing the use of a relay

⁶Laser Induced Damage Threshold

system with real plano-convex lenses. The material is fused silica, the lens thickness is 20 mm, diameter 210 mm and the surface radius is 2266.4 mm.

Table 2: Beam free space propagation and relaying by an ideal and a real 4- f system.

	Spatial profile
Input beam (order 1000)	 <p>A plot of Irradiance [IEES W/m²] versus X [m]. The x-axis ranges from -0.1 to 0.1 with major ticks at -0.1, 0, and 0.1. The y-axis ranges from 0 to 6 with major ticks at 2, 4, and 6. The plot shows a rectangular pulse with a constant irradiance of approximately 6 W/m² between X = -0.1 and X = 0.1 m, and zero elsewhere.</p>
Free space propagation (20 m)	 <p>A plot of Irradiance [IEES W/m²] versus X [m]. The x-axis ranges from -0.1 to 0.1 with major ticks at -0.1, 0, and 0.1. The y-axis ranges from 0 to 8 with major ticks at 2, 4, 6, and 8. The plot shows a central plateau of irradiance around 7 W/m² between X = -0.1 and X = 0.1 m, with oscillatory side lobes on either side.</p>
Ideal 4- f relay ($f = 5$ m)	 <p>A plot of Irradiance [IEES W/m²] versus X [m]. The x-axis ranges from -0.2 to 0.2 with major ticks at -0.2, -0.1, -0.05, 0, 0.05, 0.1, and 0.2. The y-axis ranges from 0 to 6 with major ticks at 2, 4, and 6. The plot shows a rectangular pulse with a constant irradiance of approximately 6 W/m² between X = -0.1 and X = 0.1 m, and zero elsewhere, identical to the input beam.</p>
Relay with plano-convex lenses:	 <p>A plot of Irradiance [IEES W/m²] versus X [m]. The x-axis ranges from -0.15 to 0.15 with major ticks at -0.15, -0.1, -0.05, 0, 0.05, 0.1, and 0.15. The y-axis ranges from 0 to 6 with major ticks at 2, 4, and 6. The plot shows a rectangular pulse with a constant irradiance of approximately 6 W/m² between X = -0.1 and X = 0.1 m, and zero elsewhere, similar to the input beam.</p>

7.4 Reflective Optics

The previous chapter has shown possible optical systems configurations comprising lenses only. Systems in the following text are either catoptric or catadioptric. Several design concepts are discussed in the next few paragraphs. The basic problem to be solved within ELI-Beamlines how to relay the beam from the source to the experimental room, most likely with the use of either planar and/or off-axis parabolic mirrors. Several scenarios are discussed and assessed in the following text. The feasibility of various system geometries are analysed. Also reflective reducers and telescopes for beam diagnostics are discussed.

7.4.1 Beam Relaying

The use of mirrors for beam relaying of high peak power ultrashort laser pulses is inevitable. Text in this subchapter assesses a few possible mirror configurations. The task is to define the feasibility of the following system configurations.

“U” and “Z” OAPs Configuration Comparison

One of the first tasks assigned to be analysed in VirtualLab Fusion was to assess various relaying systems containing two off-axis parabolas. A combination of parabolic surfaces can entirely eliminate spherical aberration and minimize influence of astigmatism as a consequence of optical surface tilt. These surfaces need to have an ideal or nearly ideal shape and they need to be perfectly aligned. A combination of two parabolas (and two planar mirrors) is the simplest solution for a relay telescope. There is no other solution that will be simpler than this one. Two spherical surfaces do not suffice for the required imaging quality. The solution is to use parabolic mirrors, which entirely eliminates the spherical aberration that is dominant in axial ray bundles.

Basic aberration of the telescope created by a pair of off-axis parabolas is logically caused by the aberration of each OAP. The parabolic mirror has zero spherical aberration. In the case of off-axis ray bundles (or surface tilts) there is coma and astigmatism. For a narrow ray bundle (in the case of high f -numbers), we can assume that the dominant off-axis aberration is astigmatism. Basic optical ray-tracing analysis of the “Z” and “U” OAP combinations have been conducted by Miroslav Palatka [36]. These analyses show that the dominant off-axis aberration is really an astigmatism. The main conclusion of these analyses is that the “Z” configuration enables the compensation of astigmatism due to the opposite sign of the aberration for both mirrors. Conversely, in the the “U” configuration these astigmatisms are not compensated, but rather their sum is the unfortunate result. It can clearly be seen that the “Z” type configuration is the only one that is satisfactory.

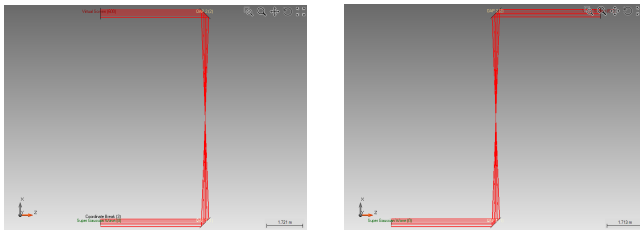


Figure 5: “U” (left) and “Z” (right) OAPs configuration – Ray Tracing (VirtualLab Fusion).

A similar investigation is conducted within VirtualLab Fusion. In contrast to Zemax Optic-Studio, so-called smart rays are available. While using these smart rays, information concerning all components of the electromagnetic field is constantly available. Moreover, instead of the typical ray bundle (square, hexapolar or random), the super-Gaussian beam can be used directly. Thus, the shape of the relayed beam can be directly observed.

As usual, first the LPDs are prepared - particularly for the “U” and the “Z” shaped relay. Both geometries have a 90° off-axis angle (as seen in Fig. 5).

As the input, a super-Gaussian beam with a squared aperture is used. With the application of an optical relay system, a similar beam is the expected output as well. Based on the previously discussed ray-tracing information, it is expected that the “Z” shaped system should perform better than the “U” shaped, mainly because of the astigmatism. The simulation conducted within VirtualLab Fusion clearly confirms this finding. While the beam being relayed by the “U” shaped system is being distorted (Fig. 6), the beam relayed by the “Z” shaped system looks exactly like the input beam (Fig. 7). Geometric Field Tracing in VirtualLab Fusion is based on the use of meshes, which are shown in the left parts of the figures. From the meshes, the rest of the beam can be reconstructed.

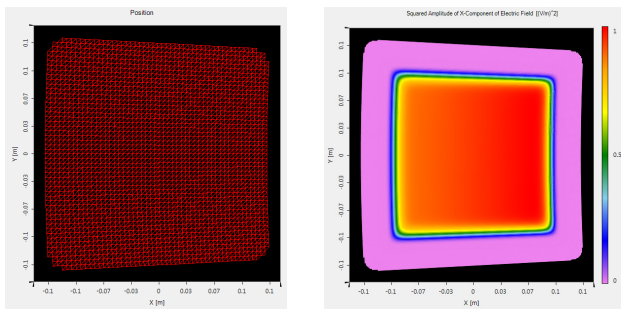


Figure 6: Super-Gaussian beam relayed by “U” OAPs configuration – meshes (left) and the reconstructed field (right).

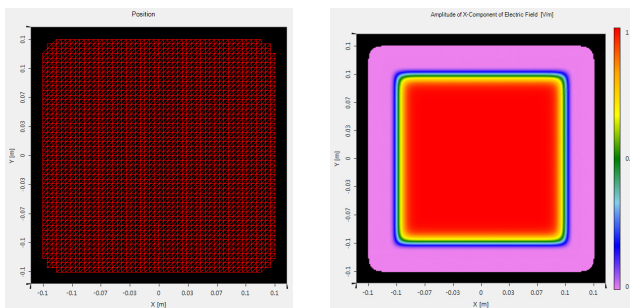


Figure 7: Super-Gaussian beam relayed by “Z” OAPs configuration – meshes (left) and the reconstructed field (right).

It is obvious, that the “U” shaped system is absolutely unfeasible for the beam relaying. Conversely, the “Z” shaped system seems to work correctly. However, one question still remains – what is the influence of the off-axis angle to beam relaying?

Angle analysis of the “Z” OAPs Configuration

The previous paragraph demonstrated that the “Z”-like shaped configuration of OAPs is much more efficient in eliminating aberrations. However, in the previous case only the super-Gaussian beam has been traced. A correctly working 4- f relay system should transform planar wave into a planar wave, and the point source (spherical wave) into a point image. The following analysis is conducted with the intent to investigating whether or not two OAPs can be possibly used in such a regime. VirtualLab Fusion’s unique Geometric Field Tracing is exploited to aid in this task.

The input spherical wave is shown in Fig. 8.

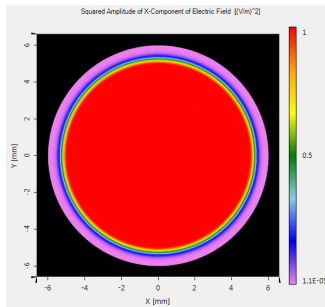


Figure 8: Input field to be relayed.

Then a similar system to the one already described is used to relay this spherical wave to the focus of the second OAP. Unlike the cases in Figs. 6 and 7, the off-axis angle is now only 5 degrees (see Fig. 9), in contrast to the 90 degrees originally used .

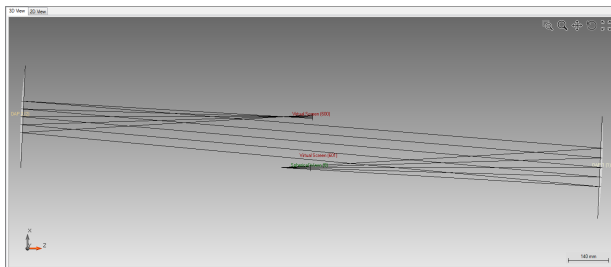


Figure 9: 5 degree “Z” OAPs configuration – Ray Tracing (VirtualLab Fusion).

The field being relayed from the focal point of the first OAP to the focal point of the second OAP is shown in Fig. 10. Fig. 10 illustrates the squared amplitude of the E_x , E_y and E_z components of the field in the focal plane. The reader will notice that the field is very similar to the input field, although there are non-zero values for the E_y and E_z components of the field.

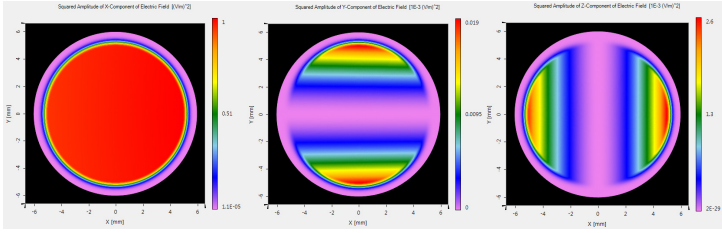


Figure 10: Comparison of the squared amplitude of the E_x , E_y and E_z components of the relayed electromagnetic field for the 5 degree angular tilt of the parabolic mirrors.

It is even more interesting to observe the field evolution while the off-axis angle is changing. The figures 11 and 12 represent the ray-tracing of the system used to precisely display the system's configuration and the squared amplitude of E_x , E_y and E_z components of the field in the focal plane, respectively.

The reader can clearly distinguish that with an increasing off-axis angle, more energy is transferred to the E_y component of the field. The E_x part of the field becomes more and more asymmetrical. This conclusion demonstrates that the relay system with 90 degree off-axis angles actually does not do exact image relaying. If image relaying is required, the off-axis angle should be as small as possible. For example the already demonstrated 5 degrees.

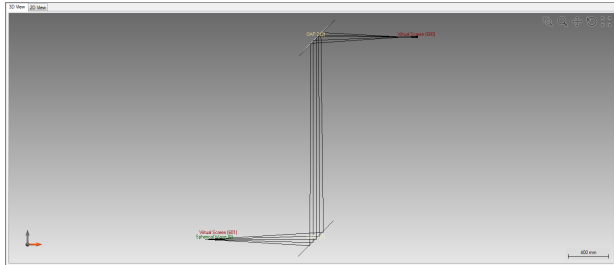


Figure 11: 90 degree "Z" OAPs configuration - Ray Tracing (VirtualLab Fusion).

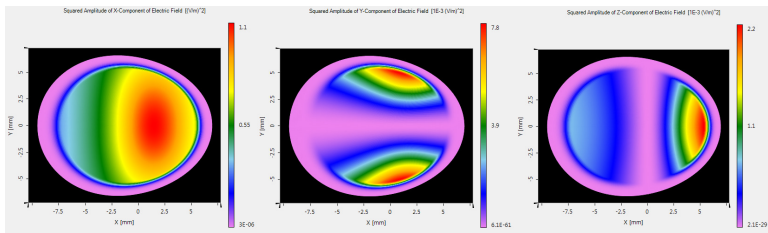


Figure 12: Comparison of the squared amplitude of the E_x , E_y and E_z components of the relayed electromagnetic field for the 90 degree angular tilt of the parabolic mirrors.

7.4.2 Catoptric Reducers

In the main beamline, only the reducers with reflective elements are feasible due to the laser induced damage threshold and GVD. Two basic system geometries are available for comparison, one with and one without the intermediate focal plane. These are equivalent to the Keplerian and Galilean systems, but with the mirrors only.

The L3 laser parameters are extraordinary (see Table 5). Therefore, the laser induced damaged threshold needs to be briefly discussed.

For our purposes it is assumed that the 1000 mJ/cm^2 is the fluence limit that a mirror can withstand without being damaged. The magnification ratio of the reducers described 2:1. The fluence on the secondary mirror of the reducers will not exceed 300 mJ/cm^2 . Nevertheless, it may be problematic to acquire large magnification ratios because of the excess fluence levels.

Table 5: L3 source beam parameters.

Parameter	Value
FWHM	214 mm
$1/e^2$	225.6 mm
$1/e$	220
Order	20
Total Energy	30 J
Power	$1.5 \cdot 10^{15} \text{ W}$
Peak fluence	65 mJ

Catoptric Reducers with an Intermediate Focal Plane

In the first case a reducer with an intermediate focal plane is analysed. The reducer contains two positive mirrors with a common focal plane as seen in Fig. 13 from Zemax OpticStudio. The first parabolic mirror has a focal length of 20 meters, whereas the second parabola has a focal length equal to 10 meters, thus reducing the beam size by half.

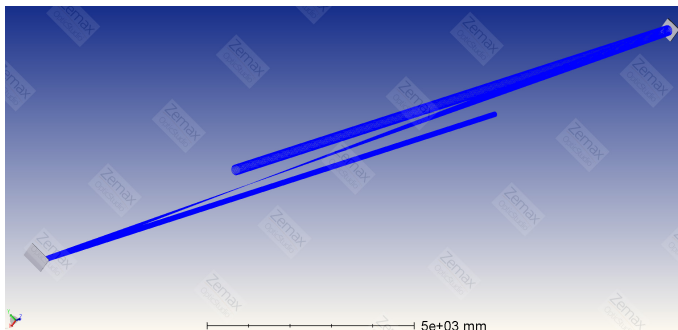


Figure 13: Ray-tracing of the reducer.

First the spot sizes are analyzed (see Fig. 14). Due to the use of this pair of parabolas, there are absolutely no aberrations in the focal plane. The residual aberrations are field curvature and distortion. Due to the use of parabolas the performance observed is extremely good.

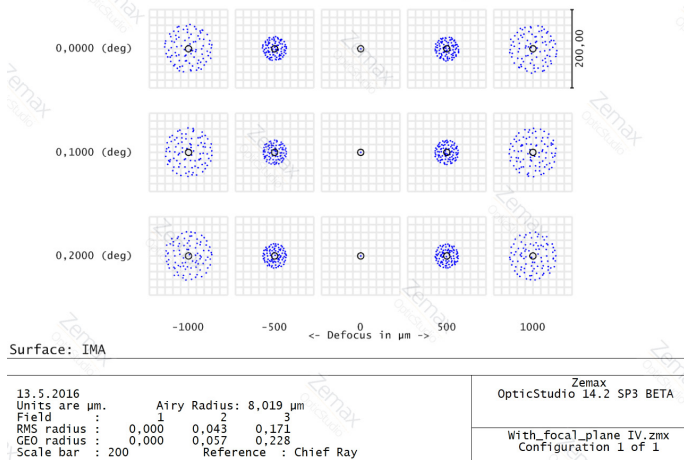


Figure 14: Spot diagrams of the reducer.

Catoptric Reducers without an Intermediate Focal Plane

In the current case, a reducer without an intermediate focal plane is analysed. The reducer contains one positive and one negative mirror. The focal length of the first concave mirror is 20 meters, whereas the second convex mirror has a focal length equal to -10 meters. The focal length of the first parabolic mirror has the same focal length as the first parabolic mirror in the previously described case. This makes the comparison of these two systems easier. Ray-tracing of the reducer is shown in Fig. 15.

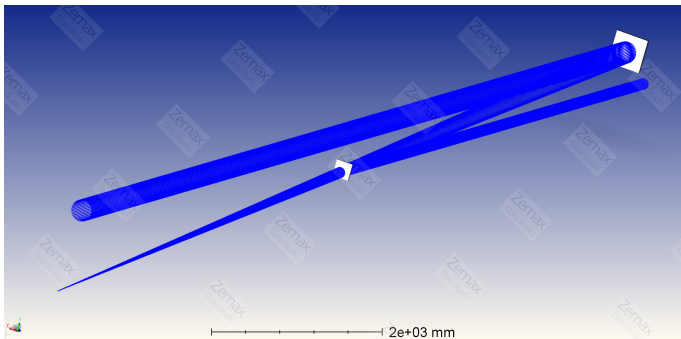


Figure 15: Ray-tracing of the reducer.

Similar to the previous reducer, the spot diagrams are observed first (see Fig. 16). Again, due to the use of a pair of parabolas, the focal spots lack any aberration.

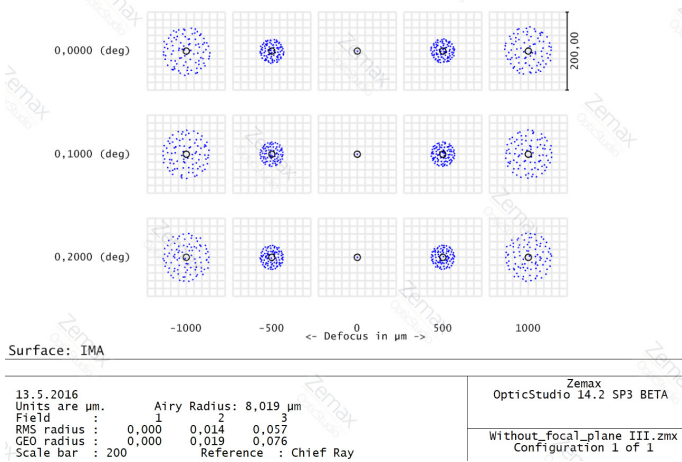


Figure 16: Spot diagrams of the reducer.

Once again, the coma and the astigmatism are compensated. Also the field curvature is similar to the previous case. The only difference is in distortion, which is half of the previous amount. The performance is slightly better in comparison to the previous case. However both results are acceptable.

Summary

Both reducer types perform very well based on the optical simulations conducted. The main reason to prefer one over the other depends on whether the intermediate focal plane (or re-imaging of the field) is needed. The main drivers are spatial filtering and ease of alignment. These two elements support the preference to use a reducer with an intermediate focal plane. Conversely, if the total length of the system is most important, then the reducer without the intermediate focal plane is more convenient.

7.4.3 Telescopes for Beam Diagnostics

Telescopes for beam diagnostics (or beam monitoring) contain both transmissive and reflective elements. These systems are intended to be placed behind so-called leak mirrors. The main task of these telescopes is to reduce the beam size so it can be imaged on the CCD of a conventional Shack-Hartmann sensor made by Thorlabs [35]. The motivation for this system is to diagnose the beams' temporal and spatial properties across each beamline. However, there are some obstacles to achieving this goal. First of all, the power typically exceeds the damage threshold of most available diagnostic systems, and secondly the beam size is too big to be imaged on the majority of sensors. The combination of a leak mirror and the beam diagnostic telescope solves both problems. Behind the leak mirror only a fraction of the power is transmitted, then the beam can be reduced by the combination of reflective and transmissive elements to the desired size in order

to match the sensor's dimensions. This system is commonly referred to as a telescope for beam diagnostics.

The inspiration for the telescope described in this dissertation comes from an achromatic beam diagnostic telescope for Astra Gemini [37] (Central Laser Facility, STFC Rutherford Appleton Laboratory).

The idea is to prepare a similar optical system out of commercially available components, especially the parabolic mirror, which is the most expensive component in the telescope. Such parabolas can be provided by companies like Edmund Optics Inc. (EO)[38] or Czech Astro Telescope Company (ATC), a. s. [39]. Both companies are capable of providing suitable parabolas with a focal length of 2 m and precision of $\lambda/8$. The current⁷ price of EO's parabola is 7450 USD, whereas ATC's parabola costs 85 000 CZK (approximately 3500 USD).

Another important part of the system is a proper negative achromatic doublet working in the NIR part of the spectrum. Corresponding optical elements working within the bandwidth of 650–1050 nm can be found in the catalogue of the Thorlabs company [40]. Suitable doublets include:

- ACN127-020-B with a -22.5 mm focal length and thus producing about hundred times demagnification and
- ACN127-025-B with a -27.7 mm focal length which produces about eighty times demagnification.

Both doublets are cost around 50 EUR, which makes them much cheaper than the parabolic mirror. Hence the design does not necessarily need to use the Thorlabs' doublets. However, they can be used to model the initial optical design used for further optimization in Zemax OpticStudio.

Based on the information presented above, the beam diagnostic telescope will look like the one presented in Fig. 17. The design is comprised of a parabolic mirror, a beam splitter and a doublet.

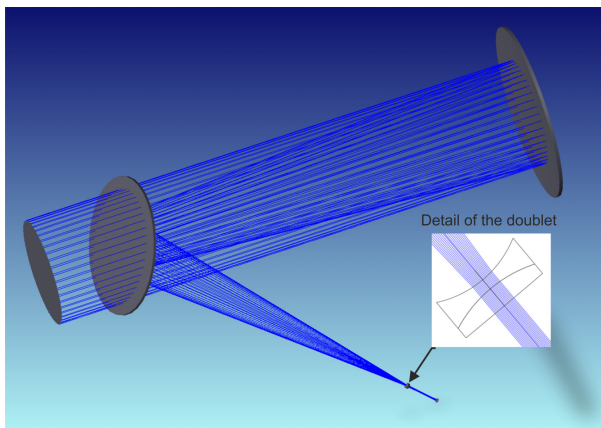


Figure 17: Ray-tracing of beam reducing telescope for diagnostics.

⁷As of April 2016.

On the following pages there is a comparison of the telescopes' performance with the commercial only components and with the custom doublet. Customization of the mirror is not considered for fiscal reasons.

Of course, customization of the doublet will greatly increase the telescope performance. Furthermore, optimization of the doublet is much cheaper than optimization of the mirror. The first, most simple comparison is to compare the Seidel aberration coefficients drawn as bars. Fig. 18 compares the original telescope with commercial only components and a telescope with a customized doublet.

The most prominent aberration in the original configuration is the spherical aberration, followed by coma and astigmatism. Customization leads to major suppression of these aberrations.

The improvement introduced by the custom doublet is illustrated in the improvement of spot diagrams (see Fig. 19). The improvement delivered with the introduction of a custom doublet is clearly visible.

Based on the results it is concluded that such beam diagnostic telescopes are feasible and easily optimized with the introduction of customized negative achromatic doublets, which are still reasonable from the fiscal point of view.

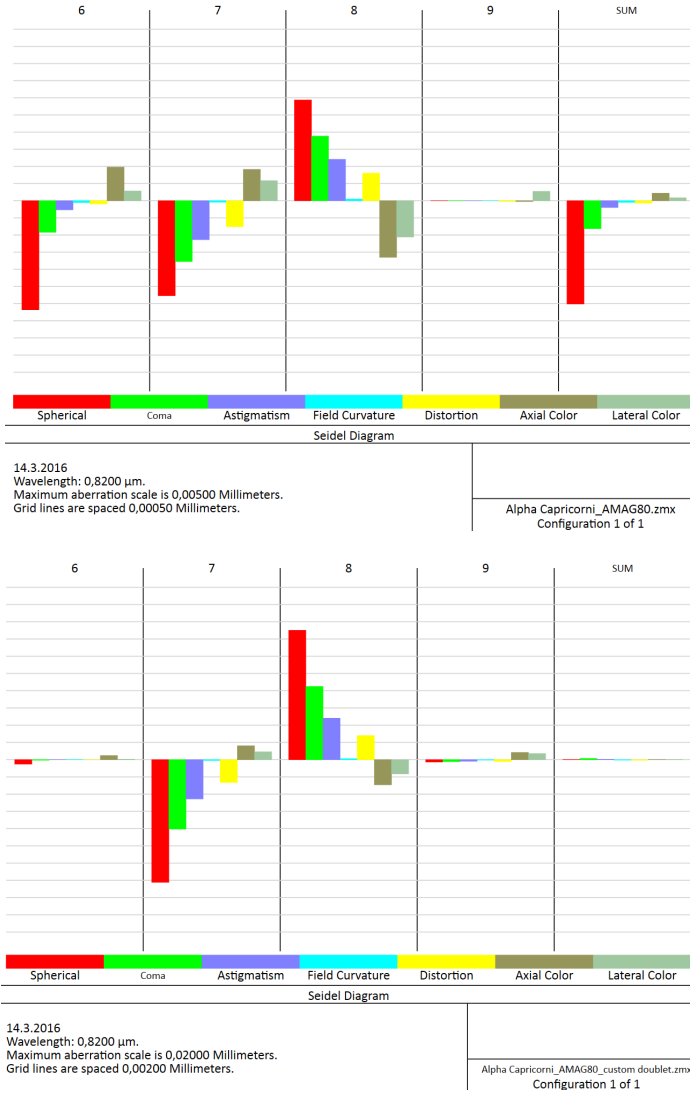
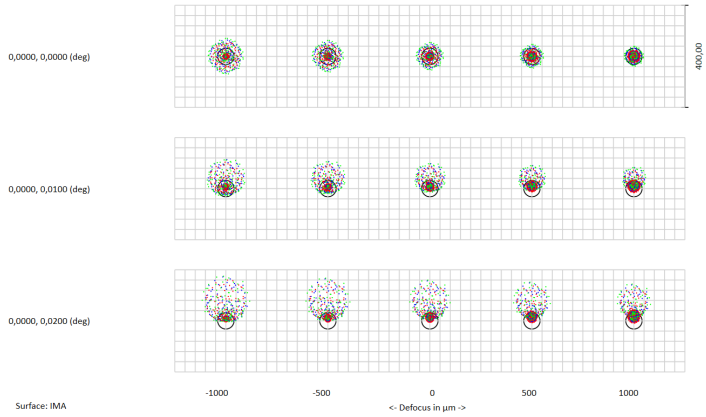
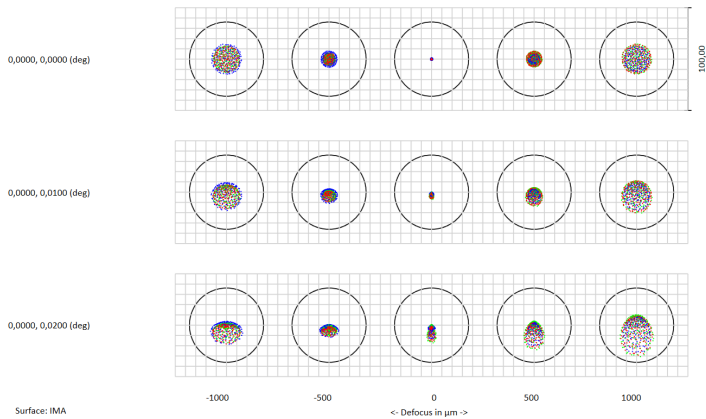


Figure 18: Seidel aberration comparison of a telescope with commercial (upper) and custom (lower) doublets.



5.5.2016
 Units are μm . Airy Radius: 32,01 μm
 Field : 1 2 3
 RMS radius : 23,855 32,843 52,335
 GEO radius : 54,865 101,279 159,656
 Scale bar : 400 Reference : Chief Ray

Alpha Capricorni_AMAG80.zmx
 Configuration 1 of 1



5.5.2016
 Units are μm . Airy Radius: 36,15 μm
 Field : 1 2 3
 RMS radius : 0,689 2,357 5,490
 GEO radius : 1,084 7,024 17,247
 Scale bar : 100 Reference : Chief Ray

Alpha Capricorni_AMAG80_custom doublet.zmx
 Configuration 1 of 1

Figure 19: Spot diagram comparison of a telescope with commercial (upper) and custom (lower) doublets.

7.5 Beamlines

Unlike the previously written text showing only specific components of beamlines (for example, reducers), in this subchapter simulations of the entire beamlines' systems are described, containing several folding mirrors and final focusing optics. The ELI-Beamlines facility contains several laser and experimental halls. One of the main purposes of each beamline is to steer the laser from the source to the target, while maintaining the prescribed requirements on the spatial and temporal quality of the beam.

Among all beamlines within the ELI-Beamlines facility, this thesis focuses primarily on the L1-E1 and the L3-E3 beamlines. Both of these beamlines are subsystems of a larger system of beamlines, the complex L1 and L3 beamlines, respectively.

Analyses in the next few subchapters focuses especially on the tolerancing simulations (in the case of L1-E1) and the beam quality influenced by the hole inside the folding mirror (in the case of L3-E3).

7.5.1 L1-E1

The reason for the following analysis is to demonstrate VirtualLab Fusion's capability to go beyond the classical tolerancing process that is usually conducted within the common ray-tracing software bundles like Zemax OpticStudio. Analysis with the use of ray-tracing has been conducted by other colleagues within the BPM team.

As usual, first the LPD of the L1-E1 is built-up, so the ray-tracing can be conducted (see Fig. 20).

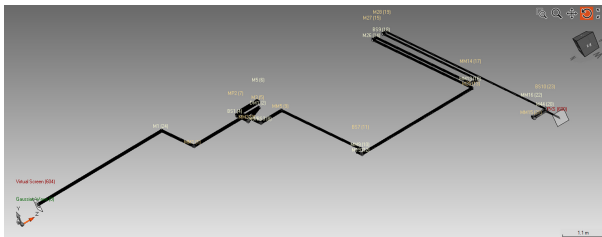


Figure 20: L1-E1 ray-tracing (VirtualLab Fusion).

Three specific tolerancing procedures are conducted: (1) Investigation of the beam clipping by a mirror for various beam diameters. (2) Beam decentering. (3) Single mirror tilt

Note, that the L1-E1 incorporates a Gaussian, rather than a super-Gaussian beam.

Beam Clipping

First, the issue of beam clipping in the thesis is described from the single element point of view. In the current case, the beam transported by the entire L1-E1 beamline is directly observed. There are three Gaussian beam sizes that are tested – 25, 50 and 75 mm. The Unified Field Tracing method within VirtualLab Fusion is used in order to examine diffraction effects as well.

From Fig. 21 the reader can see that only a 25 mm Gaussian beam is transferred by the L1-E1 system, without any clipping or edge diffraction effects.

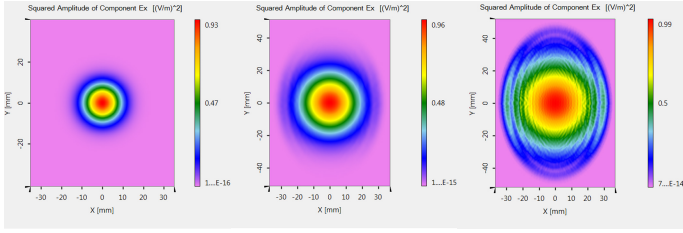


Figure 21: Beam clipping by a circular mirror with a 101.6 mm diameter. Beam diameters from left: 25, 50 and 75 mm, respectively.

Beam Decentering

Another tolerancing procedure is to observe the effects of beam decentering on the resulting beam. For that purpose three values of decentration were chosen – 5, 10 and 20 mm. Fig. 22 illustrates that even the smallest decentering will cause observable edge diffraction effects.

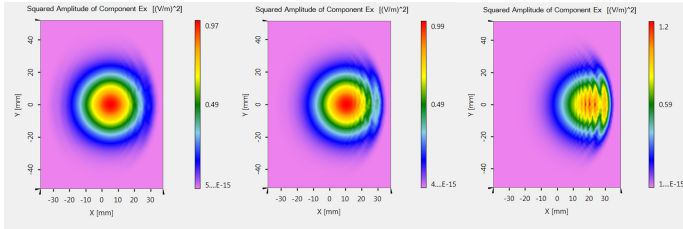


Figure 22: Beam decentering. From left: 5, 10 and 20 mm, respectively.

Single Mirror Tilt

The last tested tolerancing procedure was to observe the influence of a single mirror tilt on the beam quality. As expected, the beam quality is least resistant to mirror tilts. Even mirror tilt as small as 0.005° is clearly observable (see Fig. 23).

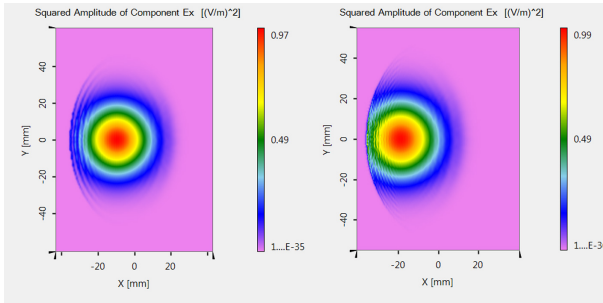


Figure 23: Tilt of a single mirror inside the beamline. From left 0.005° and 0.01° , respectively.

Summary

The conclusion is that VirtualLab Fusion is capable of bringing tolerancing procedures to another level with the use of Unified Field Tracing. It is possible to directly observe the diffraction effects caused by the tolerancing of different parameters of the beamline. The alignment of each single mirror has to be precisely controlled, especially for tilts. Most likely, it will be needed to control each optical component by other optical systems (alignment stations) in order to control their precise adjustment.

7.5.2 L3-E3

Unlike the aforementioned L1-E1 and all other beamlines, L3-E3 does not incorporate off-axis parabola as a final focusing optical element. The reader will see the ray-tracing of the system in the Fig. 24. In contrast to all beamlines, it uses a relatively cheaper spherical mirror. The use of an axial spherical mirror also makes it necessary to have a hole drilled in the middle of the last planar folding mirror, to allow the spherical mirror to focus the beam behind the folding mirror.

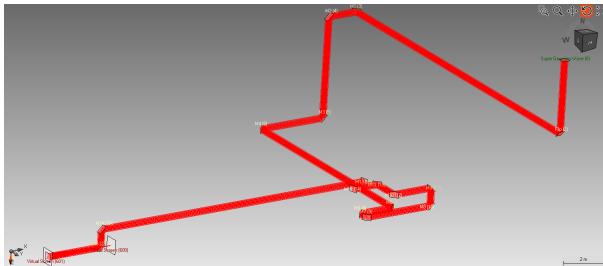


Figure 24: L3-E3 ray-tracing (VirtualLab Fusion).

Since it is necessary to drill a hole in the mirror, several questions emerge. The most obvious and important ones are: How significant is the influence of the hole diameter on the transmitted beam power? What is the beam quality after passing the holed mirror, with respect to the M^2 factor and to the encircled energy?

Answers are revealed in the following paragraphs. First the ideal case is discussed, then the surface irregularities are also taken into account.

Through the Hole Focus – Ideal Case

To know the physical limitations of the system, only the ideal components are considered. Either the planar folding mirrors and the spherical focusing mirror are free of any surface imperfections and the spectral reflectances are equal to 1 over the entire bandwidth. Also a simplification of the model, to save some computational time, has been done. The simplified system comprises the last two folding mirrors and the spherical focusing mirror ($f = 5$ m). The focal plane is 200 mm behind the folding mirror M2. This situation is depicted in Fig. 25.

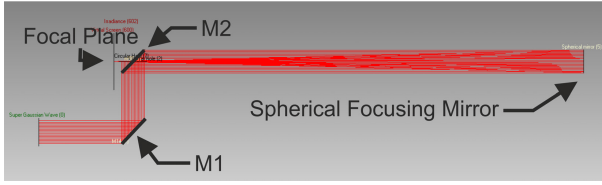


Figure 25: L3-E3 ray-tracing (VirtualLab Fusion).

First power is investigated, as focused power is the facility’s main deliverable. The reader should understand that the hole inside the folding mirror actually plays two roles. Initially, the hole acts as a stop, while in the second step the same hole acts as an aperture. In other words – the hole (*the aperture*) needs to be large enough to transmit as much focused power as possible, while simultaneously the same hole (*the stop*) needs to be as small as feasible in order to block the minimum power of the original super-Gaussian beam with a square aperture. The expectation is that there should be some peak, representing an ideal trade-off between these two requirements.

The ideal hole size is investigated with the aid of VirtualLab Fusion and its feature called The Parameter Run. A Light Path Diagram is built for the simplified system and the hole size. The stop and aperture diameter is chosen as variables. While the power in the focus is being registered. The resulting plot of the focused power is shown in percentages in Fig. 26.

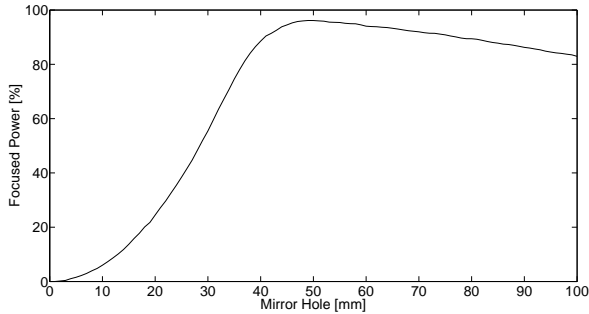


Figure 26: The percentage of focused power as a function of mirror hole diameter.

The plot clearly demonstrates that the ideal hole size for this specific geometry should be between 40 mm and 50 mm. This is only from the power transmission point of view. However, there can be other beam quality criterions. The simplest way to describe a beam quality is to use the so-called M^2 factor [84, 85], which is able to characterize the beam with a single number. Hence, it is also called a beam quality factor. Fig. 27 shows a plot of the M^2 factor for both beam axes as a function of mirror hole diameter. The lower the number, the better the beam. For the ideal TEM₀₀ (Gaussian) beam, the $M^2 = 1$.

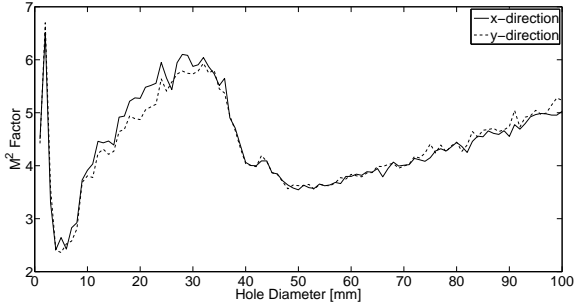


Figure 27: M^2 factor for both beam axes as a function of mirror hole diameter.

In the plot it can be seen that there are two minima, the first between 0 mm and 10 mm, which is not feasible from the transmitted power point of view. And the second one, which is near the 50 mm diameter of the mirror hole.

Another metric which illustrates beam quality is encircled energy. It is advantageous to compare the encircled energy of the real focal spots with the diffraction limited focal spot (see Fig. 28). Plots of encircled energies for both depicted hole sizes are very similar. However, the 40 mm hole size creates an encircled energy that is a little bit closer to the ideal state.

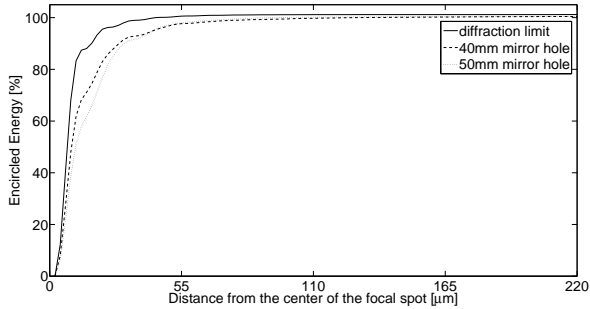


Figure 28: Encircled energy of the beam focused through the mirror hole (shown for a diffraction limited focusing and focusing through the hole with the two specific diameters).

From the previous comparisons, it is obvious that the ideal hole size should be between 40 and 50 mm in the case described. Nevertheless, it is worth demonstrating the evolution of encircled energy distribution for various mirror hole sizes (as demonstrated in Fig. 29). Readers can see for themselves that these mirror hole sizes are close to the ideal state.

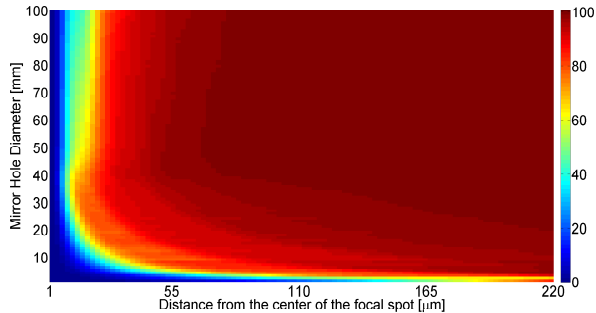


Figure 29: Encircled energies for various mirror hole diameters.

Through the Hole Focus - with Surface Irregularities

In the previous paragraph a limiting physically ideal situation, counting on ideal surfaces free of any surface irregularities was analyzed. However, in practice all optical elements have some amount of surface irregularities, which is proportional to the applied fabrication method. Consequently, the simulation must be extrapolated by introducing the presence of surface irregularities. Surface irregularities are described by the surface RMS, P-V⁸ [43] or slope error [44]. Optical manufacturers usually prepare several types of batches based on the surface RMS values – the typical range is $\lambda/4$, $\lambda/10$ and $\lambda/20$. Anything superior must be done using the custom fabrication process, thus causing additional financial expense.

To simulate the presence of surface irregularities the use of TEZI [45] operand within the Zemax tolerance feature is necessary. Provided that the surface RMS is known, the TEZI operand will calculate the corresponding Zernike polynomial creating the matching surface sag. The user needs to determine the number of Zernike coefficients used to define the polynomial. In the case described, only coefficients up to 10 are chosen, thus the polynomial only represents the low spatial frequency errors. By implementing this procedure, surface roughness cannot be simulated to the extent that any diffraction effects caused by the single-point diamond turning mirror fabrication method are visible. It is obvious that there are infinite possible Zernike polynomials with corresponding surface RMS. Hence, the Monte Carlo simulation, which creates only a limited number of random Zernike polynomials, is used. After the Monte Carlo simulation, the best and worst cases are exploited for the follow-up simulation in VirtualLab Fusion.

Surface irregularities of the planar mirrors defined by the Zernike polynomial can be easily added to VirtualLab Fusion. Only the folding mirrors are affected by the surface irregularities in the simulations performed. Surface errors generated by the Zemax TEZI operand have circular symmetry, however VirtualLab Fusion can extrapolate surface errors for the whole rectangle based on these data. A simple increase of the unit size radius within OpticStudio cannot correctly represent the surface irregularities of rectangular mirrors.

Several simulation cases are created. Specifically, mirrors with surface RMS equal to the $\lambda/4$ and $\lambda/20$. For both surface RMS, values the best and the worst case scenarios are determined. Four distinct LPDs are then created in VirtualLab Fusion – the combination of the two worst case planar mirrors with $\lambda/4$ surface RMS, the combination of the two best case planar mirrors with $\lambda/4$ surface RMS, the combination of the two worst case planar mirrors with $\lambda/20$ surface

⁸Abbreviations for peak-to-valley.

RMS and finally the combination of the two best case planar mirrors with $\lambda/20$ surface RMS. The resulting focal spots are shown in the Fig 30. Their sizes are in Table 6.

The amount of allowable surface irregularities is mainly induced by the available deformable mirrors with sufficient LIDT. So far, the author has no information on the technical specifications of the deformable mirror that will be available for the beamline. As soon as the decision is made, a precise analysis of the allowable surface irregularities for all optical components can be conducted.

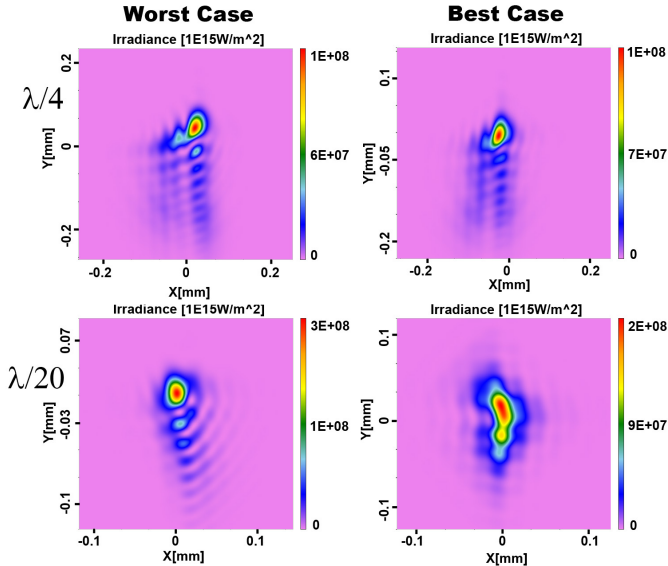


Figure 30: Resulting focal spots in the systems with surface irregularities on planar folding mirrors.

Table 6: Resulting focal spots sizes in the systems with surface irregularities on planar folding mirrors.

RMS error	Spot Size
$\lambda/4$ – Best	61.3 μm \times 135.3 μm
$\lambda/4$ – Worst	69.3 μm \times 141.2 μm
$\lambda/20$ – Best	43.3 μm \times 66.5 μm
$\lambda/20$ – Worst	41.8 μm \times 82.5 μm

Through the Hole Focus - with Coatings and fs Pulse

In the previous case, all of the mirrors used (either folding or spherical focusing) had ideal reflective surfaces. That means the reflectivity is equal to 1 over the entire bandwidth. The implication is that the temporal effects of the mirrors cannot be investigated. In reality, each mirror will have a stack of thin films deposited on their surfaces causing the pulse to stretch. Typically the high reflectivity coating stack is composed of two dielectrics with low and high refractive indices, which periodically alternate in this multilayer system. The layers used in the case described are created by a combination of SiO₂ and TiO₂ (as seen in VirtualLab Fusion's coating editor in Fig. 124). Prescriptions for these mirror stacks were kindly provided by Dr. Werner Moorhoff from LASEROPTIK GmbH [46].

The input pulse with $\lambda = 820$ nm has a Gaussian temporal profile and a duration of 31.34 fs. The duration of the pulse in the focal plane is equal to 36.79 fs.

Summary

The E3 room serves for plasma physics experiments. The results shown in the previous text will help plasma physicists to prepare their experiments with betatrons, especially to determine the conditions for the optimum electron acceleration. Focal spots calculated by VirtualLab Fusion, are used in the next step for PIC (particle-in-cell) simulations. A paper showing the already finished optical, and forthcoming PIC simulations, has yet to be completed. Results are also shown in the research report contained within the appendix of this thesis.

8 Overall Discussion and Assessment

According to the actual needs of ELI-Beamlines, several case scenarios related to the operation of the lasers inside this facility were analysed within the preceding text. A short summary, with discussion and assessment of the acquired results follows.

Topics discussed in the presented dissertation were mainly:

Free space propagation

The basic element of every consequent simulation is free space propagation. The stress was put on the propagation of the squared super-Gaussian beams of higher orders. It was demonstrated that for beams with orders near 20 (similar to the one used in ELI-Beamlines), diffraction is not a major problem when the beam is propagating to a distance of 20 m, as shown in the text. However, the non-linear effects were not taken into account. Investigation of the non-linear effects on free space propagation is planned for the future. This simulation was completely conducted with the aid of VirtualLab Fusion and its rigorous Maxwell equations solver (*SPW* operator).

Beam clipping

Another important part of optical engineering is to deal with economic factors. The price of optics exponentially increases with the aperture size as both fabrication and metrology of large aperture optics is very expensive. Therefore, it is advantageous to know what aperture size is actually required. Or in other words, what are the possible power losses for various optical element sizes based on their beam size : element size ratio? Analyses were conducted for various beam orders and for both circular and square symmetry of the input beam. Also, this simulation was entirely accomplished within VirtualLab Fusion and Classic Field Tracing.

Beam focusability with the use of an ideal lens

To have an idea about the final focusing optics performance limits, it is helpful to know the physical limits of focusing the squared super-Gaussian beams of higher orders using an ideal lens. Several metrics were employed to support this objective – fitted values of logarithmed $|E_x|$, encircled energy and the Strehl ratio. The influence of hard apertures and apodizations of different diameters were demonstrated. The results will serve the experimental team's decision as to the feasibility of possible apodizing masks for their experiments with focusing a beam into a capillar tube. The acquisition of the resulting values were done by VirtualLab, post-processing of the data and plot generation was managed within MATLAB.

Transmissive optics

The feasibility of transmissive reducers was analyzed. Three example configurations were designed in Zemax OpticStudio – Keplerian and two Galileans (with Fraunhofer and Steinheil doublet as a frontal lens group). The total system length and magnification ratio was strictly limited by the mechanical design requirements, thus radically restricting the lens design of the required system. The proposed systems match these criteria. Nevertheless, the Keplerian system performance is not satisfactory. In the designs presented, all systems had only spherical surfaces. The

aspherical surfaces would lead to the elimination of residual aberrations. They would also lead to a very high increase in fabrication and metrology expenses. Conversely, the performance of both Galilean systems is far superior. However, if spatial filtering is needed, then the Keplerian system is the only choice, because of the intermediate focal plane. All systems stretch the incoming 30 fs pulse. The shortest pulse stretching is achieved by the Galilean system with the Fraunhofer doublet (153 fs). The poorest result was attained by the Keplerian system (626 fs). Transmissive optics is, in this case, not feasible and similar reflecting alternatives are recommended. The temporal effects of the systems were investigated by VirtualLab Fusion.

Reflective telescopes and reducers

A slightly more complex analysis was conducted in the case of reflective optics. The use of reflective optics in the main beamline is inevitable due to the large aperture beams with fs pulse durations. First, comparison of the “U” and “Z” afocal OAP configurations was performed. Influence of aberrations was shown in both cases. It was demonstrated that the “U” configuration is not feasible due to output beam distortion. Both conventional methods (ray tracing within Zemax OpticStudio) and Geometric Field Tracing Plus (Beta) were used to achieve these results. In the next step the influence of the mirror’s off-axis angles in the “Z” configuration was examined for the case of a 1:1 relay. It was demonstrated how the electric field’s vectorial components change with this angle. Based on these results it is recommended to use the smallest angles possible to fulfill the conditions of image relaying. In the last case scenario, two reflective reducer configurations were demonstrated. The first one is a combination of two concave off-axis parabolic mirrors, whereas the latter one combines a concave and a convex off-axis parabolic mirror. From the geometric point of view the image for both reducers is perfect, without any aberrations. The only residual aberrations are field curvature and distortion. The choice for one reducer over the other is then mainly driven by the mechanical design restrictions and requirements for optical alignment. Convex surfaces are also more difficult to fabricate and control, thus increasing expenses. Demagnification of the input beam was also demonstrated by both VirtualLab Fusion’s techniques – Classic Field Tracing and Geometric Field Tracing Plus (Beta).

Telescopes for beam diagnostics

The main task of the optics in the ELI-Beamlines is, of course, to distribute the laser beam from the source to the target (focal plane). However, the beam needs to be inspected along its path. Thus there is a requirement for a special sort of optics called beam monitoring optics, or telescopes for beam diagnostics. In the case described a design inspired by the similar systems built for Astra Gemini was demonstrated. Economic efficiency was stressed. Thus the first proposed variant of the telescope is a combination of available stock optics. However, the acquired results were not satisfactory. Hence, the custom variant was designed with the aid of Zemax OpticStudio. Customization of the originally used doublet made by Thorlabs leads to far superior results. Correct demagnification of the input beam is demonstrated by using Geometric Field Tracing Plus (Beta) within VirtualLab Fusion.

Beamlines

Out of all the planned beamlines, the stress was put onto L1-E1 (Experimental Hall 1 – Material and biomolecular applications) and L3-E3 (Experimental Hall 3 – Plasma physics). In the case of L1-E1, the possibilities of physical optics based tolerancing were investigated. For example,

beam clipping, decentrations and mirror tilting. Unlike traditional ray tracing methods the SPW operator within VirtualLab Fusion was used. In the case of the L3-E3 system, the focusing part of the beamline was analyzed. Unlike other beamlines, instead of the typically used off-axis parabola, a spherical focusing mirror is employed. This is allowed due to the longer focal length (f -number $\gg 1$), thus the need for a holed folding mirror arises. Calculation of the ideal hole size with respect to the focused power was conducted. Also the encircled energy and the M^2 factor for various hole sizes were determined. After the analysis of the ideal system condition, the influence of surface irregularities was studied. Focal spot sizes for various surface irregularity magnitudes were exposed. In the last step, the influence of the coating stacks was also taken into account. Pulse stretch caused by the coating stacks was calculated. All the results obtained in the beamline simulations were achieved using VirtualLab Fusion. Post-processing and the generation of some of the plots was done with the help of MATLAB.

Specific results of this PhD thesis to which the author contributed are as follows:

- Determination of VirtualLab Fusion's efficiency in order to fulfill the BPM requirements – the author tested the software on several case scenarios that he prepared. In the majority of cases VirtualLab Fusion provided a step up from previously used ray-tracing methods. The author also assessed the ability of the newly introduced Geometric Field Tracing Plus (Beta), especially in the case of reducers. With the use of this new technique, the exact values of all field components were determined without the numerical effort of diffractive techniques. Unfortunately the author was not able to conduct further simulations with high NA off-axis parabolas for final focusing. This was probably because of the extraordinarily large size of both optics and beams that lead to extraordinary numerical effort. The case scenario used for smaller sizes of the beam and optics performed well, but finally was not incorporated into the thesis.
- The author has shown the influence of diffraction on the high order super-Gaussian beams of square aperture and analyzed the influence of apodization on the focusing of these beams. He demonstrated that the order 20 beam does not suffer from the diffraction effects over the required optical path distance in comparison with higher orders. For this purpose a rigorous simulation technique was used (SPW operator), which is superior to those typically used by physical optics propagation techniques within common ray-tracing software bundles.
- The author prepared several optical design suggestions, especially for reducers/expanders. The author has shown the geometric aberrations of the systems, as well as the temporal effects implied by transmissive systems. While the geometric aberrations can be well controlled by a suitable optical design, as shown by the author, the behaviour in the temporal domain is mainly limited by the GVD of the glass used, and its necessary thickness. This field tracing technique allowed the author to control the influence of the system on the fs pulses and to determine the pulse stretching caused by transmissive systems. The author calculated the exact pulse duration of the pulses reduced by these optical systems. Based on this information, the author decided that transmissive systems are not feasible for the beamline. Transmissive systems stretch the pulse above the impermissible level. Access to the temporal domain is an improvement over the ray-tracing method, thus demonstrating new possibilities in the workflow of optical engineers. These new possibilities are characterized by access to all field components and to the temporal domain allowing the system to be tailored for the use with ultra-short pulses. The author also considered the specific

requirements of the optical systems, like the total length of the system to fit inside the beamline.

- The author analysed the influence of possible relay system shapes and their influence on image relaying and concluded that the off-axis angle needs to be minimized due to the acquired values of the electric field components in the output.. Also, the “U” shape of the relay system is not feasible at all due to the sum of both parabolas’ astigmatism.
- The author suggested a design for a beam diagnostic telescope based on the design of a similar system used with Astra Gemini. Two versions of the telescope were prepared by the author – one with commercial optical components only, and the second one with a custom doublet introduced, which highly improved the image quality of this demagnifying system. After the improvement, diagrams fit well inside the Airy disk radius. The system satisfies the requirement to demagnify the beam to the size of a standard CCD used inside the Shack-Hartmann sensor made by Thorlabs, thus allowing for the measurement of the wavefront error for the beam behind the leak mirror.
- The author used the method of Field Tracing for a tolerancing analysis of the beamline, and determined the proper hole size for the folding mirror inside the beamline in order to achieve the maximum peak fluence of the focused beam using the same approach. He also determined the amount of encircled energy and the beam quality factor. Such calculations are very important for finding the required precision of gimbals, linear stages and other opto-mechanical systems and devices. The author also considered the influence of surface irregularities and coatings.

9 Conclusions and Future Work

In the beginning of the author's work there was a question of which software could be used to aid in the endeavor of ELI-Beamlines. One of the software bundles being tested during the preparation of the author's master thesis was LightTrans VirtualLab, among others. Despite of the common use of Zemax OpticStudio, there are some case scenarios that cannot be investigated with the simple geometric optics approach. Hence the combined use of these software bundles seems like an excellent solution. Zemax OpticStudio is well established software used for optical design. VirtualLab Fusion is an advanced optical modeling software based on the physical optics approach. However, it lacks classical design features that optical engineers are used to handling. With their combined use shown in this dissertation, a new perspective on optical design is gained.

Since the first version of VirtualLab Fusion used within ELI-Beamlines, a lot of new features were added by the developers. Some of them are also inspired by the needs of ELI-Beamlines. The author also had the opportunity to be involved in the development process while working as an intern on Prof. Wyrowski's team in Jena, Germany.

The reader can consider this dissertation from two different perspectives. The first perspective is software related, while the second one is optical system related. It needs to be stressed that this dissertation shows the very first official application of VirtualLab Fusion inside a high peak power laser facility.

In this thesis a new optical workflow was established. All strengths and weaknesses of both software bundles were pinpointed and the workflow was adjusted accordingly. In the case of VirtualLab Fusion, many features were improved while this dissertation was being written. A part of the author's work on the team was the preparation of various case scenarios and the assessment of new features and improvements. Some of these case scenarios were described in this dissertation.

From the system perspective, the performance of various systems to be implemented within ELI-Beamlines were analyzed, mainly the reducers, both transmissive and reflective. Telescopes for beam diagnostics were also presented in this thesis. Thorough analysis using classical aberration theory, with a combination of physical optics approaches, was presented, thereby demonstrating the need for the parallel use of Zemax OpticStudio with VirtualLab Fusion. For investigation of temporal effects, VirtualLab Fusion was the leading analysis tool. Also, the newly introduced feature, Geometric Field Tracing Plus (Beta), proved to be useful in the situations where the numerical effort for Classic Field Tracing was too high, or when the diffraction effects did not need to be included. Still, all of the electromagnetic field components are, even with this new technique, always available while the beam propagates through the system.

The first simulation, which was related to the focusability of the super-Gaussian beams, should serve as an insight for experimental teams, so that they will learn what the physical limit they should expect for focusing these beams onto their targets is.

Several optical design related recommendations emerge from the simulations described in the text of this dissertation. As demonstrated, transmissive reducers are not feasible for the L1 beamline due to the excessive pulse stretching they are causing, thus the design should lead to reflective systems only. Another recommendation is related to reflective relay telescopes and reducers. The "U" configuration of the OAPs is not recommended at all, since the output beam is distorted. For the "Z" configuration, the off-axis angles were analyzed. The optical design of such systems should lead to the minimalization of this value. An example was also presented of a beam diagnostic telescope that can be used practically. It is highly recommended to use customized negative NIR doublets in these telescopes because they improve the performance of the telescope drastically, without creating too much additional financial expense. Finally, the ideal size of the hole inside the folding mirror was calculated to achieve maximum power.

In the future, simulations should be step by step improvements towards more realistic models, including all system components and features. Also, the final focusing OAPs should be included in the simulations with femtosecond pulses. Some of these calculations will most likely require the computing power of supercomputers or clusters of computers, and are not expected to be done in the office workstation, like all the simulations presented throughout this dissertation.

It is not within the authority of this author to decide whether the VirtualLab Fusion will be permanently used within the ELI-Beamlines. The software proved its usefulness numerous times. However, the BPM project, which had the task of implementing the software has been officially cancelled by the director of Institute of Physics. Decision made was not to purchase the performance software, and especially its future custom development for the purposes of the ELI-Beamlines. Insufficient funds to cover this project were the reason for the decision. Nevertheless, a few licenses of the VirtualLab were bought and some employees still continue in their use, including the author.

References

- [1] ELI-Beamlines. [online]. [ref. 2015-09-14]. Available from: <http://www.eli-beams.eu/>
- [2] MOUROU, G. A., KORN, G., SANDNER, W., COLLIER, J. L. (Eds.): ELI - Extreme Light Infrastructure Whitebook, Science and Technology with Ultra-Intense Lasers, THOSS Media GmbH, Berlin, 2011.
- [3] MORRISSEY, M.: ELI-Beamlines Requirements of a Beam Propagation Method Software [Adobe Acrobat slides], Workshop: Beam Propagation Method Softwares for Pulse Lasers, Prague, 2014.
- [4] STANKE, L.: Application of optical elements for temporal and spatial transformation of ultra-short and ultra-intense light pulses, Univerzita Palackého v Olomouci, Přírodovědecká fakulta, Olomouc, 2012.
- [5] Applied Computational Optics group. [online]. [ref. 2015-09-14]. Available from: <http://www.applied-computational-optics.org>
- [6] LightTrans. [online]. [ref. 2015-09-14]. Available from: <http://www.lighttrans.com/>
- [7] Wyrowski Photonics. [online]. [ref. 2015-09-14]. Available from: <http://www.wyrowski-photonics.com/>
- [8] WYROWSKI, F., HELLMANN, C.: Geometrical Optics Reloaded, DGaO Proceedings 2015. Available from: http://www.dgao-proceedings.de/download/116/116_h2.pdf,
- [9] MALACARA, D., MALACARA, Z.: Handbook of Optical Design, Second Edition. Marcel Dekker, Inc., New York, 2004.
- [10] LAIKIN, M.: Lens Design, Third Edition, Revised and Expanded, Marcel Dekker, Inc., New York, 2001.
- [11] WALKER, B. H.: Optical Design for Visual Systems, SPIE, Bellingham, 2000.
- [12] LIANG, R.: Optical Design for Biomedical Imaging, SPIE, Bellingham, 2010.
- [13] TRÄGER, F. (Editor): Springer Handbook of Lasers and Optics, Springer Science+Business Media, LLC, New York, 2007.
- [14] HUNT, J. T., GLAZE, J. A., SIMMONS, W. W., RENARD, P. A.: Suppression of self-focusing through low-pass spatial filtering and relay imaging, *Applied Optics* **17**, pp. 2053–2057, 1978.
- [15] HUNT, J. T., RENARD, P. A. (1979). U.S. Patent No. 4,158,176.
- [16] BASS, M. (Editor): Handbook of Optics, Volume I, Third Edition. McGraw-Hill, New York, 2010.
- [17] KING, H. C.: The History of the Telescope, Dover Publications, Inc., Mineola, 2003.
- [18] WILSON, R. N.: Reflecting Telescope Optics I, Springer-Verlag, New York, 1996. doi: 10.1007/978-3-662-03227-5
- [19] MANLY, P. L.: Unusual Telescopes, Cambridge University Press, Cambridge, 1991.
- [20] STANKE, L., THAKUR, A., MORRISSEY, M., KHIKHLUKHA, D., LE GARREC, B.: Role of Beam Propagation Method (BPM) Software in ELI-Beamlines, Poster presented at the ELI Scientific Challenges 2015.
- [21] WYROWSKI, F., KUHN, M.: Introduction to field tracing, *Journal of Modern Optics* **58**, pp. 449-466, 2011. doi: 10.1080/09500340.2010.532237
- [22] Zemax LLC. [online]. [ref. 2015-11-09]. Available from: <http://www.zemax.com/>

- [23] OpticStudio 15 Help Files, Zemax, LLC, 2015.
- [24] GOODMAN, J. W.: Introduction to Fourier Optics, McGraw-Hill, New York, 1968.
- [25] LAWRENCE, G. N.: Optical Modeling, *Applied Optics and Optical Engineering* **11**, pp. 125-200, 1992.
- [26] LightTrans VirtualLabTM User's Manual. LightTrans GmbH, Jena, 2015.
- [27] Wyrowski VirtualLab User's Manual. Wyrowski Photonics UG (haftungsbeschränkt), Jena, 2015.
- [28] KUHN, M., WYROWSKI, F., HELLMANN, C.: Non-sequential optical field tracing. *Advanced Finite Element Methods and Applications* **66** of *Lecture Notes in Applied and Computational Mechanics*, pp. 257–273. Springer Berlin Heidelberg, 2013.
- [29] Wyrowski VirtualLab Fusion Release Notes. [online]. [ref. 2015-11-19]. Available from: <http://www.lighttrans.com/>
- [30] MAHAJAN, V. N.: Optical Imaging and Aberrations, Part I, Ray Geometrical Optics, SPIE Press, Bellingham, 1998.
- [31] MAHAJAN, V. N.: Optical Imaging and Aberrations, Part II, Wave Diffraction Optics, Second Edition, SPIE Press, Bellingham, 2011.
- [32] MAHAJAN, V. N.: Optical Imaging and Aberrations, Part III, Wavefront Analysis, SPIE Press, Bellingham, 2013.
- [33] MAHAJAN, V. N.: Strehl ratio for primary aberrations: some analytical results for circular and annular pupils. *J. Opt. Soc. Am.* **72** (9), pp. 1258–1266, 1982.
- [34] STREHL, K.: Über Luftschlieren und Zonenfehler, *Z. Instrumentenk.* **22**, pp. 213–217, 1902.
- [35] DRIGGERS, R. G. (ed.): Encyclopedia of Optical Engineering, Volume 2: Las-Pho, Marcel Dekker, Inc., Adelphi, 2003.
- [36] PALATKA, M.: OAP combination analysis, PDF slides, 2016.
- [37] HOOKER, C.: Achromatic Beam Diagnostic Telescopes for Astra Gemini, PDF document.
- [38] Edmund Optics Protected Gold, Parabolic Mirror. [online]. [ref. 2016-05-28]. Available from: <http://www.edmundoptics.com/optics/>
- [39] ATC Astro Telescope Company, a.s., ATC N 450/f2000. [online]. [ref. 2016-05-28]. Available from: <http://www.atc-astro.eu/eshop/atc-n-450f2000.html>
- [40] Thorlabs Unmounted Achromatic Doublets. [online]. [ref. 2016-05-28]. Available from: http://www.thorlabs.de/newgrouppage9.cfm?objectgroup_id=259
- [41] ISO 11146-2:2005 Lasers and laser-related equipment – Test methods for laser beam widths, divergence angles and beam propagation ratios – Part 2: General astigmatic beams.
- [42] SIEGMANN, A. E.: How to (Maybe) Measure Laser Beam Quality, Tutorial presentation at the Optical Society of America Annual Meeting Long Beach, California, October 1997 [online]. [ref. 2016-05-28]. Available from: <http://web.archive.org/>
- [43] LAWSON, J. K., AIKENS, D. M., ENGLISH, R. E. Jr., WHISTLER, W. T., HOUSE, W., NICHOLS, M. A.: Surface figure and roughness tolerances for NIF optics and the interpretation of the gradient, P-V wavefront and RMS specifications. *Proc. of SPIE* **3782** Optical Manufacturing and Testing III, 1999.
- [44] KUMLER, J. J., CALDWELL, J. B.: Measuring surface slope error on precision aspheres. *Proc. of SPIE* **6671**, Optical Manufacturing and Testing VII, 2007.
- [45] OpticStudio 15 Help Files, Zemax, LLC, 2015.
- [46] LASEROPTIK GmbH. [online]. [ref. 2016-05-28]. Available from: <http://laseroptik.de/>

List of Author's Publications

In reviewed journals with impact factor

STANKE, L., ŠMÍD, P., HORVÁTH, P., ESPI correlogram analysis by two stage application of wavelet transform with use of intensity thresholding, *Optik* (IF = 0.670), 2015, 7–8 (126), pp. 865–870. doi:10.1016/j.ijleo.2015.01.037

Available from:

<http://www.sciencedirect.com/science/article/pii/S0030402615000716>

In preparation for *Rev. Sci. Instrum.*: STANKE, L., THAKUR, A., ŠMÍD, M., GU, Y., FALK, K., Optical simulations of laser focusing for optimization of laser-produced betatron

In reviewed journals without impact factor

STANKE, L., *ELI Scientific Challenges 2015*, *Jemná mechanika a optika*, 2015, 60 (11-12), pp. 336.

STANKE, L., *Seminář o výrobě přesné optiky [Workshop on the precision optics manufacturing]*, *Jemná mechanika a optika*, 2014, 59 (4), pp. 123.

STANKE, L., ŠMÍD, P., HORVÁTH, P., Dvoufázová aplikace vlnkové transformace pro filtraci šumu a fázovou analýzu ESPI korelogramů s využitím intenzitního prahování (II. část) [Two stage application of wavelet transform for denoising and phase analysis of ESPI correlograms with use of intensity threshold, part II], *Jemná mechanika a optika*, 2014, 59 (5), pp. 133–137.

STANKE, L., ŠMÍD, P., HORVÁTH, P., Dvoufázová aplikace vlnkové transformace pro filtraci šumu a fázovou analýzu ESPI korelogramů s využitím intenzitního prahování (I. část) [Two stage application of wavelet transform for denoising and phase analysis of ESPI correlograms with use of intensity threshold, part I], *Jemná mechanika a optika*, 2014, 59 (4), pp. 122–123.

STANKE, L., CHLUP, F., *Přehled technologie laserových dálkoměrů v AČR [Review of Laser Rangefinder Technology in the Czech Army]*, *Jemná mechanika a optika* 2013, 58 (5), pp. 152 – 157.

STANKE, L., *Aplikace optických prvků pro transformaci ultrakrátkých intenzivních světelných pulzů [Application of optical elements for transformation of ultrashort intensive light pulses]*, *Jemná mechanika a optika* 2012, 57 (9), pp. 256 – 257.

Research reports

THAKUR, A., STANKE, L., *Simulation Results, L3-E3: Holey Mirror Simulations*, 2016, ELI Beamlines Internal Technical Report, Institute of Physics of the Czech Academy of Sciences.

FENTE, G. M., ZULIC, H., THAKUR, A., STANKE, L., MORISSEY, M., KHIKHLUKHA, D., *Calculations, Summary of Ongoing Optical Simulations*, 2016, ELI Beamlines Internal Technical Report, Institute of Physics of the Czech Academy of Sciences.

IVANOV, G., STANKE, L., PAVLÍČEK, P., HRABOVSKÝ, M., Opticko-mecha-nická sestava měřící triangulační jednotky k měření clonek reaktoru pro JE, Univerzita Palackého, Přírodovědecká fakulta, Olomouc, 2014, summary research report, RIV/61989592:15310/14:33151928.

SCHOVÁNEK, P., KITTLER, M., PECH, M., PALATKA, M., STANKE, L., Vývoj technologie frézování optických prvků pomocí materiálů firmy KGS, Univerzita Palackého, Přírodovědecká fakulta, Olomouc, 2013, summary research report, RIV/61989592:15310/13:33147617.

Conference contributions

BORNEIS, S. H., ACCARY, J.-B., BRABEC, L., BUCKA, M., CALDERON, S., de LUIS, D., EIMERL, D., KORN, G., HEILAND, D., HEJDUKOVÁ, J., HVĚZDA, R., KHIKHLUKHA, D., KOROUŠ, P., KRAMER, D., LAŠTOVIČKA, T., LAUB, M., LEVATO, T., MARGARONE, D., MORRISSEY, M. J., PEYROT, D. A., PUST, L., RUS, B., ŘÍDKÝ, J., SOKOL, M., STANKE, L., THAKUR, A., VACULÍK, J., WEBER, S., ZIANO, R., ELI-beamlines and its ultrahigh intensity beam transport system. (Plenary presentation, Mini-Symposium: Review of Large-Scale, High-Power Laser Facility Projects I, Laser-Induced Damage in Optical Materials 2016, Millennium Harvest House Hotel Boulder, Colorado, United States 25 - 28 September 2016).

STANKE, L., THAKUR, A., MORISSEY, M., KHIKHLUKHA, D., LE GARREC, B., Role of Beam Propagation Method (BPM) Software in ELI-Beamlines, ELI Scientific Challenges 2015, (October 19-22, 2015), Zámek Štířín, (poster).

STANKE, L., KŘEPELKA, J., PALATKA, M., SCHOVÁNEK, P., HRABOVSKÝ, M., Application of optical elements for temporal and spatial transformation of ultra-short and ultra-intense light pulses, Proc. SPIE 8697, 18th Czech-Polish-Slovak Optical Conference on Wave and Quantum Aspects of Contemporary Optics, 869702 (December 18, 2012); doi: 10.1117/12.2006163 (WOS:000319864100002) (poster and proceedings)

STANKE, L., HORVÁTH, P., ŠMÍD, P., HRABOVSKÝ, M., The use of 1-bit numerical correlation in the measurement of an object's translation by speckle correlation, OPTIMESS 2012, (April 4-5, 2012) Optical Measurement Techniques for Systems&Structures, eds. J. Dirckx, J. Buytaert, pp. 391 - 400 (poster and proceedings) (WOS:000319343800039)

Utility models

ŠMÍD, P., HORVÁTH, P., HRABOVSKÝ, M., STANKE, L., Zařízení pro bezkontaktní detekci absolutní polohy pohybujícího se předmětu s využitím jevu koherenční zrnitosti [Apparatus for contactless detection of moving object absolute position by making use of speckle], 2013-27545, 25644.

Patents

HORVÁTH, P., ŠMÍD, P., HRABOVSKÝ, M., STANKE, L., Způsob bezkontaktní detekce absolutní polohy pohybujícího se předmětu s využitím jevu koherenční zrnitosti a zařízení k provádění tohoto způsobu [Method of contactless detection of moving object absolute position by making use of speckle phenomenon and apparatus for making the same], 2013-164, CZ 304 207 (B6).

Others

STANKE, L., Metodika broušení optických elementů na CNC strojích Zeeko IRP-800G, rigorous thesis, Univerzita Palackého, Přírodovědecká fakulta, Olomouc, 2014.

STANKE, L., Elektronická interferometrie na bázi koherenční zrnitosti a její aplikace, master's thesis, Univerzita Palackého, Přírodovědecká fakulta, Olomouc, 2013.

STANKE, L., Aplikace optických prvků pro časovou a prostorovou transformaci ultrakrátkých intenzivních světelných pulsů, master's thesis, Univerzita Palackého, Přírodovědecká fakulta, Olomouc, 2012.

STANKE, L., Aplikace optických prvků pro časovou a prostorovou transformaci ultrakrátkých intenzivních světelných pulsů, Annual student competition „O cenu děkana 2012“ (“The dean's prize 2012”), VUP, Olomouc, 2012.

STANKE, L., Vliv typu numerické korelace struktur koherenční zrnitosti na měření translace zkoumaného předmětu metodou na korelace polí koherenční zrnitosti, bachelor's thesis, Univerzita Palackého, Přírodovědecká fakulta, Olomouc, 2010.

STANKE, L., Vliv typu numerické korelace struktur koherenční zrnitosti na měření translace zkoumaného předmětu metodou na korelace polí koherenční zrnitosti, Annual student competition „O cenu děkana 2010“ (“The dean's prize 2010”), VUP, Olomouc, 2010.